



**HAL**  
open science

# Development and Validation of a 3D Computational Tool to describe Damage and Fracture due to Alkali-Silica Reaction in Concrete Structures

Isabelle Comby Peyrot

► **To cite this version:**

Isabelle Comby Peyrot. Development and Validation of a 3D Computational Tool to describe Damage and Fracture due to Alkali-Silica Reaction in Concrete Structures. Engineering Sciences [physics]. École Nationale Supérieure des Mines de Paris, 2006. English. NNT : . pastel-00002096

**HAL Id: pastel-00002096**

**<https://pastel.hal.science/pastel-00002096>**

Submitted on 5 Jun 2007

**HAL** is a multi-disciplinary open access archive for the deposit and dissemination of scientific research documents, whether they are published or not. The documents may come from teaching and research institutions in France or abroad, or from public or private research centers.

L'archive ouverte pluridisciplinaire **HAL**, est destinée au dépôt et à la diffusion de documents scientifiques de niveau recherche, publiés ou non, émanant des établissements d'enseignement et de recherche français ou étrangers, des laboratoires publics ou privés.



## REMERCIEMENTS

Cette thèse s'est effectuée en collaboration entre le Centre de Mise en Forme des Matériaux (CEMEF) de l'École Nationale Supérieure des Mines de Paris et le Département Génie Civil et Environnemental (GCE) de l'École des Mines de Douai. Je remercie Monsieur Jean-Loup Chenot, Directeur du CEMEF et Monsieur Denis Damidot, Chef du Département GCE, de m'avoir donné l'occasion de réaliser ce travail.

Je tiens également à remercier Madame Angélique Vichot, Directrice de la Recherche de l'Association Technique de l'Industrie des Liants Hydrauliques (ATILH) et ses partenaires industriels pour s'être investis dans ce projet.

Mes premiers remerciements vont à Monsieur Jacky Mazars qui m'a fait l'honneur d'accepter d'être Président de mon jury de thèse. Je le remercie vivement pour l'intérêt qu'il a porté à mon travail. Mes remerciements les plus vifs s'adressent à Monsieur Christian La Borderie et Monsieur Erik Schlangen qui ont accepté d'être rapporteurs de ma thèse ainsi qu'à Madame Angélique Vichot pour sa participation au jury.

Je tiens à exprimer ma profonde reconnaissance à mes Directeurs de thèse avec qui j'ai eu la chance de travailler depuis le DEA: Eric Garcia-Diaz, Fabrice Bernard, Pierre-Olivier Bouchard et François Bay. J'ai apprécié tout au long de ces trois années les échanges scientifiques passionnants dans une ambiance amicale jusqu'à tendre parfois vers un processus incroyable où François arrivait à exprimer ce qu'Eric percevait! Je vous remercie tous pour votre enthousiasme, votre disponibilité et l'énergie que vous avez placée dans ce projet. Merci Pierre-Olivier pour la confiance que tu m'as accordée en me « léguaant » le cours sur la Rupture durant deux années. Et un grand Merci à François pour ton aide précieuse pendant cette thèse mais aussi pour l'après-thèse. Je remercie également tous les chercheurs du groupe M3P pour leur disponibilité et leur bonne humeur ainsi que tous les chercheurs du Département GCE-Douai à qui je dois notamment la découverte des spécialités culinaires (certains se souviennent encore de la tarte au Maroual). Mille mercis à Tous.

Je souhaiterais également remercier toutes les personnes qui ont m'ont aidé au cours de ce travail. Je remercie Marie-Francoise Guenegan, Sylvie Massol, Geneviève Anseeuw, Christiane Collart et Carole Delchambre pour leur disponibilité, Francis Fournier, Emmanuel Levrat pour le support informatique, Brigitte Hanot et Sylvie Michel pour leur aide dans ma recherche bibliographique, Christophe Cappalaere, Mickael D'Helft, Guillaume Potier pour leur aide pendant la campagne expérimentale et de nombreux autres !

Je voudrais remercier mes collègues de travail que j'ai eu le plaisir de côtoyer durant ces trois années au CEMEF et au Département GCE et qui ont rendu très agréables ces trois années de travail. Je pense à Stéphane, Audrey, Aliza, Ludovic, Sébastien, Claire avec qui j'ai eu la chance de partager le bureau, mais aussi Antoine, Carole, Olivier, Elise, Mehdi, Christophe et Frédéric. Je souhaite enfin bonne chance à Raphaëlle pour les trois prochaines années.

Merci à mes amis toujours présents. Je pense aux ziziteviens (Juliette, Jocelyn, Fab, Yasmine, Manuella, Jean-Luc, Ludo from Sollies, JP), à Isa, Sylvain, à Véro, Nico, Marianne, Ben, Anne-Laure, Thom, Tony et pardon à ceux que j'oublie! Toutes mes pensées vont également vers mon amie très chère Charlotte qui me manque beaucoup. Merci à tous pour votre soutien sans faille!

Un immense MERCI à toute ma famille. De simples mots ne suffiront pas à les remercier pour tous leurs encouragements et leurs générosités mais je tiens à remercier ma Grand-Mère, Marie-Ange, Abel, Martine pour leur soutien permanent et leur présence le jour de la soutenance de thèse. Je remercie aussi mes deux frères que j'adore, Guillaume et Patrick. Je voudrais aussi bien sur remercier ma Mère sans qui je ne serais pas ici et je n'aurais jamais pu réaliser mes études, ses encouragements et son soutien permanent durant toutes ces années. Merci enfin à mon mari, Matthieu, qui m'a constamment encouragé et aidé, porté et parfois même supporté :). Merci pour ton soutien et tout ton Amour ! Cette thèse vous est dédiée.

## Abstract

# Development and Validation of a 3D Computational Tool to describe Damage and Fracture due to Alkali-Silica Reaction in Concrete Structures

Isabelle Comby<sup>a,b</sup>

<sup>a</sup> *Centre de Mise en Forme des Matériaux, Ecole des Mines de Paris ; UMR 7635 CNRS, BP 207, 06904 Sophia-Antipolis Cedex, France*

<sup>b</sup> *Ecole des Mines de Douai, 941, avenue Charles Bourseul, BP 938, 59508 Douai Cedex, France*

The Alkali-Silica Reaction (ASR) induces aggregates swelling leading to irreversible degradation of concrete structures. Modelling damage and cracks in a 3D concrete structure submitted to ASR is hence of prime importance in civil engineering. FEMCAM (Finite Element Model for Concrete Analysis Method) software has been developed within this framework to model 3D numerical concrete. In this thesis, we have developed a mesoscale approach where concrete is considered as a heterogeneous material with two main phases: the mortar paste and aggregates. An elastic damage law has been successfully implemented to take into account the mortar paste behavior. The non local Mazars model with an implicit formulation is hence used to deal with damage. This model requires determining elastic and damage parameters. In this way, an experimental campaign has been carried out at the Civil Engineering Department of the Ecole des Mines de Douai to identify concrete material parameters. These experimental results have been compared with numerical ones through the inverse analysis modulus RheOConcrete. Applications on concrete (compression tests, three point bending tests and “Brazilian” splitting tests) have been also performed. The influence of the distribution, diameters and volume of aggregates on concrete behavior has been studied. The comparison between the numerical global responses of a concrete sample submitted to ASR and experimental ones are available. These comparisons are based on previous experimental works carried out at the Ecole des Mines de Douai. It leads to compare numerical and experimental approaches and to better understand the mechanism of ASR under the control of some parameters.

Finally, we have underlined the importance of describing macrocracks in concrete sample with a great accuracy to improve the model. The last part of this project concerns the implementation and the validation of a 3D Discrete Crack Propagation technique to model explicitly 3D crack propagation.

**Keywords:** Numerical modelling, Concrete, Alkali-Silica Reaction, Damage mechanics, Fracture mechanics, 3D Discrete Crack Approach, Inverse Analysis method, Multi-material structure.

## Résumé

# Développement et Validation d'un Outil Numérique Tridimensionnel pour décrire l'Endommagement et la Fissuration causés par la Réaction Alkali-Silice dans les Structures en Béton

Isabelle Comby<sup>a,b</sup>

<sup>a</sup> Centre de Mise en Forme des Matériaux, Ecole des Mines de Paris ; UMR 7635 CNRS, BP 207, 06904 Sophia-Antipolis Cedex, France

<sup>b</sup> Ecole des Mines de Douai, 941, avenue Charles Bourseul, BP 938, 59508 Douai Cedex, France

La Réaction Alkali-Silice (RAS) est une réaction chimique de dégradation des bétons occasionnant des désordres irréversibles au niveau de l'ouvrage. La modélisation de l'endommagement et de la fissuration d'une structure en béton tridimensionnelle victime de la RAS est donc de première importance en génie civil. Le logiciel FEMCAM (Finite Element Model for Concrete Analysis Method) a été développé dans ce cadre, afin de modéliser le comportement mécanique tridimensionnel des matériaux quasi-fragiles tels que les bétons. Dans cette thèse, nous avons développé une approche mésoscopique où le béton est considéré comme un matériau biphasé en présence de granulats et d'une pâte de mortier. Le modèle non local de Mazars avec formulation implicite a ainsi été implémenté et validé dans notre code Eléments Finis pour rendre compte du comportement élastique endommageable de la pâte de mortier. Nous abordons ensuite l'identification des paramètres élastiques et d'endommagement de ce modèle. Une attention particulière est portée à la campagne expérimentale menée au département Génie Civil de l'Ecole des Mines de Douai. Ces résultats expérimentaux ont été comparés aux résultats numériques via le module d'analyse inverse «RheOConcrete ». Des tests de compression, flexion trois points, essais brésiliens ont été ainsi réalisés. Les exemples d'applications proposés montrent l'influence du volume, de la répartition et du diamètre des granulats sur le comportement du béton. Nous utilisons ces résultats pour analyser les conséquences mécaniques de la RAS sur une éprouvette en béton. Les résultats numériques d'un béton soumis à un gonflement granulaire sont comparés aux résultats expérimentaux obtenus à l'Ecole des Mines de Douai. Cela permet de vérifier non seulement la cohérence du modèle numérique mais aussi de mieux comprendre l'influence de certains paramètres sur le mécanisme de la RAS. Enfin, nous soulignons l'importance de décrire avec précision les macrofissures générées par la réaction chimique. La dernière partie du mémoire concerne l'implémentation et la validation de la fissuration discrète en trois dimensions.

**Mots-clefs:** Modélisation numérique, Béton, Réaction Alkali-Silice, Mécanique de l'Endommagement, Mécanique de la Rupture, Approche de fissuration discrète en 3D, matériau composite, méthode d'analyse inverse.

## CONTENTS

### CHAPTER 1 : GENERAL INTRODUCTION

1.1	CONTEXT	1-1
1.2	STUDY DEVELOPMENT	1-2
1.3	PHD MANUSCRIPT OUTLINE	1-6

### CHAPTER 2 : A REVIEW OF MODELS FOR CONCRETE

2.1	INTRODUCTION	2-8
2.2	EXPERIMENTAL BEHAVIOR	2-8
2.3	A STATE OF THE ART REVIEW ON MODELS DESCRIBING THE MECHANICAL BEHAVIOR OF CEMENT-BASED MATERIALS (MORTAR OR CONCRETE)	2-12
2.4	STATE OF THE ART REVIEW ON HETEROGENEOUS MATERIALS	2-25
2.5	CONCLUSIONS	2-30

### CHAPTER 3 : IMPLEMENTATION AND VALIDATION OF A THREE DIMENSIONAL HETEROGENEOUS ELASTIC DAMAGE PROBLEM FOR CONCRETE

3.1	THE FEMCAM SOFTWARE	3-33
3.2	MODELLING OF CONCRETE	3-34
3.3	THE ELASTIC DAMAGE MODEL USING A MIXED-VELOCITY PRESSURE FORMULATION	3-39
3.4	SELECTION OF THE MODEL AND NUMERICAL STRATEGY	3-48
3.5	CONCLUSIONS	3-62

### CHAPTER 4 : IDENTIFICATION OF CONCRETE BEHAVIOR: THE INVERSE ANALYSIS MODULUS AND THE EXPERIMENTAL CAMPAIGN

4.1	INTRODUCTION	4-64
4.2	INVERSE ANALYSIS MODULUS	4-65
4.3	PARAMETERS IDENTIFICATION	4-68
4.4	EXPERIMENTAL CAMPAIGN	4-72
4.5	SENSITIVITY ANALYSIS	4-84
4.6	CONCLUSIONS	4-92

### CHAPTER 5: IDENTIFICATION OF CONCRETE BEHAVIOR: RESULTS AND SENSITIVITY ANALYSIS ON AGGREGATES PARAMETERS

5.1	INTRODUCTION	5-94
5.2	STARTING HYPOTHESES	5-94
5.3	CONCRETE PARAMETERS: FIRST TECHNIQUE	5-94
5.4	CONCRETE PARAMETERS: SECOND TECHNIQUE	5-107
5.5	APPLICATION TO THE "BRAZILIAN" SPLITTING TEST	5-120

5.6	SENSITIVITY ANALYSIS ON AGGREGATES PARAMETERS	5-123
5.7	CONCLUSIONS	5-131

## **CHAPTER 6 : MODELLING OF THE MECHANICAL EFFECTS OF THE ASR**

6.1	INTRODUCTION	6-133
6.2	DESCRIPTION OF THE MODEL PROPOSED BY THE CIVIL ENGINEERING DEPARTMENT OF THE ECOLE DES MINES DE DOUAI	6-134
6.3	THE SELECTED MODEL IN FEMCAM	6-137
6.4	MODELLING OF THE CONSEQUENCES OF THE ASR AFTER SEVEN DAYS	6-141
6.5	CONCLUSIONS	6-154

## **CHAPTER 7 : IMPROVEMENT OF THE DESCRIPTION OF THE ASR THROUGH THE DISCRETE CRACK APPROACH**

7.1	INTRODUCTION	7-157
7.2	STATE OF THE ART REVIEW ON 3D NUMERICAL APPROACHES OF FRACTURE	7-158
7.3	IMPLEMENTATION OF THE DISCRETE CRACK APPROACH IN THE FINITE ELEMENT CODE FEMCAM	7-170
7.4	VALIDATION OF THE 3D CRACK MODEL	7-186
7.5	CONCLUSIONS	7-196

## **CHAPTER 8 : GENERAL CONCLUSION AND PERSPECTIVES**

8.1	CONCLUSIONS	8-198
8.2	PERSPECTIVES	8-200

<b>ANNEXES</b>	A-1
<b>REFERENCES</b>	R-1

## LIST OF SYMBOLS

(only the most frequently used)

$\tilde{c}$	Characteristic parameter for the implicit formulation
$D$	Scalar damage variable in isotropic damage model
$da$	Crack length
$d_{\max}$	Maximum size of the aggregate
$d_{\min}$	Minimum size of the aggregate
$dw$	Crack opening
$E$	Young modulus for concrete
$E_0$	Initial Young modulus of the compressive uniaxial stress-strain curve
$E^C$	Young modulus of concrete
$E_A^C$	Young modulus for the aggregate
$E^M$	Young modulus for mortar
$E_{MP}^C$	Young modulus for the mortar paste of concrete
$e$	Deviatoric part of the strain tensor
$F$	Reached load
$f$	body forces per mass unit
$G_f$	Fracture energy
$G_C$	Critical Energy Release Rate
$g$	aggregate volume in a volume unit of concrete
$h$	Mesh size
$K_{IC}$	Critical Stress Intensity Factor
$K_I$	Stress Intensity Factor in mode I
$K_{II}$	Stress Intensity Factor in mode II
$K_{III}$	Stress Intensity Factor in mode III
$L$	Tangent modulus
$l_c$	Characteristic length for the integral formulation
$\bar{m}, \mu_F$	Coefficients for the friction law
$p$	Spherical part of the stress tensor
$r$	Distance to the crack front
$s$	Deviatoric part of the stress tensor

$\vec{n}$	Normal to the section surface
$t$	Time
$v$	velocity field
$V_R$	Real volume of aggregates generated with Femcam
$V_T$	Theoretical volume of aggregates in a concrete sample
$\alpha_T, D_T$	Scalar damage variable for tensile damage mechanism
$\alpha_C, D_C$	Scalar damage variable for compressive damage mechanism
$\bar{\alpha}$	Mean compactness of the whole volume
$\Delta t$	Time step
$\varepsilon_1$	First principal strain
$\varepsilon_2$	Second principal strain
$\varepsilon_3$	Third principal strain
$\varepsilon_{D0}$	Initial damage threshold of damage growth
$\varepsilon^{ASR}$	Strain due to the ASR
$\dot{\varepsilon}_{ij}^{ASR}$	Strain velocity induced by the chemical swelling in the aggregate
$\dot{\varepsilon}_{ij}^{el}$	Elastic strain velocity
$\varepsilon_{Ti}$	Principal values of the strains due to positive stresses
$\varepsilon_{Ci}$	Principal values of the strains due to negative stresses
$\tilde{\varepsilon}_{crit}$	Initial crack threshold
$\tilde{\varepsilon}_T^{Crit}$	Initial crack threshold in tension
$\tilde{\varepsilon}_C^{Crit}$	Initial crack threshold in compression
$\chi$	Compressibility modulus
$\nu$	Poisson ratio
$\nu_{MP}^C$	Poisson ratio for the mortar paste of concrete
$\nu_A^C$	Poisson ratio for the aggregate
$\nu^M$	Poisson ratio for mortar
$\mu$	Shear modulus
$\rho$	volumic mass
$\sigma$	Total stress tensor
$\tilde{\sigma}$	Effective stress tensor

$\delta_{ij}$  Identity tensor:  $\delta_{ij} = 1$  if  $i = j$   
 $\delta_{ij} = 0$  if  $i \neq j$

$\sigma_c$  Compression strength

$\sigma_t$  Tension strength

$\sigma_1$  First principal stress

$\sigma_2$  Second principal stress

$\sigma_3$  Third principal stress

$\sigma_0$  Initial stress

## CHAPTER 1 : GENERAL INTRODUCTION

### 1.1 Context

The discovery of the Alkali-Aggregate Reaction (AAR) goes back to the 40's in the United States in concrete pavements. In 1935 Holde observed the existence of chemical reactions between cements and certain aggregates in concrete. Stanton specified in 1940 the nature of the reagents at the origin of the disorders observed. This phenomenon was identified in France only since 1976. In 1993, Hornain classed the AAR in three major types:

- alkali-carbonate reactions;
- alkali-silica reactions (ASR);
- alkali-silicate reactions.

The most frequent reaction is the Alkali-Silica Reaction (ASR). This study will focus on this specific reaction.

The ASR product is a gel that increases in volume. The swelling forces generated may be sufficient to disrupt aggregate and the surrounding concrete, causing expansion, cracking, and associated deterioration. Typically, ASR results in the formation of map-pattern cracking of the concrete. It leads to the following consequences at a macroscopic scale:

- strain and displacement;
- network of cracks or cracks parallel to the armatures;
- Fragments breaking out of the surface (pop-out) [Bournazel 1997];
- A drop in the mechanical properties (mechanical strength and Young modulus);
- The disappearance of lichens and mosses along cracks.

These reactions have the particularity to be localised and distributed randomly in concrete.

Concrete deterioration caused by the ASR is generally slow, but progressive. Cracking generally becomes visible when concrete is five to ten years old. ASR has been implicated in the deterioration of various types of massive concrete structures, including dams, pavements, bridges, and other structures. The ASR is a major damage phenomenon for dams; this is due to the high humidity rate, the important mass of the structure and to the fact that dams do not usually contain steel reinforcement to restrain the expansion. Cracks facilitate the entry of de-icing salt solutions that may cause corrosion of the reinforcing steel, thereby accelerating deterioration and weakening of the structure.

Even though there are no documented cases of concrete structures failing due to ASR, it is a serious form of deterioration. Even since the problem was recognised, everything possible has been done to prevent it, adding mixtures for instance. So far over the last twenty or so years there have been no more major signs of the concrete “cancer” appearing in the newer buildings which have been produced, but there is always time.

Figure 1-1 presents two example of structures submitted to ASR.

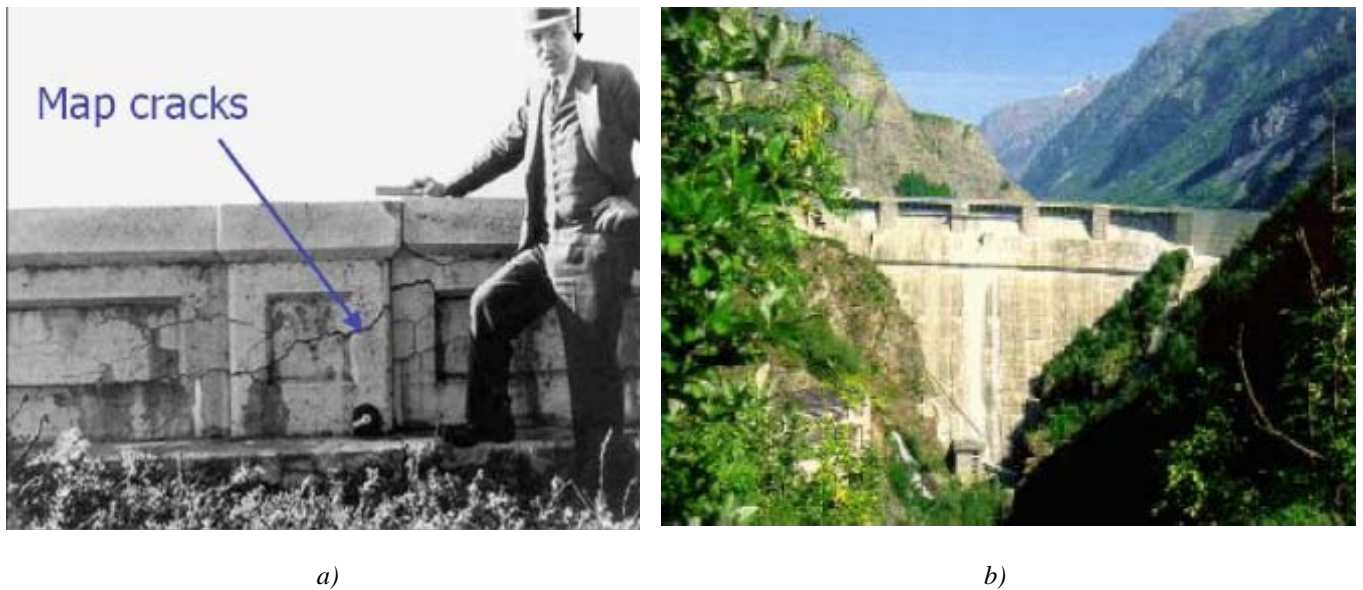


Figure 1-1. a) Thomas E. Stanton next to a wall submitted to ASR - California, 1936; b) Chambon's Dam (first French dam where RAS has been discovered in France, 1976)

**Preventive solutions** (limitation of the alkali content of concrete, the use of supplementary cementing materials, the use of non reactive aggregates: but we have to be sure that the subject aggregates to be used are, in fact, nonreactive etc.) and **curative solutions** (waterproofing of concrete, injection of epoxides resins in cracks in order to limit the effects of the ASR etc.) exists. Moreover some recommendations have been made to avoid ASR as long as possible. **But all these methods are inefficient and cost a lot. Only preventive action could lead to an eradication of this pathology.**

## 1.2 Study development

The objective of the whole projects is:

- To understand the coupling relationship between the chemical reaction and the mechanical consequences on the structures;
- To improve diagnosis tools by defining a methodology based on the quantitative relationship between the chemical advancement of the reaction and the induced swelling.

Works have been already led by the Ecole des Mines de Douai (GC-Douai) on flint aggregates from almost ten years. The used methodology has clarified the coupling relationship between the chemical advancement and the macroscopic swelling. Now it is time to consider a numerical approach of this phenomenon. This modelling is developed within the framework of collaboration between the CEMEF ("Ecole des Mines de Paris") and the GC-Douai of the Ecole des Mines de Douai. This type of modelling induces a coupling between the chemical reaction and the swelling, knowledges on the mechanical degradation of the material, concept of cracks and multicracks. **The aim of the numerical approach is to**

understand the mechanism of the ASR under the controls of some parameters (hydration, number of aggregates, shapes of the aggregates, formulation etc.) which is difficult to analyse from the experimental side. In this way it is important to define in a first time the framework of this work.

### 1.2.1 Which scale can be used to describe the mechanical consequences of the ASR with the best accuracy?

Figure 1-2 divides the three main scales in concrete. With the type of computer facilities available today it is impossible to describe the reaction from the micro to the macro scale. It is then necessary to do some hypotheses.

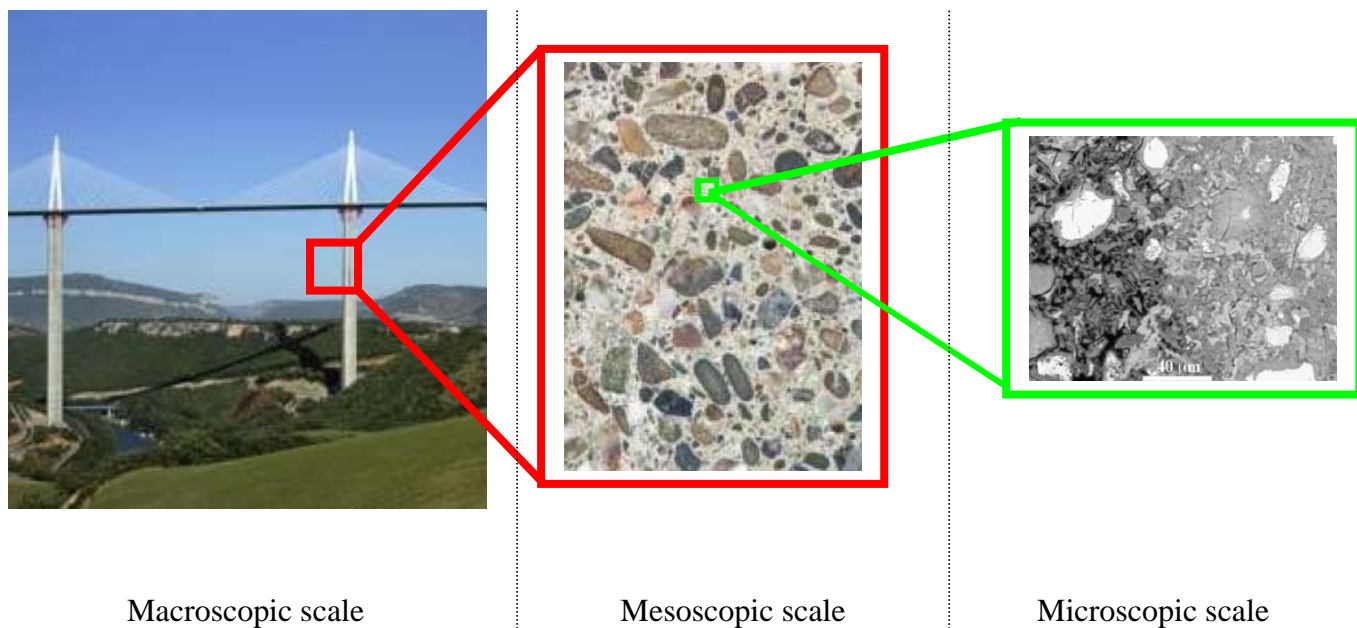


Figure 1-2. From the macroscopic scale (Millau viaduct, France) to the microscopic scale.

At a macroscopic scale, the heterogeneous aspect of concrete is neglected. This level is useful in the framework of study of behavior concrete at a structural level.

At a microscopic scale local properties and type of cement (water-cement ratio, temperature, porosity, moisture content and hydration degree) are studied to understand the complex physical, chemical and mechanical behavior of the hardened cement paste.

At a mesoscopic scale, three main phases appear [Bentz et al. 1995]:

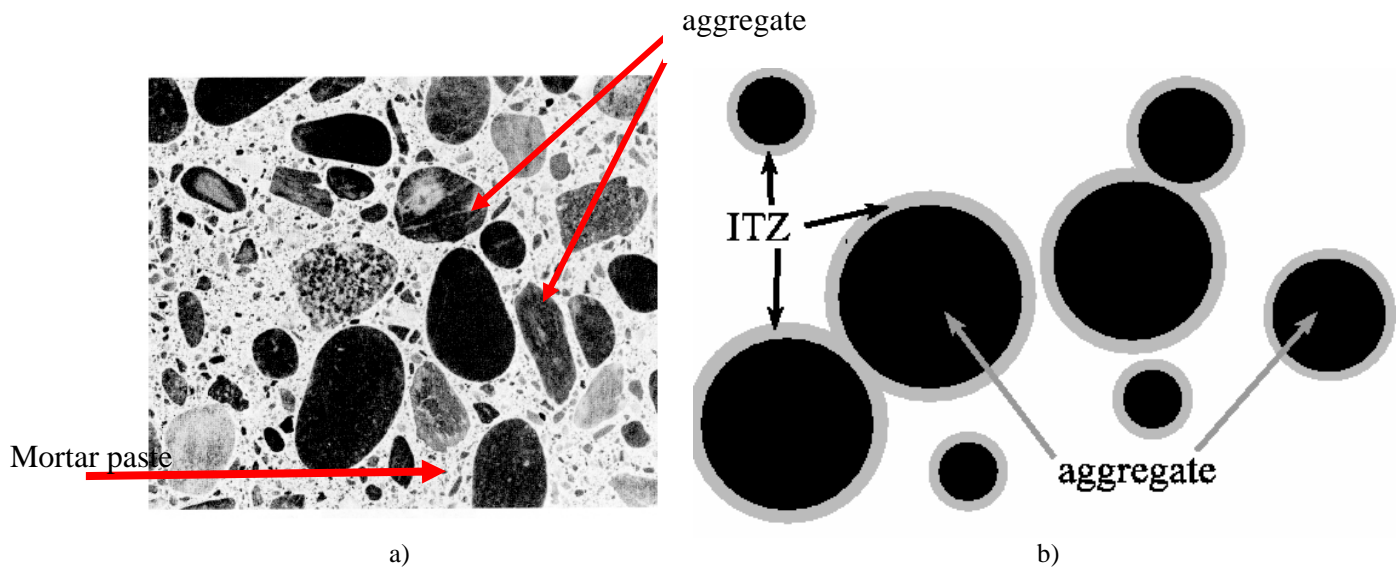


Figure 1-3. a) The Concrete composition. Two main components are visible: the aggregates and the mortar paste [Mehta et al. 1993], b) Modelling of the Interfacial Transition Zone (ITZ)

### 1.2.1.1 The cement paste

The cement paste (mixture of cement and water) fill the existing vacuums between the grains. The paste plays the role of lubricant and adhesive.

### 1.2.1.2 Aggregates

The aggregates are natural materials of varying size and shape. Types of aggregates (geometry, physicochemical characteristics) are defined by standards. The term “coarse aggregates” refers to aggregate particles larger than 4.5 mm. The term “fine aggregate” takes into account aggregates with a diameter between 0.75 and 4.5 mm. Sand is commonly used for fine aggregate with a diameter lower than 0.75 mm.

The aggregates are not very deformable. They improve the tensile strength of the mortar paste by limiting microcracks of concrete.

### 1.2.1.3 The Interfacial Transition Zone (ITZ)

It has been discovered in 1956 by Farran [Farran 1956]. The Interfacial Transition Zone (ITZ) has mechanical properties very different from the mortar paste. The ITZ refers to the mortar paste located in the immediate vicinity of the coarse aggregate particles (as shown in figure 1-3.b). Its size ranges from 20 to 50  $\mu\text{m}$  depending on the mineralogical origin of the aggregate, the Water/Cement (W/C) ratio, the cement type etc.

It plays a fundamental role in the cracking process. Because the ITZ typically has a slightly higher W/C ratio than is observed in the entire *mortar paste* and because of the physical boundary between the different materials, the ITZ is weaker than the remainder of the *mortar paste*.

In this definition the contact between the aggregate and the mortar paste (possible decohesion, friction etc.) and the weaker zone around each aggregate are merged under the term of ITZ. The manuscript will distinguish clearly the contact and the weaker zone, which we will call ITZ, around the aggregate. Figure 1-3 describes the concrete composition at a mesoscopic scale.

\*\*\*\*

**The heterogeneous character of concrete is thus introduced. In the manuscript the mortar paste denotes the homogenization of the cement paste, with sand and fine aggregates, and the ITZ.** We will consider **the consequences in concrete at a mesoscopic scale** as analysis appears to be the most practicable and useful approach for evaluating the composite behavior of concrete. Furthermore aggregates play a major role in the ASR:

- This chemical reaction is not localised and affect randomly aggregates in the structure;
- It also induces micro and macro cracks in the sample. The aggregates location will determine the crack path in the sample. It is thus important to describe as well as possible the aggregates locations and the mortar paste. It will also be important to quantify the number of reactive aggregates by representing them;
- It is also important to take into account the ITZ which is the privileged place of cracks initiation.

## **1.2.2 Which size adopts to be representative of a massive structure?**

In the classical approximations of heterogeneous materials the representative volume element (RVE) is usually considered to be infinitively large in comparison to the length scales of the microstructure. But the RVE size depends on the studied mechanical behavior. This size will be so much higher than the mechanical behavior will be complex. For concrete the RVE is about three times the size of the larger aggregates [La Borderie 2003]. The CSTB (Centre Scientifique et Technique du Bâtiment) has shown that computations converge when the size is ten times higher than the most larger aggregate, or when the volume is ten times higher than the volume of the largest aggregate [Mounajed 2002]. In fact it ensures that the tools of the continuum mechanics are available. In this way for an aggregate with a diameter of 20 mm, a study at a mesoscopic scale will be lead on sample with a 100 mm size. It corresponds in fact of the range size of samples used commonly for classical tests on concrete.

## **1.2.3 How link the results at a mesoscale with the micro and macro scales?**

A macroscale description of the heterogeneous concrete is limited by the power of computations. However on the future a good description of the material will be necessary to understand the effect of the ASR on concrete at a macro scale. The approach of the “equivalent homogeneous continuum” considers the heterogeneous volume has a homogeneous volume when the studied volume is rather than a physical scale. The objective of this method is to determine the global mechanical fields of the material using the knowledge of the local properties of the material components. In this way the main interest is

to compute a relation between the mesoscopic strains with the macroscopic mechanical behavior. A method for obtaining such a relation is referred to *homogenisation* or *theory of effective properties*, by which the heterogeneous material is replaced by an equivalent homogeneous continuum. The method is performed on a statistically representative sample of material, referred to as a representative volume element (RVE). Early approximations for the effective properties of heterogeneous materials were first developed by Voigt [Voigt 1889], Reuss [Reuss 1929] and Hill [Hill 1963]. In 1957, Eshelby [Eshelby 1957] obtained a relatively compact solution which has been a basis for many approximation methods. One of the most efficient numerical methods is the Finite Element Method, whereby the effective response can be obtained by volumetrically averaging numerical solutions of RVEs. From the micro to the mesoscopic scale a coupling with other software would be used. Some advanced softwares give us a state of the microstructure in durability problems. The software VCCTL (Virtual Cement and Concrete Testing Laboratory) [Bentz et al. 2002] is applied to predict a variety of physical properties of cement pastes. In our work these aspects will be not studied.

### 1.3 PhD manuscript outline

The manuscript is divided in eight chapters.

The starting point of this study is a review of models for concrete. We analyse the numerical methods which enables to model this behavior and we also analyse the different ways to represent the heterogeneous aspects of concrete.

The third chapter is devoted to the numerical implementation of the model in FEMCAM (**F**inite **E**lement **M**odel for **C**oncrete **A**nalysis **M**ethod) selected to simulate the degradation of concrete. We describe the model and the equations used in the software. The numerical model is then validated and justified.

The fourth and fifth chapters underline the method we have used to identify the model parameters. We explain the experimental campaign we have carried out and the inverse analysis module “RheOConcrete” we have used to identify material parameters. Parameters are identified on compression and three point bending tests. We validate the parameters identification on the “Brazilian” splitting test. A sensitivity analysis concludes on the influence of the aggregates on the global response.

In chapter six, we focus on applications about the mechanical consequences of the ASR. We examine the numerical results and compared them to the experimental ones. Furthermore some tests will be made to understand the impact of the repartitions or the size of the aggregates on the swelling. This underlines also how we shall improve this numerical tool.

The seventh chapter describes a way to improve the numerical tool by developing an efficient crack module in order to describe cracks in the sample with a great accuracy. We present the “Discrete crack approach” we have developed and validated.

Conclusions are drawn and suggestions for further investigations are proposed.

---

**CHAPTER 2 : A REVIEW OF MODELS FOR CONCRETE**

2.1 INTRODUCTION .....	2-8
2.2 EXPERIMENTAL BEHAVIOR .....	2-8
2.2.1 <i>Uniaxial compression test</i> .....	2-8
2.2.2 <i>Uniaxial tension test</i> .....	2-9
2.2.3 <i>Multi-axial behavior</i> .....	2-10
2.2.4 <i>Crack closure effects</i> .....	2-11
2.3 A STATE OF THE ART REVIEW ON MODELS DESCRIBING THE MECHANICAL BEHAVIOR OF CEMENT-BASED MATERIALS (MORTAR OR CONCRETE).....	2-12
2.3.1 <i>Elastic plastic models</i> .....	2-13
2.3.2 <i>Damage models</i> .....	2-13
2.3.2.1 Elastic damage model.....	2-15
a) The equivalent strain in the Mazars model .....	2-15
b) Damage threshold .....	2-15
c) Damage decomposition .....	2-16
2.3.2.2 Damage-plasticity coupling.....	2-17
2.3.3.3 Damage model with induced anisotropy .....	2-18
2.3.3.4 Unilateral damage model .....	2-18
2.3.3 <i>Localization and mesh sensitivity</i> .....	2-19
2.3.3.1 Non local damage mechanics .....	2-19
2.3.3.2 Gradient formulations .....	2-20
2.3.3.3 Internal length value .....	2-21
2.4 STATE OF THE ART REVIEW ON HETEROGENEOUS MODELS.....	2-25
2.4.1 <i>Statistical approach</i> .....	2-25
2.4.3 <i>Aggregates particles generation algorithms</i> .....	2-26
2.4.4 <i>Real microstructure based on mesh generation</i> .....	2-27
2.4.4.1 Projecting a specific mesh to the random aggregate structure .....	2-27
2.4.4.2 Projection of a regular mesh on the random aggregate structure.....	2-29
2.5 CONCLUSIONS .....	2-30

## 2.1 Introduction

A bibliographic study on different experimental results is first presented to underline different possible modelling of mechanical behavior of concrete under various loadings.

The second part deals with the constitutive laws which aim at describing the behavior of quasi-brittle material as concrete or mortar\*. Many theories describe the macroscopic behavior of these materials. We present a bibliographic study of these models describing the mechanical behavior of concrete. For the constitutive modelling, the focus here is mainly on continuum theories such as plasticity theory and continuum damage mechanics. We will underline how some of these models should be improved, thanks to the non local approaches. Advantages and drawbacks of constitutive models will be examined in this chapter to provide a general background and motivation for this study.

The different ways of modelling concrete are discussed in the fourth part. Two very different models appear: homogeneous models in order to simplify the numerical approach versus heterogeneous models. We will detail these different models.

We will conclude on the model we have chosen to describe the mechanical behavior of concrete. Special attention is given to starting hypotheses for this model.

## 2.2 Experimental behavior

Classical uniaxial tests (tension, compression) give us some important information on the mechanical behavior of concrete. Hence it is very useful to understand the role of the micro and macro cracks, friction, viscosity etc. We present here classical uniaxial and multiaxial tests for monotonic and cyclic loadings. Dynamic loadings will not be considered here since they do not have any impact on ASR.

### 2.2.1 Uniaxial compression test

Damage behavior is often studied for compressive stress states because of their importance at the industrial level. It is usually characterized using a uniaxial compression test on a cylindrical sample. The load-displacement curve obtained for such a test enables to identify the yield stress  $\sigma_c$  in compression. Figure 2-1 shows results obtained by Ramtani. We can observe four stages in the material behavior. We first have a linear behavior of the material up to 50% of the  $\sigma_c$  value (stage 1). From 50% to 80% of the  $\sigma_c$  value, interfacial cracks start to grow and the behavior stops being linear (stage 2). From 80% to 90% of  $\sigma_c$ , interfacial cracks start to join, thus leading to macro-cracks initiation (stage 3). In the last stage, there is a fast degradation of mechanical characteristics which is related to the fast evolution of microcracks (stage 4).

---

\* Quasi-brittle means materials that show small plastic deformation after full fracture and relatively exhibit a relatively large cohesive process zone ahead of a pre-existing macrocrack where the interdependence between stresses and strains is nonlinear.

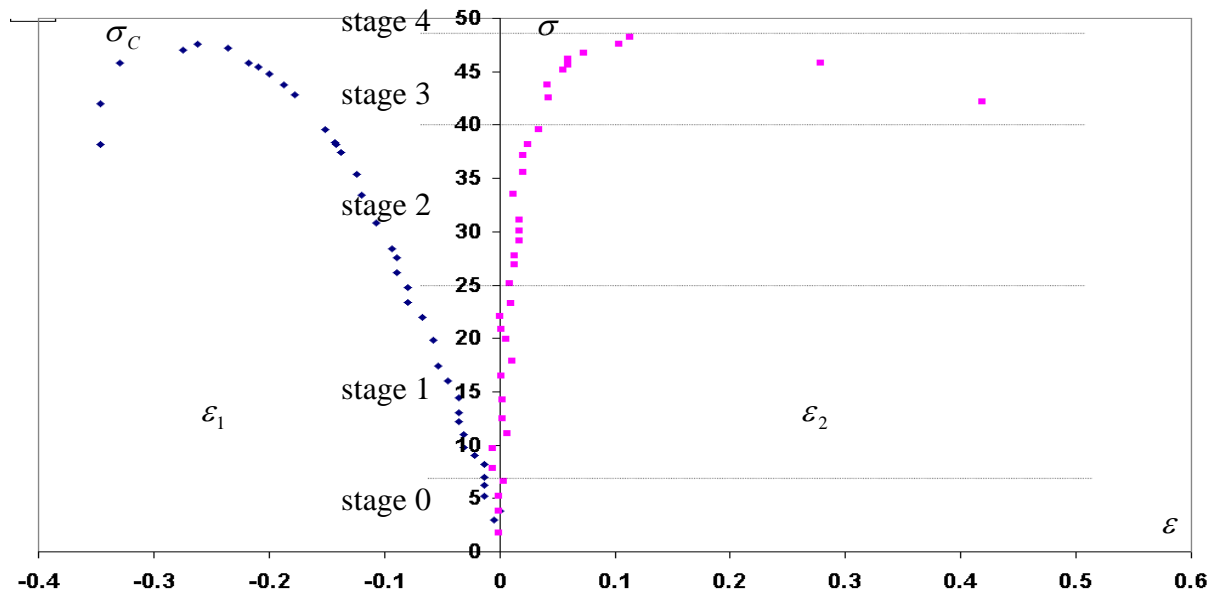


Figure 2-1. Stress-strain curve for a compression test.  $\epsilon_1$  is the principal maximal strain. [Ramtani 1990, as presented by Menou 2004]

## 2.2.2 Uniaxial tension test

Strength in **tension** is measured by tests such as Brazilian splitting test, three point bending test, and direct tensile tests.

The results in figure 2-2 clearly display two main stages, with a fracture zone much more localised than in compression. The behavior is linear almost up to the peak. Tests monitored by sound emission confirm that almost no degradation takes place before reaching the peak-value. In the post-peak stage, material degradation gets faster. **Non-linearity and damage correspond to the initiation and growth of microscopic cracks** which, when the peak load is reached, are located in a material band and end up being organized in macro-cracks. The stress drops quickly and becomes stable after a certain strain level. By the end of the test, the specimen stiffness is ten times smaller than the initial one.

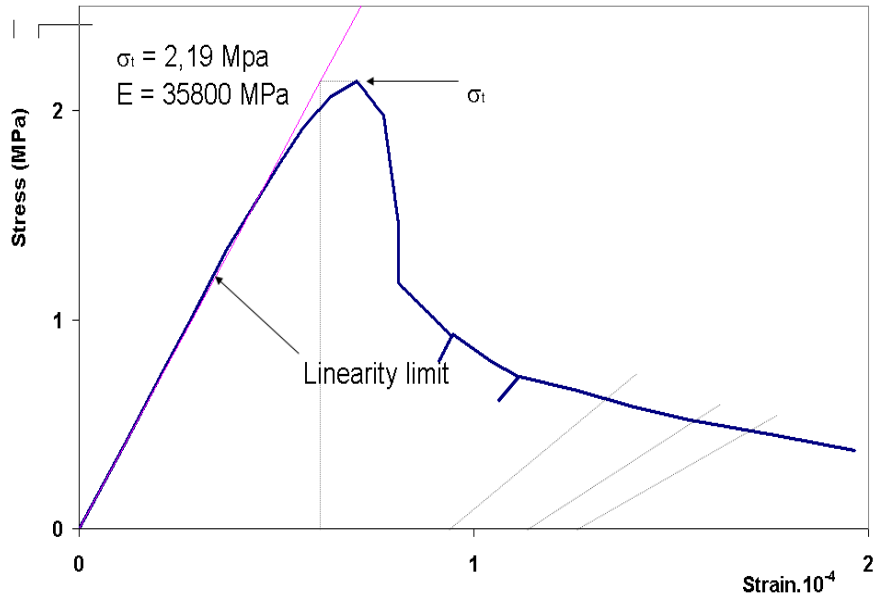


Figure 2-2. Stress-strain curve for a direct tensile test. [Terrien 1980]

### 2.2.3 Multi-axial behavior

Under combinations of biaxial compressive stress, quasi-brittle materials exhibits strengths and stress-strain behavior which are different from that under uniaxial loading conditions. Concrete behavior under biaxial loading is characterized by an increase of the strength in comparison with the uniaxial behavior. We can quote the experimental tests of Kupfer [Kupfer et al. 1969]. Figure 2-3 shows the biaxial strength envelope of concrete under proportional loading.

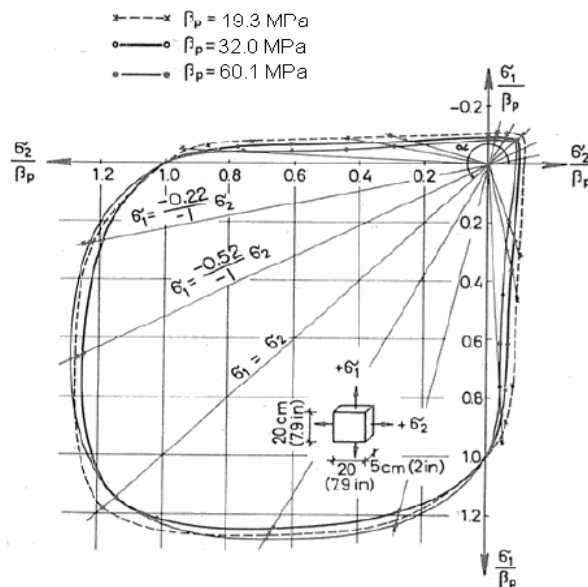


Figure 2-3. Strength failure envelope under biaxial stress [Kupfer et al. 1969].  $\beta_p$  is the correspondent unconfined uniaxial compressive strength.

Under biaxial compression the quasi-brittle materials exhibits an increase in compressive strength up to 16% of the uniaxial compressive strength, when the stress ratio  $\sigma_1 / \sigma_2$  is 0.5. The applied boundary conditions, during the tests, have a great importance, on experimental results. These tests lead to the determination of envelopes areas in the principal stress space ( $\sigma_1, \sigma_2, \sigma_3$ ).

## 2.2.4 Crack closure effects

This phenomenon appears when the **material is subjected to alternated loads**. The uniaxial cyclic tensile tests underline the unilateral behavior of concrete. This phenomenon consists in a recovery of the stiffness between the tensile loading (damage and microcracks initiation) and a compression loading. The microcracks creation does not change material characteristics in compression. And it leads to a closure of microcracks and thus to a restoration of the material stiffness. Figure 2-4 underlines the unilateral behavior of concrete.

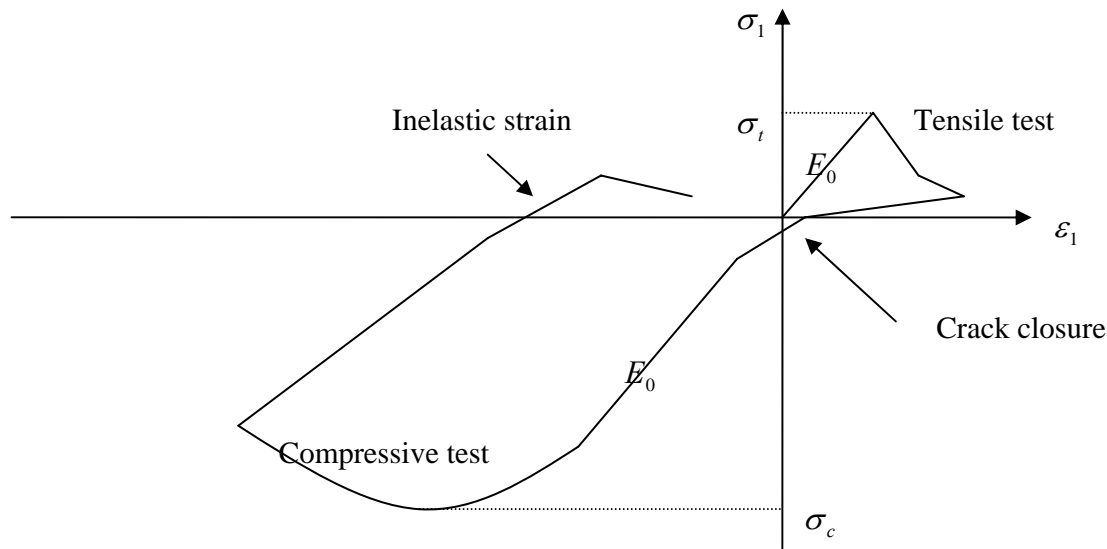


Figure 2-4. Unilateral behavior of a quasi-brittle material under uniaxial test.  $E_0$  is the initial material stiffness.

A specific test on concrete with metallic bars glued on the lateral surfaces of the sample to generate a distributed state of damage during the direct tensile test [Mazars et al. 1989] has underlined the unilateral characteristic of concrete.

The experimental behavior of concrete is rather complex. It is important to underline the different behaviors in compression and in tension. It is in fact a combination of phenomena such as linear elasticity, viscosity, microslidings (leading to permanent strains) and microcrackings (inducing a lower stiffness of the material). The relative importance of such phenomena depends on the type of solicitation. Modelling of concrete will have to take into account these aspects.

## 2.3 A State of the art review on models describing the mechanical behavior of cement-based materials (mortar or concrete)

Quasi-brittle materials, such as concrete, belong to a heterogeneous material class whose non-linear behavior is rather complex. There is a very wide literature on experimental aspects of the mechanical behavior of these materials. The standard uniaxial tests provide information for modelling. Damage impacts the mechanical behavior of concrete in several ways:

- Modification of the elastic behavior which results in a change of the mechanical characteristics;
- Modification of the plastic behavior (for concrete, these microstructural changes correspond to decohesion in aggregate or in the mortar paste, or between them, slips along surface of decohesion).

Many theories describe the macroscopic behavior of quasi-brittle materials. Various models of gradually increasing complexity have been proposed (see figure 2-5):

- Plastic models, in which the permanent unrecoverable strains appear after unloading;
- Damage models divided into two main groups:
  - o Elastic-brittle, in which irreversible strains are negligible;
  - o Plastic-brittle, in which the permanent unrecoverable strains appear after unloading, in addition to the modification of elastic properties (modelled with damage model).

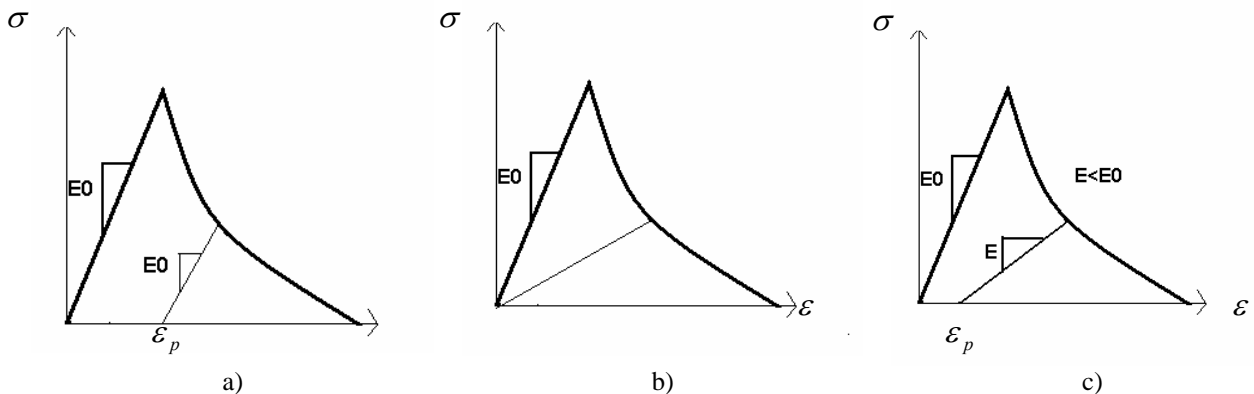


Figure 2-5. Typical stress-strain diagrams a) elastic-plastic material; b) elastic-damage material; c) elastic-plastic damage material.

Some models of these two main groups are going to be detailed and we will then focus on the Mazars model. Fracture in quasi-brittle materials such as mortar or concrete is a difficult issue because it induces localization and discontinuity in the displacement field. During the test, the stress-strain curve presents a negative slope:  $\frac{d\sigma}{d\varepsilon} < 0$  (Hill criterion). Pijaudier-Cabot explains

why this behavior leads to important numerical problems: the differential equations which govern equilibrium do not have any more the adapted mathematical form [Pijaudier-Cabot et al. 1997]. Therefore the stability criterion proposed by Hill is violated. Several models have been proposed. We will present in a second part models developed to avoid any mesh dependency.

### 2.3.1 Elastic plastic models

Elastic plastic models provide a description of the development of plastic strain after the elastic stage. The first approach of the mechanical behavior of concrete supposes concrete as elastic perfectly plastic. We can quote several authors who have developed this approach. Lin and Scordelis [Lin et al. 1975] have largely developed this approach. The concrete is assumed to be elastic plastic in compression, but brittle in tension (see figure 2-6).

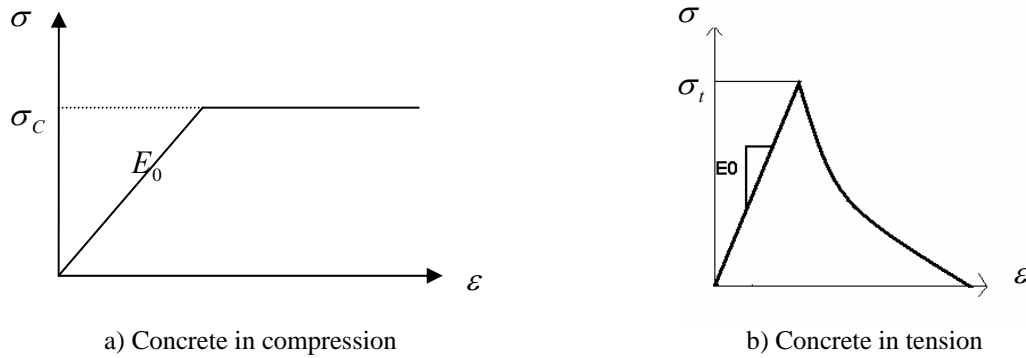


Figure 2-6. Assumed stress-strain diagram for concrete [Lin et al. 1975].

Reynouard [Reynouard 1974], Frantzeskakis [Frantzeskakis 1987] consider concrete as perfectly elastic in tension until fracture, and elastic plastic with hardening in compression.

Fracture criterion dependent on pressure, as the Rankine criterion can describe crack in tension. In compression several criteria can be used such as the Mohr-Coulomb (1911) or the Drucker-Prager (1952) criterion (see figure 2-7).

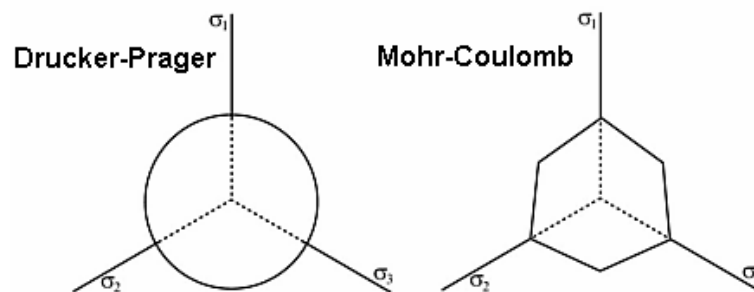


Figure 2-7. Representation of the Drucker-Prager and Mohr-Coulomb criteria in the stress deviator plane  $(\sigma_1, \sigma_2, \sigma_3)$ .

Some of these models have been already implemented in FE code such as Adina (1982), Castem (1988) or Abaqus (1989).

### 2.3.2 Damage models

The concept of damage applied to quasi-brittle materials behavior was initially introduced by Kachanov in 1958 [Kachanov 1958] then developed by many other authors [Lemaître et al. 1992]. Damage mechanics is a theory describing the progressive reduction of the mechanical properties of material due to initiation, growth and coalescence of microscopic

cracks. These internal changes lead to the degradation of mechanical properties of the material.

The distinction between a sound and a damaged material, at the base of this theory, has led to the concept of **effective stress**, defined by Kachanov.  $S$  denotes the section surface of one volume element,  $\vec{n}$  being the outer normal, and  $S_D$  the damaged surface (voids, cracks).  $\tilde{S}$  denotes the effective resistant surface ( $\tilde{S} < S$ ) and takes into account the geometrical discontinuities and stress concentrations:

$$\tilde{S} = S - S_D \quad (2-1)$$

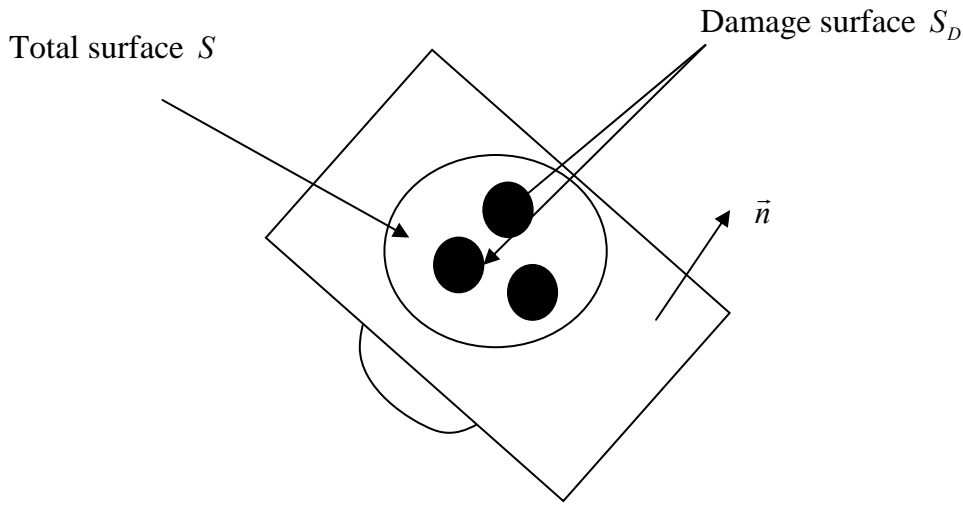


Figure 2-8. Uniaxial damage according to Kachanov.

The measure of the damage tensor  $D_n$ , with respect to the normal  $\vec{n}$ , is given by the following relationship:

$$D_n = \frac{S_D}{S} = \frac{S - \tilde{S}}{S} \quad (2-2)$$

If we consider that the defaults are uniformly distributed in each direction (isotropic damage), damage  $D_n$  does not depend on  $\vec{n}$ :

$$D_n = D \quad (2-3)$$

$D$  is a scalar such as  $0 \leq D \leq 1$ , with  $D = 0$  (undamaged material) and  $D = 1$  (completely damaged material). The damage variable  $D$  links damage and the mechanical behavior through the effective characteristic of the material. By definition:

$$\begin{aligned} E &= E_0(1 - D) \\ \sigma &= \frac{\sigma_0}{1 - D} \end{aligned} \quad (2-4)$$

$E$  and  $\sigma$  are respectively the effective Young modulus and the effective stress.  $E_0$  and  $\sigma_0$  are respectively the initial Young modulus and the initial stress. The effective stress concept introduced by Kachanov has been successfully applied to concrete by Mazars [Mazars 1984].

### 2.3.2.1 Elastic damage model

The Mazars model (Mazars 1984) aims at modelling the modification of the elastic behavior; in this model, the damage variable is isotropic: it is modelled using the scalar variable  $D$  which affects stiffness.

#### a) The equivalent strain in the Mazars model

The concept of the equivalent strain introduced by Mazars takes into account the state and the intensity of local extension. The Mazars model thus considers only positive principal strains. This choice is well suited for quasi-brittle materials - and thus for mortar and concrete. The expression of the equivalent strain  $\tilde{\varepsilon}$  with respect to positive principal strains is given by:

$$\tilde{\varepsilon} = \sqrt{\sum_{i=1}^3 \langle \varepsilon_i \rangle_+^2} \quad (2-5)$$

where  $\langle \varepsilon_i \rangle_+ = \left( \frac{\varepsilon_i + |\varepsilon_i|}{2} \right)$  and  $(\varepsilon_i)_{i \in [1,3]}$  denote the principal strain components.

#### b) Damage threshold

An evolutive threshold is introduced, depending on the damage variable  $D$ . Thus for a given damage state  $D$ , the form of the loading function is:

$$f(\varepsilon, D) = \tilde{\varepsilon} - K \quad (2-6)$$

where  $K$  represents the variable related to the history of the damage. Damage  $D$  grows when the equivalent strain reaches a threshold  $K$  initialized at  $\varepsilon_{D0}$ .

$$\text{If } f(\varepsilon, D) = \tilde{\varepsilon} - K = 0 \text{ then } \begin{cases} D = D(K) \\ K = \tilde{\varepsilon} \end{cases} \quad (2-7)$$

Figure 2-9 illustrates the threshold area in the stress plane:

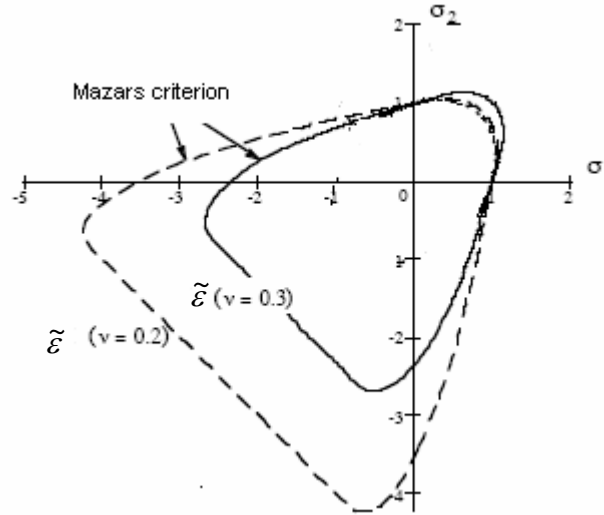


Figure 2-9. Mazars model - Plot of the threshold area in the stress plane  $(\sigma_1, \sigma_2)$ . [Mazars 1984]

### c) Damage decomposition

It has been experimentally found that the response of concrete is different in tension and in compression. Damage  $D$  defined by Mazars is thus split into two parts:

$$D = \alpha_T^\beta D_T + \alpha_C^\beta D_C \quad (2-8)$$

The parameter  $\beta$  is fitted from the response of the material to shear. It is usually considered as a constant. This coefficient is very sensitive. When  $\beta = 1$ , the shear strength is underestimated (here  $\beta = 1.05$ ).  $D_T$  and  $D_C$  are respectively the tensile and compressive parts of the damage variable  $D$ .

$$D_{T,C} = 1 - \frac{\varepsilon_{D0}(1 - A_{T,C})}{\tilde{\varepsilon}} - \frac{A_{T,C}}{\exp[B_{T,C}(\tilde{\varepsilon} - \varepsilon_{D0})]} \quad (2-9)$$

$A_C$ ,  $A_T$ ,  $B_C$  and  $B_T$  are four material parameters. The weights  $\alpha_T$  and  $\alpha_C$  are defined such that:

$$\alpha_C = \sum_{i=1}^3 H_i \frac{\varepsilon_{Ci}(\varepsilon_{Ti} + \varepsilon_{Ci})}{\tilde{\varepsilon}^2} \quad \text{and} \quad \alpha_T = \sum_{i=1}^3 H_i \frac{\varepsilon_{Ti}(\varepsilon_{Ti} + \varepsilon_{Ci})}{\tilde{\varepsilon}^2} \quad (2-10)$$

and the principal strains  $(\varepsilon_i)_{i \in [1,3]}$  check:

$$\varepsilon_i = \varepsilon_{Ti} + \varepsilon_{Ci} \quad (2-11)$$

$H_i = 1$  if  $\varepsilon_i \geq 0$ , otherwise  $H_i = 0$ . For pure tension cases,  $\alpha_C = 0$  and  $D$  tends towards  $D_T$ ; for pure compression,  $\alpha_T = 0$  and  $D$  tends towards  $D_C$ ; for mixed loads, the values of  $D_T$  and

$D_C$  depend on the amplitude of tensile and compressive stresses and  $\alpha_T + \alpha_C = 1$  if  $\beta = 1$ . Let us note that if all principal strains are positive or null,  $\alpha_T = 1, \alpha_C = 0$  and  $D = D_T$ . Reversely,  $\alpha_T = 0, \alpha_C = 1$  and  $D = D_C$ . Figure 2-10 presents the results obtained by Mazars in 2D for a uniaxial tension test and a uniaxial compression test. These plots have been obtained with specific material parameters.

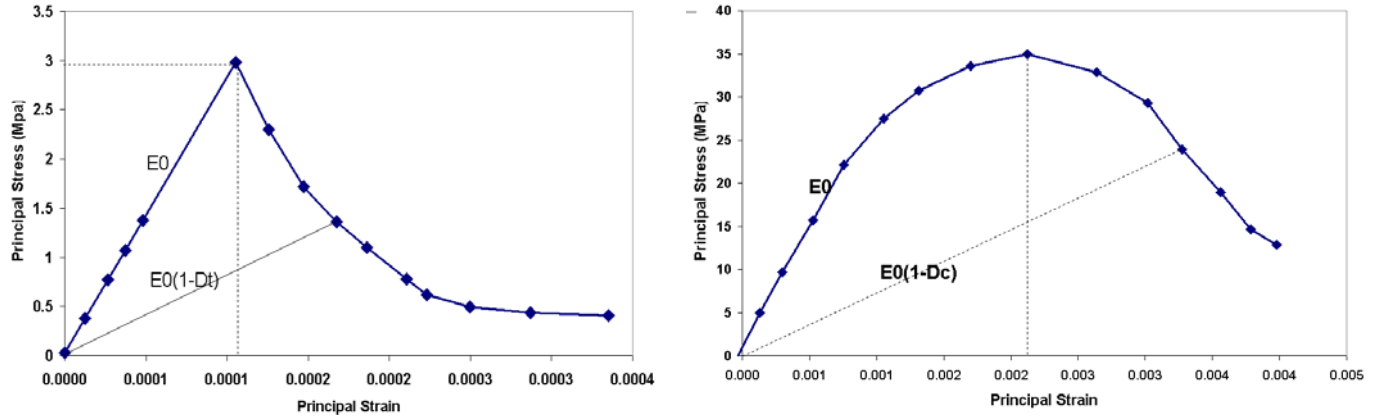


Figure 2-10. Mazars model in tension and in compression. [Mazars 1984]

The Mazars model is quite popular (easy to implement, robust etc.). However this model does not take into account the permanent strains and the unilateral effect. Most other damage models are an extension of this model (improvements for permanent strains, unilateral effect, anisotropic damage).

### 2.3.2.2 Damage-plasticity coupling

Damage models are motivated by the gradual initiation and propagation of microcracks and microvoids, and they describe the corresponding stiffness reduction. If the basic material between the defects remains elastic and the defects can close perfectly, the unloading branch of the stress-strain curve returns to the origin; real materials usually exhibit both permanent strain and a reduction of stiffness, and the unloading branches are somewhere between these two extremes. This induces the development of models that combine the frameworks of damage and plasticity. Bazant and Kim [Bazant et al. 1979] have proposed a damage-plasticity coupling (“Plastic-Fracturing”). It associates the damage theory with the fracture mechanism based on Dougill theory [Dougill 1976]. The La Borderie model adds a supplementary term  $\varepsilon^p$  to describe permanent strains. We assume here that only the elastic modulus is decreased by material damage according to the theory of continuum damage mechanics. The stress-strain relationship is the following:

$$\sigma = (1 - D)E_0(\varepsilon - \varepsilon^p) \quad (2-12)$$

And the damage criterion includes permanent strains, by adopting the assumption of small strains:

$$f(\varepsilon, D) = \tilde{\varepsilon} - K, \text{ with } \tilde{\varepsilon} = \tilde{\varepsilon}^e + \tilde{\varepsilon}^p = \sqrt{\sum_i (\varepsilon_i^e)_+^2} + \sqrt{\sum_i (\varepsilon_i^p)_+^2} \quad (2-13)$$

where  $\langle \varepsilon_i^e \rangle_+$  et  $\langle \varepsilon_i^p \rangle_+$  are the principal parts of the elastic and plastic strain tensor. The La Borderie model has been implemented in the FE code Castem 2000.

### 2.3.3.3 Damage model with induced anisotropy

If an initially isotropic material is subjected to a general loading that leads to microcracks propagation, stiffness degradation is usually faster in specific directions. Consequently, the macroscopic properties of the material become anisotropic. Some theories take into account this property. To generalize the concept, the damage value becomes a fourth order tensor. The generalized relation gives [Ramtani 1990]:

$$\sigma = (1 - D_n)\sigma_0 \quad (2-14)$$

One of the major difficulties of this model is to keep the stress tensor symmetric.

### 2.3.3.4 Unilateral damage model

When damage  $D$  takes place under a cyclic loading, the previous formulation cannot capture the stiffness recovery observed during the stress reversal [La Borderie 1991]. This model distinguishes damage due to tension from damage due to compression. Since damage cannot decrease two independent scalars, damage  $D_T$  and  $D_C$  are used. If loadings are complex, damage may be a combination of  $D_T$  and  $D_C$ . We use a decomposition of the stress tensor into a positive part  $\langle \tilde{\sigma} \rangle_+$  and a negative part  $\langle \tilde{\sigma} \rangle_-$ . The effective stress tensor can be written:

$$\tilde{\sigma} = \langle \tilde{\sigma} \rangle_+ + \langle \tilde{\sigma} \rangle_- \quad (2-15)$$

In which  $\langle \tilde{\sigma} \rangle_+$  is built with the positive eigenvalues and  $\langle \tilde{\sigma} \rangle_-$  with the negative ones, which leads to

$$Tr(\tilde{\sigma}) = Tr\langle \tilde{\sigma} \rangle_+ + Tr\langle \tilde{\sigma} \rangle_- \quad (2-16)$$

The La Borderie model enables to introduce unilateral effect according to the sign change and the anelastic strain part. The main difficulty of this model is that this formulation is very difficult to implement in a FE code. The reason is that the behavior law has to be inversed at each loading step. Furthermore it is not very well adapted to shearing effects.

### 2.3.3 Localization and mesh sensitivity

Damage model for quasi-brittle materials can lead to a fast growth of damage after reaching the elastic limit in order to describe the softening behavior observed in experiments. As a consequence of this fast damage growth, local loss of ellipticity of partial differential equations governing equilibrium occurs immediately after reaching the damage threshold in quasi-brittle damage models (see example in 1D in appendix A.1). The loss of ellipticity of partial differential equations corresponds to a situation in which the number of linearly independent solutions to the equilibrium equations is infinite. This convergence of the finite element approximation to the actual, non physical solution of the problem is the origin of the **apparent mesh sensitivity of damage models** and other discontinuous descriptions of fracture.

We call “regularisation” methods the methods used to avoid the pathological localisation of deformation and damage growth by improving the continuum model. These techniques consist in introducing a "**characteristic length**" which enables to specify the localization zone width while preventing possible numerical problems which are dependent on it. The characteristic length can be introduced under various formulations:

- Nonlocal theories;
- gradient based formulation;
- Viscous or time-dependant terms in the constitutive model may prevent the loss of ellipticity of the original, time-independent behavior of solids [Needleman et al. 1988], [Sluys et al. 1994];
- *Cossera's continua* introduce micro-rotations as degrees of freedom, in addition to the conventional displacements. However this method does not lead to results in good agreement with experiment in the case of mode I loading [Mülhaus et al. 1987].

The non local and gradient approaches, which are closely related, are the most generally applicable techniques.

#### 2.3.3.1 Non local damage mechanics

We denote  $\bar{\varepsilon}$  the average of  $\tilde{\varepsilon}$  in a representative volume surrounding a point  $x$ . It is this variable which will control damage growth at point  $x$ :

$$\bar{\varepsilon} = \frac{1}{V_r(x)} \int_V \tilde{\varepsilon}(s) \alpha(s, x) ds$$

$$V_r(x) = \int_V \alpha(s, x) ds$$
(2-17)

$V$  is the volume of the structure,  $\tilde{\varepsilon}$  is the equivalent strain at point  $s$ .  $\alpha(s, x)$  is a homogeneous and isotropic weight standardized function which depends on the distance  $|s - x|$  between the points  $s$  and  $x$ .  $l_C$  represents the **material internal length**.  $l_C$  is proportional to the smallest size of the damaged zone [Pijaudier-Cabot et al. 1993].

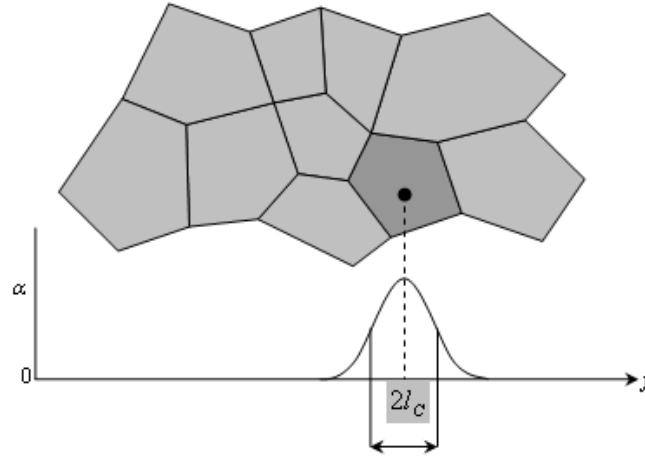


Figure 2-11. Weighted average for an irregular microstructure

Several functions have been considered in the literature to express  $\alpha$ . Among them, the Gaussian function is the most popular:

$$\alpha(s, x) = \exp\left(-\frac{4|s-x|^2}{l_c^2}\right) \quad (2-18)$$

The  $\bar{\varepsilon}$  value - which can be considered as the non local equivalent strain - is the variable that controls the growth of damage in accordance with the following conditions:

$$f(\bar{\varepsilon}, K) = \bar{\varepsilon} - K \quad (2-19)$$

### 2.3.3.2 Gradient formulations

For sufficiently smooth  $\bar{\varepsilon}$ -fields, the integral relation Eq. ( 2-17) can be rewritten in terms of gradient of  $\tilde{\varepsilon}$  by expanding  $\tilde{\varepsilon}$  into a Taylor series [Peerlings et al. 1996]:

$$\begin{aligned} \tilde{\varepsilon}(s) &= \tilde{\varepsilon}(x) + \frac{\partial \tilde{\varepsilon}}{\partial x_i}(s_i - x_i) + \frac{1}{2!} \frac{\partial^2 \tilde{\varepsilon}}{\partial x_i \partial x_j}(s_i - x_i)(s_j - x_j) \\ &+ \frac{1}{3!} \frac{\partial^3 \tilde{\varepsilon}}{\partial x_i \partial x_j \partial x_k}(s_i - x_i)(s_j - x_j)(s_k - x_k) \\ &+ \frac{1}{4!} \frac{\partial^4 \tilde{\varepsilon}}{\partial x_i \partial x_j \partial x_k \partial x_l}(s_i - x_i)(s_j - x_j)(s_k - x_k)(s_l - x_l) \\ &+ \dots \end{aligned} \quad (2-20)$$

Neglecting terms of order four and higher in Eq. ( 2-20), definition of Eq. ( 2-16) of the non local equivalent strain can be replaced by:

$$\bar{\varepsilon} = \tilde{\varepsilon} + \tilde{c} \nabla^2 \tilde{\varepsilon} \quad (2-21)$$

In Eq. ( 2-21) the derivative of order second of the local equivalent strain introduce a spatial interaction in the numerical model (dependence of  $\bar{\varepsilon}$  on the Laplacian of the local

equivalent strain). Nevertheless the explicit dependence of  $\bar{\varepsilon}$  in relation to  $\tilde{\varepsilon}$  and its Laplacien reduces the distance of interaction to an infinitesimal volume. The variation of  $\tilde{\varepsilon}(y)$ , to a finite distance from  $x$ , has no effect on  $\tilde{\varepsilon}(x)$  and  $\nabla\tilde{\varepsilon}(x)$  and so on  $\bar{\varepsilon}(x)$ . This disadvantage can be avoided as follows:

$$\bar{\varepsilon} - \tilde{c}\nabla^2\bar{\varepsilon} = \tilde{\varepsilon} \quad (2-22)$$

The non local strain is not given explicitly in terms of  $\tilde{\varepsilon}$  and its derivatives but as the solution of the boundary value problem:

$$\begin{cases} \bar{\varepsilon} - \tilde{c}\nabla^2\bar{\varepsilon} = \tilde{\varepsilon} \\ \frac{\partial\bar{\varepsilon}}{\partial\bar{n}} = 0 \end{cases} \quad (2-23)$$

$\bar{n}$  denotes the external normal unit vector. The boundary condition must therefore be defined not only on the boundary of the problem domain but also on the internal boundary which surrounds the crack area. The physical interpretation of this type of boundary conditions remains an unresolved issue.

This is a local model in a mathematical sense, because the non local strain in a point depends only on the local strain and its gradient in the same point. Spatial interactions are therefore limited to the immediate neighbourhood in this model. **This remark will influence the choice of the non local model in our code, more particularly for the modelling of problem with heterogeneous materials or with cracks.** Compared to a classical model with an integral formulation, which directly modifies the equivalent strain (in the case of the Mazars model), this method can be used with any constitutive law. Indeed it is based on the computation of a non local strain tensor and used to evaluate any invariant (isotropy, anisotropy, plasticity etc.). The difficulty of this method is the evaluation of strain tensors instead of a scalar for the integral formulation.

### 2.3.3.3 Internal length value

Regarding the choice of the internal length value, it has a physical meaning: with the starting of the macroscopic fracture, the microscopic cracks coalesce, which is characteristic of a non-linear behavior, to form macrocracks or a Fracture Process Zone (FPZ) surrounded by a damaged material zone. A localization band is created when the strains cannot be described locally but have to take into account the interactions with the nearest points.

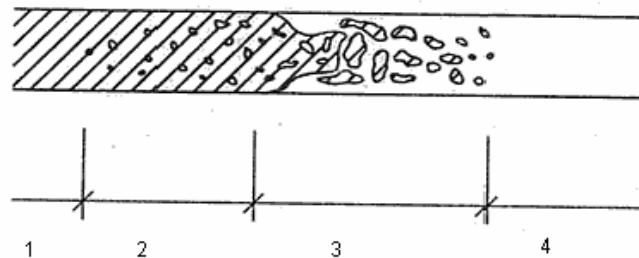


Figure 2-12. Section inside a FPZ; 1) « sound zone », 2) « damage zone »: some microcracks appear; 3) « Crack-damage zone »: the crack is visible on the surface but a part of the internal section is still active; 4) « Crack zone »: the fracture is complete.

From a modelling point of view, this localisation band cannot be described with classical continuous models. The non local approach enables to describe this FPZ. Its shape is controlled by the strain softening response of the material and by the internal length. Different methods exist: integral formulation, implicit gradient formulation etc. Each of them includes a non local parameter to identify. But the internal length is an additional parameter which is difficult to obtain directly by experiments.

A new theory of “fictitious crack” has been introduced by Hillerborg in 1976 and by Bazant [Bazant et al. 1983] with the “Crack Band Model” to idealise the behavior of a crack. The crack opening law is governed by three parameters: tensile strength, fracture energy  $G_f$ , and the shape of the softening curve. The model is based on the assumption that  $G_f$  is considered as a constant internal parameter of the material. It leads hence to consider that the smooth part of the stress strain curve in tension depends on the characteristic length  $l_C$ . In this formulation the crack strain is related to the mesh size used. A first simple estimation was proposed by Rots for 2D configurations [Rots 1988]:

$$l_C = r\sqrt{A_{FE}} \quad (2-24)$$

Where  $A_{FE}$  is the area of the considered finite element and  $r$  is a parameter which is function of the finite element used. It is fixed to  $\sqrt{2}$  for linear finite elements. In the case of a 3D study:

$$l_C = \sqrt[3]{V} \quad (2-25)$$

Where  $V$  is the volume of the finite element. It means that the non local parameter depends on the mesh size, the type of finite elements, and their position in the mesh. This approach is very easy to use but is insufficient for non regular meshes.

[Bazant 1989] have linked the internal length  $l_C$  to the FPZ with a proportional relationship (see figure 2-13). If we consider that the area under the “a” curve is the same than the “b” curve, the following relationship can be established:

$$l_{FPZ} = \alpha \times l_C \quad (2-26)$$

The value  $\alpha = 1.93$  has been established by many authors.

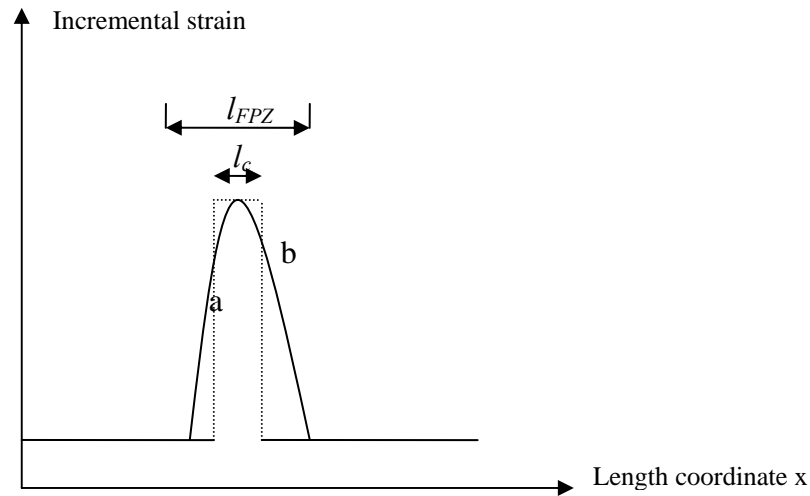


Figure 2-13. Schematic profile of strain obtained analytically. [Pijaudier-Cabot et al. 1987, as presented by Haidar 2002]

Hence it is possible to measure the displacement field with a great accuracy in this zone and compare it to a numerical model [Geers et al. 1996]. The most accurate way of reaching the internal length is by a semi-inverse technique which is based on computations on size effect tests. The complete explanation of this effect is described in [Bazant et al. 1998]. This is due to the redistribution of the stored strain energy inside the structure where the size of each specimen can change but where the FPZ is constant. Hence scale effect tests can indirectly determine the parameter of the non local model. These tests are carried out on geometrically similar specimens on different sizes. But such identification requires many computations.

An approximation of the internal length  $l_c$  was obtained by Bazant and Pijaudier-Cabot. Physically it is thus generally assumed that the  $l_c$  value is between  $3 d_{max}$  and  $5 d_{max}$  [Bazant et al. 1983], where  $d_{max}$  is the diameter of the larger aggregate. Relationships between the internal length  $l_c$  for the integral non local model and  $\tilde{c}$  for the gradient approaches have been discussed by many authors. Theoretically, Peerlings considers the following relationship:

$$\tilde{c} = \frac{l_c^2}{2} \quad (2-27)$$

Jason [Jason 2004] has carried out a numerical campaign where he has compared load-displacement curves on three points bending tests between the results obtained with an integral non local model and a gradient approach. He found:

$$\tilde{c} \approx \frac{9d_{max}^2}{16} \quad (2-28)$$

Concrete exhibits a quasi-brittle behavior and the degradation process is linked to the macrocracks initiation and evolution in the sample. It induces a loss of stiffness, a strain localisation and irreversible strains. It is thus important to take into account this non-linear behavior.

Among the different numerical approaches, the elastic plastic and damage-elastic approaches are commonly used if we consider monotonic loading. We have chosen to use the classical Mazars model. This model is robust. It is also well adapted in the framework of this first 3D numerical description of the degradation of concrete submitted to the ASR as we consider a monotonic swelling of the sample.

We have also noticed the importance of introducing “regularization” methods to avoid localization of deformation. Two main approaches exist. The gradient approach seems to be more adapted for the description of heterogeneous material as concrete.

Experiments and numerical models reflect the complexity of the material. Whereas these numerical models try to model the global mechanical behavior of concrete as accurately as possible, they neglect the strong heterogeneity of concrete and consider it as a homogenised material. However figure 2-14 shows differences between the mechanical behaviors of the main concrete components. It underlines hence that aggregates induce a modification of the mechanical behavior of the mortar paste and that ductility has its origin in the bond between the aggregates and the mortar paste.

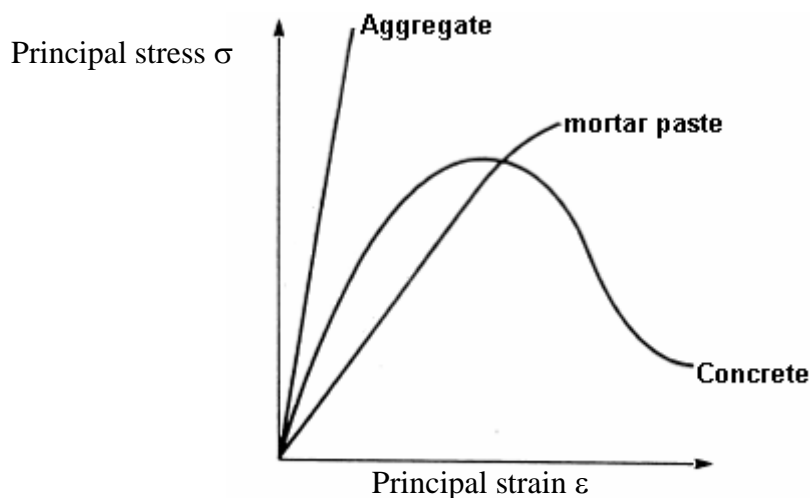


Figure 2-14. Typical stress-strain curves for aggregates, mortar paste and concrete.

The properties of complex composite material are not equal to the sum of the components. Aggregates are generally linear elastic and the mortar paste has an elastic damage behavior. We will detail in the next part some of these models. However these approaches are:

- Unsuitable to characterise the entire fracture process from initiation to propagation and coalescence of macrocracks in concrete (fracture is often initiated at the ITZ and its evolution depends on the heterogeneity of the structure);

- Unsuitable to model the randomness of concrete mesostructures and consequently insufficient to understand the fracture process of concrete.

Hence different numerical models for the simulation of the fracture process in concrete at a **mesoscopic scale** have been proposed in recent years. Taking into account the heterogeneous aspect of concrete, they have the advantages to:

- estimate and understand local mechanisms of deformation;
- better simulate mechanisms of damage (damage is piloted by local values as the ITZ);
- become a precious tool for concrete formulations;
- describe accurately chemical degradation involving changes in mesostructures.

## 2.4 State of the art review on heterogeneous models

Few studies take into account the heterogeneous aspect of concrete, because of its complexity. We recall the three main phases which appear at a mesoscopic scale:

- The hydrated mortar paste;
- The aggregates;
- The Interfacial Transition Zone (ITZ).

Numerical simulations of concrete are generally based on homogenization techniques in order to simplify the numerical approach. However only a few models exist (mainly for 2D configurations) because of computer storage, computation time, difficulties to represent 3D structures etc. We present them hereafter.

### 2.4.1 Statistical approach

A way to take into account the heterogeneous aspect of concrete is to distribute randomly the Young modulus and the strength on the mesh elements. The 2D Cesar LCPC probabilistic model is based on this concept. This randomly distribution leads to simulate the material heterogeneity and so a random cracking mode. This distribution follows a normal law, where the mean and the standard deviation are empiric functions of experimentally identified parameters. They depend on two parameters:

- The compressive strength  $\sigma_c$ ;
- The ratio  $V_T/V_g$  where  $V_T$  is the sample volume and  $V_g$  is the volume of the most larger grain.

This model takes into account scale effects due to the heterogeneity of concrete [Rossi et al. 1992]. The aggregates shape plays an important role on the stress distribution and fracture energy of heterogeneous materials (they can be spherical or angular depending on their origin). However this model does not respect the aggregates geometry. Furthermore the ITZ is not taken into account. The contact is considered as perfect.

### 2.4.3 Aggregates particles generation algorithms

An interesting method consists in building the microstructure directly from an image (by the use of the scanning electron micrograph of a concrete specimen) of a real piece of material. Using image processing techniques the image can be splitted into three phases: mortar paste, aggregates and ITZ. *But this method is very limited as it needs to ever have an experimental concrete sample and the microtomographic techniques requires using samples with standard (usually very small) dimensions.* First simulations were considering aggregates as perfectly spherical. We can quote the model developed by Schlangen and Van Mier [Schlangen et al. 1992], Mounajed [Mounajed 2002] in the Symphonie code (CSTB). Figure 2-15 shows a few examples of modelling of aggregates in 2D and 3D. The 2D mechanical computation imposes a big hypothesis: we consider an identical aggregate repartition in the whole volume. This is hence the major drawback of the 2D aspect as we miss the random position of aggregates in the volume.

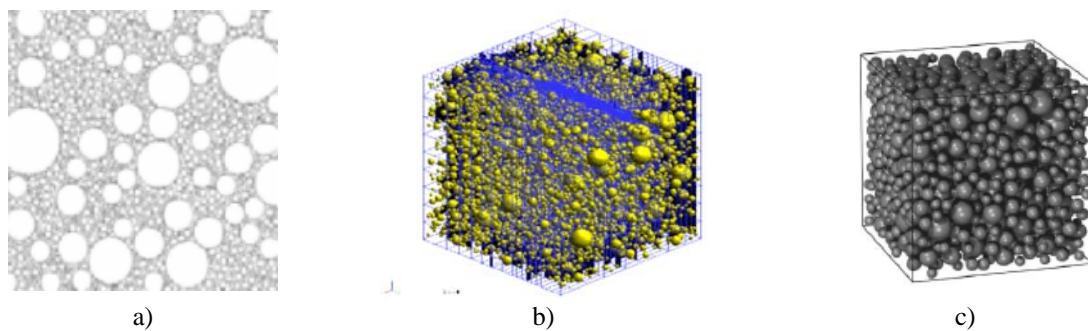


Figure 2-15. Modelling of spherical aggregates in 2D-CSTB (a) or 3D (b) [Mounajed 2002]; c) Modelling of a granular skeleton in a cube of 24 mm size. [Lilliu 2002]

Other models ([Leite et al. 2003], [Häfner et al. 2006]) have been developed considering spherical or ellipsoidal aggregates (figure 2-16).

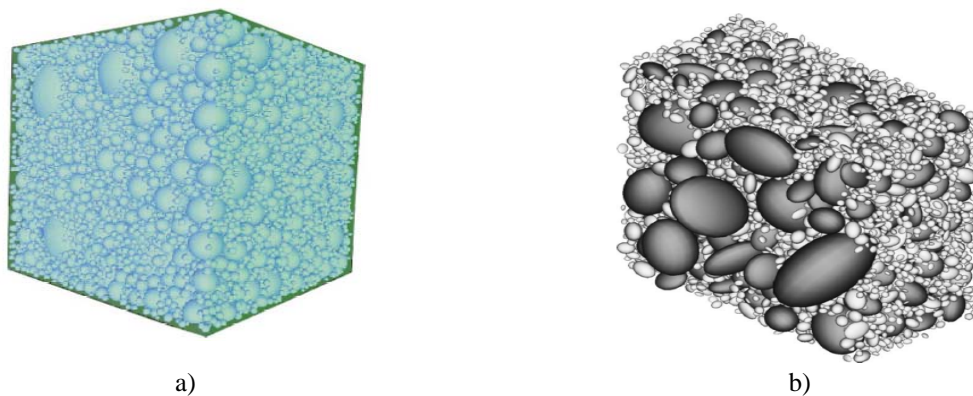


Figure 2-16. a) Generated 3-D specimen with 60% aggregate content [Leite et al. 2003]; b) View on the section of a three-dimensional geometrical mesoscale model. [Häfner et al. 2006].

One of the drawbacks of this model is the spherical or ellipsoidal shape of the cells which is not compatible with reality. Wang [Wang et al. 1999] developed a procedure for generating a random structure for spherical and angular aggregates (figure 2-17).

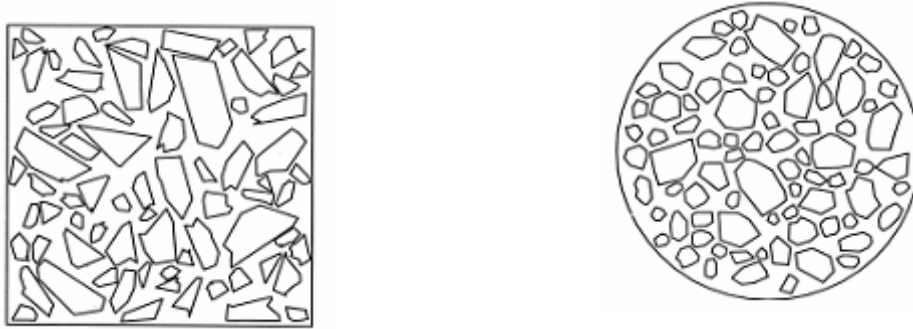


Figure 2-17. Random aggregate structures generated for different elongation and finite element mesh generated [Wang et al. 1999] on a  $150 \times 150$  mm square or 150 mm diameter circles.

All these models are based on random generation algorithms of aggregates such as Monte Carlo method or a random number generator. There are different techniques to generate these particles.

We can mention the *take-and-place methods* ([Wang et al. 1999], [Schlangen et al. 1992], [Mounajed 2002], [Wittmann et al. 1993]). This method is commonly used and consists in placing aggregates one by one. If an aggregate overlaps another aggregate, the random generation is used and another place is found until the complete generation. The mechanism to generate the whole grain structure is the following:

- *Particle generation*: determination of the size and shape of all aggregates particles in order to match the precise size distribution and aggregate content;
- *Particle allocation*: the allocation of the particles in the 3D Euclidian space.

Alternatively a *stochastic-heuristic algorithm* can be used [Leite et al. 2003]. The big difference with the take-and-place method is that the allocation of particles is performed successively starting with the largest ones. Initially, a random position of the particle is obtained. If the particle is completely inside the specimen and does not overlap previously placed ones, the position is fixed. In the other case, the particle is shifted or rotated in order to get away from the specimen boundary or overlapping particles. If this procedure does not solve the conflict, then the procedure can be repeated. Direction and magnitude of the movement are calculated by using a specific algorithm.

Other algorithms as a *random particle drop method* can be also noticed [Vervuurt 1997]. It consists in generating all the particles with a random generator first. Then they are dropped into the volume and they find the deepest position. A disadvantage of this effective algorithm is that the obtained meso-level structure is quite different from those observed in real concrete samples.

## 2.4.4 Real microstructure based on mesh generation

### 2.4.4.1 Projecting a specific mesh to the random aggregate structure

A method of direct construction consists in starting from a real microstructure picture. The coordinates of the boundary (to define the frontier) and inside the domain (interior points) are obtained by choosing directly some digitalized point on the picture [Wang 1994]. The automatic Delaunay triangulation begins to connect the interior points and the boundary points to create elements.

Another way is to project a mesh on the random aggregate structure and assign different material properties, respectively to the elements according their locations [Wittmann et al. 1993].

The 2D « Numerical Concrete » has been developed by Wittmann and his coworkers [Sadouki et al. 1988]. The random structure of the material is created with an appropriate assembly of finite elements and particular properties of evolution. The inclusions follow a grain size distribution and are shaped according to the morphological law of Rhône Valley gravel. The mortar paste has an elastic behavior until stress reaches the tensile strength  $\sigma_t$ . The material parameters have been identified with experiments and they are distributed statistically to represent concrete inhomogeneities. The fictitious crack model (see chapter 7 for more details) is then used to simulate crack propagation in concrete according to two possible modes: mode I and mode II. The matrix-aggregate interface is also taken into account with the creation of interfacial elements between the nodes of the elements belonging to the mortar paste and the nodes of the aggregates.

Roelfstra has also developed this approach in 3D as we can see in figure 2-18.

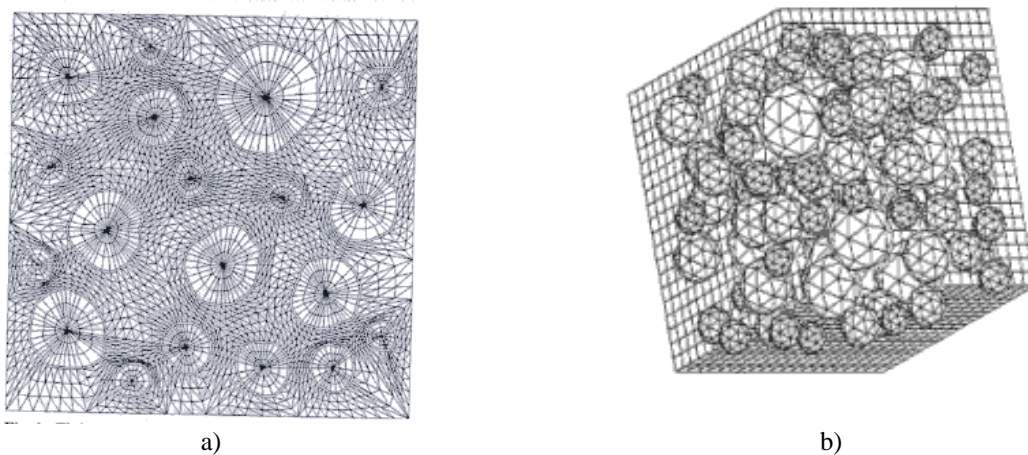


Figure 2-18. a) Computer generated finite element mesh of the analyzed concrete structure [Sadouki et al. 1988]; b) Aggregate volume content of 0.28 in a  $160 \times 160 \times 160 \text{ mm}^3$  cube. 100 aggregates have been generated thanks to the Fuller curve. [Roelfstra 1989]

However the quality of these generated meshes generated is not very good because many poor quality elements are contained in the mesh. Wang [Wang et al. 1999] has improved this technique by using an “advancing front method” (figure 2-19).

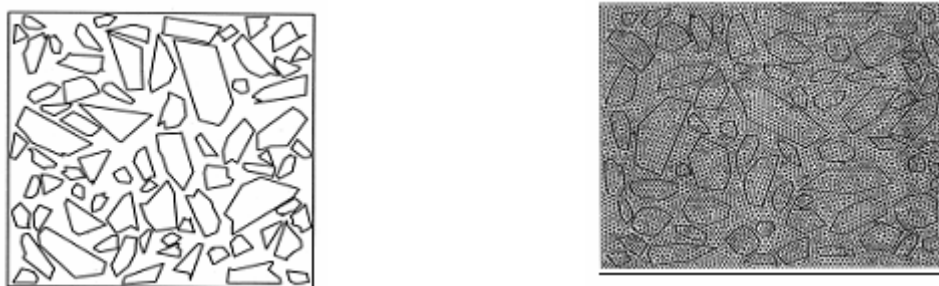


Figure 2-19. Finite element mesh generated (thick lines represent interface elements).

The possible decohesion between mortar paste and aggregate (the weak zone of concrete) can be also considered to model crack initiation. The interface elements used are

“zero-thickness” isoparametric elements. They are inserted between standard continuum finite elements to discretize the interface between the matrix and aggregates discretization [Lopez et al. 2001], [Wang et al. 1999].

The nodes belonging to the aggregate phase and the corresponding nodes belonging to the mortar matrix have the same coordinates. They are, however, treated as different nodes. In this way these models have the capacity to simulate crack initiations at the interface between matrix and aggregates.

#### 2.4.4.2 Projection of a regular mesh on the random aggregate structure

Another method consists in realizing a mean of the local properties at the scale of the finite element [Mounajed 2002]. If  $C_e$  and  $C_g$  are the values of the element and the aggregate property and  $V_e$  and  $V_g$  the associated volume, the new value of the property on the whole element can be written as:

$$C_e^m = \left( \frac{C_e(V_e - V_g) + C_g V_g}{V_e} \right) \quad (2-29)$$

Figure 2-20 shows the elements affected by the mechanical behavior of the aggregates according to the above equations.

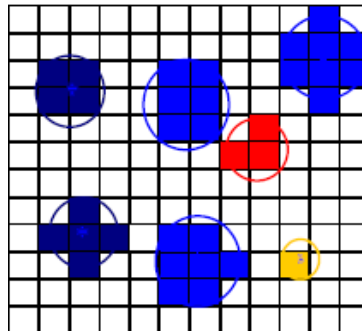


Figure 2-20. Example of elements affected by the mechanical behavior of the aggregates. [Mounajed 2002].

Other methods are largely used to model concrete at a mesoscopic scale. They have been developed first by physicists [Hermann et al. 1989]. The 2D Lattice model with beam element is one of the most popular to explain fracture in concrete at a mesoscopic scale. A network of beams is projected on the generated grain structure. Some square, triangular or random lattices can be generated. The beam stiffness and the strength are chosen in such a way to represent the different phases of concrete material, namely, aggregate, matrix and interface. The tensile stress in each beam is calculated. When the tensile stress is larger than the strength of the material constituent, the beam element is supposed to break and is removed from the network.

The lattice model is close to the truss model developed by Bazant et al. [Bazant et al. 1990] and the framework model developed by Schorn and Rode [Schorn et al. 1991].

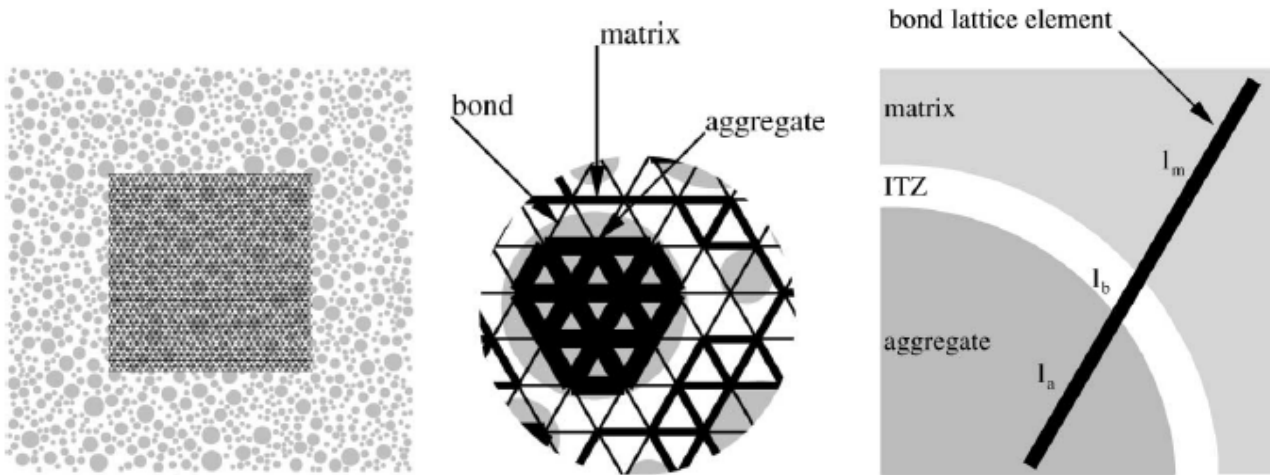


Figure 2-21. « Numerical Concrete » model, Microlab, Delft University of Technology. [Lilliu 2002]

Figure 2-21 shows that it is also possible to take into account the ITZ. The equivalent elastic modulus is evaluated in function of the elastic modulus of the aggregate, the mortar and the ITZ and in function of the associated length  $l_a$ ,  $l_m$ ,  $l_b$ . However we have not found in 3D applications using this technique in the literature. The contact is here considered as perfect.

2D analyses suffer from a number of limitations. We have described some methods to represent aggregates particles in 3D. We have noticed that a good generation of aggregates is strongly linked to its capacity to physically represent the grains. Some methods, based on microtomography, exist but are often limited. We have hence noticed the advantage of the “take and place” method which can represent angular aggregates.

We have also presented the methods to integrate this grain size distribution into a mesh: the use of lattice models is easy but it cannot describe complex mechanical behaviors. One other solution is the average of the mechanical properties of the aggregates and the mortar paste on the finite element mesh but this technique cannot lead to represent physically aggregates. Therefore **we have chosen to use the “take and place” method based on a 3D existing mesh**. It enables to obtain a physical grain size distribution and to model complex mechanical behaviors for each phase of the numerical concrete. Each finite element will have hence a specific mechanical property corresponding to its location in the mesh (into the aggregates, the ITZ or the mortar paste). We do not consider in this study the contact between aggregates and the mortar paste.

## 2.5 Conclusions

In order to describe as well as possible concrete, our numerical model will be developed at a **mesoscopic scale**. The good knowledge of concrete is of prime importance to describe the evolution of damage and cracks in the sample.

We have noticed that many numerical models can describe the mechanical behavior of concrete with more or less accuracy. For our study **the non local Mazars model** is then very well adapted as it is easy to implement, robust and gives a good description of concrete behavior for uniaxial loadings.

The non local approach is a convenient way to avoid mesh dependency. Quantitatively the differences between the implicit and non local approaches are limited. The integral formulation is well adapted for homogeneous material as mortar. When cracks and heterogeneous aspects intervene we have noticed that the implicit model becomes more interesting to use. The next chapter develops the implementation of this one in our FE code FEMCAM. We will explain also the choice of the non local model based on numerical tests.

We have underlined the importance to represent the active components of concrete. Three main phases appear: mortar paste, aggregates and the ITZ. The ITZ is important as it is in general the location of cracks initiation. But the thickness of this zone is very low compared to the sample size. It is thus difficult to mesh such a thin geometrical zone. In the following work, we have decided to represent concrete using two main parts: **the mortar paste and the aggregates**. The contact between the mortar paste and the aggregates will be considered as perfect. The multi-domain version of FEMCAM should be used to account for possible friction between aggregates and the mortar paste, but this would require high CPU time.

Few models take into account the heterogeneous aspects of concrete. The state of the art review on these models has shown that there were most of the time limited to 2D configurations. Consequently we have decided to develop **a new model based on the “take and place” method, where concrete is considered as a 3D heterogeneous material**. This model, developed in our FE code FEMCAM, is presented in the next chapter.

## CHAPTER 3 : IMPLEMENTATION AND VALIDATION OF A THREE DIMENSIONAL HETEROGENEOUS ELASTIC DAMAGE PROBLEM FOR CONCRETE

3.1 THE FEMCAM SOFTWARE .....	3-33
3.2 MODELLING OF CONCRETE .....	3-34
3.2.1 <i>Physical aspects</i> .....	3-34
3.2.1.1 Distance of exclusion .....	3-34
3.2.1.2 Edge effects .....	3-35
3.2.2 <i>Random generation of aggregates</i> .....	3-36
3.2.2.1 Algorithm for random aggregates generation .....	3-36
a) The algorithm .....	3-36
b) Discussion .....	3-38
3.2.2.2 Representation in FEMCAM .....	3-38
3.3 THE ELASTIC DAMAGE MODEL USING A MIXED-VELOCITY PRESSURE FORMULATION... 3-39	
3.3.1 <i>The equilibrium equations</i> .....	3-39
3.3.1.1 The dynamic equilibrium .....	3-39
3.3.1.2 The incompressibility condition.....	3-40
3.3.1.3 The boundary conditions.....	3-40
3.3.2 <i>Constitutive equations</i> .....	3-41
3.3.2.1 Deviatoric part.....	3-42
3.3.2.2 Spherical part.....	3-42
3.3.3 <i>The weak formulation</i> .....	3-43
3.3.4 <i>Discretization</i> .....	3-43
3.3.4.1 Choice of the finite element .....	3-44
3.3.4.2 Discrete weak formulation .....	3-44
3.3.4.3 Resolution of the finite element problem.....	3-45
3.3.5 <i>General outline of an elastic damage problem resolution in FEMCAM</i> .....	3-46
3.3.5.1 Weak coupling.....	3-48
3.3.5.2 Strong coupling .....	3-48
3.4 SELECTION OF THE MODEL AND NUMERICAL STRATEGY .....	3-48
3.4.1 <i>Local versus non local model</i> .....	3-49
3.4.1.1 Numerical test .....	3-49
3.4.1.2 Choice of the non local model.....	3-53
3.4.1.3 Choice of the internal length for the non local model.....	3-54
3.4.2 <i>Weak coupling versus strong coupling</i> .....	3-55
3.4.3 <i>Adaptive time step</i> .....	3-58
3.4.3.1 Local approach .....	3-58
3.4.3.2 Global approach .....	3-59
3.4.3.3 Comparison of the methods.....	3-60
3.5 CONCLUSIONS .....	3-62

### 3.1 The FEMCAM software

The FEMCAM software (Finite Element Method for Concrete Analysis Model) is derived from the commercial software Forge3® developed by CEMEF. Forge3® is a process simulation tool, based on the Finite Element Method. It was initially dedicated to simulate forging. It predicts material and thermal flow during 3D forming processes. The flexible Forge3® tool kinematic structure enables to simulate a large range of complex processes such as shape rolling, floating dies etc. Forge3® is based on an updated Lagrangian formulation and can deal with a 3D thermo-mechanical coupled computation. Figure 3-1 shows an example of the hot forging process of an automotive part.

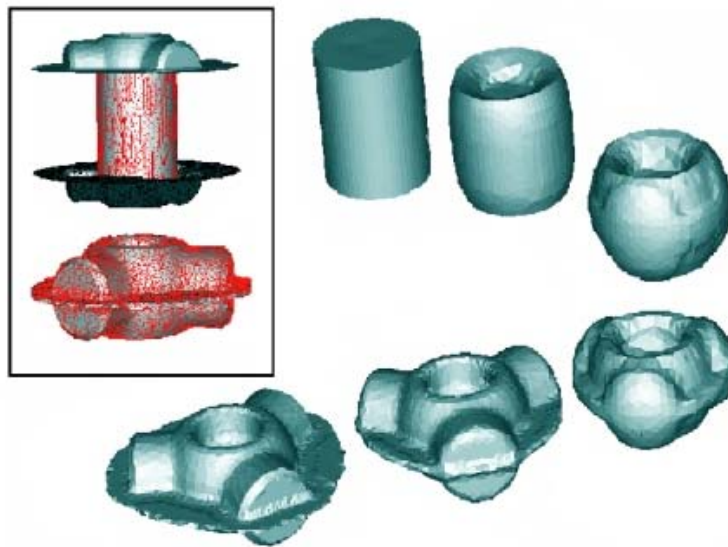


Figure 3-1. A hot forging of an automotive part with Forge3®.

**This software is also well adapted to civil engineering problems.**

Forge3® enables to simulate a large range of material behaviors as elastic, elastic plastic, elastoviscoplastic, damageable material or with a thermo-dependant behavior. *This aspect is important as it indicates that Forge3® is initially an efficient tool to take into account the non-linear mechanical behavior of quasi-brittle materials.* A Newton Raphson algorithm with Pre-conditioned Conjugate Gradient Solver is used to solve the discretized system.

Forge3® can handle self contact and contact between multiple deformable bodies automatically; It can model sliding, bilateral sticking contact or friction contact. We use bilateral sticking contact to simulate a perfect contact with adhesion between two bodies. If we want to model friction (strong or low) between the tools and the sample (unilateral contact) we can use various friction laws (see appendix A.2 for more details).

A fully automatic tetrahedral meshing and remeshing enables to simulate very complex shapes. *This other aspect shows this numerical tool is powerful enough to model even if it is a complex case with cracks.* This point is very important in our study to model concrete samples fracture. Forge3® can deal with multimaterial bodies, which is interesting in

our case to model concrete at the mesoscopic scale (matrix and aggregates). A completely parallel solver enables faster and more accurate computations.

Forge3® has been recently extended to a multi-domain version in order to deal with the effect of the contact between different bodies.

## 3.2 Modelling of concrete

To model the granular skeleton, we consider two different parts: the mortar paste and the aggregates. The complex contact between the aggregates and the mortar paste is neglected to simplify the problem. So we consider a perfect contact between all finite elements. Furthermore the algorithm, that we have implemented, takes into account the following features:

- The aggregates position must be absolutely random;
- Grain size can be provided by a real grain size distribution;
- Spacing between coarse grains.

Based on these rules, an algorithm has been set up in FEMCAM in order to model and position aggregates in concrete. The algorithm provides a specific rheology for each finite element in the mesh, based on whether this element belongs to the mortar paste or to the aggregate. Thus contact between the aggregate and the mortar paste will be considered as bilateral sticking.

### 3.2.1 Physical aspects

Two main physical aspects are taken into account in our algorithm: distance of exclusion and edge effects.

#### 3.2.1.1 Distance of exclusion

The distance between the largest aggregates is called the “Maximum Paste Thickness” (*MPT*). It represents the mean distance between two aggregates, considering that each aggregate is surrounded by a paste layer, whose thickness is proportional to the aggregate diameter. The *MPT* may be chosen to describe the maximum effective area of such model element. The *MPT* can be calculated as follows:

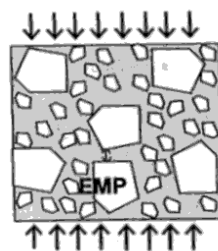


Figure 3-2. Concrete defined as a dry stacking injected with the mortar paste. [de Larrard 1999]

Caquot law provides this distance [Caquot 1937]:

$$l = d_{\max} \left( \sqrt[3]{\frac{g^*}{g}} - 1 \right) \quad (3-1)$$

where  $d_{\max}$  is the maximum size of the aggregate,  $g$  is the aggregate volume in a volume unit of concrete. For rounded aggregate,  $g^*$  can be calculated with the following equation [de Larrard 1999]:

$$g^* = 1 - 0.47 \left( \frac{d_{\min}}{d_{\max}} \right)^{0.22} \quad (3-2)$$

where  $d_{\min}$  is the aggregates minimum size.

### 3.2.1.2 Edge effects

$V_p$  is the volume located between the edge and the distance  $d/2$ , where  $d$  is the aggregate diameter considered. The compactness in the volume  $V_p$  is thus weaker than the compactness  $\alpha$  in the centre of the sample.

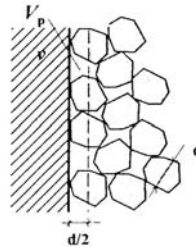


Figure 3-3. Wall attachment effect on a stacking of grains of unique size. [de Larrard 1999]

The mean compactness  $\bar{\alpha}$  in the whole volume is equal to [de Larrard 1999]:

$$\bar{\alpha} = (1 - V_p) \alpha + V_p k_w \alpha \quad (3-3)$$

with  $k_w = 0.88$  for rolled aggregates and  $k_w = 0.73$  for crushed aggregates. It enables to know how aggregates will be generated for each aggregate size range in the volume  $V_p$ .

## 3.2.2 Random generation of aggregates

### 3.2.2.1 Algorithm for random aggregates generation

#### a) The algorithm

An algorithm has been implemented in the code FEMCAM. It generates completely randomly a granular skeleton. To distinguish aggregates from the mortar paste, a table gives a different behavior for each phase. We consider aggregates as a sphere with a radius  $R$  given by the grain-size distribution. Figure 3-4 details the random algorithm for aggregates generation.

Starting from the largest one, aggregates are sequentially placed into the mortar paste. In fact it is generally easier to pack the particles into the concrete.

It is also essential to have no contact between aggregates (nodes in common) in the aggregates skeleton. If some nodes belong to two aggregates at the same time, the code cannot handle the concrete degradation due to the damage evolution in the mortar paste located between aggregates. The aim is hence to have free spaces between aggregates to take into account the mortar paste and the ITZ between aggregates.

Furthermore the algorithm stops when the number of aggregates to generate is reached or when the volume of the previous granular skeleton is also reached. It enables to obtain a granular skeleton with a very accurate global volume compared to the experiments.

The mesh plays an important role in the generation of this skeleton. The mesh size must exceed the radius of the aggregate to generate. A fine mesh enables the insertion of a maximum number of aggregates. On the contrary if the sample is discretized with few finite elements, the algorithm will not be able to generate the granular skeleton because of a lack of elements. To generate this skeleton, the discretization depends on:

- The size of the sample;
- The number of aggregates to generate;
- The edges effects and the *MPT*.

Furthermore we have tested the influence of the mesh size on the sphere volume to generate. Indeed a small mesh size leads to a sphere with a volume nearest from the experiment than a sphere in a coarse mesh.

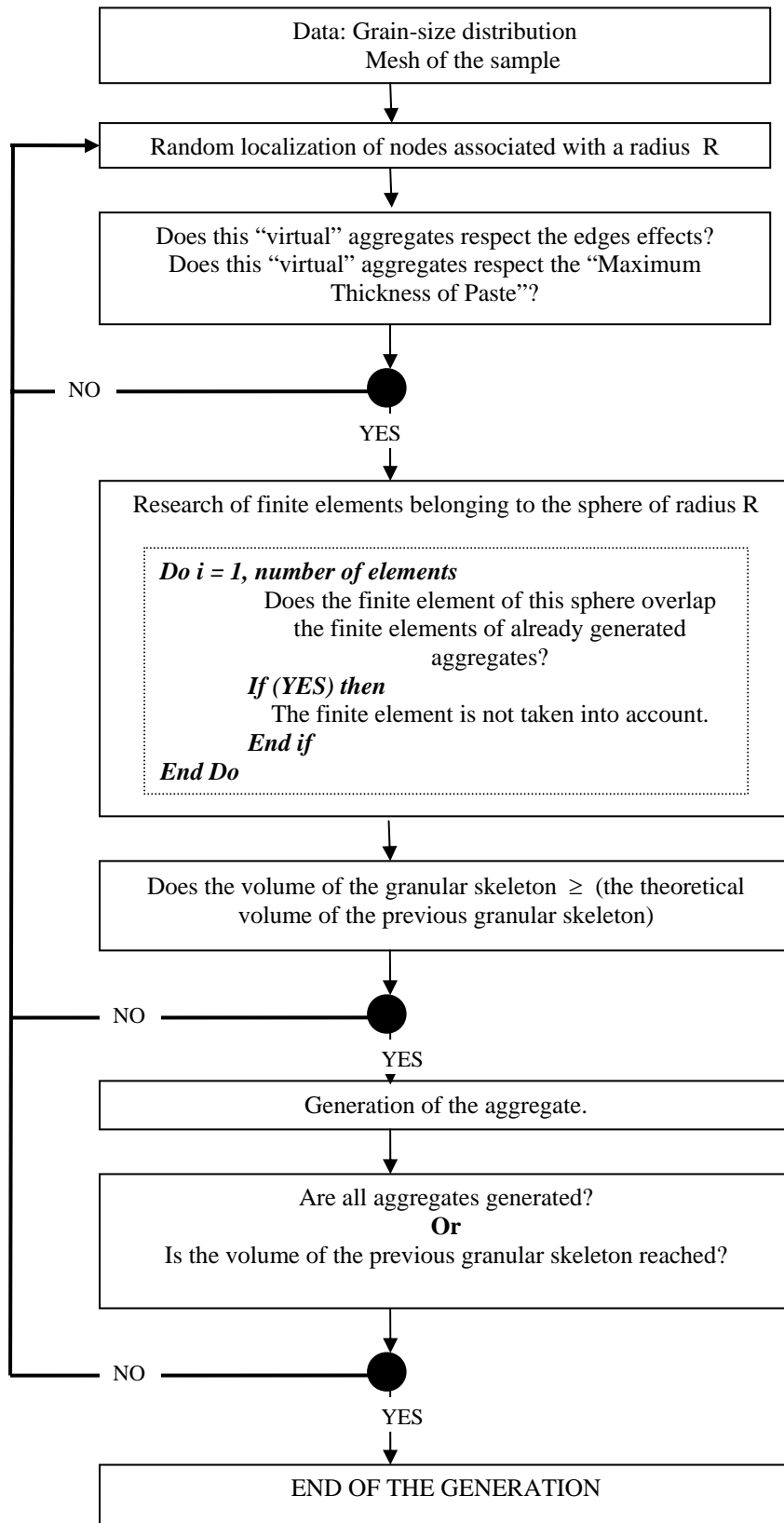


Figure 3-4. Random algorithm of aggregates generation.

## b) Discussion

We presently face a problem of storage capacity when a lot of aggregates with a very fine diameter have to be generated. Moreover the meshing stage is not yet parallelized. So two solutions emerge:

- Reduce the size of the sample;
- Consider larger aggregates embedded in a mortar paste constituted of sand grains, small aggregates and a cement paste.

The first solution is not efficient. Indeed, with a number of constant finite elements, a reduction by eight of the volume of the sample divides the size of the mesh only by two. Consequently we choose the second approach. **A minimal aggregate diameter must be set.** This threshold depends on the smoothness of the generated mesh and the granular skeleton to generate.

### 3.2.2.2 Representation in FEMCAM

The sample is parallelepipedic with a size of 280×70×70 mm. Table 3-1 represents the selected grain-size distribution based on experimental data:

Average diameter of aggregates (mm)	18	14.25	11.25	9	7.15
Number of aggregates	38	101	162	244	389

Table 3-1. Selected grain-size distribution with 935 aggregates.

The maximum diameter of the grains generated being of 18 mm, **MPT is evaluated to 2.6 mm**. About 65 million grains should be modelled in this sample to represent the sand grains. The second approach which considers two phases, aggregates embedded in a mortar paste, is thus well justified. So only the aggregates with a diameter between 7.15 and 18 mm are represented. The following mesh corresponds to the actual limit of the generation of a mesh by a standard computer (Intel Xeon Machine, 1.7 GHz, 512 Mo Ram). The mesh size is about 2 mm. The time needed to generate this skeleton is about one hour.

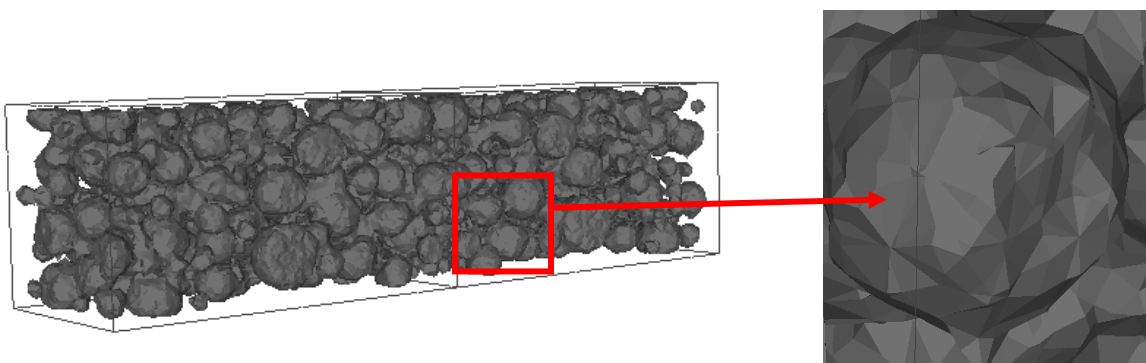


Figure 3-5. a) Heterogeneous sample generated in FEMCAM - 165 669 nodes; 902 826 elements; b) zoom on one aggregate in the sample.

Figure 3-5 shows numerical aggregates do not have a very regular shape, depending on the mesh structure. Thus contrary to other models considering aggregates as perfectly spherical (see chapter 2, section 2.4), **this method generates a sufficiently realistic granular skeleton in comparison with the real aggregates observed.**

The generation algorithm of the granular skeleton is based on three main aspects:

- The algorithm takes into account *physical parameters* as the edges effects and the “MPT”;
- *This generation is mesh dependent.* A very fine mesh allows obtaining a result closer to the desired grain-size distribution. Conversely the consequences of a coarse mesh are obtaining a sample whose grains have sizes values far away from the desired initial sizes;
- *The algorithm generates aggregates whose size is superior to a minimal diameter.* This hypothesis is necessary because of the limitation of the storage capacity of a standard computer.

Now we use this 3D multi field code to simulate concrete behavior. In the next part we introduce mechanical behaviors attributed to mortar paste and to aggregates.

### 3.3 The elastic damage model using a mixed-velocity pressure formulation

At the mesoscale, we distinguish two behaviors to simulate concrete specimen:

- Aggregates behavior;
- Mortar paste behavior.

Aggregates are considered as purely elastic. We have studied the different possibilities to simulate mortar paste behavior (see chapter 2, section 2.3). We have chosen here the elastic damage behavior with the Mazars model. This section deals with the implementation of the **Non Local Mazars model** in the 3D FE code FEMCAM. A specificity of this code is its mixed velocity-pressure formulation.

#### 3.3.1 The equilibrium equations

##### 3.3.1.1 The dynamic equilibrium

Let us consider a 3D domain  $\Omega$ . The classical equilibrium equations for a solid subject to a mechanical load can be expressed in a local form by:

$$\operatorname{div}(\sigma) + \rho f = \rho \gamma \quad (3-4)$$

where  $\sigma$  denotes the stress field in the solid,  $f$  the body forces per mass unit,  $\rho$  is the volumic mass and  $\gamma$  is the acceleration. The problem to be solved is expressed in FEMCAM using a velocity-pressure formulation. Thus the stress field tensor is classically expressed as the sum of its deviatoric part  $s$  and its spherical part  $p$ :

$$\sigma = s - pId \quad (3-5)$$

$Id$  is the identity tensor and  $p = \frac{-1}{3} \operatorname{Tr}(\sigma)$ .  $s$  is evaluated using a local resolution of the behavior law. The classical equilibrium equations for a solid submitted to a mechanical load can be expressed by:

$$\begin{cases} \text{Find } (v, p) \text{ such as :} \\ \operatorname{div}(s) - \operatorname{Grad}(p) + \rho f = \rho \gamma \end{cases} \quad (3-6)$$

### 3.3.1.2 The incompressibility condition

In addition to Eq. ( 3-6), we introduce the incompressibility condition on the velocity field  $v$ :

$$\operatorname{div}(v) = 0 \quad (3-7)$$

This condition will be modified to be adapted for concrete behavior.

### 3.3.1.3 The boundary conditions

We also prescribe some boundary conditions on the surface  $\partial\Omega = \partial\Omega_v \cup \partial\Omega_\tau$ .

- A surface load  $\tau_{imp}$  or an imposed velocity  $v_{imp}$  can be applied to  $\Omega$  on its boundary  $\partial\Omega_\tau$  :

$$\begin{aligned} \tau = \sigma.n = \tau_{imp} \quad \text{on} \quad \partial\Omega_\tau \\ \text{or} \\ v = v_{imp} \quad \text{on} \quad \partial\Omega_\tau \end{aligned} \quad (3-8)$$

in which  $\vec{n}$  is the normal to the part.

- One of the boundaries  $\partial\Omega_v$  of  $\Omega$  can be in contact with a tool. The contact can be defined with:

- a friction condition:

$$\tau = \sigma.n - (\sigma.n).n \quad (3-9)$$

- or a non penetration condition between a slave node and a master triangular face. It corresponds to the Signorini conditions:

$$\begin{aligned} (v - v_{tool}) \cdot n &\leq 0 \\ \sigma_n &\leq 0 \\ [(v - v_{tool}) \cdot n] \sigma_n &\leq 0 \end{aligned} \quad (3-10)$$

where  $v_{tool}$  is the tool velocity and  $\sigma_n = \sigma n \cdot n$  is the contact pressure at the normal of the surface of the part. More details on these techniques can be found in [Pichelin et al. 2001].

### 3.3.2 Constitutive equations

A classical one step Euler scheme is used to compute the solution at time  $t + \Delta t$  when the solution at  $t$  is known. In the case of a pure elastic behavior, the Young modulus  $E$  remains constant during simulation. In this case, there is no variation of the shear modulus  $\mu$  and the compressibility modulus  $\chi$  between  $t$  and  $t + \Delta t$ . In the case of an elastic damage model, the Young modulus  $E$  depends on the damage value. It thus affects the values of  $\mu$  and  $\chi$  which can change between time  $t$  and time  $t + \Delta t$ .

The material is assumed to be an elastic damage material. The elastic strain  $\varepsilon$  is related to the stress field tensor  $\sigma$  through the Hooke law:

$$\sigma = 2\mu\varepsilon + \lambda Tr(\varepsilon)Id \quad (3-11)$$

$$\text{with } \begin{cases} \mu = \frac{E(D)}{2(1+\nu)} & \text{with } \mu : \text{shear modulus} \\ \lambda = \frac{E(D)\nu}{(1-2\nu)(1+\nu)} & \text{with } \lambda : \text{Lamé coefficient} \end{cases}$$

$D$  denotes the damage which affects the Young modulus value  $E$  in order to the model material degradation. Using the Hooke law, we thus obtain the expression of the deviatoric part  $p$  and the spherical part  $s$ :

$$\begin{cases} s = \sigma - \frac{1}{3} Tr(\sigma)Id \\ Tr(\sigma) = (2\mu + 3\lambda) Tr(\varepsilon) \end{cases} \Rightarrow \begin{cases} s = 2\mu e \\ p = -\chi Tr(\varepsilon) \end{cases} \quad (3-12)$$

with  $\chi = \frac{E(D)}{3(1-2\nu)}$  with  $\chi$ : compressibility modulus and  $e = \varepsilon - \frac{1}{3} Tr(\varepsilon)Id$  is the deviatoric part of the strain tensor. The following paragraphs give the expressions of the deviatoric part  $s$  and the spherical part  $p$  if we consider their possible evolutions between  $t$  and  $t + \Delta t$ .

### 3.3.2.1 Deviatoric part

By definition:

$$s^{t+\Delta t} = 2\tilde{\mu}^{t+\Delta t} e^{t+\Delta t} \quad (3-13)$$

Furthermore:

$$\begin{aligned} \tilde{\mu}^{t+\Delta t} &= \tilde{\mu}^t + \Delta\tilde{\mu}^{t+\Delta t} \\ e^{t+\Delta t} &= e^t + \Delta e^{t+\Delta t} \end{aligned} \quad (3-14)$$

Expressing  $s$  as a function of time  $t$ , we get:

$$\begin{aligned} s^{t+\Delta t} &= 2(\tilde{\mu}^t + \Delta\tilde{\mu}^{t+\Delta t})(e^t + \Delta e^{t+\Delta t}) \\ s^{t+\Delta t} &= 2\tilde{\mu}^t e^t + 2\tilde{\mu}^t \Delta e^{t+\Delta t} + 2\Delta\tilde{\mu}^{t+\Delta t} e^t + 2\Delta\tilde{\mu}^{t+\Delta t} \Delta e^{t+\Delta t} \end{aligned} \quad (3-15)$$

which can be rewritten:

$$s^{t+\Delta t} = s^t + 2\tilde{\mu}^{t+\Delta t} \Delta e^{t+\Delta t} + 2\Delta\tilde{\mu}^{t+\Delta t} e^t \quad (3-16)$$

which is equivalent to the following system:

$$s^{t+\Delta t} = s^t + 2\tilde{\mu}^{t+\Delta t} \Delta t \dot{e}^{t+\Delta t} + \left( 2 \frac{\tilde{\mu}^{t+\Delta t}}{\tilde{\mu}^t} e^t \tilde{\mu}^t - 2e^t \tilde{\mu}^t \right) \quad (3-17)$$

Eq. ( 3-17) thus becomes:

$$s^{t+\Delta t} = \frac{\tilde{\mu}^{t+\Delta t}}{\tilde{\mu}^t} s^t + 2\tilde{\mu}^{t+\Delta t} \Delta t \dot{e}^{t+\Delta t} \quad (3-18)$$

with  $\dot{e} = \frac{\Delta e^{t+\Delta t}}{\Delta t} = \frac{e^{t+\Delta t} - e^t}{\Delta t}$ . We draw your attention on the fact that the term  $\frac{\tilde{\mu}^{t+\Delta t}}{\tilde{\mu}^t}$  is:

- equal to 1 within the framework of a pure elastic material.
- lower or equal to 1 within the framework of an elastic damaged material.

### 3.3.2.2 Spherical part

In the same way that above, it can be shown that at time  $t + \Delta t$ :

$$p_{t+\Delta t} = \frac{\chi_{t+\Delta t}}{\chi_t} p_t - \chi_{t+\Delta t} \Delta t \operatorname{div}(v) \quad (3-19)$$

In the same way, the term  $\frac{\chi_{t+\Delta t}}{\chi_t}$  is:

- equal to 1 within the framework of a pure elastic material.
- lower or equal to 1 within the framework of an elastic damaged material.

### 3.3.3 The weak formulation

We only consider the case of a quasi-static analysis. The inertia terms are thus neglected. We use the constitutive equations (see Eq. (3-19)) to rewrite the equation of behavior and the equation of incompressibility of the elastic damage strain part in the following way:

$$\begin{cases} \text{div}(s) - \text{Grad}(p) = 0 \\ \text{div}(v) - \frac{\dot{p}}{\chi} + \frac{\dot{\chi}}{\chi^2} p = 0 \end{cases} \quad (3-20)$$

This constitutes the strong formulation of the problem. In order to solve this problem, let us consider its weak formulation by introducing the following virtual fields\* :

$$\begin{aligned} V &= \left\{ v, v \in \{H^1(\Omega)\}^3, (v - v_{tool}) \cdot n \leq 0 \text{ on } \partial\Omega_v \right\} \\ V_0 &= \left\{ v, v \in \{H^1(\Omega)\}^3, v \cdot n \leq 0 \text{ on } \partial\Omega_v \right\} \\ P &= L^2(\Omega) \end{aligned} \quad (3-21)$$

Thanks to the Virtual Work Principe (VWP), we get the weak velocity–pressure formulation associated to the mechanical problem:

$$\begin{aligned} \text{Find } (v, p) &\in V \times P \\ \left\{ \begin{aligned} \int_{\Omega} s(v) : \dot{\varepsilon}(v^*) d\Omega - \int_{\Omega} p \text{div}(v^*) d\Omega - \int_{\partial\Omega} \tau_{imp} \cdot v^* dS &= 0 \\ \int_{\Omega} p^* \left[ -\text{div}(v) - \frac{\dot{p}}{\chi} + \frac{\dot{\chi}}{\chi^2} p \right] d\Omega &= 0 \end{aligned} \right. & (3-22) \\ \forall (v^*, p^*) &\in V^0 \times P \end{aligned}$$

### 3.3.4 Discretization

Let us consider a finite element discretization of the 3D domain  $\Omega$ .

$$\Omega = \bigcup_e \Omega_e, e \in E \subset N \quad (3-23)$$

---

\*  $L^2(\Omega)$  is the space of the functions which are square integrable on  $\Omega$  and  $H^1$  is the Sobolev space of  $L^2$  integrable functions.

### 3.3.4.1 Choice of the finite element

We use here P1+/P1 elements [Coupez 1991]. These are linear tetrahedral elements. "+" means we use an additional degree of freedom for velocity interpolation, at the centre of the element. This additional degree of freedom enables to comply with the Brezzi-Babuska compatibility relation between spaces for discretization of velocity and pressure [Babuska 1973]: the associated shape function is the bubble function. Velocity and pressure are interpolated linearly on the element and the degrees of freedom are located at each node of the element. The pressure field is linear and continuous.

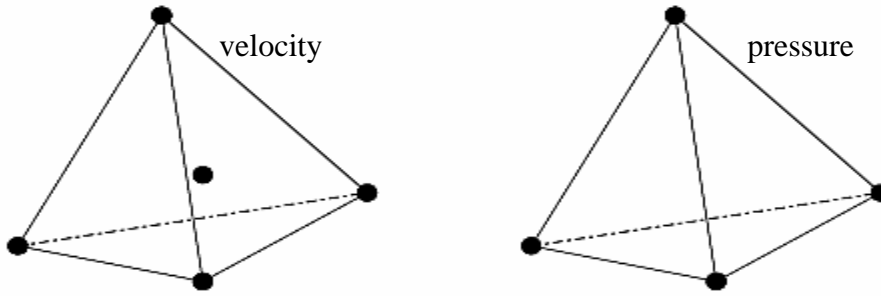


Figure 3-6. Representation of the P1+/P1 element.

### 3.3.4.2 Discrete weak formulation

We consider  $V_h \subset V$  and  $P_h \subset P$ . The  $B_h$  space stands for the bubble function discretization.

$$\begin{aligned}
 V_h &= \left\{ v_h, v_h \in (C^0(\Omega))^3 \text{ and } v_h|_{\Omega_e} \in (P_1(\Omega_e))^3, \forall e \in E \right\} \\
 P_h &= \left\{ p_h, p_h \in C^0(\Omega) \text{ and } p_h|_{\Omega_e} \in P_1(\Omega_e), \forall e \in E \right\} \\
 B_h &= \left\{ b_h, b_h \in (C^0(\Omega))^3, b_h = 0 \text{ on } \partial\Omega_e, \forall e \in E, b_h|_{\Omega_{e_i}} \in (P_1(\Omega_{e_i}))^3, i \in 1 \dots 4 \right\}
 \end{aligned} \tag{3-24}$$

$(C^0(\Omega))^3$  is the space of continuous functions on the field  $\Omega \in \mathfrak{R}^3$ .  $(P^1(\Omega_e))^3$  denotes the space of linear functions on the element  $\Omega_e \subset \mathfrak{R}^3$ \*

The velocity field  $v$  interpolated on element P1+/P1 is decomposed:

$$w_h = v_h + b_h, \text{ where } w_h \in W_h = V_h \oplus B_h \tag{3-25}$$

where  $v_h$  is the linear component of the velocity field and  $b_h$  the bubble-related component. Let  $Nbnoe$  and  $Nbelt$  be respectively the number of nodes and of elements associated to the

\*  $\Omega_{e_i} \Big|_{i=1, \dots, 4}$  represents all the tetrahedra  $\Omega_e$  of the triangulation, the sub-tetrahedra for which the tetrahedron centre is a classical node.

space triangulation with  $\Omega$ . Consequently, the velocity field can be expressed at any point  $x$  of space through the finite element approximation:

$$w_h(x) = \sum_{k=1}^{nbnoe} N_k^l(x) V_k + \sum_{j=1}^{nbelt} N_j^b(x) B_j \quad (3-26)$$

where  $w_h \in W_h$ .  $(N_k^l)_{k=1\dots nbnoe} \in V_h$  are related to interpolation of the linear element associated the node  $k$  and  $(N_j^b)_{j=1\dots nbelt} \in B_h$ , the bubble function associated with the element  $j$ .

Pressure can be expressed at any point  $x$  by:

$$p_h(x) = \sum_{k=1}^{nbnoe} N_k^l(x) P_k \quad (3-27)$$

Based on these approximation spaces, it is now possible to write the discrete elastic damage problem:

$$\begin{aligned} & \text{Find } (v_h, b_h, p_h) \in V_h \times B_h \times P_h \text{ such as :} \\ & \left\{ \begin{aligned} & \int_{\Omega} s(v_h + b_h) : \dot{\varepsilon}(v_h^*) dV - \int_{\Omega} p_h \operatorname{div}(v_h^*) dV - \int_{\partial\Omega_v} \tau(v_h) v_h^* dS = 0 \\ & \int_{\Omega} s(v_h + b_h) : \dot{\varepsilon}(b_h^*) dV - \int_{\Omega} p_h \operatorname{div}(b_h^*) dV = 0 \\ & \int_{\Omega} p_h^* [-\operatorname{div}(v_h + b_h) - \frac{\dot{p}_h}{\chi} + \frac{\dot{\chi}}{\chi^2} p_h] dV = 0 \\ & \forall (v_h^*, b_h^*, p_h^*) \in V_h^0 \times B_h^0 \times P \end{aligned} \right. \quad (3-28) \end{aligned}$$

### 3.3.4.3 Resolution of the finite element problem

The problem Eq. (3-28), after using a time integration scheme on time step  $\Delta t$ , gives a nonlinear system of equations where the unknowns are  $v_h, b_h, p_h$ .

$$\begin{cases} R^l(v_h, b_h, p_h) = R^{ll} + R^{lb} + R^{lp} + R^l = 0 \\ R^b(v_h, b_h, p_h) = R^{bl} + R^{bb} + R^{bp} + R^b = 0 \\ R^p(v_h, b_h, p_h) = R^{pl} + R^{pb} + R^{pp} + R^p = 0 \end{cases} \quad (3-29)$$

where

$$\begin{aligned}
 R^{ll} &= \int_{\Omega} s(v_h) : \dot{\varepsilon}(v_h^*) dV & R^{lb} &= \int_{\Omega} s(b_h) : \dot{\varepsilon}(v_h^*) dV & R^{lp} &= \int_{\Omega} s(v_h) : \dot{\varepsilon}(v_h^*) dV \\
 R^{bl} &= \int_{\Omega} s(v_h) : \dot{\varepsilon}(b_h^*) dV & R^{bb} &= \int_{\Omega} s(b_h) : \dot{\varepsilon}(b_h^*) dV & R^{bp} &= -\int_{\Omega} p_h^* \operatorname{div}(b_h) dV \\
 R^{pl} &= -\int_{\Omega} p_h^* \operatorname{div}(v_h) dV & R^{pb} &= -\int_{\Omega} p_h^* \operatorname{div}(b_h) dV & R^{pp} &= -\int_{\Omega} p_h^* \left[ \frac{\dot{p}_h}{\chi} + \frac{\dot{\chi}}{\chi^2} p_h \right] dV \\
 R^l &= -\int_{\partial\Omega_v} \tau(v_h) \cdot v_h^* dS & R^p &= 0 & R^b &= -\int_{\Omega} \rho g b_h^* dV
 \end{aligned} \tag{3-30}$$

where  $\dot{p}_h = \frac{P_{n+1} - P_n}{\Delta t}$

The nonlinear system Eq. ( 3-29) is solved using a Newton-Raphson iterative method. The stiffness matrix is assembled from the local matrices:

$$K^{xy} = \frac{\partial R^{xy}}{\partial y} \tag{3-31}$$

where  $(xy) = \{(ll); (lb); (lp); (bl); (bb); (bp); (pl); (pb); (pp)\}$  and  $y = \{v_h, b_h, p_h\}$ . This matrix is symmetrical. Thus for each iteration of the Newton-Raphson method, the linear system to be solved has the following form:

$$\begin{bmatrix} K^{ll} & K^{lb} & K^{lp} \\ K^{lb} & K^{bb} & K^{bp} \\ K^{lp} & K^{bp} & K^{pp} \end{bmatrix} \begin{pmatrix} \delta v \\ \delta b \\ \delta p \end{pmatrix} = - \begin{pmatrix} R^l(v_n, b_n, p_n) \\ R^b(v_n, b_n, p_n) \\ R^p(v_n, b_n, p_n) \end{pmatrix} \tag{3-32}$$

$\delta v, \delta b, \delta p$  are the iterative corrections of fields  $v$ ,  $b$  and  $p$ .

$$\begin{cases} v_{n+1} = v_n + \delta v \\ b_{n+1} = b_n + \delta b \\ p_{n+1} = p_n + \delta p \end{cases} \tag{3-33}$$

According to the definition of space  $B$ , the bubble is an internal degree of freedom to the element. It is indeed equal to zero on the edges. Consequently, it can be determined in the system at the element level. At each Newton-Raphson iteration, the resolution gives the nodal corrections  $\delta v, \delta p$  in order to compute  $v_{n+1}$  and  $p_{n+1}$  from  $v_n$  and  $p_n$ . The determination of  $b_{n+1}$  is then carried out at the element level. These steps are carried out until convergence.

### 3.3.5 General outline of an elastic damage problem resolution in FEMCAM

Figure 3-7 shows a schematic diagram of the algorithm used to solve an elastic damage problem in FEMCAM. The strain  $\varepsilon^i$  is updated at each time step. The stress deviator  $s$  and the tangent modulus  $L$  are then calculated, the tangent modulus is used in the Newton-

Raphson algorithm. The loading is then incremented. Damage can be weakly or strongly coupled to the material behavior.

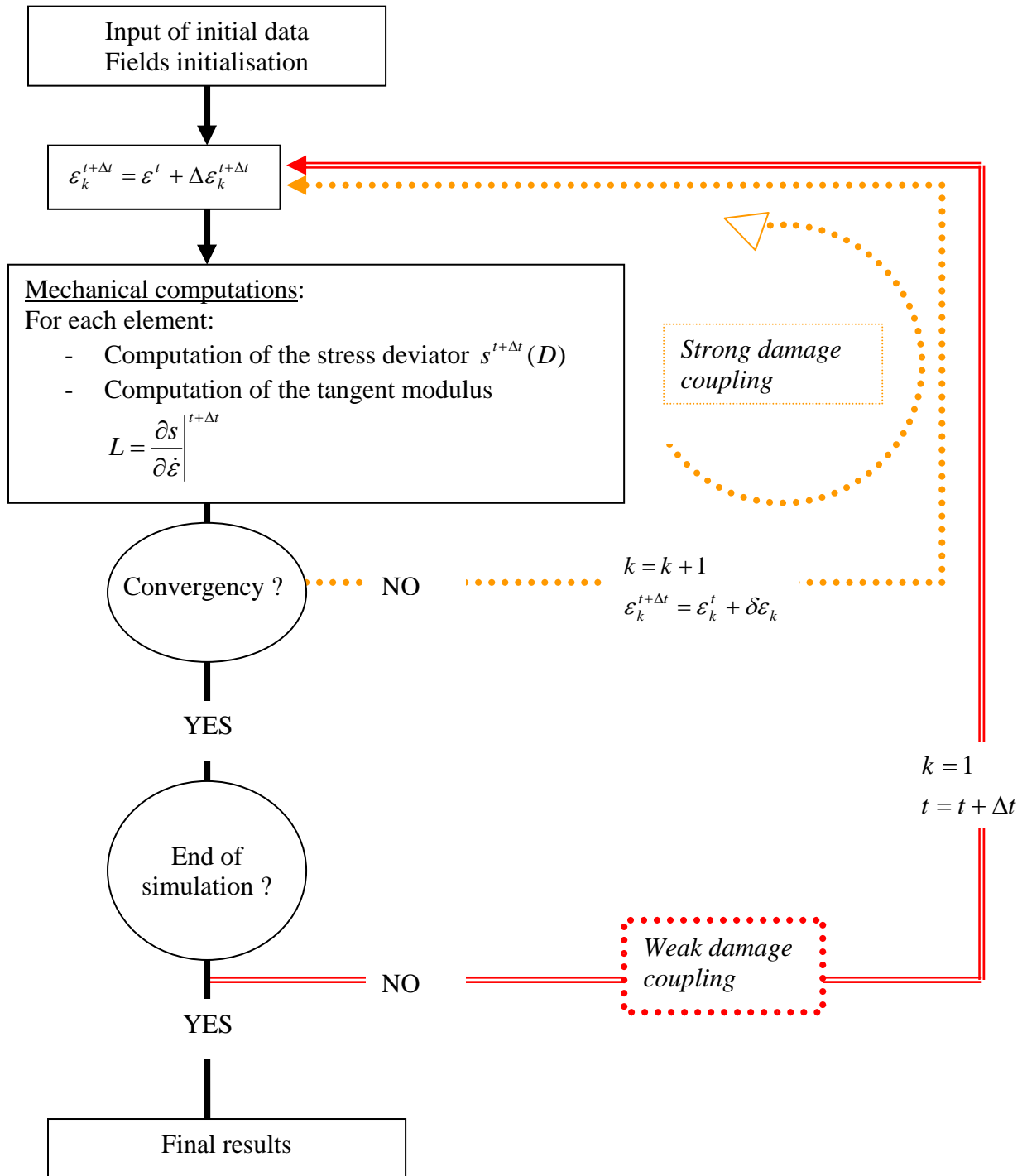


Figure 3-7. Resolution of an elastic damage problem.

### 3.3.5.1 Weak coupling

Damage is evaluated at the beginning of the time step using strains and stresses computed at the previous time step. The damage value  $D$  calculated at the end of the previous time step affects the Young modulus  $E$  for the following time step.

### 3.3.5.2 Strong coupling

Once the strain has been computed, a corresponding damage  $D$  is evaluated at the same time. The Young modulus  $E$  is then affected. Weak coupling does not lead to a mechanical balance of the problem. In a strong coupling procedure, the strains are thus corrected within the Newton-Raphson loop. Once the equilibrium has been reached, the loading is incremented and the process continues.

The tangent modulus is also affected by an additional term within the framework of a strong coupling. At time  $t + \Delta t$ :

$$L^{t+\Delta t} = \frac{\partial s^{t+\Delta t}}{\partial \dot{\varepsilon}^{t+\Delta t}} = -2\tilde{\mu}^0 \frac{\partial D^{t+\Delta t}}{\partial \tilde{\varepsilon}^{t+\Delta t}} \frac{\partial \tilde{\varepsilon}^{t+\Delta t}}{\partial \varepsilon^{t+\Delta t}} \frac{\partial \varepsilon^{t+\Delta t}}{\partial \dot{\varepsilon}^{t+\Delta t}} e^{t+\Delta t} + 2\Delta t \tilde{\mu}^{t+\Delta t} \frac{\partial \dot{\varepsilon}^{t+\Delta t}}{\partial \dot{\varepsilon}^{t+\Delta t}} \quad (3-34)$$

Where  $\tilde{\mu}^0$  denotes the initial shear modulus and  $\tilde{\mu}^{t+\Delta t}$  the reactualized one. Hence, we can obtain:

$$L^{t+\Delta t} = \frac{\partial s^{t+\Delta t}}{\partial \dot{\varepsilon}^{t+\Delta t}} = \boxed{-\Delta t \frac{\tilde{\mu}^0}{\tilde{\mu}^{t+\Delta t}} \frac{\partial D^{t+\Delta t}}{\partial \tilde{\varepsilon}^{t+\Delta t}} \frac{\partial \tilde{\varepsilon}^{t+\Delta t}}{\partial \varepsilon^{t+\Delta t}} s^{t+\Delta t}} + \boxed{2\Delta t \tilde{\mu}^{t+\Delta t} \frac{\partial \dot{\varepsilon}^{t+\Delta t}}{\partial \dot{\varepsilon}^{t+\Delta t}}} \quad (3-35)$$

  
 (a)

  
 (b)

As the term (a) is nonlinear with respect to the strains, the bubble tangent modulus remains identical to those calculated within the framework of a purely elastic problem (linear part of the tangent modulus). The assumption that part (b) is negligible leads us to use a tangent modulus identical to the pure elastic case. This assumption is justified as long as it does not prevent convergence.

## 3.4 Selection of the model and numerical strategy

The constitutive law is now going to be validated. We shall check the efficiency of the non local model and we test the two possible implementations of this model (weak or strong coupling).

### 3.4.1 Local versus non local model

#### 3.4.1.1 Numerical test

We wish to underline here the interest of the nonlocal model with an integral formulation (see chapter 2, section 2.3.2.2). A 3D tensile specimen with a centred hole has been simulated using both non local and local Mazars model. Dimensions of the specimen are 200×200×2.5 mm. Due to symmetry only a quarter of the sample is discretized as shown in figure 3-8.

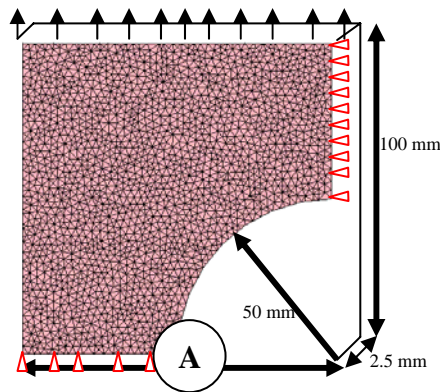


Figure 3-8. Tensile specimen.

The behavior corresponds to an elastic damage law. We have used the following arbitrary parameters for these simulations (see table 3-2).

$E$ (GPa)	$\nu$	$A_C$	$B_C$	$A_T$	$B_T$	$\varepsilon_{D0}$	$\tilde{\varepsilon}^{Crit}$	$\beta$	$l_C$ (mm)
30	0.2	1.4	1700	0.8	20000	$1 \cdot 10^{-4}$	$1 \cdot 10^{-3}$	1.05	15

Table 3-2. Material parameters.

We study here the mesh dependency of results using the local and non local Mazars model. Figure 3-9 shows the five different meshes  $h$  used for this study. When the equivalent strain  $\tilde{\varepsilon}$  reaches  $\tilde{\varepsilon}^{Crit}$ , the “Kill element” method is used; the element mechanical contribution to the stiffness matrix is set to zero.

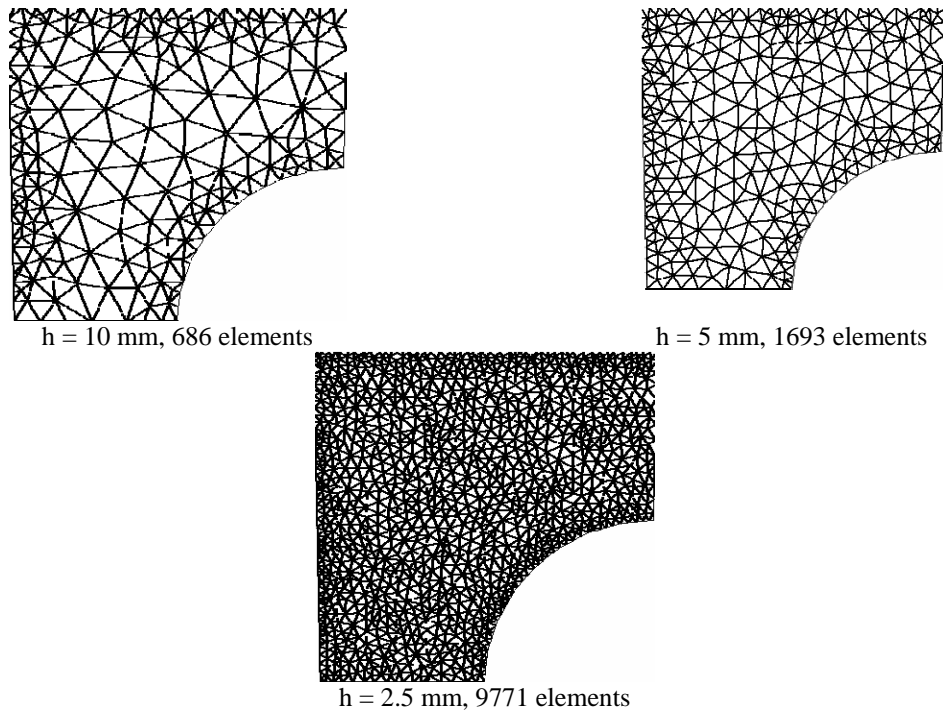


Figure 3-9. Finite element meshes with different mesh sizes  $h$ .

We test here the effect of the non local model on the material response.

We have plotted at location A the damage evolution versus displacement predicted by Mazars model in its local version (figure 3-10.a) and the non local version (figure 3-10.b). Points on the different curves are arbitrary placed and do not correspond to the time step of the simulation.

This tensile test shall physically induce crack initiation of the sample at point A. The local model gives a damage which evolves with different velocity to 1 for  $h = 10$  mm and  $h = 2.5$  mm. However we can see that the local model gives a damage response for  $h = 5$  mm which does not converge to 1. How can we explain this behavior? The sample first damages at point A. Then a crack initiates in the sample - but not at point A. The local model is thus responsible of this non-physical behavior. Consequently damage is distributed differently and stagnates ( $D \approx 0.5$  at the end of the simulation).

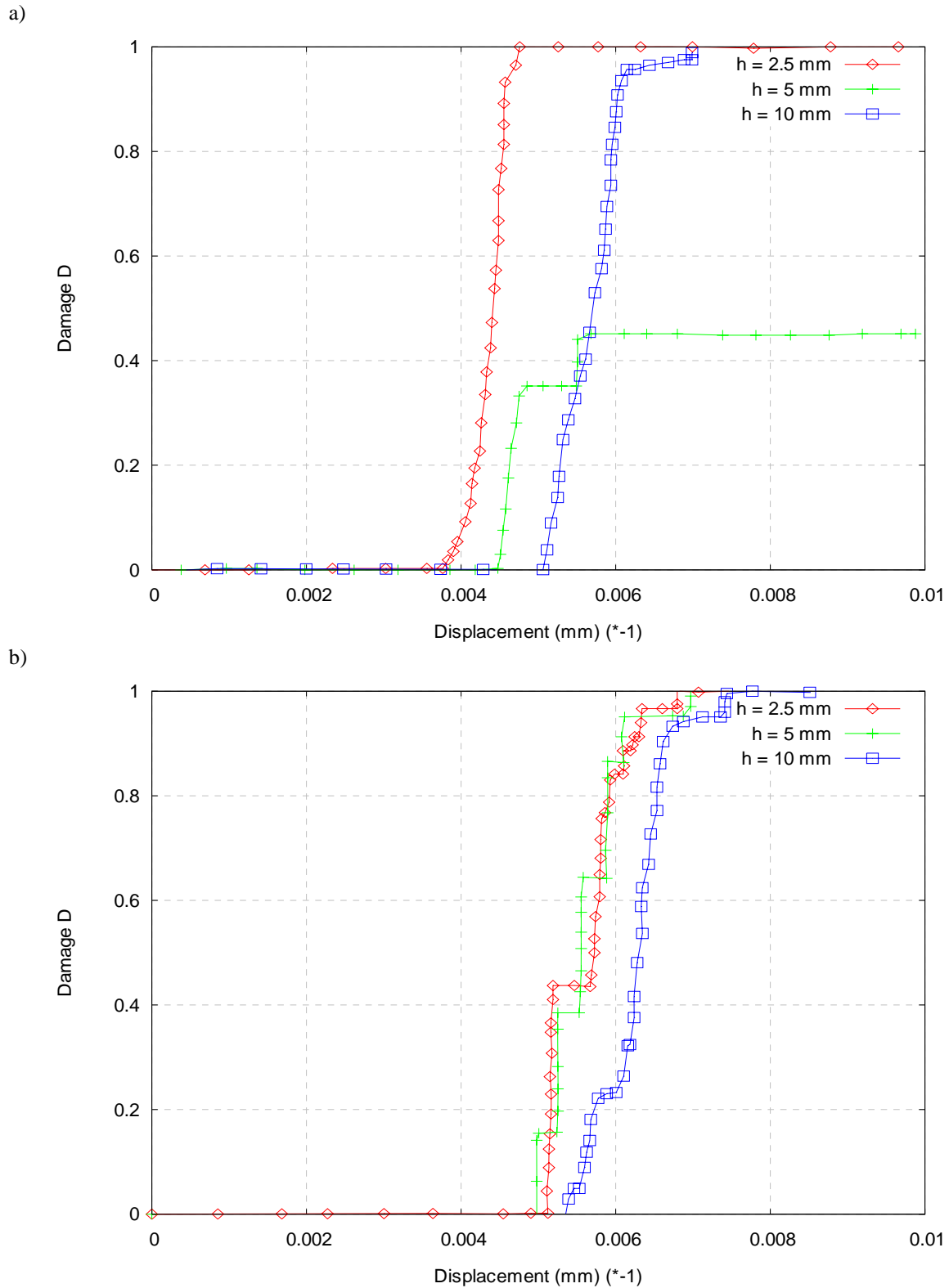
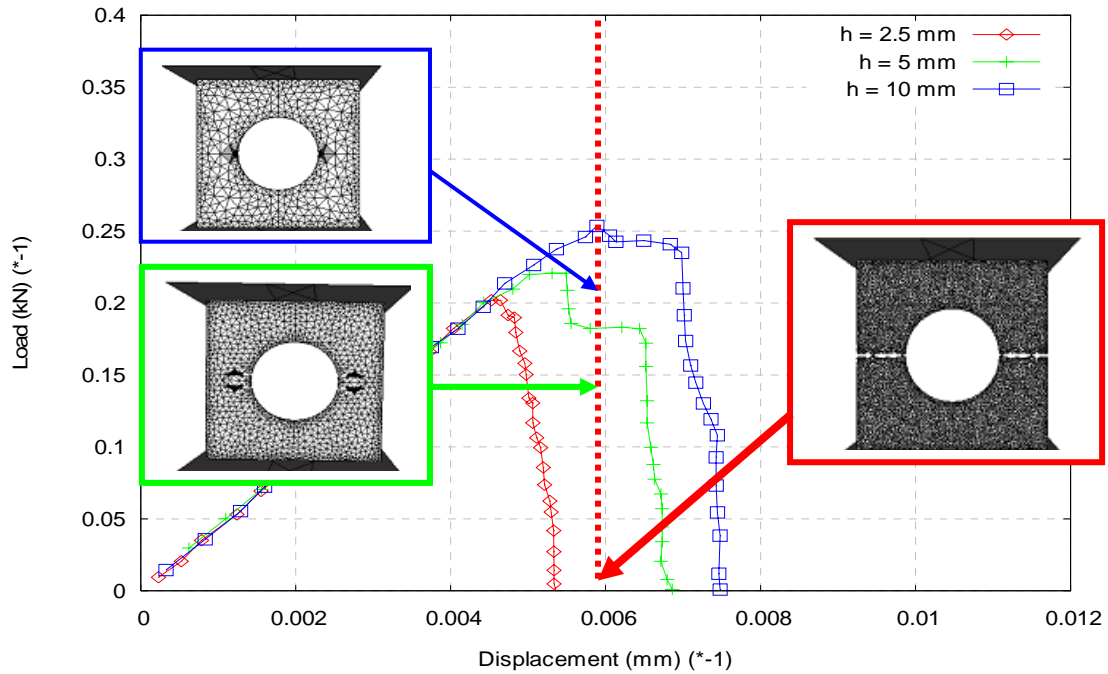


Figure 3-10. Damage evolution: a) local model, b) non local model.

Figure 3-11 compares the load-displacement curves obtained using different mesh refinements for a classical damage model (figure 3-11.a) and for the non local damage model

(figure 3-11.b) with an integral formulation. Points on the different curves are arbitrary placed and do not correspond to the time step of the simulation.

a)



b)

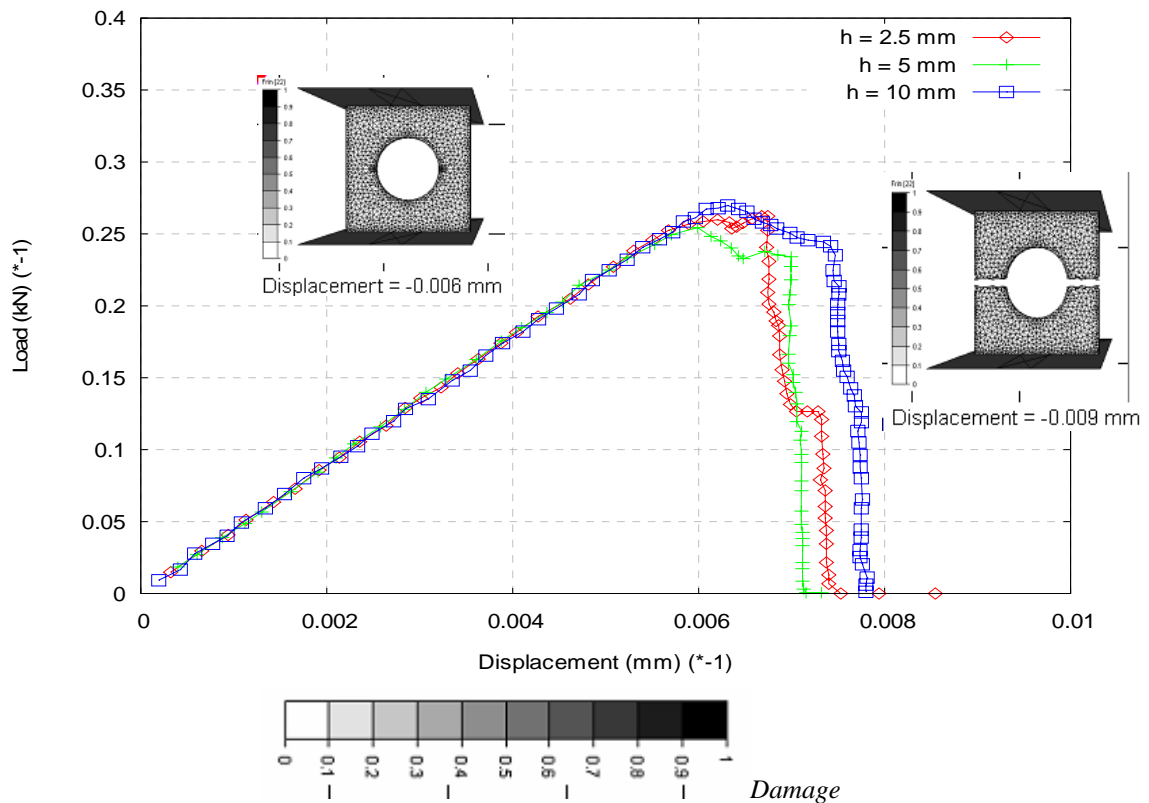


Figure 3-11. Load-displacement curves: a) local model, b) non local model.

In the case of the local Mazars model, damage evolution in point A (figure 3-10)

differs according to the mesh size  $h$ . Moreover we can see that the load-displacement curve is unstable in the damaged part. For example, the load-displacement curve, corresponding to the mesh size equal to 1.25 mm, evolves very differently in the damaged part in comparison with the other curves. It underlines the different evolutions of damage in the whole sample according to the mesh size. On the contrary, the nonlocal model shows its effectiveness whatever the mesh refinement:

- Damage evolution in A is insensitive with respect to the mesh size;
- The load-displacement curve is stable in the damaged part;
- It can be seen that damage increase is more important with a finer mesh. Mesh dependency of the results is clearly less sensitive for the non local approach.

Mesh dependency is thus clearly less important for the non local approach.

### 3.4.1.2 Choice of the non local model

We have noticed the mesh independence of the non local model with an integral formulation. But, associated to the “Kill element” method, the integral formulation may give unaccurate results. The area used to regularize the solution (based on the characteristics length) for a node close to the crack, may include a node located on the other side of the crack, which is non realistic. This problem is shown figure 3-12.

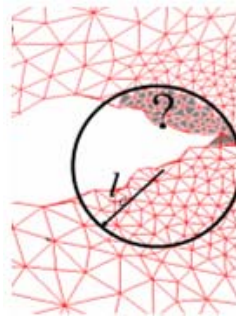


*Figure 3-12. A 2D case where the evaluation of the finite elements belonging to the representative volume for the non local model with an integral formulation leads to a problem when it is associated to a crack.*

There are some solutions to this problem: the distance between elements can be evaluated differently. We can estimate the “real” distance by circumventing the crack. However this method is heavy to integrate in a finite element code.

Furthermore it leads to a dependence of the computation time in function of the number of finite elements. Figure 3-13 compares the computation time between a local model (LM), a non local model with an integral formulation (NLM) and a non local model with an implicit model (NLIM) for different numbers of elements. Each test is performed on a standard computer (Intel Xeon Machine, 1.70 GHz, 1 Go RAM).

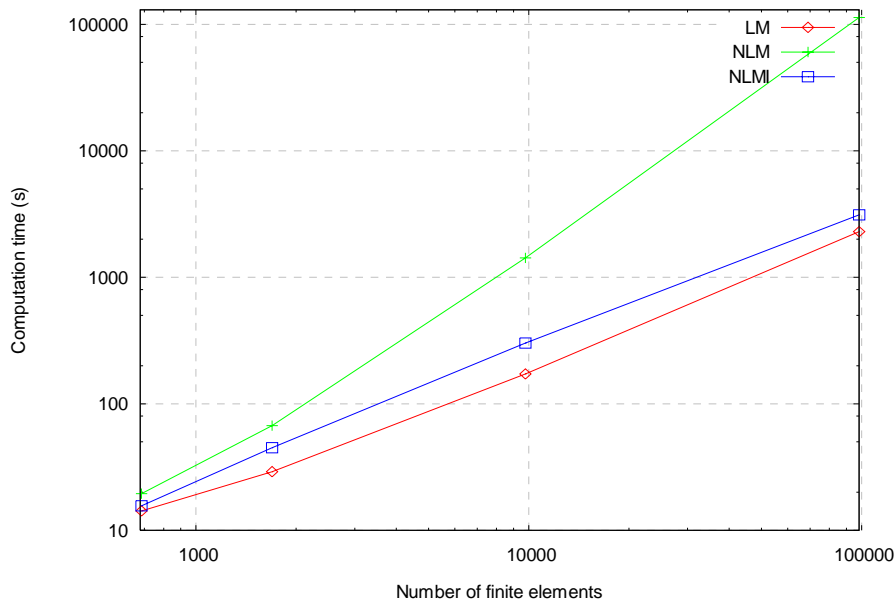


Figure 3-13. Comparison of the computation times between local and non local models

We notice that the computation time increases linearly with the number of elements for the local model (LM) and for the non local model with an implicit formulation (NLMI). The CPU time of the local model is the faster. For the non local model with an integral formulation (NLM) this increase is exponential with the number of finite elements. For 100 000 elements, the CPU time is multiplied by almost 100, which is gigantic. Nevertheless it could be interested to optimize the algorithm to decrease CPU time. A solution is to use *the Evolutive Non Local Model (ENLM)*: The integral formulation is used at the beginning of the simulation and stops being used once damage has reached a critical value in the sample. The “ENLM” model provides a good balance between CPU time requirements and results accuracy. In this way the “ENLM” model is smaller than for the NLM almost 2.5 times faster than the classical non local model (NLM) but almost fifteen times higher than for the local model (LM).

But the implicit formulation leads to the best result in term of CPU time. Whereas this method is an approximation of the non local approach, it is also well adapted to 3D multi-materials simulations as we have demonstrated that the calculus time is not so high than for a non local approach. Furthermore the evaluation of  $\tilde{\varepsilon}$  is independent of the behavior of the neighbouring elements. It is so well adaptive for heterogeneous materials and for simulations which used fracture mechanics. **We have thus selected this implicit model for our future numerical tests.**

### 3.4.1.3 Choice of the internal length for the non local model

A three point bending test has been performed with the non local model associated to an implicit formulation (more details on this test will be given in section 4.5.1.1). Table 3-3 shows the arbitrary parameters we have chosen:

$E^M$ (GPa)	$\nu^M$	$\varepsilon_{D0}$	$A_T$	$B_T$	$\tilde{\varepsilon}^{Crit}$
30	0.2	$3.4625 \cdot 10^{-5}$	1.29	25 316	$1.385 \cdot 10^{-4}$

Table 3-3. Second set of parameters used to verify the objective function.

Numerically, we have observed that the use of a non local model leads to an independence on the mesh choice in the linear part and during the damage initiation in the sample (see section 3.4.1.1). And the internal length is an important parameter since the maximal load reached depends on its value. For different internal lengths values, different sets of parameters can be found. Here we have evaluated the effect of the parameter  $\tilde{c}$  on the load-displacement curve. We use here the same mesh (the mesh size used is equal to 2.5 mm) to compare numerical results.

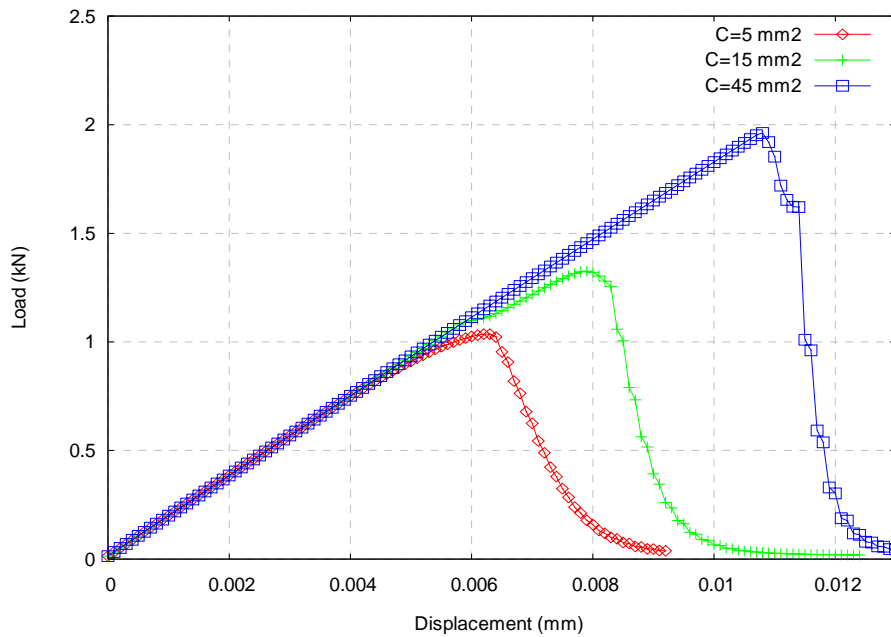


Figure 3-14. Comparison of the load-displacement curve for a three point bending test for different internal length.

Figure 3-14 underlines the importance of the choice of the internal parameter  $\tilde{c}$ . The introduction of this one modifies the damage evolution and the maximum load reached. When the  $\tilde{c}$  value is small with respect to the mesh size, the non local model has no effect on the global response. We are thus close to the local model. It is then important to correlate the  $\tilde{c}$  value and the mesh used. When the  $\tilde{c}$  value increases, the non local model has an influence on the global response. We do not converge to a unique solution. It is therefore necessary to adapt parameters identification in function of  $\tilde{c}$ .

### 3.4.2 Weak coupling versus strong coupling

The influence of coupling on the material response is investigated here. In order to simplify interpretation of results, we work on a single element submitted to tension (figure 3-15). Three symmetries are imposed on the three faces of the tetrahedron in order to prevent any rigid body motion.

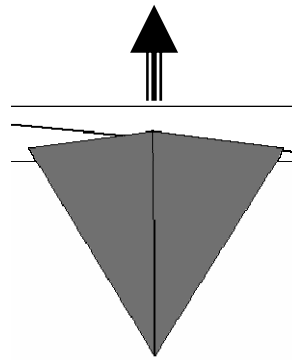


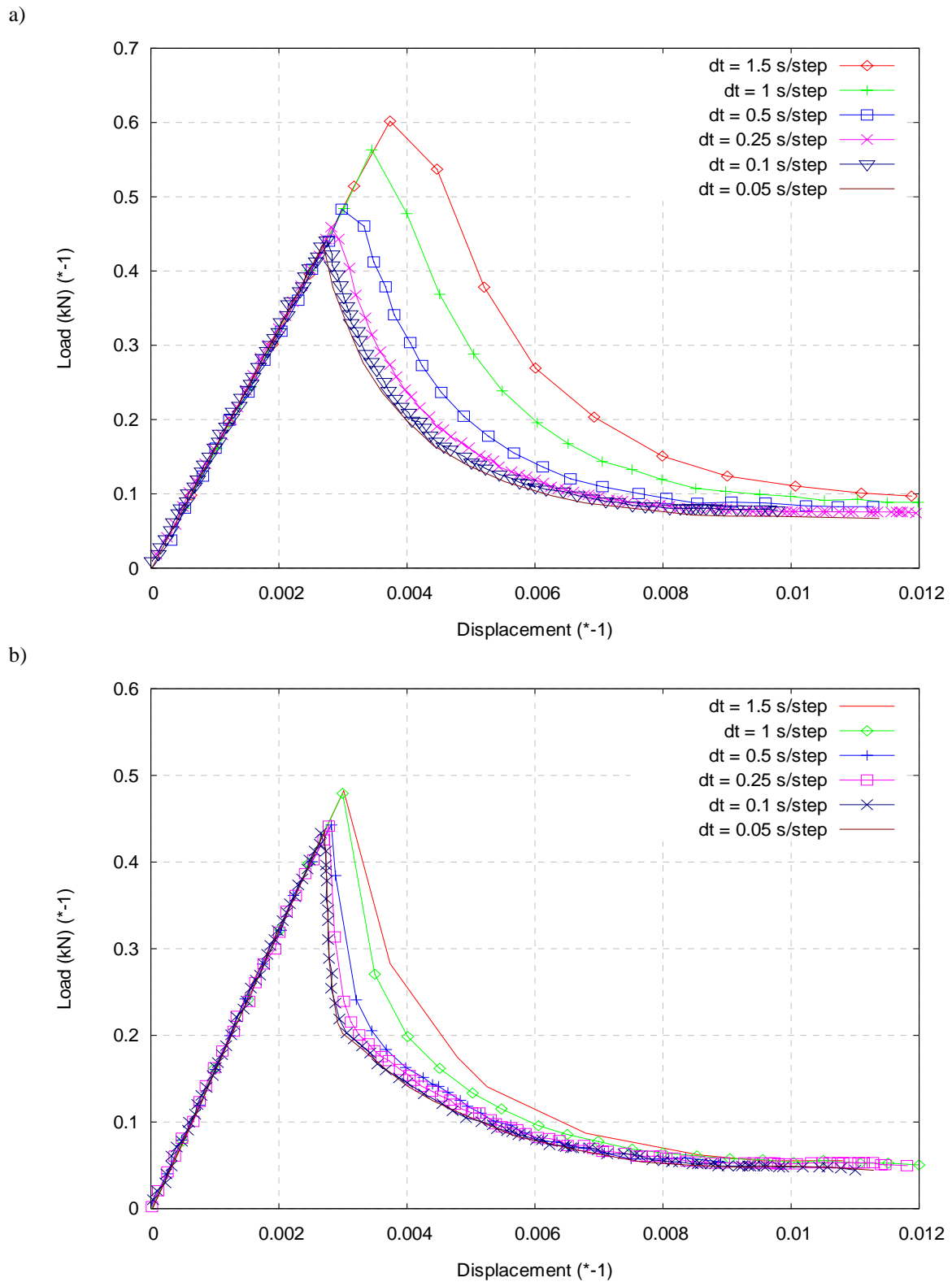
Figure 3-15. Single element submitted to a tensile test.

The constitutive law is an elastic damage law. Table 3-4 gives the material parameters.

$E$ (GPa)	$\nu$	$A_C$	$B_C$	$A_T$	$B_T$	$\varepsilon_{D0}$	$\beta$
30	0.2	1.4	1700	0.8	20000	$1.10^{-4}$	1.05

Table 3-4. Material parameters.

Here the influence of the time step on the material global response is tested. Figure 3-16 shows the load-displacement curves for each time step using a weak coupling (figure 3-16.a) or a strong coupling (figure 3-16.b). It can be noted that results are less dependent on the time step for strong coupling. However a strong coupling leads to higher computation times. It can become unacceptable for large multimaterial cases. In this case, it can be thus preferable to use a weak coupling in conjunction with an adaptive time step.



### 3.4.3 Adaptive time step

In order to improve the convergence of the Mazars model without decreasing the time step over the whole time interval we have developed a specific procedure module in the FEMCAM software enabling time step adaptation with respect to damage evolution.

#### 3.4.3.1 Local approach

The first method is based on the damage evolution in each finite element (*Adaptive Time Step n° 1*). In Mazars model case, the first solution is to compute the time step  $dt_n$  using the following formula:

$$dt_n = \begin{cases} \text{Min}(dt_0, a\tilde{\varepsilon}_{calc}^2 + b\tilde{\varepsilon}_{calc} + c) & \text{if } 0 \leq \tilde{\varepsilon}_{calc} \leq \varepsilon_{d0} \\ \text{with } a = \frac{1}{\varepsilon_{d0}^2}; b = -2a\varepsilon_{d0}; c = dt_0 \\ \text{Min}(dt_0, a\tilde{\varepsilon}_{calc} + b) & \text{if } \tilde{\varepsilon}_{calc} > \varepsilon_{d0} \\ \text{with } a = \frac{1}{\tilde{\varepsilon}^{Crit} - \varepsilon_{d0}}; b = -a\varepsilon_{d0} \end{cases} \quad (3-36)$$

$\tilde{\varepsilon}_{calc}$  corresponds to the value on the element for which the equivalent strain is the nearest to  $\varepsilon_{D0}$ ;  $\varepsilon_{D0}$  is the equivalent strain threshold in the Mazars model and  $\tilde{\varepsilon}^{Crit}$  is the equivalent strain beyond which damage is initiated.  $dt_0$  corresponds to the initial time step. The polynomial has been specifically chosen to integrate these important data. It enables to reduce time step when the equivalent strain is close to the equivalent strain threshold. Figure 3-17 shows the evolution of the time step for  $\varepsilon_{D0} = 10^{-4}$  and  $\tilde{\varepsilon}^{Crit} = 10^{-3}$ .

Figure 3-17 shows that the time step decreases when the equivalent strain  $\tilde{\varepsilon}_{calc}$  becomes close to the equivalent strain threshold  $\varepsilon_{D0}$ . When  $\tilde{\varepsilon}_{calc}$  is equal to  $\varepsilon_{D0}$  there is a minimum value for the global time step. If  $\tilde{\varepsilon}_{calc}$  exceeds  $\varepsilon_{D0}$ , time step increases linearly until it reaches a maximal value. However this local approach can be inappropriate in the case of complex problems where damage does not evolve with the same rate in different areas of the sample. Consequently it leads to a very fine time step during almost all the simulation. Though it may give good results, the method can be improved in order to save on computation time. Thus we introduce a global approach.

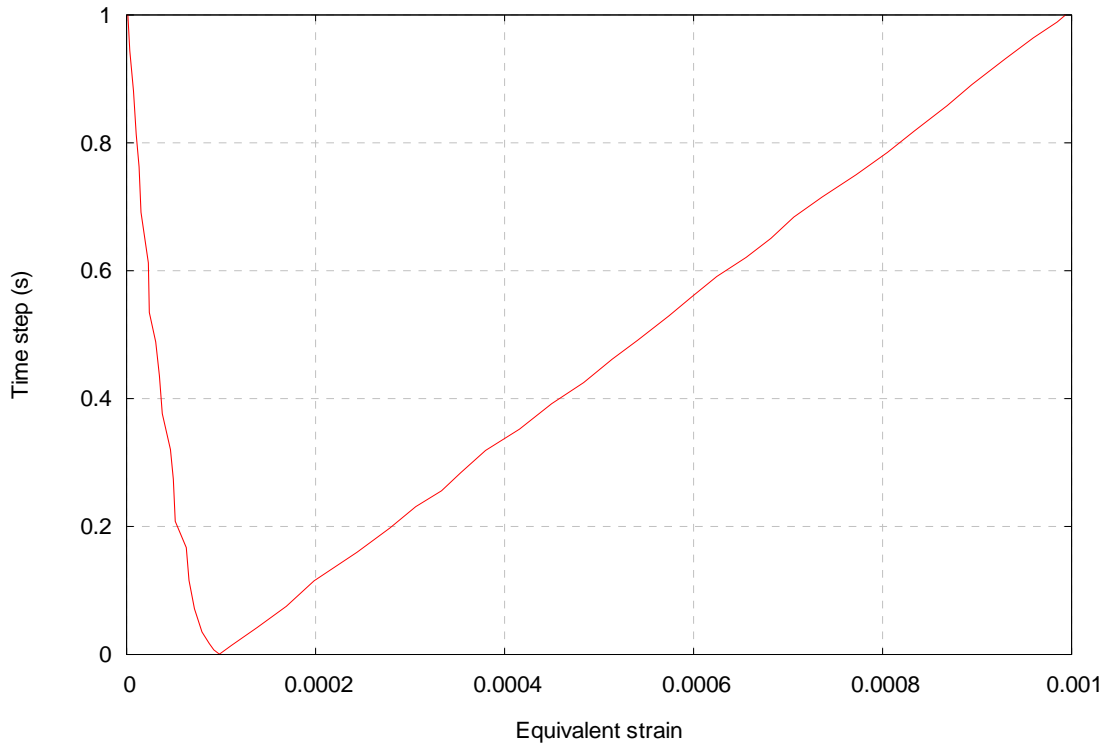


Figure 3-17. Evolution of the time step with respect to the evaluated equivalent strain  $\tilde{\epsilon}_{calc}$ .

### 3.4.3.2 Global approach

The other possibility to adapt the time step is based on the global response of the material (*Adaptive Time Step n° 2*). We test the current slope  $\alpha_{t+\Delta t} = \frac{\partial F}{\partial d}$  of the load-displacement curve for the solution a time  $t + \Delta t$  compared to the previous slope at time  $t$ . Then the time step  $dt_n$  is adjusted with the following formulae:

$$dt_n = \begin{cases} \min \left( dt, dt_0 \times \left( \frac{\alpha_{t+\Delta t}}{\alpha_t} \right)^p \right) & \text{if } F_{t+\Delta t} \geq F_t \\ \min \left( dt, dt_0 \times \left( \frac{\alpha_t}{\alpha_{t+\Delta t}} \right)^p \right) & \text{else if.} \end{cases} \quad (3-37)$$

The parameter  $p$  controls the weight of the time step decrease.

### 3.4.3.3 Comparison of the methods

We first compare these methods on the case of a single element subject to tension. The load–displacement curves for classical and adaptive time step (n° 1 and n° 2) are compared (figure 3-18). The initial time step of the adaptive time step case is one second. The behavior law is an elastic damage law. The parameters used for these simulations are those of table 3-4. We have set  $p$  to 20 for the second approach.

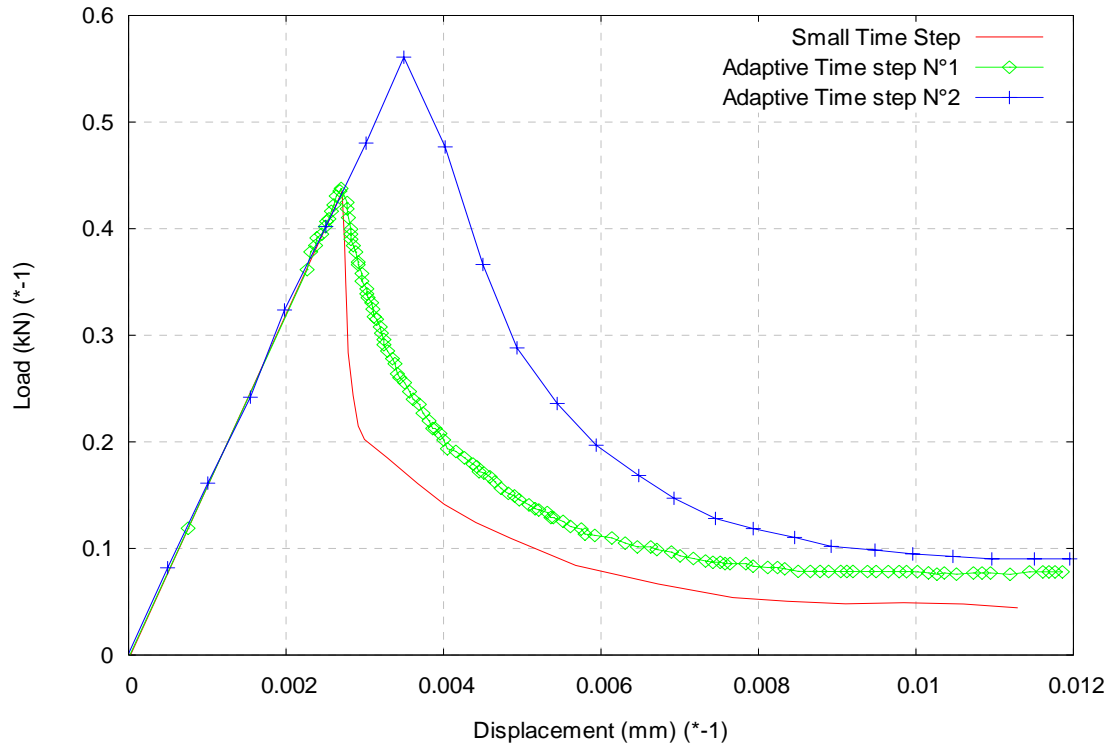


Figure 3-18. Comparison of load-displacement curves in function of the type of time step.

We see that adaptive time step n° 1 gives good results; the maximal load is as accurate as when using a very small constant time step. CPU time results with this approach and a small time step are also compared in table 3-5.

	<i>Very small time step</i>	<i>Adaptive time step n°1</i>
<i>Time (s)</i>	150	51.80

Table 3-5. CPU time for the two methods.

The “Adaptive time step” procedure is almost three times faster than the classical time step one. On the contrary the adaptive time step n° 2 is not efficient in this case. Indeed as the test is only on one element, the smooth part of the load-displacement curve is too fast and this approach cannot help out.

Now we test these approaches on a 3D tensile specimen with a centred hole subject to a tension test with the implicit formulation ( $\tilde{c} = 15 \text{ mm}^2$ ). We use the same damage

parameters as in table 3-4. Figure 3-19 shows the load-displacement curves corresponding to each method.

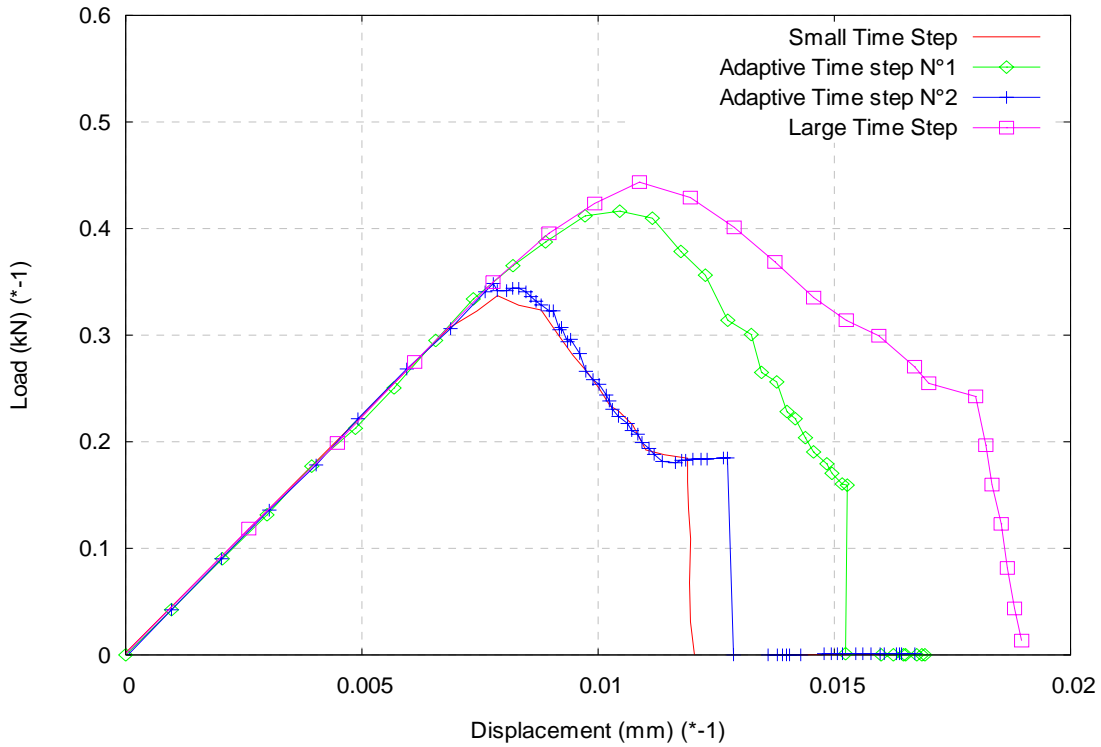


Figure 3-19. Load-displacement curve for a compression test.

Figure 3-19 shows the good results of the “Adaptive Time Step” compared to the small time step. Furthermore we notice that the “Adaptive Time Step” n°2 describes better the smooth part of the curve as the code can control the weight of the parameter  $p$  in order to decrease the time step (here  $p = 40$ ). This method would be more appropriated to describe the behavior of quasi-brittle material as mortar and concrete. Table 3-6 notices the computation time for each method.

	<i>Large Time Step</i>	<i>Small Time Step</i>	<i>ATS n°1</i>	<i>ATS n°2</i>
<i>Time (s)</i>	9	77	28	50

Table 3-6. CPU time for the two methods

We notice that it is also more interesting to use the second method for computation time reasons. For this problem, the difference does not appear clearly between the two methods. But we can estimate that for a complex behavior (concrete for example), the second method will be more adapted as the time adaptation is global and does not take into account local variation of damage which may decrease the time step.

First the correlation between the model and the mesh size is established. It is shown that a non local model leads to results independent on the mesh size. Three types of non local model can be chosen: a non local model with an integral formulation, an “evolutive non local model” and a non local model with an implicit formulation. It appears that the implicit model is the most adapted model for concrete.

Furthermore for strong coupling, the model is completely independent on time discretization. For the weak coupling a small time step is necessary. However, for matters of convergency and CPU time, the weak coupling procedure will be used. In order to get the most accurate maximum load value, we shall use an adaptive time step which enables to remain accurate and to reduce the CPU time.

### 3.5 Conclusions

The model we have implemented in the FE code FEMCAM enables to model concrete as a heterogeneous material. The algorithm we have implemented can generate randomly aggregates from a real grain size distribution. We consider aggregates have a purely elastic behavior. We assume also mortar paste to have an elastic damage behavior. We have chosen to model it with a non local version of the Mazars model. The specificity of this code is its velocity-pressure formulation.

The damage model can be implemented through a weak or a strong coupling. Whereas accuracy is lower than for strong coupling, we can **adapt automatically the time step** without losing accuracy.

The non local model has shown its advantages. Compared to a classical local model, the main drawback of the non local model is its high CPU time. We are currently working on the optimization of the procedure devoted to the research of the neighbours of each element; **we will use the non local model with an implicit formulation**. Indeed this formulation seems to be more appropriate for problems with a large number of finite elements as the heterogeneous problems.

Now we have validated the model on mortar and on concrete. The next chapter will explain in detail how we have determined elastic and damage parameters to use this model in the specific framework of the ASR. An experimental campaign has been carried out to provide data for the identification procedure.

## CHAPTER 4 : IDENTIFICATION OF CONCRETE BEHAVIOR: THE INVERSE ANALYSIS MODULUS AND THE EXPERIMENTAL CAMPAIGN

4.1 INTRODUCTION .....	4-64
4.2 INVERSE ANALYSIS MODULUS.....	4-65
4.2.1 Identification procedure.....	4-65
4.2.2 Analysis inverse models and methods used.....	4-65
5.2.2.1 Determinist approach .....	4-65
4.2.2.2 Stochastic methods.....	4-66
4.3 PARAMETERS IDENTIFICATION.....	4-68
4.3.1 Parameters .....	4-68
4.3.2 Numerical tests.....	4-69
4.3.2.1 Model <b>identifiability</b> .....	4-69
4.3.2.2 Stability of the objective function .....	4-69
4.4 EXPERIMENTAL CAMPAIGN.....	4-72
4.4.1 Components.....	4-72
4.4.1.1 Cement .....	4-72
4.4.1.2 Sand [non reactive limestone (0-4 mm)].....	4-72
4.4.1.3 Aggregates.....	4-73
4.4.2 Formulation.....	4-74
4.4.3 Preparation of samples .....	4-75
4.4.3.1 Experiments.....	4-75
4.4.3.2 Strain gauges and displacement sensors.....	4-76
a) Compression tests.....	4-76
b) Three point bending tests .....	4-77
4.4.3.3 Data given by strain gauges and displacement sensors.....	4-77
4.4.4 Testing procedure.....	4-78
4.4.4.1 Tests on mortar.....	4-79
a) Compression tests.....	4-79
b) Three point bending tests .....	4-80
4.4.4.2 Tests on concrete.....	4-81
a) Compression test .....	4-81
b) Three point bending tests .....	4-83
c) Brazilian splitting test .....	4-83
4.4.4.3 Data given by strain gauges and displacement sensors.....	4-83
4.5 SENSITIVITY ANALYSIS .....	4-84
4.5.1 Influence of friction .....	4-85
4.5.1.1 Model configuration.....	4-85
4.5.1.2 Numerical test .....	4-85
4.5.3 Material parameters.....	4-88
a) Influence of $\varepsilon_{D0}$ .....	4-89
b) Influence of $A_T$ .....	4-89
c) Influence of $B_T$ .....	4-89
d) Influence of $\tilde{\varepsilon}_T^{Crit}$ .....	4-89
4.6 CONCLUSION .....	4-92

## 4.1 Introduction

A fine simulation requires material parameters to be determined with a great accuracy. We have seen in the previous sections that concrete is a very heterogeneous material, basically made out of two main components: the mortar paste and aggregates. We shall consider here the mortar paste as an elastic damage material, whereas aggregates will be considered as purely elastic. We use the Mazars model to represent damage behavior of the mortar paste of concrete. This model requires us to determine the Young modulus, the Poisson ratio and damage parameters as  $\varepsilon_{D0}, A_C, B_C, A_T, B_T$  and  $\tilde{\varepsilon}^{Crit}$ . Therefore, we shall have to determine as exactly as possible the elastic and damage behavior parameters for these two components in order to model the consequences of the ASR with accuracy.

We shall use an inverse analysis tool “RheOConcrete”, developed at CEMEF. The inverse analysis consists in minimizing an objective function. Let  $M$  be a vector in  $\mathfrak{R}^{NbMeas}$ , with a number of measures  $Nbmeas$  for the physical system, and  $\mathfrak{S}$  an application from  $\mathfrak{R}^{NbParam}$  to  $\mathfrak{R}^{NbMeas}$ . We suppose that  $\mathfrak{S}$  is obtained from a numerical simulation which aims at modelling this physical system. The inverse problem consists in finding the set of parameters  $\lambda$  such as  $\mathfrak{S}(\lambda)$  gets as close as possible to  $M$  (in a least squares meaning). Figure 4-1 shows how this modulus works.

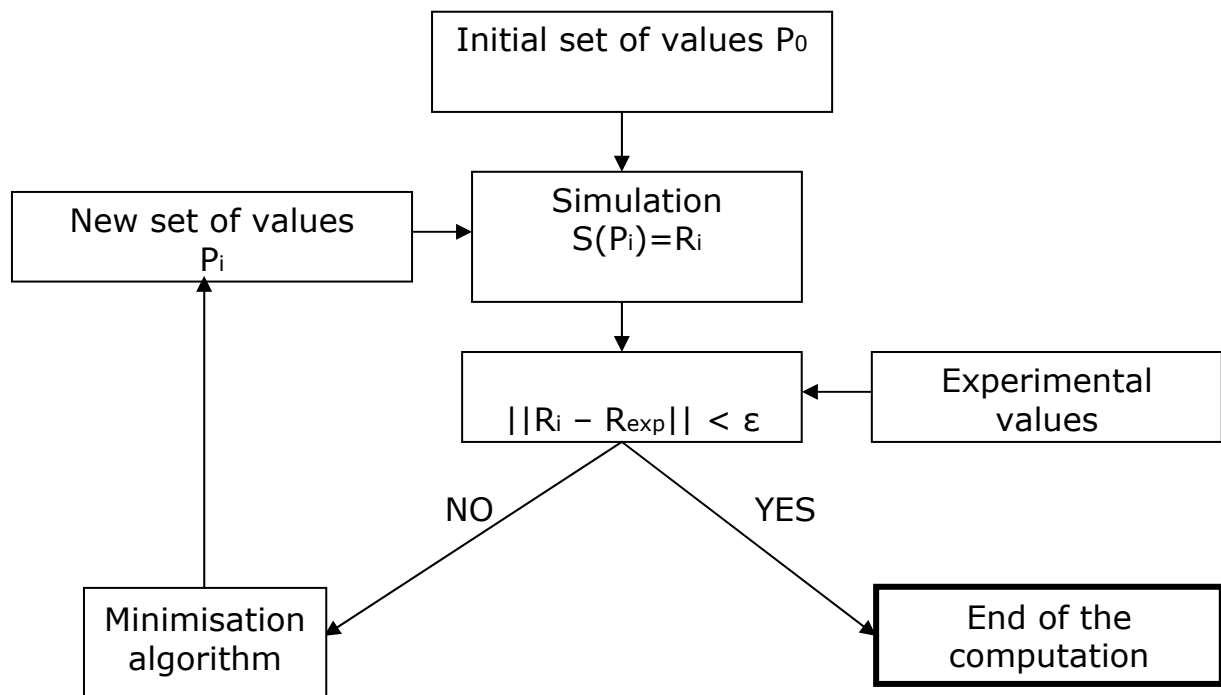


Figure 4-1. Inverse analysis modulus.

This modulus has the advantage that it can be coupled with various software tools (Abaqus, Forge3®, FEMCAM etc.). Different methods used to identify material parameters can be used. We can classify them in two main methods:

- determinist approaches;
- stochastic methods.

The identification of model parameters plays a crucial part in the development of constitutive models for concrete. Consequently the inverse analysis has to be:

- *robust*: the minimisation method needs to ensure that the algorithm converges to the real solution whatever the initial set of parameters used;
- *Accurate*: it is highly important to obtain very accurate parameters; however this accuracy is often set by the convergence rate in the algorithm. So the accuracy depends on this value and has to be well adapted to the incertitude of the problem. In this way we have to choose a good balance between computation time and accuracy.

We shall then explain in detail parameters to identify. The parameter identification is not an easy process especially for complicated constitutive models such as non local or gradient enhanced damage models. It is hence important to check the system identifiability and the objective function stability.

The parameters identification will be carried out independently in tension and in compression, thanks to the capability of the proposed Mazars model in distinguishing tensile and compressive responses. In order to get the physical measures, an experimental campaign has been led at the Ecole des Mines de Douai (GC-Douai). A sensitivity study, for parameters to be identified, is presented. Friction parameters are first tested on a three point bending test. we analyse the influence of damage parameters on the global response of the material.

## 4.2 Inverse analysis modulus

### 4.2.1 Identification procedure

The identification process enables to find a good approximation of the numerical value that we search to identify. This process is based on experimental data, which are compared to numerical data. At each simulation, a criterion is used to estimate if it is necessary to improve the accuracy of numerical parameters. The problem consists in iterating the process in order to minimize this criterion.

### 4.2.2 Analysis inverse models and methods used

Many methods exist to identify experimental parameters. Forestier [Forestier 2004] presents in detail these methods. Two methods are used in the inverse analysis modulus “RheOConcrete”. We present them here.

#### 5.2.2.1 Determinist approach

It is the most commonly used method in identification problems. These determinist methods follow this algorithm:

- a) Choice of a first admissible solution  $i$ ;
- b) Generation of a solution  $j$  in the neighbourhood of  $i$ ;
- c) If  $\mathfrak{S}(j)$  is better than  $\mathfrak{S}(i)$  then  $j$  is chosen and we return to step b).

The algorithm stops when there is no more improvement of the current solution. There are many determinist approaches: gradient approach, simplex algorithm, “tunnelling” method etc. One of the algorithms of “RheOConcrete” is based on the gradient approach.

The gradient approach is one of the oldest methods and it requires the objective function to be at least differentiable up to the first order. We chose a starting point and we evaluate the gradient  $\nabla\mathfrak{F}(x_0)$  in  $x_0$ . As the gradient indicates the direction of strongest increase for  $\mathfrak{F}$ , we decrease of a quantity  $\lambda_0$  in the opposite sense of the gradient. And we define  $x_1$ :

$$x_1 = x_0 - \lambda_0 \frac{\nabla\mathfrak{F}(x_0)}{\|\nabla\mathfrak{F}(x_0)\|} \quad (4-1)$$

This process is repeated and we create the point  $x_0, x_1, x_2, \dots, x_k$ . Thus at each stage we approach the solution:

$$x_{k+1} = x_k - \lambda_k \frac{\nabla\mathfrak{F}(x_k)}{\|\nabla\mathfrak{F}(x_k)\|} \quad (4-2)$$

$\lambda_k$  can be constant (predetermined step) or can be changed during the algorithm. These methods have the properties to converge quickly. However it may end up on a local minimum. It is thus very dependant of the initial set of value. An alternative to this problem is the multistart method. More details are given in [Berro 2001].

#### 4.2.2.2 Stochastic methods

The stochastic methods are based on a creation of random point in the state space. We can quote the Monte-Carlo algorithms, the evolution algorithms etc. The main advantages of these methods are:

- their easy implementation;
- the good quality of the approximate solution.

The evolution algorithm is used in the modulus “RheOConcrete” [Rechenberg 1973]. The evolution algorithms are research algorithms based on the mechanisms of natural selection. They are based on Darwin evolution law: survival of the fittest. The genetic pool of a given population potentially contains the solution, or a better solution, to a given adaptive problem. This solution is not "active" because the genetic combination on which it relies is split between several subjects. Only the association of different genomes can lead to the solution. During reproduction and crossover, new genetic combination occurs and, finally, a subject can inherit a "good gene" from both parents. The best individual represents the optimal solution. The evolution algorithms are different from standard optimization and search procedures in four ways (see figure 4-2).

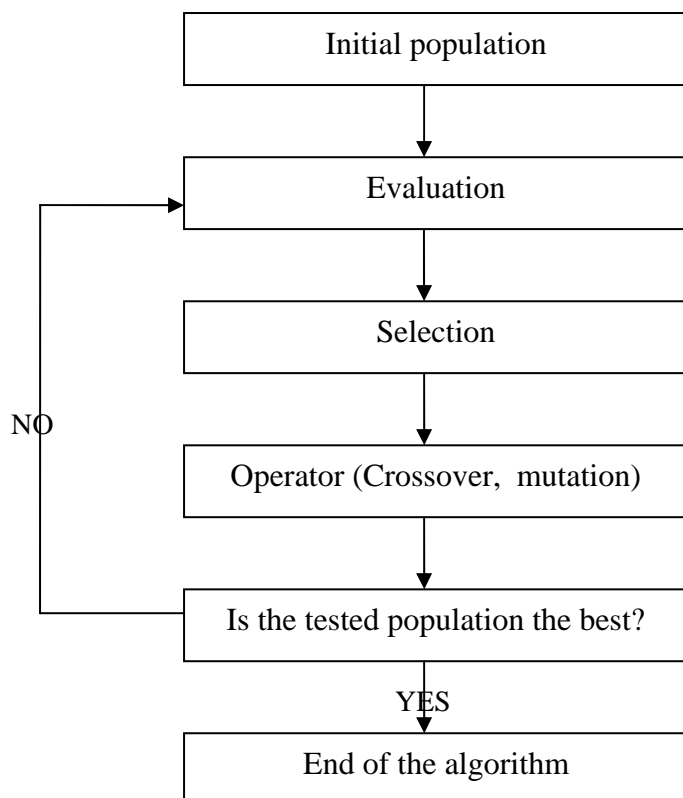


Figure 4-2. Organigram of the evolution algorithm.

The specificities of the stochastic methods are the following ones:

- The evolution algorithm works with a coding of the parameter set, not the parameters themselves;
- The evolution algorithm searches the solution out of a population of points, not a single point;
- They can treat simultaneously several individuals and are inherently parallel. Thus, the probability of reaching only a local minimum is reduced with respect to direct search methods. The evolution algorithms are thus more robust than direct search methods;
- The evolution algorithms use the information of the objective function, not derivatives or other auxiliary knowledge;
- The evolution algorithms use probabilistic transition rules, not deterministic rules.

Unlike many methods, the evolution algorithm use probabilistic transition rules to guide their search. The fact that they use a random choice is a tool to guide a search toward regions of the search space with likely improvement. **The identification of the elastic and damage parameters will be done with the evolution algorithms.**

## 4.3 Parameters identification

### 4.3.1 Parameters

The previous section shows that we need to identify twelve parameters if we wish to characterize fully the material behavior. We can divide them in two groups: the **elastic and the damage parameters** (tensile parameters, compression parameters and damage threshold) and an internal length. We have specified that the  $l_c$  value is between  $3 d_{max}$  and  $5 d_{max}$ . So it means that the  $\tilde{c}$  value is between  $\frac{9}{400} l_c^2$  and  $\frac{l_c^2}{16}$  (see chapter 2, section 2.3.3.3). As we considered that the larger grains for the mortar paste are about equal to 5 mm, we have chosen to set the  $\tilde{c}$  value to  $15 \text{ mm}^2$ . Table 4-1 shows the other parameters and how to identify them:

<i>Parameters to identify</i>	<i>Meaning</i>
$E_{MP}^C$	Young modulus of the mortar paste of concrete
$\nu_{MP}^C$	Poisson ratio of the mortar paste of concrete
$E_A^C$	Young modulus of the aggregates
$\nu_A^C$	Poisson ratio of the aggregates
$A_C$	Related to damage evolution in compression
$B_C$	Related to damage evolution in compression
$A_T$	Related to damage evolution in tension
$B_T$	Related to damage evolution in tension
$\varepsilon_{D0}$	damage threshold
$\tilde{\varepsilon}_T^{Crit}, \tilde{\varepsilon}_C^{Crit}$	fracture threshold

Table 4-1. Parameters to identify.

$\tilde{\varepsilon}_C^{Crit}$  and  $\tilde{\varepsilon}_T^{Crit}$  are respectively the damage to fracture threshold in compression and in tension. The macrocracks threshold for a test combining compression and tension is evaluated as following:

$$\tilde{\varepsilon}^{Crit} = \alpha_T \tilde{\varepsilon}_T^{Crit} + (1 - \alpha_T) \tilde{\varepsilon}_C^{Crit}, \quad 0 \leq \alpha_T \leq 1 \quad (4-3)$$

Where  $\alpha_T$  is defined as in Eq. (2-10) (see chapter 2, section 2.3.2.1). It appears that two types of tests need to be carried out in order to identify the mortar paste and aggregates behavior:

- **Compression tests;**
- **Three point bending tests.**

These tests have been made on mortar and on concrete to identify material parameters on concrete on compression and on tension. Each test has been carried out on after 7, 14 and 28

days. Tests on concrete, but also on mortar, induce two possible ways to identify material parameters and we will explain in details why we have carried out an experimental campaign on these two materials (see chapter 5 for more details). “Brazilian” splitting test have been also carried out at ages of 7 and 28 days to validate our numerical model on concrete, using the material parameters we will have identified with the compression tests and the three point bending tests.

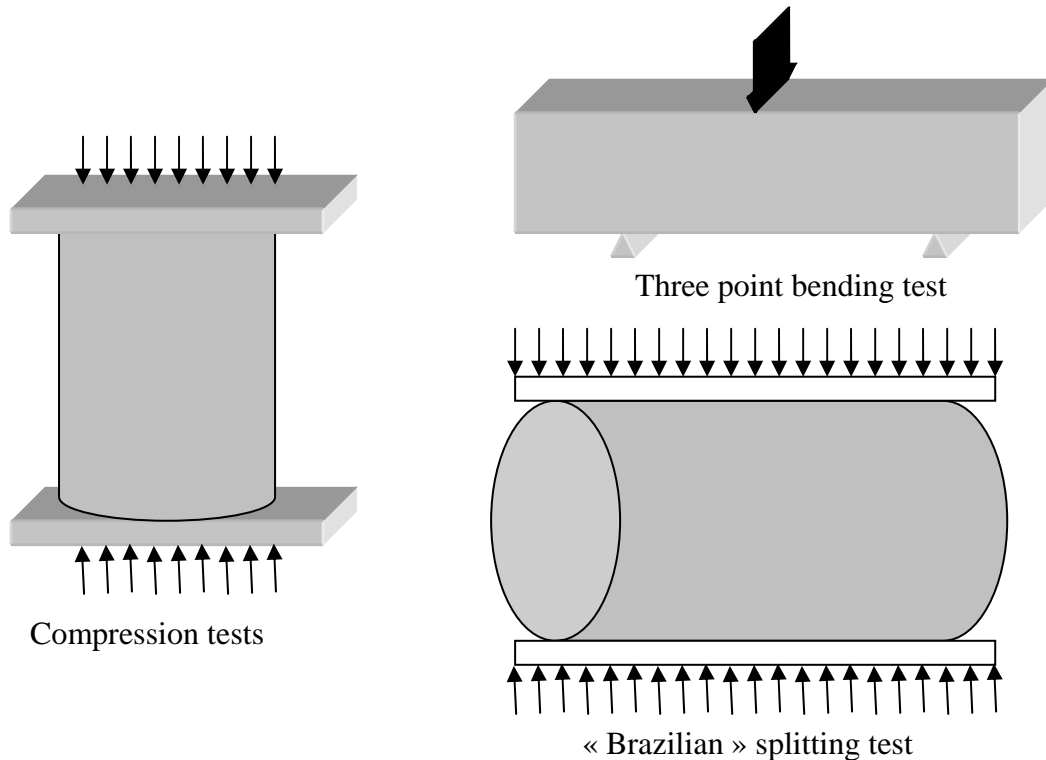


Figure 4-3. Test to identify and validate the 3D numerical model for concrete.

## 4.3.2 Numerical tests

### 4.3.2.1 Model **identifiability**

The first step is to check that we can identify elastic parameters with the experimental data. We can define the **identifiability** of a system by: the numerical system is all the more identifiable that the observables have a maximal sensitivity to parameters to be identified. However the identification of the non local damage model is correlated with the difficulty of getting at the same time the parameters involved in the damage evolution. Le Bellego has shown the lack of objectivity of the model [Le Bellego 2003].

### 4.3.2.2 Stability of the objective function

We can adopt a local approach to check the stability of the objective function. We choose an initial set of value  $\lambda_0$  and we simulate the uniaxial tests. We then carry out the same computations with a slight variation on parameters. We have tested the stability of the objective function on a mortar submitted to a three point bending test. The material has an elastic damage behavior.

The initial parameters we have used are listed in table 4-2.

$E^M$ (GPa)	$\nu^M$	$\varepsilon_{D0}$	$A_T$	$B_T$	$\varepsilon_{D0}$
30	0.2	$1.10^{-4}$	0.8	20 000	$1.10^{-3}$

Table 4-2. Parameters used to check the objective function.

$(E^M, \nu^M)$  denote the Young modulus and the Poisson ratio of mortar. We then make a variation of 1% on these parameters and we evaluate the Gauss-Newton matrix  $G$ . We recall that the components of the Gauss-Newton matrix are defined as:

$$G_{ij} = \left\langle \frac{dF}{dP_i}, \frac{dF}{dP_j} \right\rangle = \sum_k \frac{dF_k}{dP_i} \cdot \frac{dF_k}{dP_j} \quad (4-4)$$

where  $F$  is the load reached during each simulation and  $P = \{A_T, B_T, \varepsilon_{D0}, \tilde{\varepsilon}^{Crit}\}$  the set of parameters to identify. It thus consists in calculating, all values  $F_k(P)$ , using the first set of parameters, as well as perturbed values  $F(P + \delta P_i)$ , where  $\delta P_i$  represents a small perturbation of the corresponding parameter  $P$ :

$$\frac{dF}{dP_i} = \frac{F(P + \delta P_i) - F(P)}{\delta P_i} \quad (4-5)$$

We obtain the following symmetric matrix:

$$G = \begin{bmatrix} 875.1 & 4.8.10^{-3} & -1.42.10^6 & -7.10^3 \\ & 4.07.10^{-8} & -13.14 & -0.13 \\ & & 5.44.10^9 & 4.5.10^7 \\ & & & 1.24.10^6 \end{bmatrix} \quad (4-6)$$

First of all we notice that this matrix is not very well conditioned. After the computation of the eigenvalues we obtain a condition number equal to  $\rho = 1.15.10^{11}$ , which means that a small perturbation of the system may lead to a very different global response of the material. Furthermore the matrix  $G$  can lead to the evaluation of the parameters correlation with the calculation of:

$$C_{ij} = \cos \left( \frac{dF}{dP_i}, \frac{dF}{dP_j} \right) = \frac{G_{ij}}{\sqrt{G_{ii} G_{jj}}} \quad (4-7)$$

We obtain these values:

$$\begin{aligned}
 \cos\left(\frac{dF}{dB_T}, \frac{dF}{d\varepsilon_{D0}}\right) &= 0.88 & \cos\left(\frac{dF}{dA_T}, \frac{dF}{dB_T}\right) &= 0.804 \\
 \cos\left(\frac{dF}{dA_T}, \frac{dF}{d\varepsilon_{D0}}\right) &= 0.65 & \cos\left(\frac{dF}{dB_T}, \frac{dF}{d\tilde{\varepsilon}^{Crit}}\right) &= 0.57 \\
 \cos\left(\frac{dF}{d\varepsilon_{D0}}, \frac{dF}{d\tilde{\varepsilon}^{Crit}}\right) &= 0.54 & \cos\left(\frac{dF}{dA_T}, \frac{dF}{d\tilde{\varepsilon}^{Crit}}\right) &= 0.21
 \end{aligned} \tag{4-8}$$

We can see that some parameters are strongly correlated, as their associated vectors are almost collinear. For instance the parameter  $\varepsilon_{D0}$  is strongly correlated with the damage threshold  $A_T$  and  $B_T$ . It means that the identification of the damage parameters will be very difficult and it will be necessary to adapt the research to a specific set of range. On the contrary  $\tilde{\varepsilon}^{Crit}$  is less correlated with other parameters.

We can go even further with a second verification: we can choose an initial set of value  $\lambda_1 \neq \lambda_0$ . If the final results are the same than for  $\lambda_0$ , we will consider that the problem is well identifiable. Table 4-3 shows the parameters we have chosen for this second study:

$E^M$ (GPa)	$\nu^M$	$\varepsilon_{D0}$	$A_T$	$B_T$	$\tilde{\varepsilon}^{Crit}$
30	0.2	$3.4625 \cdot 10^{-5}$	1.29	25 316	$1.385 \cdot 10^{-4}$

Table 4-3. Second set of parameters used to verify the objective function.

We can evaluate the Gauss-Newton matrix  $G$ :

$$G = \begin{bmatrix} 0.9314 & 1.30 \cdot 10^{-4} & -9.12 \cdot 10^4 & -4814.5 \\ & 2.307 \cdot 10^{-8} & -14.2 & -0.77 \\ & & 1.21 \cdot 10^{10} & 5.18 \cdot 10^8 \\ & & & 2.81 \cdot 10^7 \end{bmatrix} \tag{4-9}$$

We notice that the conditioning of this matrix is equal to  $\rho = 1.41 \cdot 10^{12}$  which is very similar to the condition number evaluated before. Furthermore we can evaluate the correlation between parameters. It gives:

$$\begin{aligned}
 \cos\left(\frac{dF}{dB_T}, \frac{dF}{d\tilde{\varepsilon}^{Crit}}\right) &= 0.95 & \cos\left(\frac{dF}{dA_T}, \frac{dF}{d\tilde{\varepsilon}^{Crit}}\right) &= 0.94 \\
 \cos\left(\frac{dF}{dA_T}, \frac{dF}{dB_T}\right) &= 0.88 & \cos\left(\frac{dF}{d\varepsilon_{D0}}, \frac{dF}{d\tilde{\varepsilon}^{Crit}}\right) &= 0.88 \\
 \cos\left(\frac{dF}{dA_T}, \frac{dF}{d\varepsilon_{D0}}\right) &= 0.85 & \cos\left(\frac{dF}{dB_T}, \frac{dF}{d\varepsilon_{D0}}\right) &= 0.84
 \end{aligned} \tag{4-10}$$

The correlation between parameters is stronger in this case for each parameter. This result proves even more the need for defining an adapted range for each material parameter before starting the identification.

## 4.4 Experimental campaign

### 4.4.1 Components

Materials used for this formulation are:

- Cement of Heming;
- Aggregates from “Boulonnais” with its fines ;
- Aggregates from “Savreux”.

#### 4.4.1.1 Cement

We have used cement CEM I 42,5 R from Heming, supplied by the Obourg corporation. We have chosen this cement because of its high alkaline content (it is the equivalent of 0.99%) which speeds up the ASR development (see appendix A.3 for the chemical analysis of the cement).

#### 4.4.1.2 Sand [non reactive limestone (0-4 mm)]

This sand is commonly called sand from “Boulonnais”. It is a 90% limestone sand which contains few silica (7%). The particle size distribution of the sand has been experimentally determined. The percentage of fines is then equal to 5.2% (7% is specified in the technical document). **This sand can be fall into sands tended to fines.**

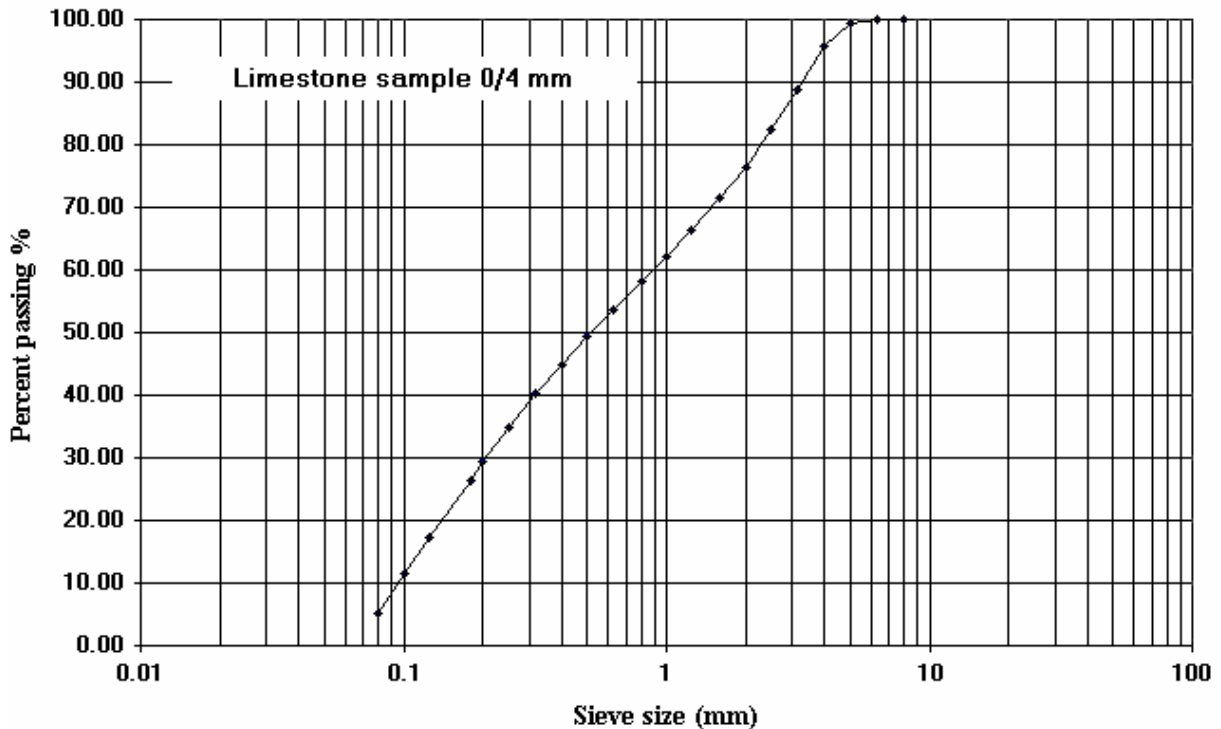


Figure 4-4. Particle size distribution of sand.

This sand has a fineness modulus equal to 2.3. It is thus well adapted to the preparation of standard concrete ( $2.1 < \text{fineness modulus} < 2.9$ ). This is the same sand, which is used, to make mortar and concrete samples.

#### 4.4.1.3 Aggregates

We use two types of aggregates:

- The aggregates from « Boulonnais » (4/20 mm). This aggregate is composed with non reactive limestone (98%);

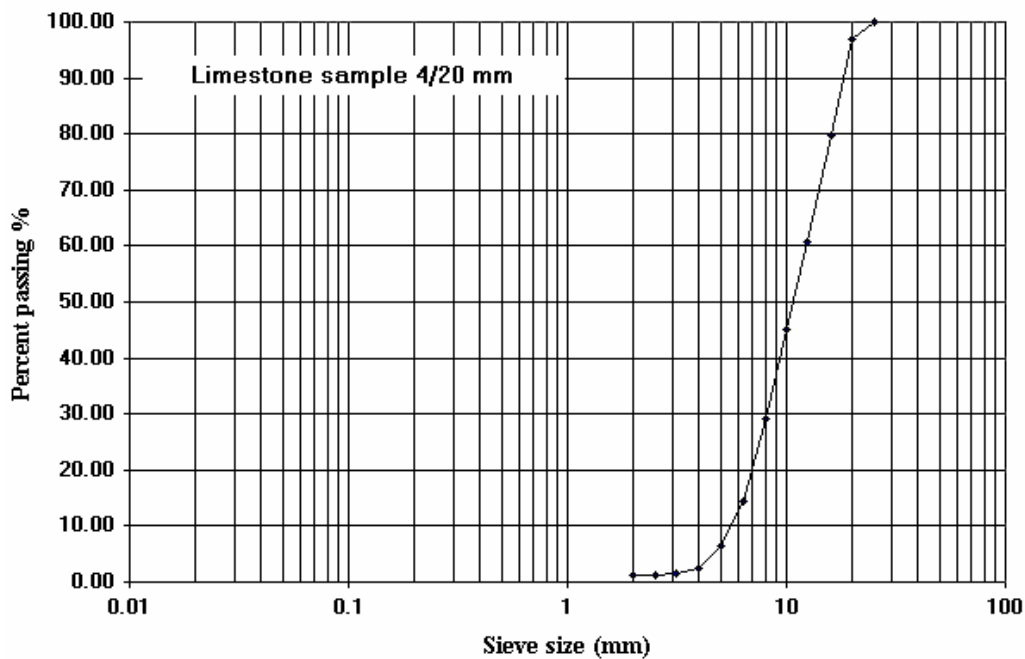


Figure 4-5. Particle size distribution of limestone aggregate.

- The aggregates from Savreux (0/22.5 mm): Aggregates from « Savreux » come from the Crotoy area and they are extracted from flint shingle and sea sand. They are composed of rolled and crushed flints. It is made out of silica (87%) for the main part.

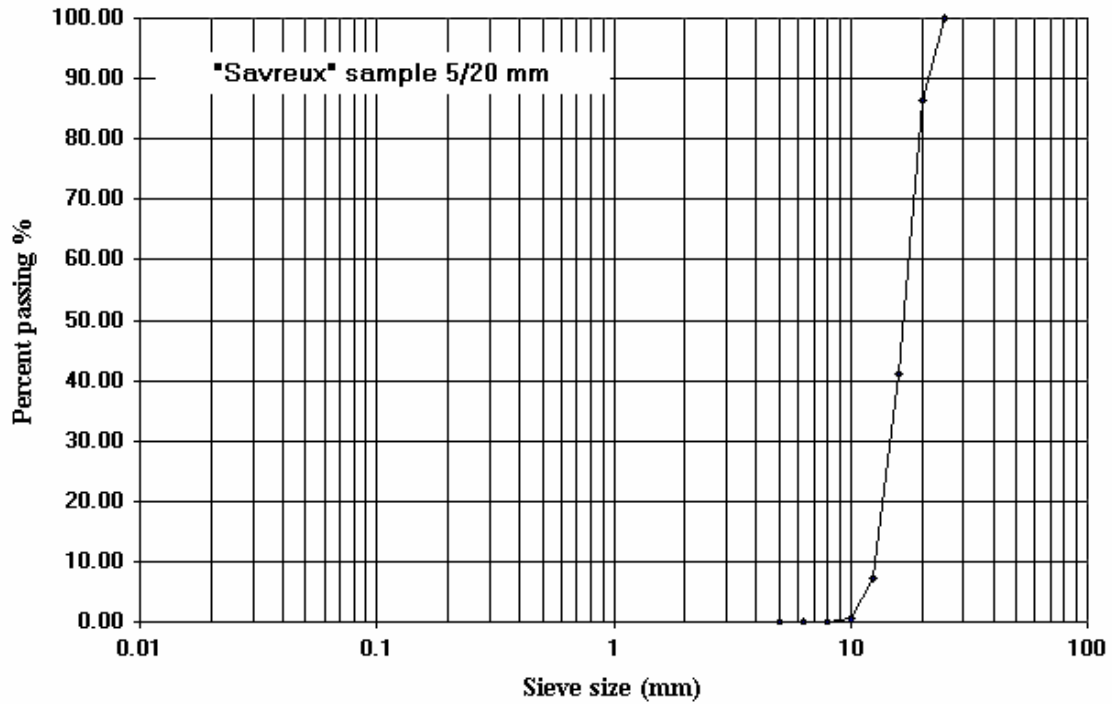


Figure 4-6. Particle size distribution of flint aggregate.

#### 4.4.2 Formulation

We have carried out some experiments on mortar and on concrete. Mortar formulation is based on concrete formulation. The following tables show the formulation used for each of them:

	Composition (kg/m <sup>3</sup> )	Density (g/cm <sup>3</sup> )
Cement CPA CEM I 42,5 d'Heming	500	3.16
Sand (0-4 mm)	552	2.65
Water	200	

Table 4-4. Mortar formulation.

	Composition (kg/m <sup>3</sup> )	Density (g/cm <sup>3</sup> )
Cement CPA CEM I 42,5 d'Heming	500	3.16
Sand (0-4 mm)	552	2.65
Flint aggregates "Savreux"	583	2.6
Limestone aggregates "Boulonnais"	583	2.65
Water	200	

Table 4-5. Concrete formulation.

The ratio  $\frac{\text{Water}}{\text{Cement}}$  (W/C) is equal to 0.4. This formulation is issued from the Dehaut study [Dehaut 2000]. **He has shown that this formulation corresponds to the most reactive formulation for the ASR without adding adjuvant.** The high content of cement allows a greater reactivity.

### 4.4.3 Preparation of samples

Samples have all been prepared at the same time in order to avoid any bias. For the three point bending tests, the samples geometries are:

- 40×40×160 mm parallelepipedic samples of mortar;
- 70×70×280 mm parallelepipedic samples of concrete.

For the compression and Brazilian splitting tests, the samples geometries are:

- 110×220 mm cylindrical samples of mortar;
- 160×320 mm cylindrical samples of concrete.

#### 4.4.3.1 Experiments

Mortar is a mixture of sand, cement and water. Mortar components are introduced in the following order: water, then cement and sand. For concrete, sand is first introduced, then cement and aggregates and eventually water. To make concrete and mortar samples, we have used:

a) A *small mixer* to make mortar beams: materials have been mixed mechanically. Cement is first poured in. It is then mixed at slow speed during thirty seconds. Sand is then added in during one minute. The mixer then runs ninety seconds at slow and at medium speed. After the mixing, two steps are carried out (according the ASTM C 305 Mortar mixing schedule):

- We fill the mould up to 2/3 and we use the stacking method (24 stacking per filling) in order to homogenise and delete air bubbles in mortar;
- We fill all the mould and we reuse the stacking method.

b) A *bigger mixer* to make cylindrical samples of mortar and all the samples for concrete. Coarse aggregates, sand and cement are first introduced. The mixing starts with the add of water. The mixer runs during about three minutes, then stops for two minutes and then runs for two minutes. We use the stacking method in order to homogenise the matter. There are two fillings. For concrete beams, we use a vibrating table.



a) Small mixer to make mortar samples



b) Big mixer

Figure 4-7. Materials used to make mortar and concrete samples.

After 48 hours, they are stored in saturated water (100% hygrometry) in a temperature regulated room.

#### 4.4.3.2 Strain gauges and displacement sensors

Two types of strain gauges are glued after the sample surface has been cleaned with chemical cleaners and sand paper:

- unidirectional strain (type Kyowa, 30 mm length, gauge resistance = 120 MPa);
- strain rosettes: we can measure simultaneously in a point of the sample, the strains in different directions (type Kyowa, 10 mm ray, gauge resistance = 120.2 MPa).

The protocol used is the following one: one day before each test, samples are settled in an oven to dry. The temperature is 40°C. This is not a high temperature in order to avoid some effects due to temperature and microcracks initiation for instance.

##### a) Compression tests

Four strain gauges are applied on cylinder samples:

- two longitudinal gages;
- two rosettes.

They are used to measure strains in different directions at the same point. In this way we choose a surface enough smooth to apply these strain gauges. The surface is cleaned and the strain gage is glued with the “M Bond 2000” glue and a catalyst to improve results.

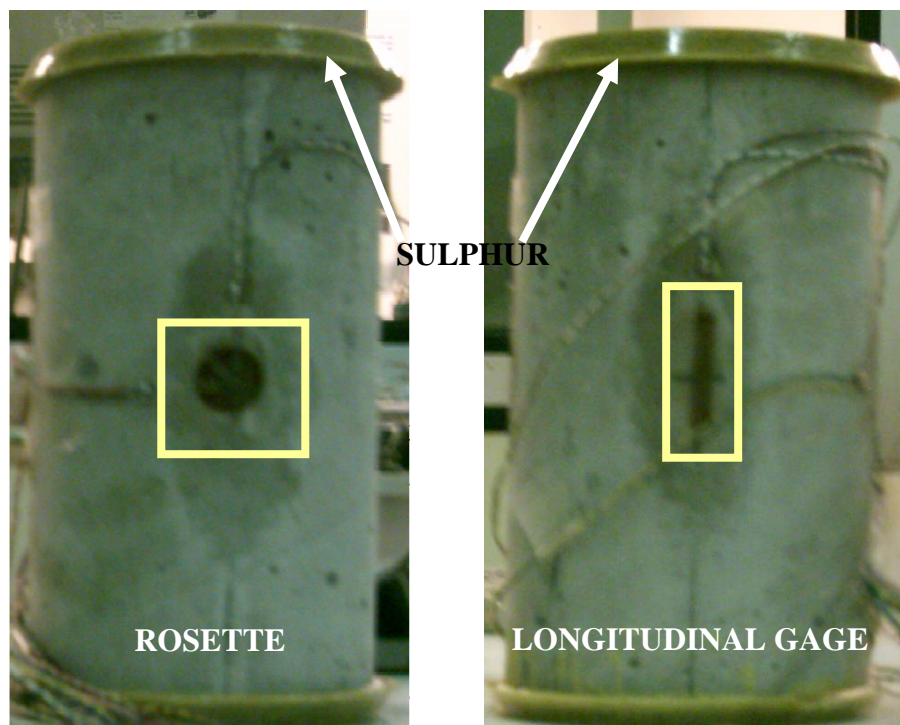


Figure 4-8. Location of the strain gauges on a 11×22 cm mortar samples.

### b) Three point bending tests

One longitudinal strain gauge is glued under the prismatic sample. A *displacement sensor* is also placed to measure the deflection of the beam submitted to the three point bending test (see figure 4-9).



Figure 4-9.a) Displacement sensor; b) Strain gauge is located horizontally on the concrete beam for the three point bending test.

#### 4.4.3.3 Data given by strain gauges and displacement sensors

In this experimental campaign, we estimate that the strain gauges give us the global displacement field of the sample (for the compression tests and the “Brazilian” splitting tests) based on the local strain field. Indeed it is impossible to use the displacement given by the upper tool of the presses: movement and possible rotations of the mechanism, inside the upper tool, disturb the measured displacement. The use of these strain gauges leads then to two major questions:

- Can this information be used to evaluate the global mechanical behavior of mortar and of concrete?
- Is the size representative of the mechanical behavior of the whole volume?

This hypothesis is even more questionable if the strain gage is considered too small compared to the aggregate diameter. Indeed if a strain gage is glued facing a coarse aggregate, the measured strain can be strongly influenced locally by this aggregate. On the contrary if the strain gauge is bigger than the aggregate size, the approximation stays right and we can obtain representative strains of the whole volume. If the strain gauge is too large, we will lose accuracy in the high strain gradient areas.

This question is hence linked to the second one. If we consider the height of the concrete sample in compression ( $H = 320$  mm), we notice that the longitudinal strain gauge is ten times smaller (30 mm), and if we consider the diameter of the larger grain  $d_{\max} = 22.5$  mm, the longitudinal strain gauge has approximately the same length. It would be better to use larger strain gauge to have a more representative strain state of the material. But we have used four strain gauges on each sample for the compression tests. We consider that the mean value gives a sufficiently good approximation of the global displacement. Another solution has been the use of displacement sensors to obtain the displacement field with a direct measure. Displacement measures are made with three sensors (LVDT type). They are

setted every  $60^\circ$  at the exterior of the sample. These measures give us the Young modulus in the elastic phase.

Furthermore, in the case of test with localized damage (three point bending test for example) too large gages could have negative consequences as it leads to an average value over a too large area and so it does not highlight the damage zone.

#### 4.4.4 Testing procedure

Compression tests have been performed after 7, 14 and 28 days. Three point bending tests and “Brazilian” splitting tests have been performed after 7 and 28 days. The testing device should not introduce any additional loads on the specimens. For the three point bending tests, it may be sufficient to increase specimen size so that boundary conditions do not contribute to the stress state at the critical section. However, for some tests, it may be necessary to apply loads using brushes or to lubricate the contact surface of the specimens in order to reduce the undesirable stresses introduced at the specimen-load frame interface. Cylinder samples are planished and lubricated (with sulphur) to obtain parallel faces and in order to obtain better results.

Loading is conducted using displacement control with a closed-loop system in order to maintain a uniform rate of loading. **During tests, we can measure the maximal load  $F_{\max}$ , corresponding displacement (with the strain gauges and displacement sensors), longitudinal and transverse strains.** We carry out compression tests and Brazilian splitting tests with a 100 tons press (Instron, 8505 piloted with some jacks and a pivot). The three point bending tests are realized with a 15 tons press (Instron, 8500).



Figure 4-10. left) 100 t. press, type INSTRON 8505 (compression test); right) 15 t. press type INSTRON 8500.

Data are collected on a system of data acquisition (5110, Vishay). It records the press load and the strain of the gages. Tests are carried out up to complete fracture (the results at ages of 14 and 28 days are presented in the appendix A.4). Three samples are tested for each test; the black curve corresponds to a mean of the three tests.

We will show the load-displacement curves for each test at seven days. Stress-strain curves would be also interesting to use as it give local information of the material degradation. And material parameters would be easier to identify as material parameters have a physical meaning at the scale of the stress-strain curves. However the inverse analysis modulus “RheOConcrete” enables now to compare automatically experimental and numerical load displacement curves. In the future, it would be interesting to compare automatically numerical and experimental stress-strain curves in some specific area of the sample (more particularly with the three point bending test).

#### 4.4.4.1 Tests on mortar

##### a) Compression tests

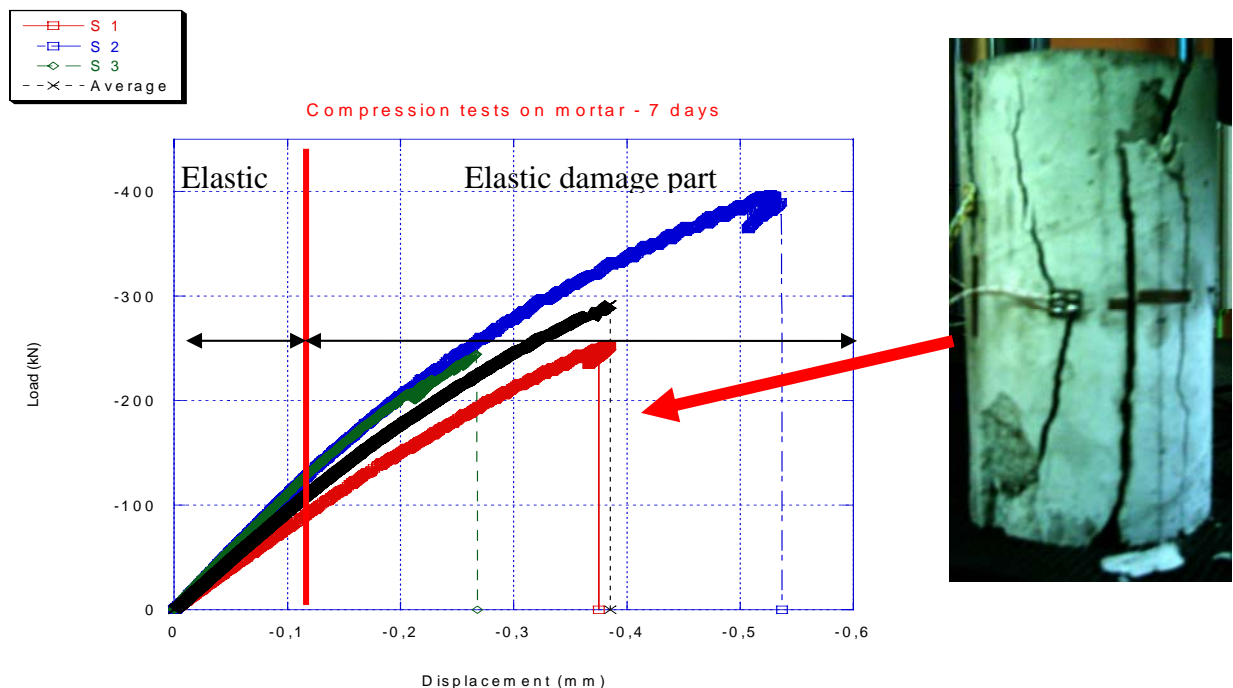


Figure 4-11. Load displacement curves for compression tests on mortar after seven days.

The elastic stage is almost the same for all three samples. The press velocity is equal to  $8 \cdot 10^{-3} \text{ mm} \cdot \text{s}^{-1}$ . Strain gauges give the value of the Young modulus for the elastic stage. Finally macro cracks increase and fracture occurs.

After the elastic stage, the non-linear load increases in the sample is related to the microcracks initiation stage: damage appears and the Young modulus is affected by the damage evolution in the sample. We can see that results are non homogeneous in the

smoothing part. For this damage stage, the press velocity is equal to  $5.10^{-3} \text{ mm.s}^{-1}$  which is the lower limit of the testing machine. This velocity has been chosen to observe the fracture zone with a great accuracy.

We see here a fast fracture development due to the fact that the strain gauges are damaged during the macrocracks propagation. This brittle behavior is probably due to the high cement content. The dispersion on maximum load is characteristic of a brittle behavior. The picture next to the load-displacement curve shows us the vertical cracks at the end of the experiment. Figure 4-12 shows the Young modulus evolution in function of the samples age.

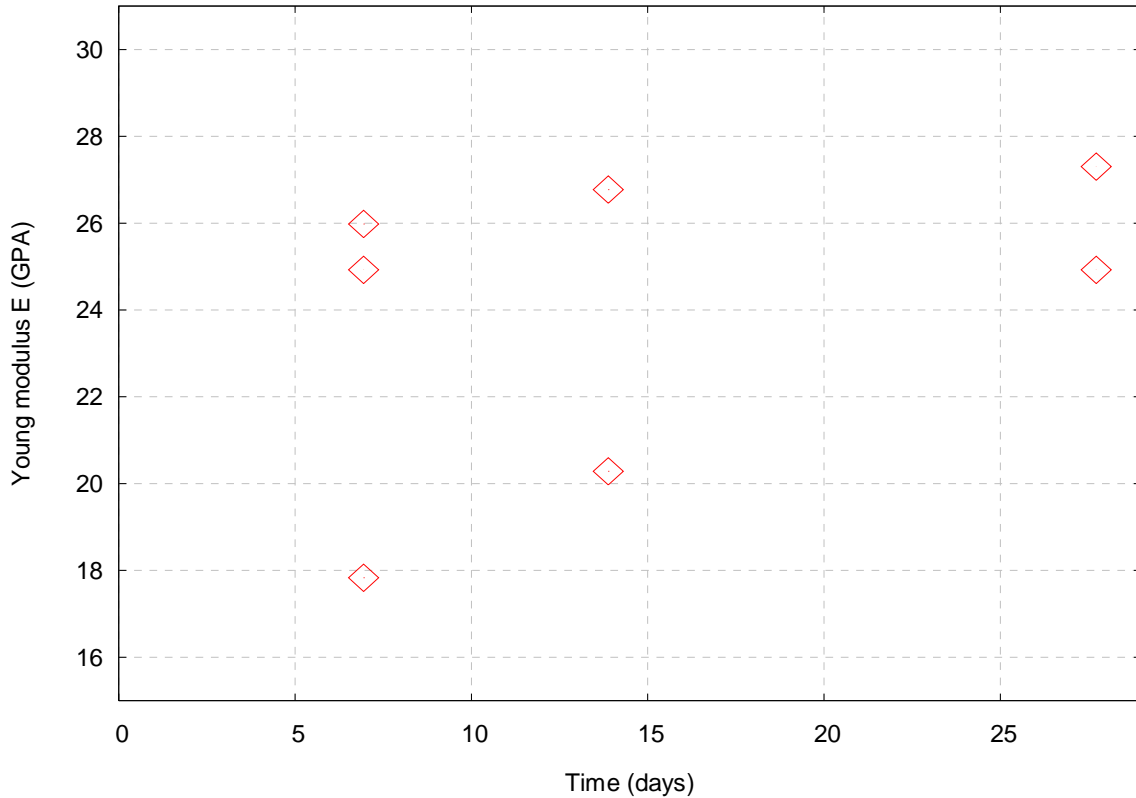


Figure 4-12. Evolution of the Young modulus E in mortar.

Results are dispersed between different ages. We notice here that mortar behavior evolves with respect to age. The measured Poisson ratio is roughly to 0.2.

### b) Three point bending tests

Direct tension testing of concrete requires specialized equipment, procedures and consideration of boundary conditions. As a result, it is rarely performed. Instead, either the three point bending test or the splitting tension test is used to estimate mortar parameters in tension.

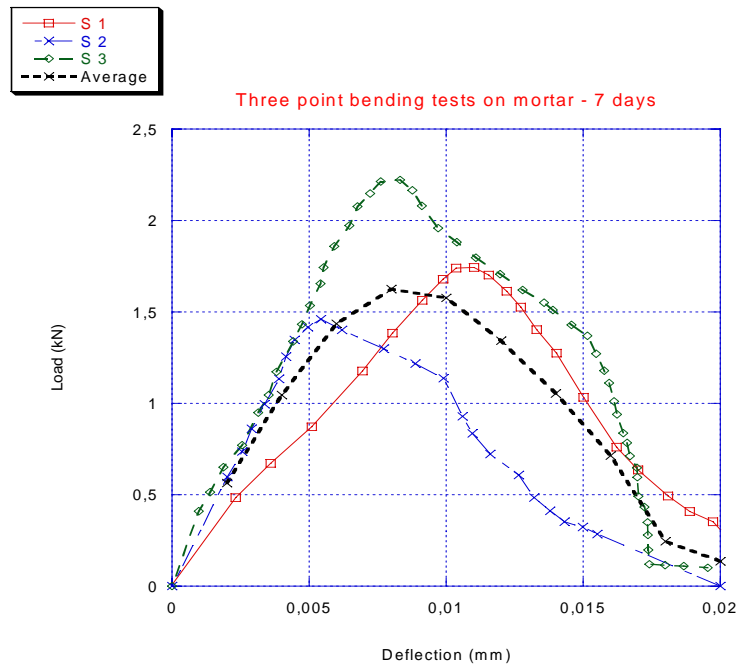


Figure 4-13. Load displacement curves for three point bending tests on mortar at 7 days.

For the elastic and the damage stage, the press velocity is equal to  $5.10^{-3} mm.s^{-1}$  which is the lower limit of the press. We observe first a linear response then damage and cracks evolve quickly in the sample and lead to the ruin of the sample. The load displacement curves show also that it is very difficult to obtain homogeneous results for three point bending tests in the smooth part.

#### 4.4.4.2 Tests on concrete

##### a) Compression test

Figure 4-14 shows the load-displacement curve for concrete at age of seven days. The evolution of the load-displacement curves is identical for each sample in the elastic and the damage elastic part. The press velocity is equal to  $8.10^{-2} mm.s^{-1}$ . Very small velocities ( $v = 2.10^{-3} mm.s^{-1}$  and  $v = 5.10^{-4} mm.s^{-1}$ ) for the upper tool have been used to describe respectively the damage and the fracture stage with a great accuracy. However we have spread out results for the fracture zone. Table 4-6 summarizes the maximal stress  $\sigma_1$  for each test:

Samples	7 days	14 days	28 days
$\sigma_1$ for S 1 (MPa)	35.46	39.36	36.52
$\sigma_1$ for S 2 (MPa)	35.96	42.31	39.29
$\sigma_1$ for S 3 (MPa)	26.25	27.46	40.15
Mean of $\sigma_1$ (MPa)	32.56	36.38	38.65

Table 4-6. Evolution of the maximal stress (in MPa) at different ages.

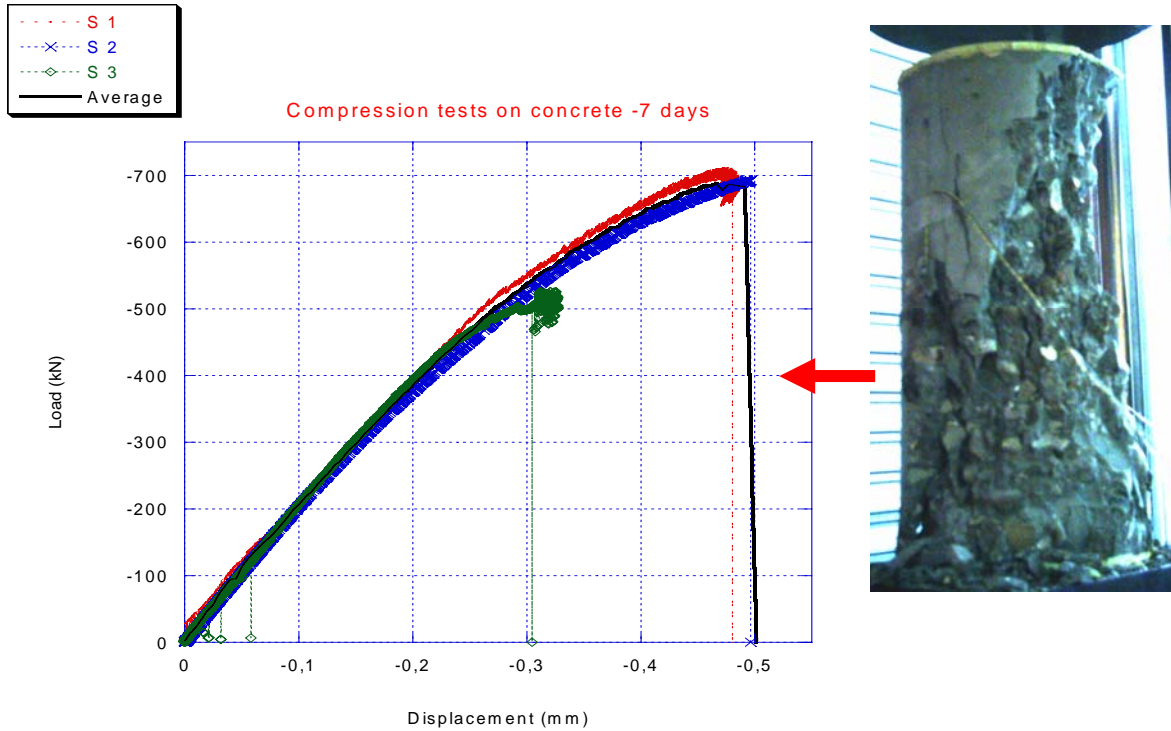


Figure 4-14. Load-displacement curve for the concrete under compression at 7 days.

We notice that the maximal stress increases between 7 and 14 days by more than 11%. Between 14 and 28 days the evolution is of only 6%. It means that the concrete **hardening** is very fast with this specific formulation. At 28 days the maximal stress  $\sigma_1$  classified our concrete in moderate-strength concrete. It is also possible to observe the evolution of the Young modulus. Figure 4-15 presents this evolution:

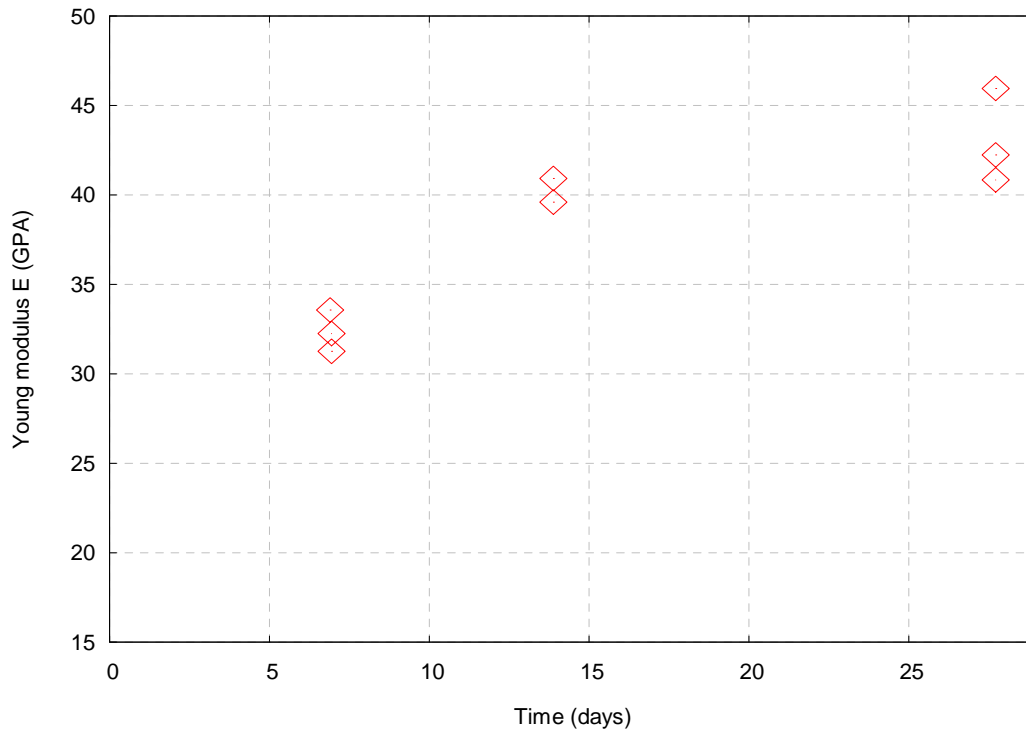


Figure 4-15. Evolution of the Young modulus E in concrete.

We can note the less dispersion obtained on concrete sample. It is probably due to a lower mortar paste content than in mortar.

### b) Three point bending tests

Figure 4-16 shows the correspondent load-displacement curves.

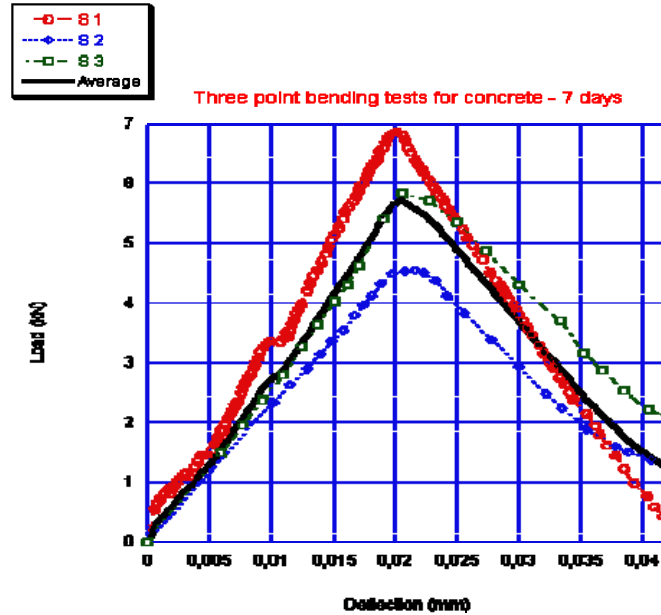


Figure 4-16. Load deflection curves for three point bending tests on concrete at 7 days.

We would like to underline that the strength value obtained is higher than the one obtained through uniaxial tension test (compression effects etc.). Moreover, it is observed that the three point bending test is dependent on the size of the beam tested. An empirical expression relates tensile strength to the beam size [CEB 1990].

$$\sigma_t = \sigma_{t,fl} \frac{2 \cdot \left(\frac{D}{D_0}\right)^{0.7}}{1 + 2 \left(\frac{D}{D_0}\right)^{0.7}} \quad (4-11)$$

Where  $\sigma_t$  is the tensile strength,  $\sigma_{t,fl}$  the value of the flexural tensile strength,  $D$  the beam depth and  $D_0$  is the reference size equal to 100 mm. This expression is applicable to beam depths of more than 50 mm.

### c) Brazilian splitting test

Figure 4-17 shows the load-displacement curve for two of the three tests. We notice first the elastic behavior and then the fast evolution of damage and cracks during the experiment.

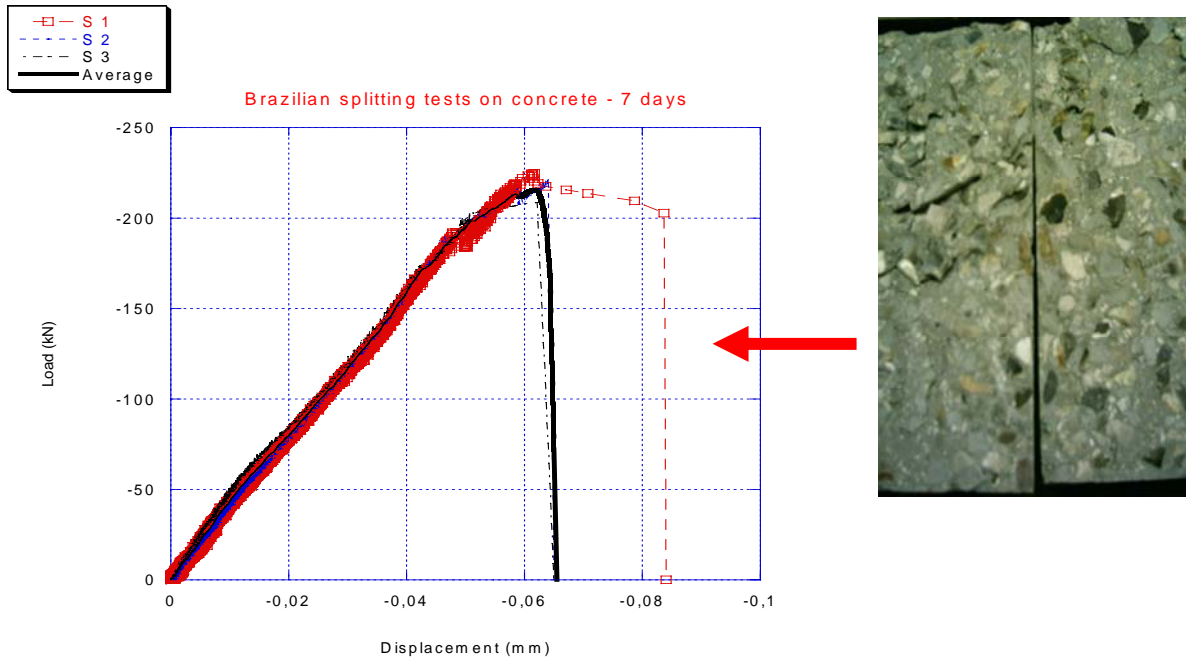


Figure 4-17. Load-displacement curve for the Brazilian test at seven days.

Figure 4-17 shows the state of one of the cylinders tested at the end of the experiment. We see that the fracture is very clear and this figure shows the two parts of the cylinder at the end of the experiment.

This experimental campaign aims at identifying damage parameters for our numerical model. We shall now test the sensitivity of the material parameters to evaluate the quality of the parameters identification.

## 4.5 Sensitivity analysis

A sensitivity study has first been carried out on experimental procedure and numerical parameters. We test the numerical influence of the contact between the tool and the sample and we also evaluate the influence of the “Kill element” method on the parameters identification. A sensitivity analysis has then been carried out to study the influence of damage parameters.

All numerical tests are performed under displacement control, by prescribing a displacement rate to the upper loading plate. For each configuration presented, damage is associated to the “**Kill element**” method to simulate macrocracks propagation.

## 4.5.1 Influence of friction

A sensitivity study has been carried out the friction effects in tension. We test here a mortar beam submitted to a three point bending test.

### 4.5.1.1 Model configuration

We first present the model configuration. Figure 4-18 shows the geometry and an example of the mesh used.

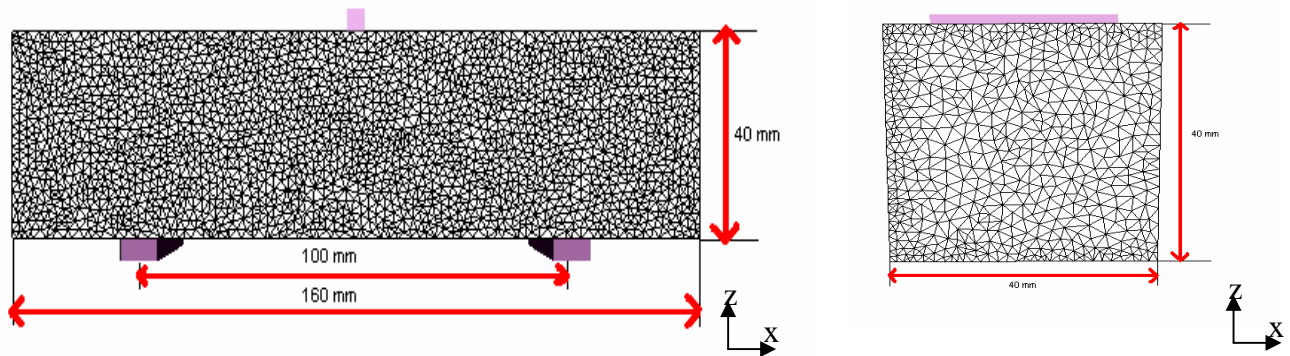


Figure 4-18. Mesh of the  $40 \times 40 \times 160$  mm three points-bending test; 7 394 nodes; 36 261 elements. The average element size is roughly to 2 mm.

The contact between the upper tool and the sample is bilateral sticking. We use the non local Mazars model with an implicit formulation. The internal parameter  $\tilde{c}$  is equal to  $15 \text{ mm}^2$ . And we use arbitrary damage parameters, which are already defined in table 4-3. Furthermore we use the adaptive time step  $n^{\circ 2}$  (see chapter 3 section 3.4.3.2 for more details) to adapt automatically time in function of the damage initiation. The upper tool goes down very slowly to capture with the best accuracy damage initiation ( $1.10^{-4}$  mm per numerical step at the beginning of the simulation).

### 4.5.1.2 Numerical test

We **modify friction between the lower tools and the sample** in order to study its influence on the global response. We test the influence of a sliding contact, a friction contact (strong) and a bilateral sticking contact. Concerning the friction law, a Coulomb law limited by the Tresca law is used (with these arbitrary parameters  $\bar{m} = 0.4, \mu_F = 0.2$ ) corresponding physically to a strong friction. Figure 4-19 shows the results obtained for different types of contacts.

The bilateral contact imposes a higher stress in the beam. It induces a greater rigidity. In the case of friction or sliding contact the damage evolution is almost the same. The higher the friction, the higher the peak load and the lower the slope of the softening curve after the peak. The small difference observed between these two types of contacts is due to the more or less high dissipation of energy during the three point bending test.

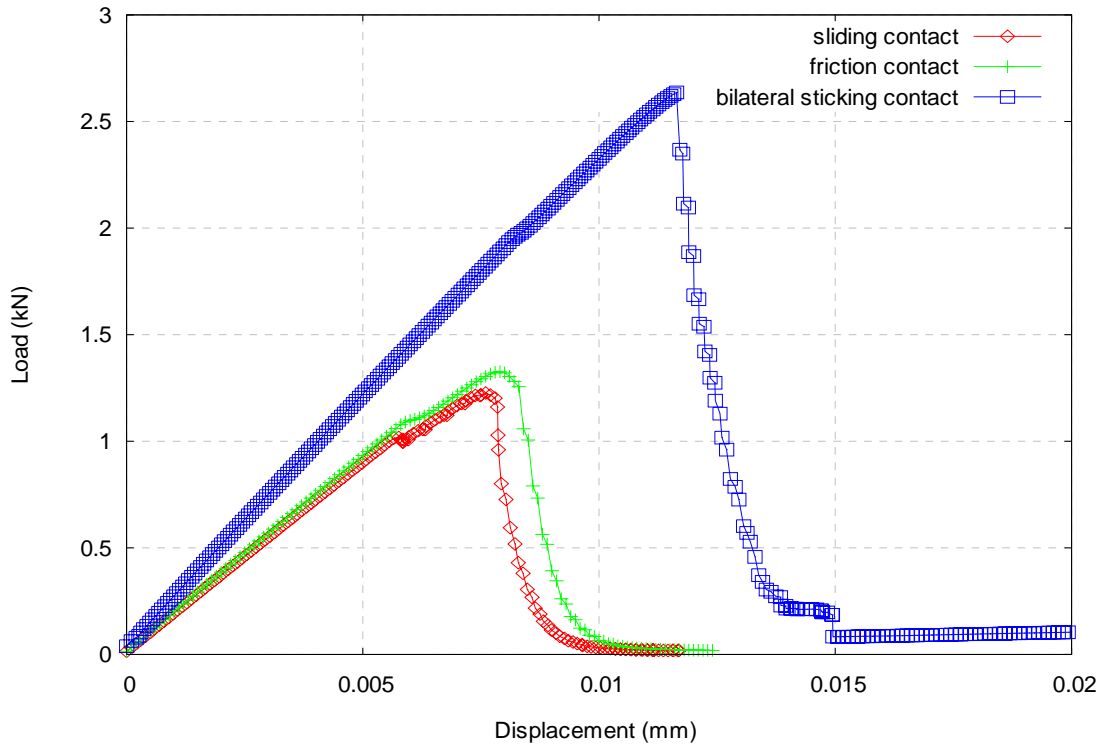


Figure 4-19. Load-displacement curve of the beam submitted to a three point bending test in function of the contact.

Even if we do not consider bilateral sticking contact, which is not very realistic, these results show that **contact still has an influence on the global response of the test**. The parameter identification will be hence influenced by the friction conditions. Friction needs to consider being representative of the experiments. It is also more appropriate than the bilateral contact as this can enable a possible movement of the beam in the  $(x,z)$  axes. Figure 4-20 shows the displacement vector on the beam during the loading when a friction contact is imposed between the lower tool and the sample.

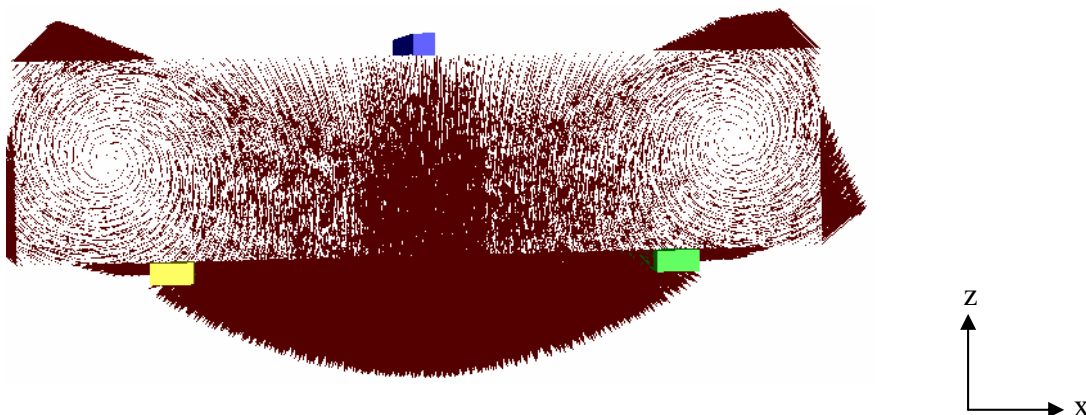


Figure 4-20. Displacement vector during the simulation with friction between the lower tools and the sample.

## 4.5.2 Influence of the “Kill element” method

We test the influence of the “Kill element” method on the load-displacement curve and so on the parameters identification. We consider a mortar sample submitted to a three point bending test. We use the same configuration and data than in section 4.5.1.1. Damage isovalues are displayed in figure 4-21.

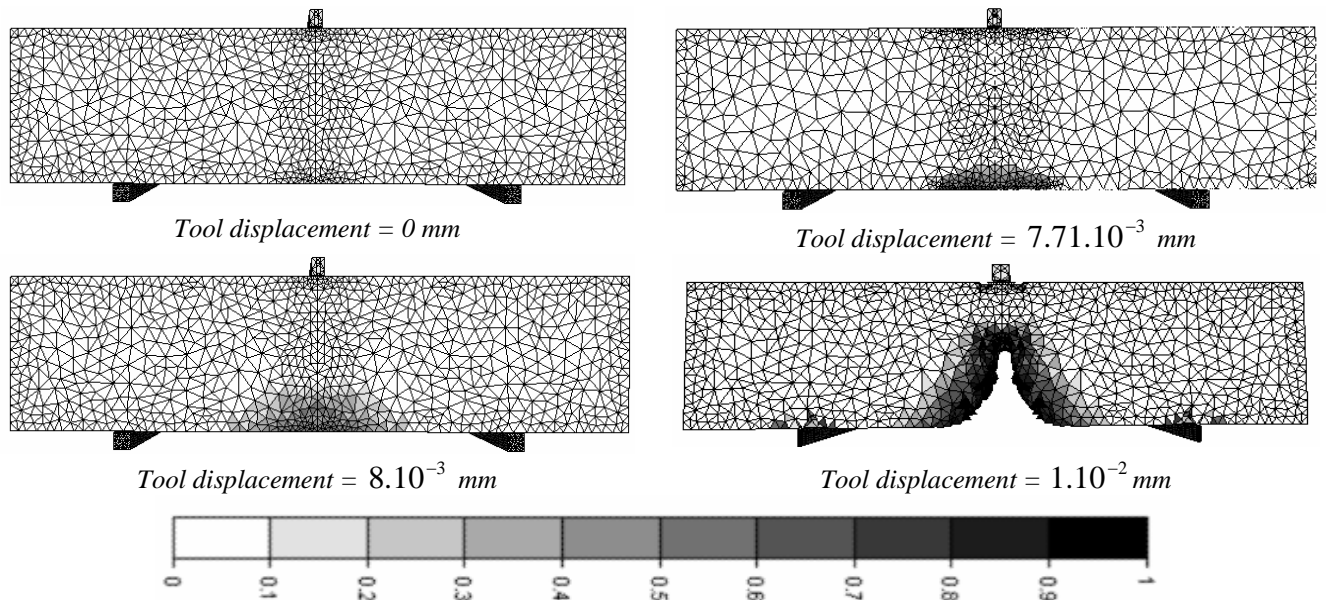


Figure 4-21. Damage evolution for different values of displacement of the upper tool.

The macrocrack is initiated at the location where the equivalent strain  $\tilde{\varepsilon}$  reaches the critical equivalent strain  $\tilde{\varepsilon}_T^{Crit}$ . It corresponds also to the location where the maximal principal stress  $\sigma_1$  reaches the critical tensile strength  $\sigma_t$ .

Figure 4-22 underlines the influence on the load-displacement curves using or not the “Kill element” method. The first part of the curve and the load peak are equally described. We can see that the identification of the elastic parameters will be not influenced by the “Kill element” method. But we can observe some significant differences during the post-peak stage. When we do not use the “Kill element” method, the load does not return to zero. We also notice a difference in the post-peak part. One reason can explain this difference. We use **the “Kill element” method** which is mesh dependent, whereas the mesh is relatively fine in this test. This means that a coarse mesh will provide an abrupt post-peak stage since big elements are deleted when damage reaches the critical value. This numerical test shows the difficulty to model a quasi-brittle material and to identify with a great accuracy the damage parameters in the post-peak part of the load-displacement curve.

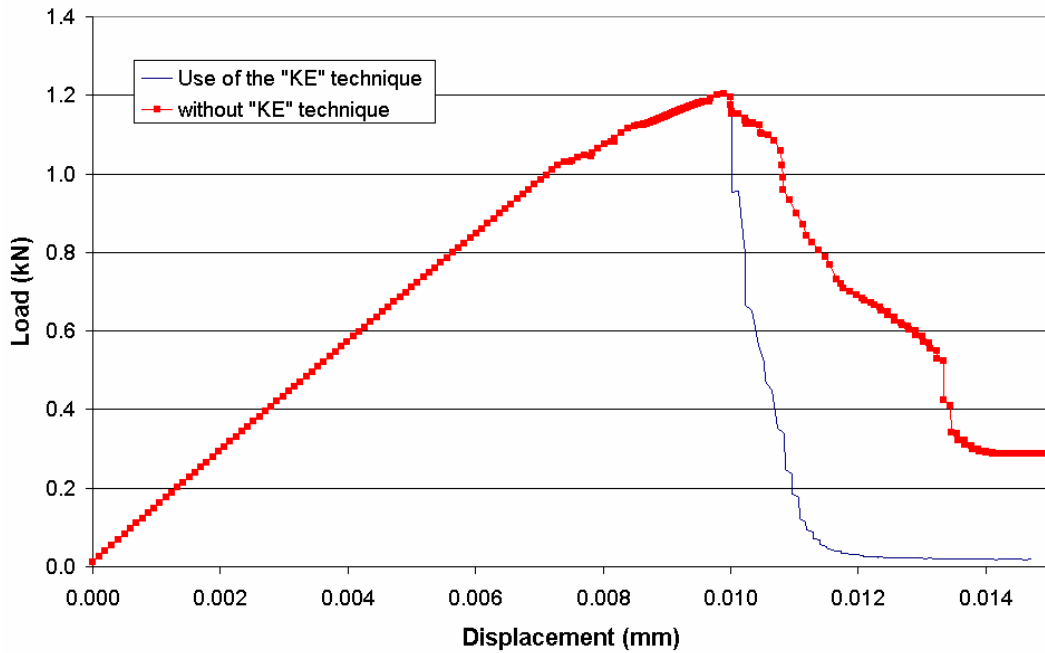


Figure 4-22. Load-displacement curve of mortar submitted to a three point bending test.

### 4.5.3 Material parameters

The identification of the  $B$  value underlines the degradation velocity of the material in compression. The higher  $B$ , the faster the degradation of the material. The  $A$  value means that the load-displacement returns to zero at the end of the simulation ( $A$  is closed to 1). These conclusions are based on the paper of Mazars [Mazars 1984] who has studied the effect of each parameter on the stress-strain curve (see figure 4-23).

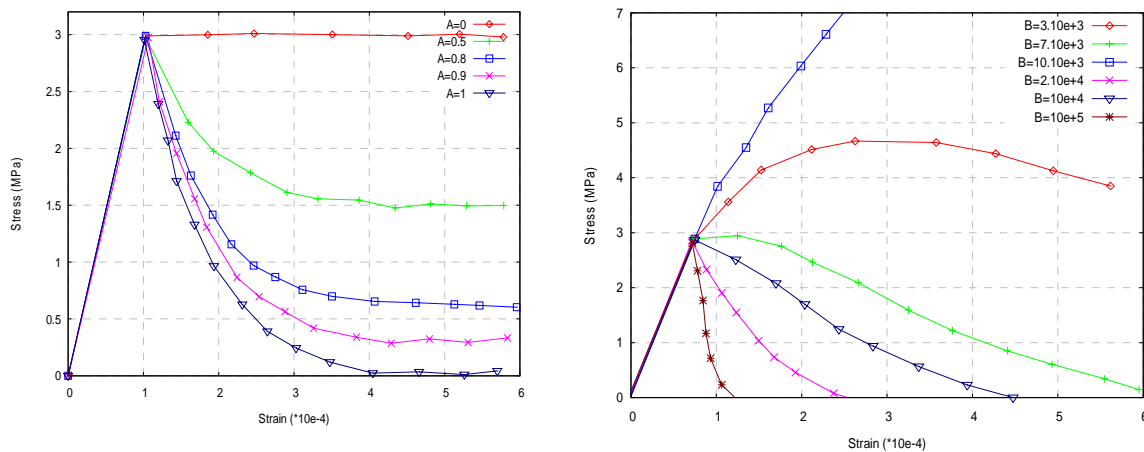


Figure 4-23. Influence of the  $A$  and  $B$  parameters

We check now these conclusions in tension with our numerical model. We consider a mortar sample submitted to a three point bending test. We use the same configuration and data than in section 4.5.1.1.

**a) Influence of  $\varepsilon_{D0}$**

We test the influence of the threshold of the equivalent strain  $\varepsilon_{D0}$ .  $\varepsilon_{D0}$  controls the damage initiation. Its role is so very important. Figure 4-24 underlines the role of  $\varepsilon_{D0}$  for several values.

**b) Influence of  $A_T$**

We test the influence of  $A_T$  on the response of material. We compare the model when  $A_T = 0.7$ ,  $A_T = 1.29$  and  $A_T = 1.5$  (see figure 4-25). The  $A_T$  parameter controls the starting point of the smooth part of the curve. The higher the parameter  $A_T$ , the more brittle the material behavior. We observe a difference with results obtained by Mazars (see figure 4-23). Indeed we use  $\tilde{\varepsilon}^{Crit}$  in our model (return to zero of the load-displacement curves).

**c) Influence of  $B_T$**

We study the influence of the parameter  $B_T$  on the load-displacement curves. We test three cases with:  $B_T = 1000$ ,  $B_T = 25316$ ,  $B_T = 100\ 000$ . Figure 4-26 shows the great influence of the parameter  $B_T$  on the global response. It influences at the same time the peak load and the slope of the curve in the smooth part. It also explains why inverse analysis has some difficulties to converge because of this strong correlation.

**d) Influence of  $\tilde{\varepsilon}_T^{Crit}$**

Usually macro cracks appear before damage becomes complete ( $D=1$ ). We test here the influence of  $\tilde{\varepsilon}_T^{Crit}$  on the global response of the elastic damage material. Figure 4-27 underlines the fact that our model is dependent on this value. It is hence necessary to identify with a great accuracy the  $\tilde{\varepsilon}^{Crit}$  parameter in order to describe as well as possible damage and cracks evolution.

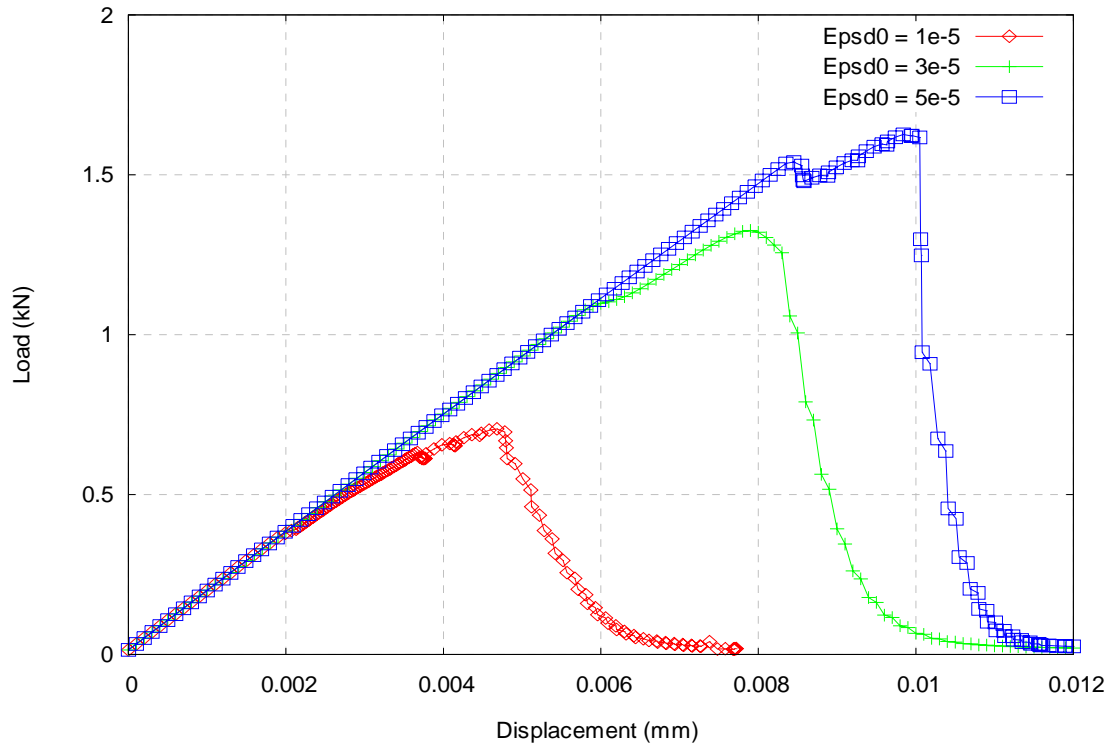


Figure 4-24. Influence of  $\epsilon_{D0}$  on the load-displacement curves.

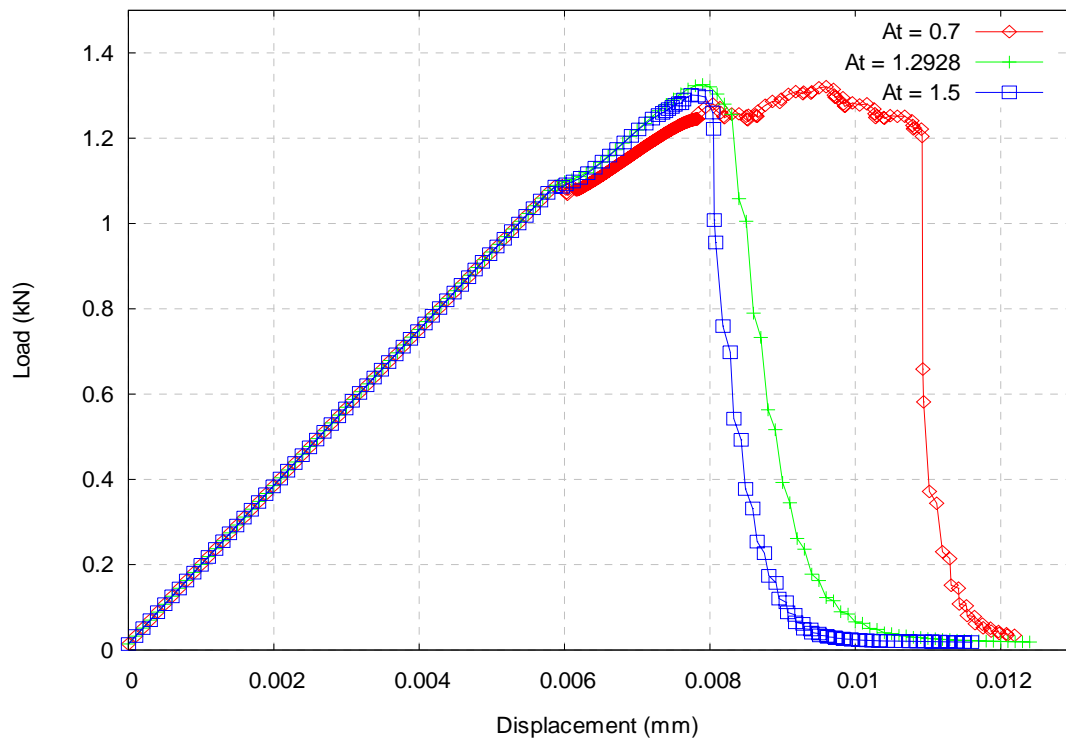


Figure 4-25. Influence of  $A_T$  on the load-displacement curves.

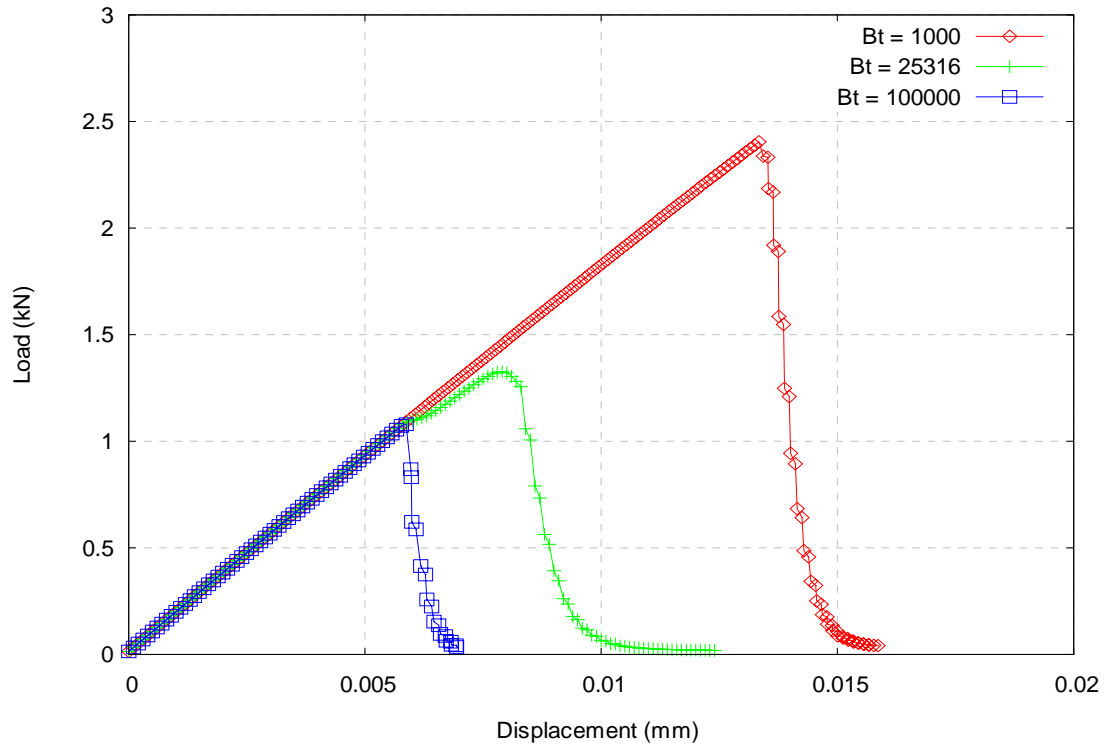


Figure 4-26. Influence of  $B_T$  on the load-displacement curves.

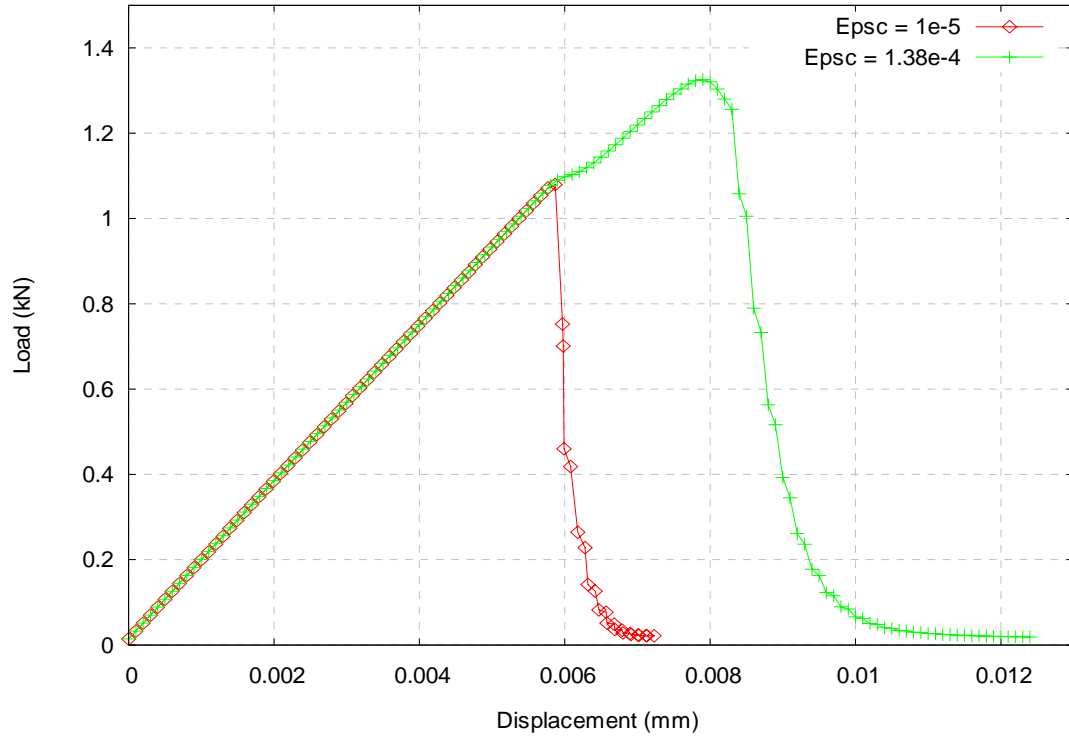


Figure 4-27. Load-displacement curves for different  $\tilde{\epsilon}_T^{Crit}$ .

The sensitivity study has shown that all parameters do not have the same effect on the numerical model. We have seen that friction plays an important role in the identification of the material parameters. The “Kill element” technique influences the smooth part of the load-displacement and consequently influences the identification of the material parameters. We have also seen that material parameters do not have the same influence on the load-displacement curves.  $B_T$  has indeed a great influence on the global response of the material.

## 4.6 Conclusion

We have carried out the experimental campaign and introduced the inverse analysis model on mortar and on concrete.

The experimental campaign has been carried on mortar and on concrete at the Ecole des Mines de Douai. For each case, three tests have been made at ages of 7, 14 and 28 days to be able to identify material parameters in compression and in tension. These tests include compression tests, three point bending tests and “Brazilian” tests.

The evolution algorithm of the “RheOConcrete” modulus has been used to identify automatically the elastic and damage parameters. This identification will be difficult as we have noticed that the inverse analysis problem is not easy to identify.

This study has underlined first the influence of external parameters as the conditions of contact, the influence of “Kill element” technique to simulate macrocracks, the correlation between material parameters and the importance of some damage parameters as the  $B_{T,C}$  parameter in the model.

The next chapter will explain in detail how we have identified the elastic and the damage parameters on the basis of this experimental campaign. We have used in this study experimental data given at age of seven days. A sensitivity study is also carried out to study the aggregates influence (repartition, volume) on the global response.

## CHAPTER 5 : IDENTIFICATION OF CONCRETE BEHAVIOR: RESULTS AND SENSITIVITY ANALYSIS ON AGGREGATES PARAMETERS

5.1 INTRODUCTION .....	5-94
5.2 STARTING HYPOTHESES .....	5-94
5.3 CONCRETE PARAMETERS: FIRST TECHNIQUE.....	5-94
5.3.1 <i>Verification of the method on a compression test</i> .....	5-96
5.3.1.1 Mortar paste identification .....	5-96
a) Model configuration.....	5-96
b) Elastic parameters .....	5-96
c) Parameters identification on mortar .....	5-101
d) Global response of the material .....	5-102
5.3.1.2 Identification of the elastic parameters of the aggregates .....	5-104
5.3.1.3 Validation on concrete .....	5-105
5.3.1.4 Discussion .....	5-106
5.4 CONCRETE PARAMETERS IDENTIFICATION: SECOND TECHNIQUE .....	5-107
5.4.1.1 Theoretical analysis.....	5-109
5.4.1.2 Inverse analysis .....	5-109
5.4.2.1 Model configuration.....	5-109
5.4.2.2 Identification of tensile parameters .....	5-111
5.4.2.2 Global response .....	5-112
5.4.4 Identification of the damage parameters of the mortar paste in compression	5-114
5.4.4.1. Model configuration.....	5-114
5.4.4.2 Identification of parameters in compression .....	5-115
5.4.4.3 Global response of the material.....	5-115
5.4.4.4 Local behavior of concrete.....	5-117
5.4.4.5 Comparison between the mechanical behavior of mortar and of the mortar paste (of concrete) .....	5-118
5.5 APPLICATION TO THE “BRAZILIAN” SPLITTING TEST.....	5-120
5.6 SENSITIVITY ANALYSIS ON AGGREGATES PARAMETERS.....	5-123
5.6.2 <i>Influence of the volume of aggregates</i> .....	5-125
5.6.3 <i>Influence of the maximal diameter of aggregates</i> .....	5-128
5.7 CONCLUSIONS .....	5-131

## 5.1 Introduction

We have identified two ways to identify material parameters of concrete. On the one hand concrete can be identified based on the results obtained on the mortar and on concrete. In this way it can be assumed that the mortar paste of concrete has the same mechanical behavior than mortar. Once we have identified the mechanical behavior of the mortar paste, the mechanical behavior of the aggregates can be identified on the experimental results on concrete by knowing the mechanical behavior on the mortar paste. On the other hand, we can adopt the following methodology: the mechanical behavior of aggregates is known a priori. In this way the mechanical behavior of the mortar paste is directly deduced from the experimental campaign on concrete. And so in this last case the experimental results on mortar are not necessary.

We present first the parameters we have identified. We use here the same notations used in chapter 4, table 4-1. In a second part we present the validation on concrete with a “Brazilian” splitting test. The third part is devoted to the sensitivity analysis on the effect of inclusions within a concrete sample.

## 5.2 Starting hypotheses

In order to avoid localization of strains and damage, the mechanical model is enriched with a non local approach. As explained previously, it is more convenient to use the non local Mazars model (see chapter 2, section 2.3.2.1) implemented in FEMCAM with an implicit gradient formulation where the internal parameter  $\tilde{c}$  is fixed to  $15 \text{ mm}^2$  for the whole chapter. We also use for each test of this chapter the Adaptive Time Step  $n^{\circ 2}$  (see chapter 3 section 3.4.3.2).

Tools are considered as infinite rigid bodies. All numerical tests are performed using a constant displacement rate prescribed on the upper loading plate. In the framework of the parameters identification, we consider that tools displacement corresponds to the experimental displacement in the sample. We underline also that experimental displacements on load displacement curves are given by strain gauges (compression and “Brazilian” splitting tests) and sensor displacements (three point bending tests).

## 5.3 Concrete parameters: first technique

This first approach consists in identifying the mechanical behavior of mortar in a first time. We shall then assume that: **the mechanical behavior of the mortar paste (of concrete) is the same than the mechanical behavior of mortar alone**. Figure 5-1 summarizes this approach:

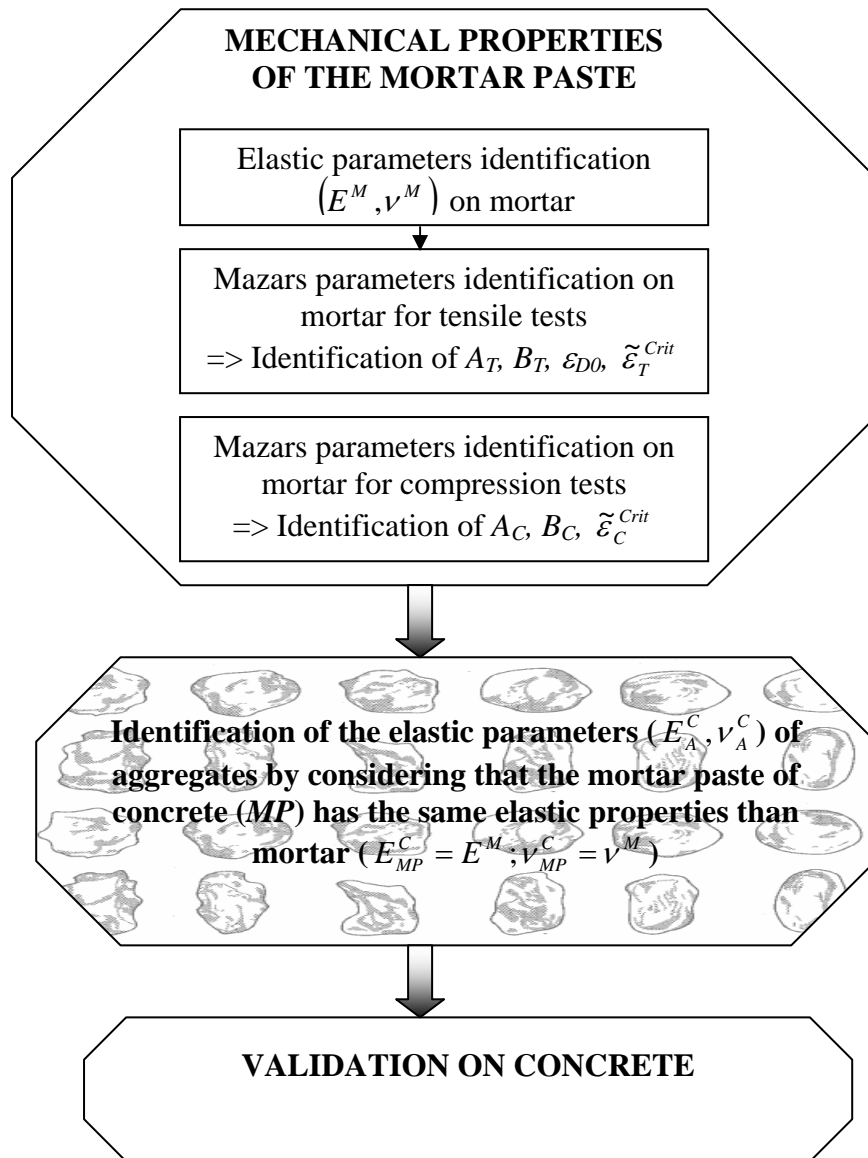


Figure 5-1. First approach to identify the mechanical behavior of concrete.

Thus we know the mechanical behavior of one of the main part of concrete. We still have to identify the mechanical behavior of the aggregates. We will consider that flint and limestone aggregates have the same purely elastic behavior.

## 5.3.1 Verification of the method on a compression test

### 5.3.1.1 Mortar paste identification

#### a) Model configuration

A compression test on a quasi-brittle material has been performed. In this case, the load is applied via uniform prescribed displacement on the top side of the specimen while lateral displacements are allowed. The specimen is a cylinder with a diameter of 110 mm and a height of 220 mm. Due to symmetry conditions, only a quarter of the sample is discretized. Figure 5-2 presents the mesh used for this simulation.

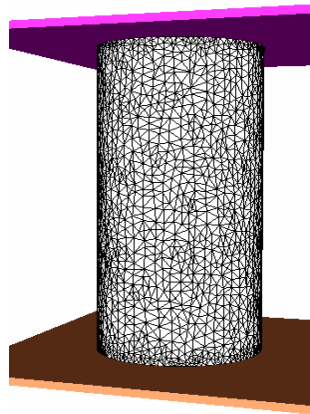


Figure 5-2. Simulation of a compression test on mortar; 10 066 nodes, 47 941 elements. The average element size is approximately 5.2 mm.

The contact between the tools and the sample is considered as frictional to be as close as possible to experimental conditions. We use the Coulomb law ( $\bar{m} = 0.05, \mu_F = 0.02$ ) which corresponds to a low friction.

#### b) Elastic parameters

Two parameters characterize the material behavior in the elastic phase: the Young modulus and the Poisson ratio. It is possible to evaluate:

- The mean value of the three Young modulus with the experimental stress-strain curves. Table 5-1 shows the experimental evolution of the Young modulus for mortar we have tested in this experimental campaign (see chapter 4, figure 4-12):

<i>Elastic parameters</i>	<i>7 days</i>	<i>14 days</i>	<i>28 days</i>
$E^M$ (GPa)	22.9	23.99	26.33

Table 5-1. Experimental evolution of the Young modulus for mortar.

- The mean value of the Poisson ratio can be determined experimentally by measuring the radial or circumferential expansion of a standard concrete cylinder subjected to compression loading (thanks to the rosette gages which gives us the information:  $\frac{\epsilon_{yy}}{\epsilon_{xx}}$ ). A common used value is 0.2. The trend of the Poisson ratio evolution, based on our experiments, indicates a decreasing evolution from 7 to 28 days.

<i>Elastic parameters</i>	<i>7 days</i>	<i>14 days</i>	<i>28 days</i>
$\nu^M$	0.22	0.21	0.18

Table 5-2. Experimental evolution of the Poisson ratio for mortar.

In this way we try to bear out the experiment with the inverse analysis modulus. We identify these two parameters in the elastic part of the load-displacement curves in a set of range, between 17 and 30 GPa for the Young modulus  $E^M$  and between 0.15 and 0.35 for the Poisson ratio  $\nu^M$ . The initial set of values for this test is:  $E^M = 20$  GPa,  $\nu^M = 0.2$ . The set of parameters, for a seven days mortar, has been obtained after one hundred iterations of “RheOConcrete”; the CPU time is roughly two hours.

$$\begin{aligned} E^M &= 20.3 \text{ GPa (20272.9 MPa)} \\ \nu^M &= 0.24 \end{aligned} \tag{5-1}$$

Figure 5-3 shows the estimated least squares error  $\tilde{\epsilon}$  at the mean for each “RheOConcrete” iteration:

$$\tilde{\epsilon} = \sum_{i=1}^N \left( F_{\text{exp}}^i - F_{\text{num}}^i \right)^2 \tag{5-2}$$

Where  $N$  is the number of points on the considered load-displacement curve.  $F_{\text{exp}}^i$  and  $F_{\text{num}}^i$  are respectively the experimental and numerical loads. This figure shows the good convergence of the problem.

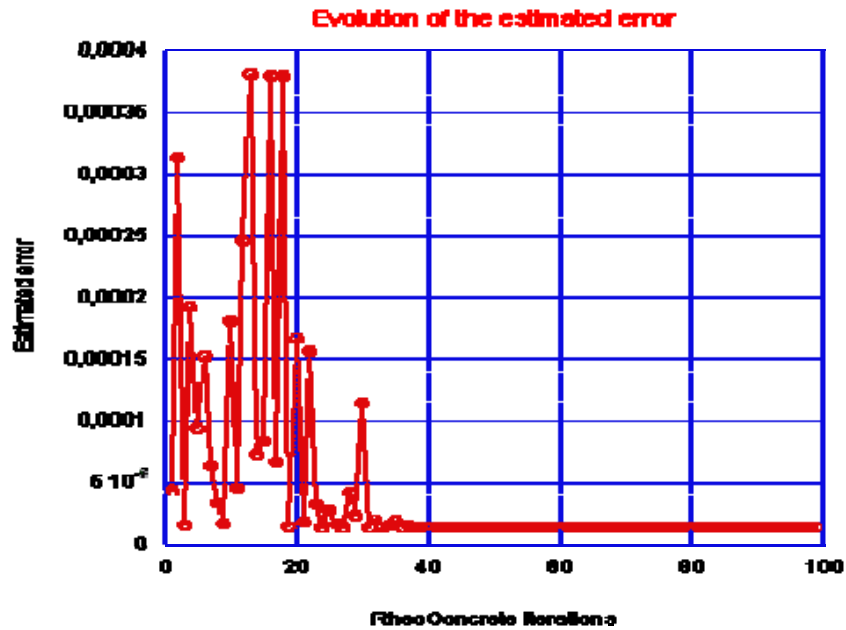


Figure 5-3. Estimated error in function of the RheoConcrete iterations at age of seven days.

Table 5-3 summarizes the identified values and the correspondent estimated error:

Elastic parameters for mortar	7 days	14 days	28 days
$E^M$ (MPa)	20272.9	20582.1	20785.1
$\nu^M$	0.24	0.28	0.27
The estimated error	$1.36 \cdot 10^{-5}$	$5.87 \cdot 10^{-6}$	$1.49 \cdot 10^{-5}$

Table 5-3. Identification of the elastic parameters of mortar.

Table 5-3 shows that the Young modulus does not evolve so much between 7 and 28 days. However the Poisson ratio evolves between 7 and 14 days and stays stable after 14 days. Furthermore these values are far away from the values deduced from the experimental results. It would mean that the Poisson ratio identification is impossible with the only data given by the load-displacement curves. We are going to verify the objectivity of this solution with a sensitivity study. The objective of this analysis is to test which parameters influence the more the global response. We use the experimental test at age of 28 days.

We prescribe first the Young modulus. The aim is to better analyze the influence of the Poisson ratio on the global response of the material. We test the model for three different Young modulus:  $E^M = 15$  GPa,  $E^M = 22$  GPa and  $E^M = 29$  GPa at the same age (28 days). The Poisson ratio can evolve between 0.15 and 0.3 which are admissible values for mortar. Table 5-4 shows the minimum estimated error reached during the simulation and the correspondent Poisson ratio.

	$E^M = 15 \text{ GPa}$	$E^M = 22 \text{ GPa}$	$E^M = 29 \text{ GPa}$
$\nu^M$	0.299415	0.152295	0.1522
The estimated error	$4.86 \cdot 10^{-4}$	$3.52 \cdot 10^{-5}$	$9.62 \cdot 10^{-4}$

Table 5-4. Estimated error when the Poisson ratio is unknown.

Figure 5-4 shows that “RheOConcrete” has some difficulties to converge for each value of the Young modulus. The best result is obtained for  $E^M = 22 \text{ GPa}$ , which is much closer from the result obtained with “RheOConcrete” when the research has been lead on the both two parameters. However the Poisson ratio obtained ( $\nu^M = 0.15$ ) is far away from the value found by the inverse analysis.

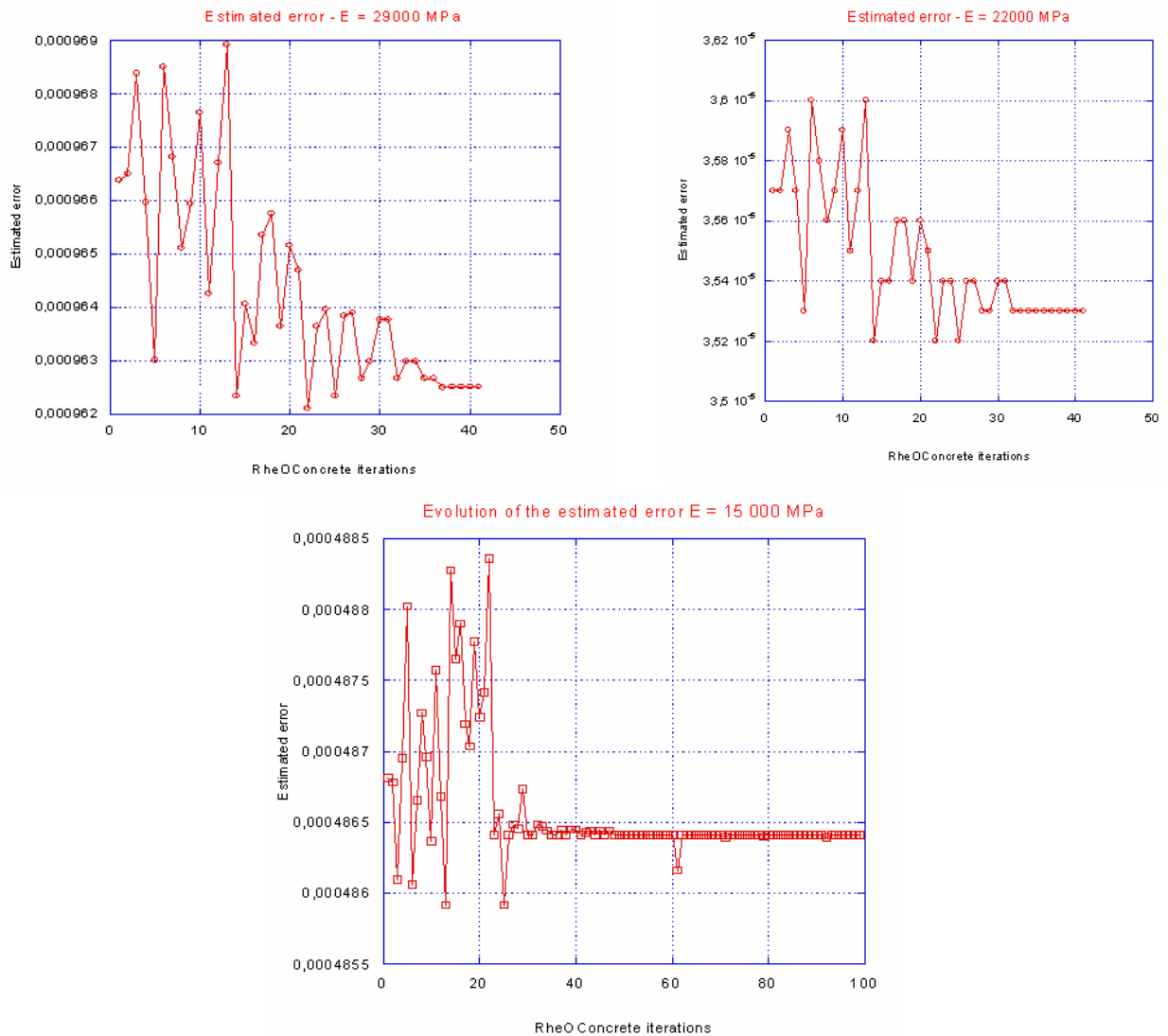


Figure 5-4. Estimated error for the identification of the Poisson ratio.

Figure 5-4 underlines the lack of objectivity of the identification. We can now run the same tests by prescribing the Poisson ratio in order to observe the influence of the Young modulus  $E^M$  on the inverse analysis.

We now set the Poisson ratio. We study the influence of the Young modulus  $E^M$  on the global response of the material. We test the model for three different Poisson ratios:  $\nu^M = 0.15$ ,  $\nu^M = 0.2$  and  $\nu^M = 0.3$  at the same age (28 days). The Young modulus  $E^M$  can evolve between 15 and 30 GPa which are also admissible values for mortar. Table 5-5 shows the minimum estimated error reached during the simulation and the correspondent Young modulus.

	$\nu^M = 0.15$	$\nu^M = 0.2$	$\nu^M = 0.3$
$E^M$ (GPa)	20.80	20.79	20.78
The estimated error	$1.48.10^{-5}$	$1.48.10^{-5}$	$1.49.10^{-5}$

Table 5-5. Estimated error when the Young modulus is unknown.

We plot then the estimated error versus the ‘‘RheOConcrete’’ iterations (see figure 5-5). Eventually it appears that the parameter, which influences results the most, is the Young modulus  $E^M$ . In this way, we can retain the values obtained by the inverse analysis for the Young modulus. **So from now we will consider that  $\nu^M = 0.2$  for the mortar paste**, which is the experimental value we have measured after seven days.

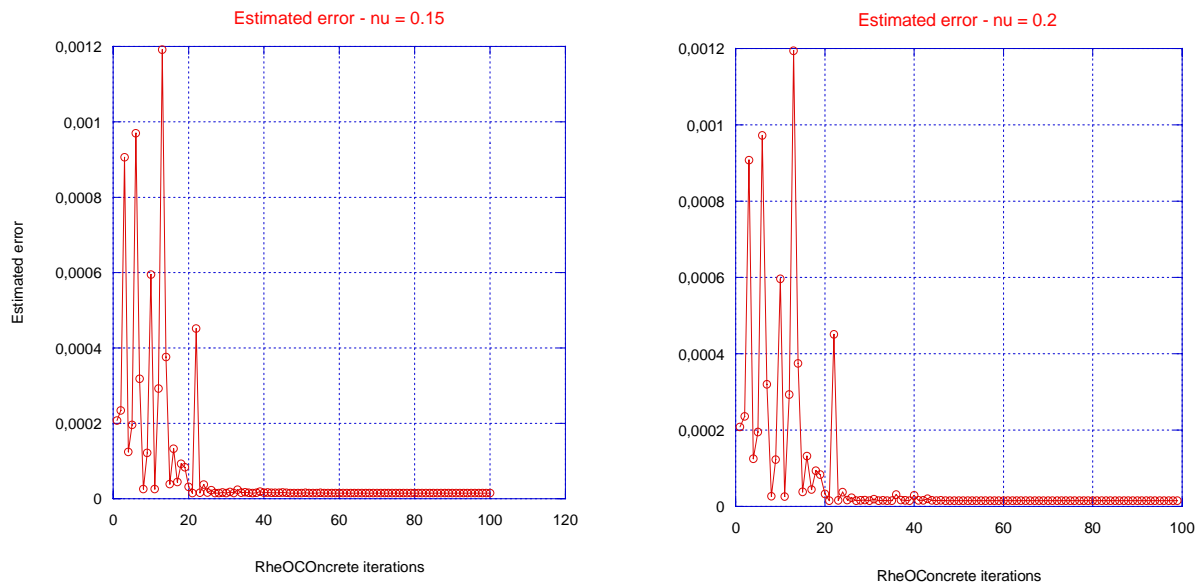


Figure 5-5. Estimated error for the identification of the Young modulus for  $\nu = 0.15$  and  $\nu = 0.2$ .

Now the Young modulus and the Poisson ratio ( $E^M, \nu^M$ ) are known. Some other parameters characterize the mechanical behavior in the damage elastic damage part. The process is the following: we identify first damage in tension with the three point bending test. Then we identify damage in compression with the compression test. We now present results of parameters identification in compression.

**c) Parameters identification on mortar**

We shall identify:  $A_C, B_C, \varepsilon_{D0}, \tilde{\varepsilon}_C^{Crit}$  in this set of range:

$$\begin{aligned}
 A_C &\in [1;1.5] \\
 B_C &\in [200;2\ 000] \\
 \varepsilon_{D0} &\in [1.10^{-5};3.5\ 10^{-4}] \\
 \tilde{\varepsilon}_C^{Crit} &\in [1.10^{-4};5.10^{-3}]
 \end{aligned}
 \tag{5-3}$$

This set of range has been defined thanks to a preliminary study. During this study the set of range was very wide corresponding to a classical set of range defined by Mazars ( $0.5 \leq A_C \leq 1.5; 3.10^3 \leq B_C \leq 10^5; 1.10^{-5} \leq \varepsilon_{D0} \leq 3.10^{-5}; 3.10^{-5} \leq \tilde{\varepsilon}_C^{Crit} \leq 1.10^{-2}$ ). Hence we have determined the set of range defined in Eq. ( 5-3) by cancelling the parameters which lead to load-displacements which are too far from the experimental results. Moreover this study enables to improve (in term of computation time) in the research of parameters to identify. Table 5-6 presents the set of parameters after one hundred ‘‘RheOConcrete’’ iterations.

$A_C$	$B_C$	$\varepsilon_{D0}$	$\tilde{\varepsilon}_C^{Crit}$
1.27879	457.085	$3.10^{-5}$	$1.52.10^{-3}$

Table 5-6. Damage identification of mortar parameters in compression.

The CPU time required to identify these parameters is about five hours. It corresponds to an estimated error of  $8.1.10^{-5}$ . Figure 5-6 shows the difficulties that encounter the inverse analysis to converge.

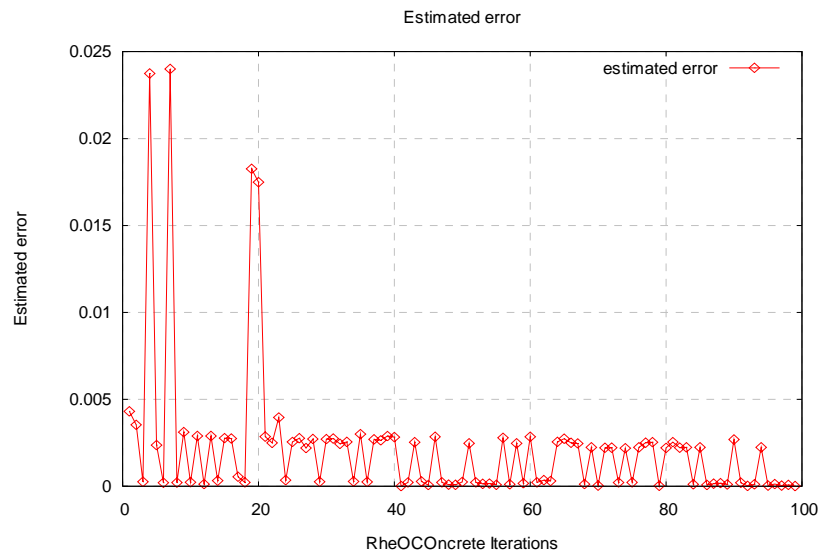


Figure 5-6. Estimated error on the identification of damage parameters on a compression test for mortar.

#### d) Global response of the material

Figure 5-7 shows the evolution of damage. Damage does not take place uniformly over the whole cylinder due to the frictional contact between the upper tool and the sample. Damage is initiated preferentially near the contact with the tools and then evolves equally in the sample. Indeed we can separate the cylinder in three zones: two zones, which are near to the tools and a third zone in the middle of the cylinder without any effect of the contact on the response of the material. Once damage has reached a specific critical value, fracture intervenes in the middle of the sample.

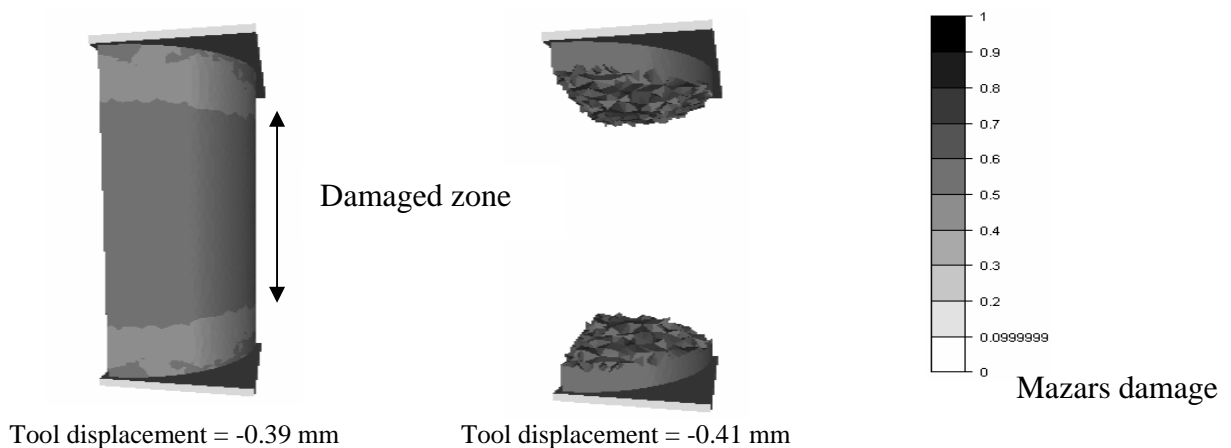


Figure 5-7. Damage evolution for different values of displacement of the tools.

Figure 5-8 presents the corresponding load-displacement curve. Simulation results are in good agreement with experimental observations on a mortar at seven days. The evolutive trends of elasticity, damage and fracture are shown on this load-displacement curve. **The experimental mean load reaches about 285 kN - which corresponds to a global strength of 29.9 MPa for a mortar after seven days.**

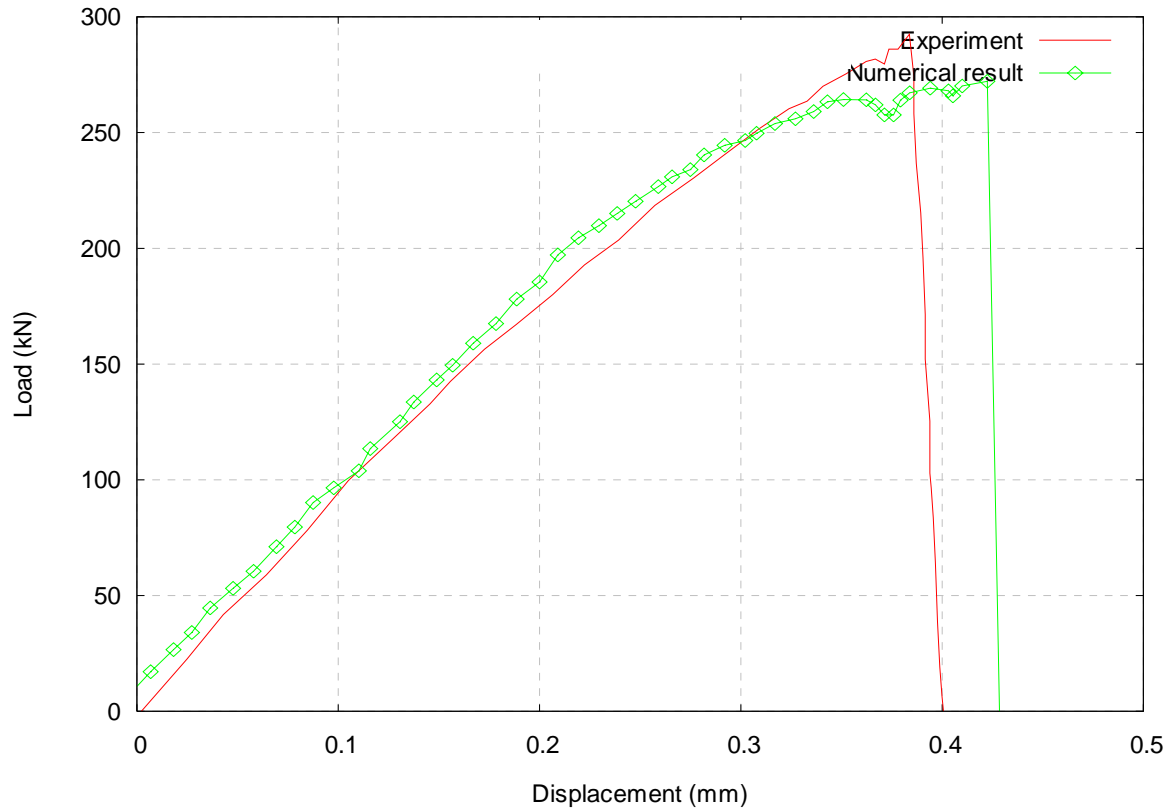


Figure 5-8. Load-displacement curve for a compressive test.

Damage does not take place uniformly over the whole cylinder due to the frictional nature of contact between the tools and the sample. Hence we do not observe clearly the X-shaped diagonal shear band which we would observe in the case of a bilateral sticking contact. It would be interesting to test the influence of contact conditions on the damage distribution. Figure 5-9 presents the damage distribution, in the mortar sample under uniaxial compression, near the upper tool and at the end of the simulation. Only an eighth of the sample is represented. We notice that damage initiates at the centre of the sample with an amplitude depending on the type of contact used.

*To improve this model, we have to consider a statistical distribution of voids and micro cracks in the sample before the loading starts. These defects would orient preferentially damage and macrocracks during the compression test.*

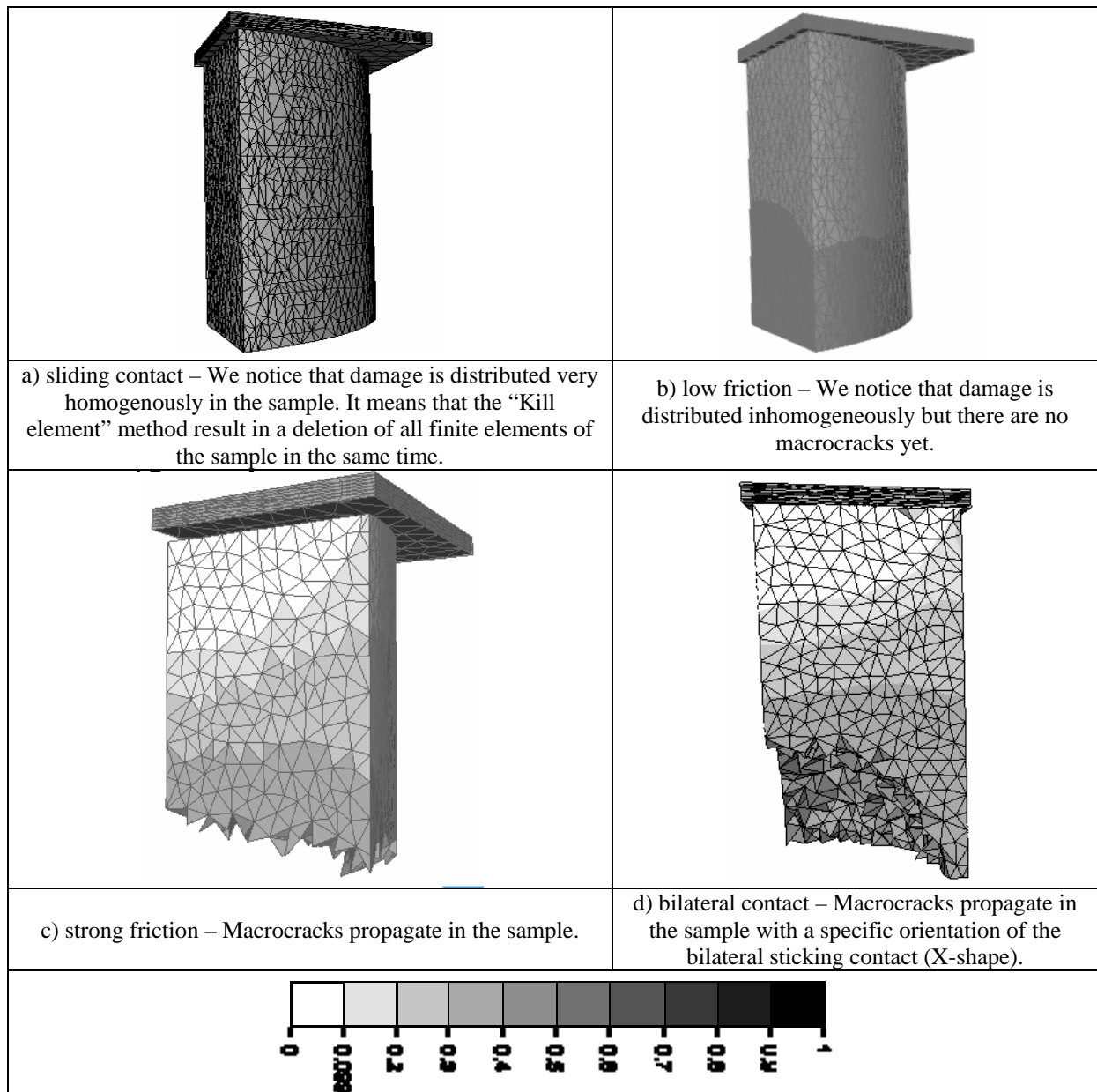


Figure 5-9. Damage repartition in the quarter of the sample in function of the contact between the tools and the mortar sample for the same displacement tool ( $h = -0.3956$  mm).

### 5.3.1.2 Identification of the elastic parameters of the aggregates

The “trisphere” model [de Larrard et al. 1999] can lead to evaluate the Young modulus of the mortar paste ( $MP$ )  $E_{MP}^C$  in function of the Young modulus of the aggregates ( $A$ )  $E_A^C$  and the homogenised Young modulus of concrete  $E$ :

$$\begin{cases} E = \frac{(2 - g^*)E_{MP}^C + g^* E_{MP}^C}{g^* E_{MP}^C + (2 - g^*)E_A^C} E_A^C \\ g^* = 1.0475 \sqrt{\frac{d_{\min}}{d_{\max}}} \end{cases} \quad (5-4)$$

Where  $g$  denotes the granular concentration. If we considers  $E = 43$  GPa according to the experimental results (see Eq. ( 5-4)),  $E_{MP}^C = 20$  GPa for the mortar paste (we consider here that  $E_{MP}^C = E^M$ ) and  $g^* = 0.61$  according to the grain size distribution (the minimum diameter in the mortar paste is 4 mm) then **the “trisphère” model gives a Young modulus for the aggregates paste equal to  $E_A^C = 65$  GPa.**

**The inverse analysis gives us  $E_A^C = 50$  GPa,** for the Young modulus of the aggregate if we consider  $E_{MP}^C = 20$  GPa. This result is low in comparison with results that can be found in literature. Indeed it is commonly stated that  $E_A^C$  is close to 70-80 GPa.

### 5.3.1.3 Validation on concrete

We now test on concrete the model with the identified parameters. We use the compression tests. The “Kill element” technique has not been used in this case as this method has some difficulties to converge. This difficulty is directly linked to the compression test which induces contacts between the finite elements and some conflicts between the “Kill element” method and the current geometry of the sample. Figure 5-10 shows the stress-strain curves for a compression test. The initial time step is fixed to 0.1 mm per step and the upper tool has an initial velocity of  $0.1 \text{ mm.s}^{-1}$ . The stress has been obtained by dividing the load by the initial section.

The numerical compression strength is about  $\sigma_{\max} = 55$  MPa versus about 34 MPa experimentally obtained. **Damage effects are underestimated.** It means that damage parameters on compression are well identified on mortar but it does not represent the physical mechanical behavior of the mortar paste. The CPU time to simulate this compression test is about sixteen hours.

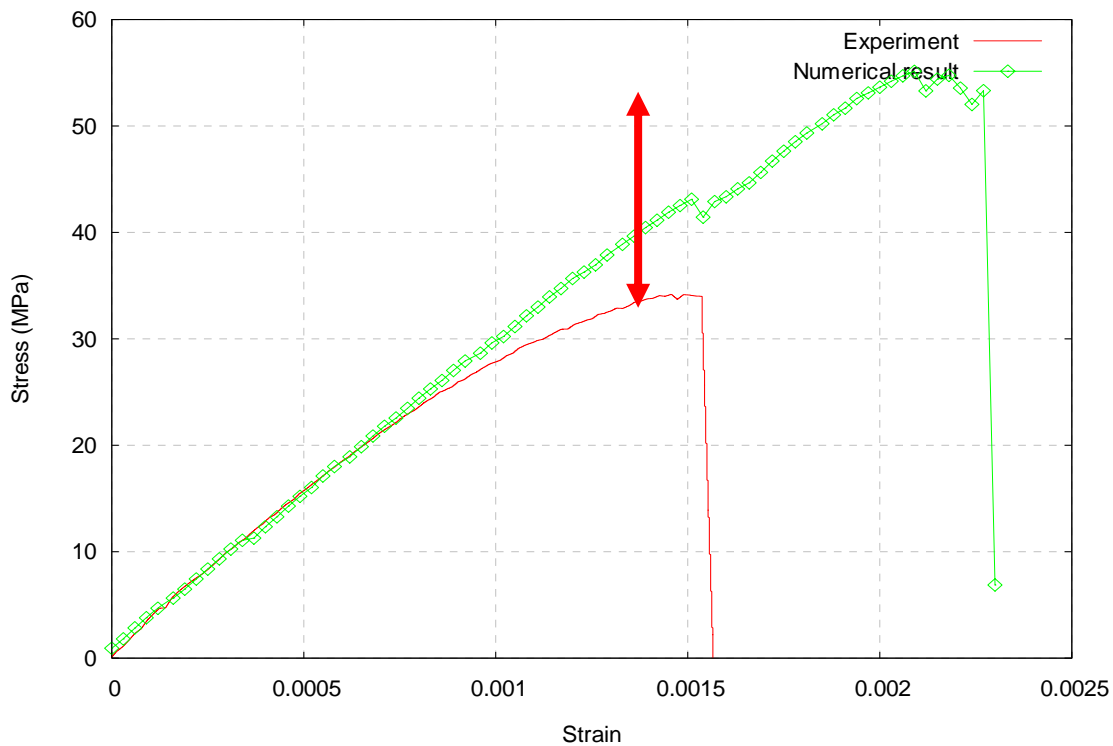


Figure 5-10. Comparison of the experimental and numerical load-displacement curves for a compression test on concrete.

#### 5.3.1.4 Discussion

The analysis of this result shows that this first approach is not well adapted to model concrete. **It shows that it is impossible to consider the mortar paste of concrete with the same mechanical behavior as mortar.** Several hypotheses can explain this result.

- **Damage parameters may be not very well adapted.** These damage parameters have been identified using an inverse analysis modulus. However this method has its limitations. We consider here that the mortar paste has the same mechanical behavior than mortar. But the reality is different. When concrete is made, a network of microcracks is initiated due to a prevention of internal shrinkage by aggregates. These important phenomena need to be taken into account:

- Formation of microcracks due to a shrinkage phenomenon;
- Creation of an ITZ between the aggregates and the mortar paste. By identifying the mortar paste (of concrete) with mortar only, we do not consider the mechanical effect of the ITZ;
- We consider a perfect sticking contact between the aggregates and the mortar paste which can be questionable.

Whereas we use the same formulation, these phenomena induce a mechanical behavior of the mortar paste different from mortar. **The ITZ is not represented through the mechanical behavior of the mortar paste.** However it is considered as a weaker zone where cracks are often initiated. In the same way porosity and cleavage between aggregates and the mortar paste has not been taken into account. It also explains why inverse analysis gives us a Young Modulus of aggregates very low compared with results in the literature (about 30% of variation). The possible explanations show that the mechanical behavior of the mortar paste is over estimated. Consequently the identified aggregates mechanical behavior rigidity embeds microcracks effects, cleavage etc.

## 5.4 Concrete parameters identification: Second technique

The approach we have chosen considers concrete as aggregates included in a mortar paste. We identify the mechanical behavior of the mortar paste on concrete. Figure 5-11 summarizes this approach:

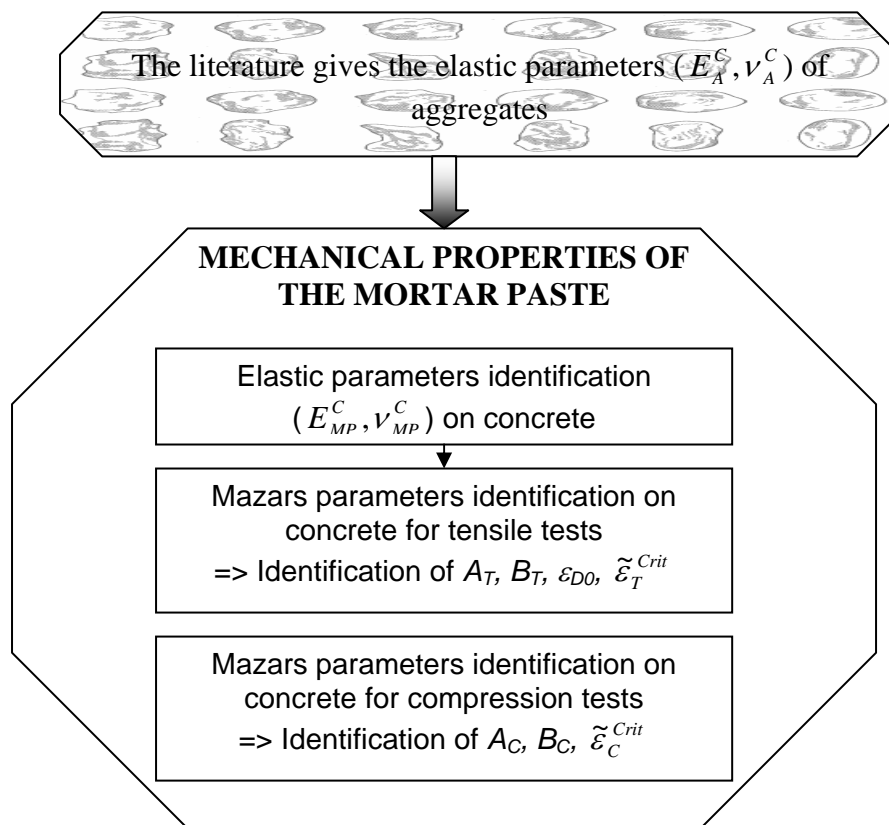


Figure 5-11. Second approach to identify the mechanical behavior of concrete.

We consider aggregates as purely elastic with these commonly used parameters:

$E_A^C$ (GPa)	$\nu_A^C$
70	0.2

Table 5-7. Elastic parameters for aggregate.

We want to identify now the behavior of the mortar paste. So the process is as following:

- we identify the elastic parameters with a compression test;
- we then use the elastic parameters to identify damage parameters in tension with a three point bending test;
- we identify damage parameters in compression with an uniaxial compression test.

**This way of identification enables homogenize the mechanical behavior of the mortar paste, the ITZ and the contact between aggregates.** As we dissociate the aggregates from the rest of the concrete, we consider that the numerical mortar paste is constituted of the mortar paste (of concrete) with a weaker zone around each aggregate and a specific contact around each of them. Nevertheless the identification of the material properties of the ITZ and the contact used is global and is not considered at the grain scale (see figure 5-12).

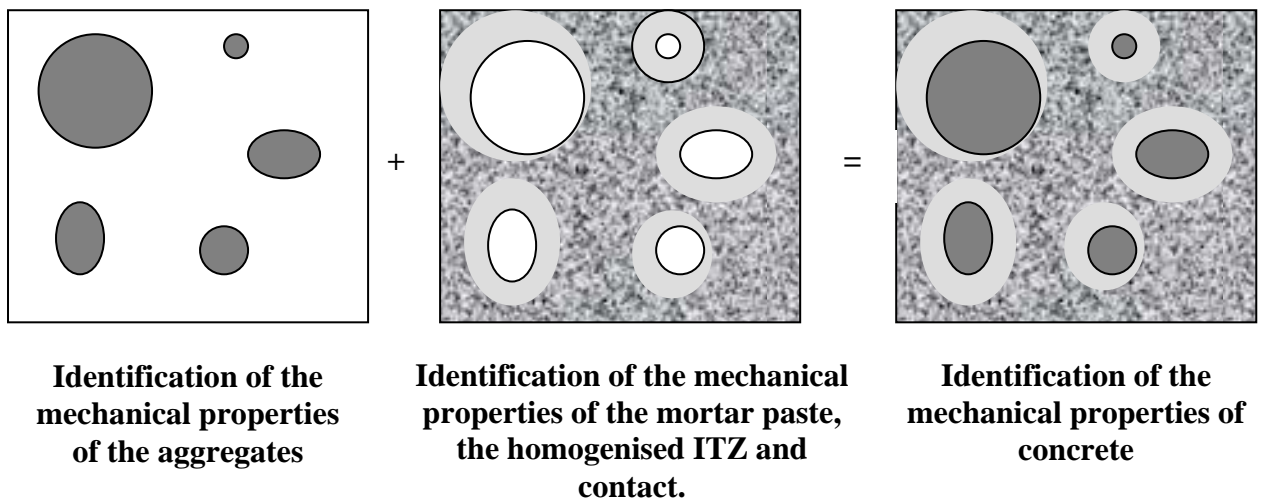


Figure 5-12. Identification of the mechanical properties of concrete with the second approach.

### 5.4.1 Identification of the elastic parameters of the mortar paste

We first identify the mechanical behavior of the mortar paste in the elastic part. During the **hydration period** the concrete mix undergoes a gradual phase change: from plastic to a rigid consistency. At the plastic state, the Poisson ratio has been found to be between 0.4 and 0.45. The material is quasi-incompressible. During the change in phase, the Poisson ratio has

to be gradually changed. [Germann and al. 1998] has proposed a relation between the Poisson ratio and time:

$$\nu(t) = -0.05 \ln(t + 1.11) + 0.425 \quad (5-5)$$

Where  $t$  is concrete age after setting (in hours). For instance after 80 hours, the Poisson ratio is estimated to be equal to  $\nu(t=80)=0.20$ . At age of seven days,  $\nu(t=80)=0.17$ . But if we consider the mortar paste, the Poisson ratio becomes higher ([0.24-0.27]). We observe it on our experiment where  $\nu=0.22$  at age of seven days. Furthermore the prediction of the Poisson ratio evolution is very dependant on the formulation used. Hence a mortar with a high cement content has a different compressibility evolution than a mortar with a formulation poor in cement content. We consider Poisson ratio of the mortar paste equal to the Poisson ratio of the aggregates:  $\nu_{MP}^C = 0.2$ .

#### 5.4.1.1 Theoretical analysis

The Young modulus of concrete is influenced by elastic properties of aggregates, conditions of curing, age of concrete, mix proportion, type of cement. A common value is 30 GPa. The “trisphère” model (see Eq. ( 5-4)) leads to evaluate  $E_{MP}^C$  in function of  $E_A^C$  and the Young modulus of concrete  $E$ . If we considers  $E=43$  GPa according to the experiments,  $E_A^C=70$  GPa and  $g^*=0.61$  according to the grain size distribution (the minimum diameter in the mortar paste is 4 mm) then the “trisphère” model gives a Young modulus for the mortar paste equal to  $E_{MP}^C=18.69$  GPa.

#### 5.4.1.2 Inverse analysis

**The inverse analysis identifies the Young modulus  $E_{MP}^C$  to 18.69 GPa.** The research has been lead between 15 GPa and 40 GPa. It confirms the theoretic analysis of the “trisphère” model. This is the value we will use to identify the other parameters.

### 5.4.2 Identification of the damage parameters of the mortar paste in tension

#### 5.4.2.1 Model configuration

A three point bending test on a quasi-brittle material has been performed (see figure 5-13). The contact between the upper tool and the sample is bilateral sticking. And the contact between the lower tool and the sample is frictional. A Coulomb law limited by the Tresca law (with arbitrary parameters  $\bar{m}=0.4$ ,  $\mu_F=0.2$ ) corresponds physically to a strong friction. The upper tool displacement is equal to  $2.5 \cdot 10^{-3}$  mm per step. For this test, a particle size distribution is considered with a maximum grain size of  $d_{max}=22.5$  mm and a volumetric density of 40 %. It corresponds to the specific formulation used for the study of the ASR.

Average diameter (mm)	22.5	18	14.25	11.25	9	7.15
Number of aggregates	8	62	106	91	128	236

Table 5-8. Particle size distribution with 631 aggregates.

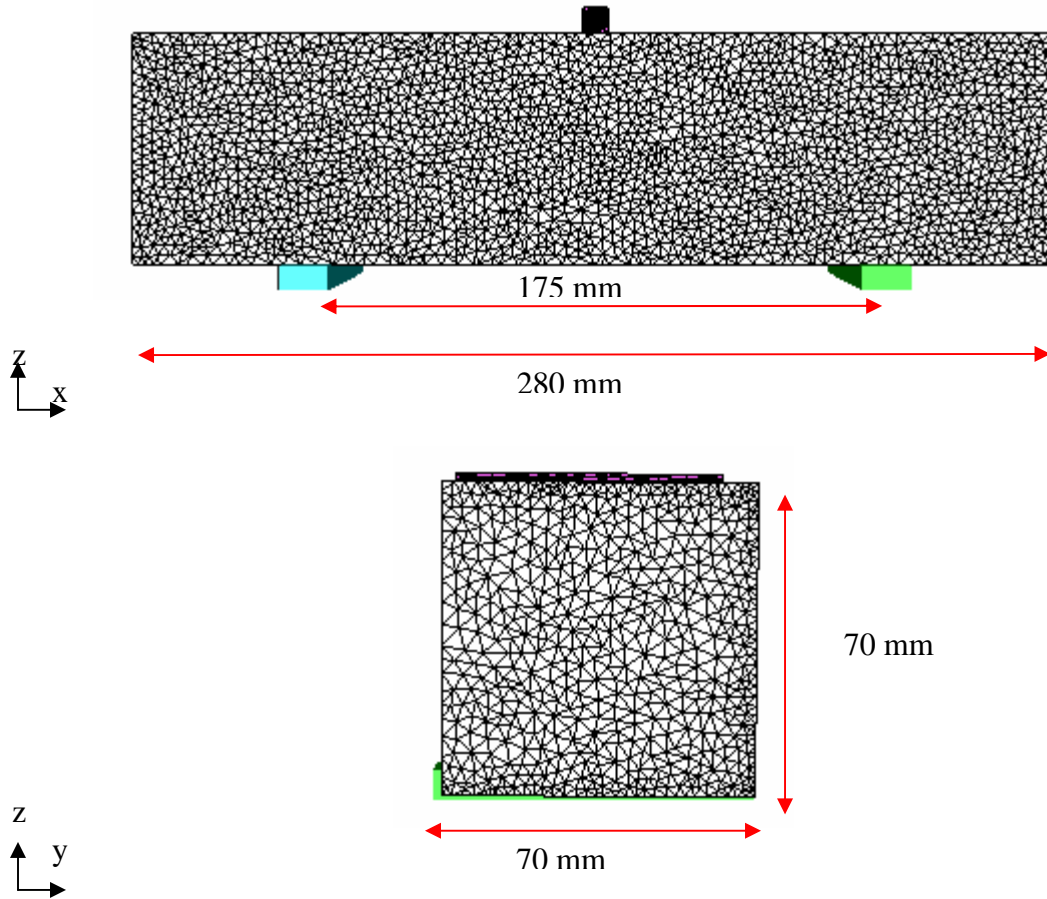


Figure 5-13. Geometry of the three point bending test. 36 178 nodes, 186 314 elements.

The aggregates random generation algorithm presented in chapter 3 has been used. Figure 5-14 shows the heterogeneous aspect of the sample.

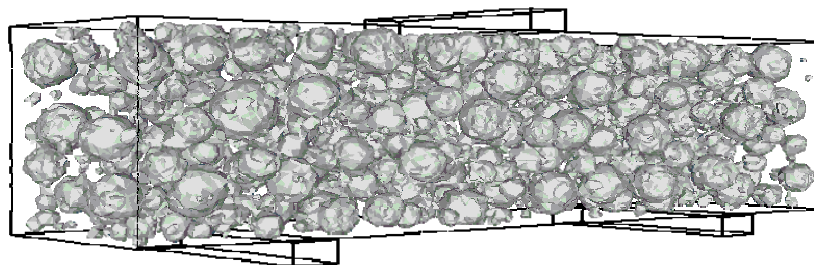


Figure 5-14. Heterogeneous aspect of the work piece.

### 5.4.2.2 Identification of tensile parameters

The identification of these parameters is made within the following range:

$$\begin{aligned}
 A_T &\in [0.7;1.5] \\
 B_T &\in [10\,000;110\,000] \\
 \varepsilon_{D0} &\in [1.10^{-5};5.10^{-4}] \\
 \tilde{\varepsilon}_T^{Crit} &\in [1.10^{-4};1.10^{-3}]
 \end{aligned}
 \tag{5-6}$$

Results of the identification have been obtained after about seventeen days. It corresponds to about one hundred simulations. The computation time to obtain this simulation is about four hours for a non local implicit model. With the same mesh, this simulation requires about twenty hours of computation time with a non local model with an integral formulation. The best results obtained are the following:

$A_T$	$B_T$	$\varepsilon_{D0}$	$\tilde{\varepsilon}_T^{Crit}$
1.18	50 000	$9.1.10^{-5}$	$1.63.10^{-4}$

Table 5-9. Damage parameters in tension for the mortar paste.

The estimated error associated is presented in figure 5-15. It shows the incapacity of the inverse analysis model to tend to a unique solution.  $\varepsilon_{D0}$  is twice lower than the value identified for mortar.

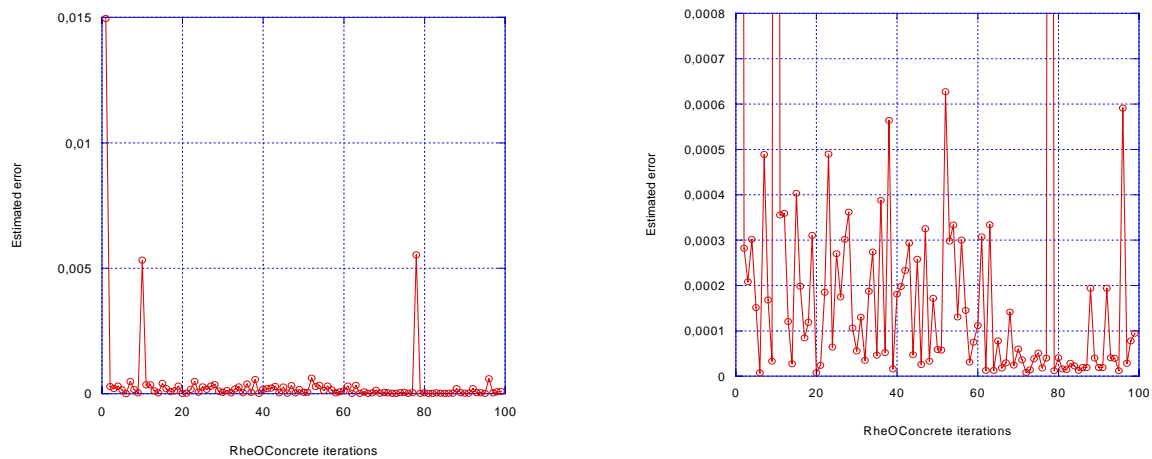


Figure 5-15. Estimated error in function of the "RhEOConcrete iterations".

### 5.4.2.2 Global response

Iso values of damage during the simulation for an implicit model associated with the “Kill element” method are given in figure 5-16.

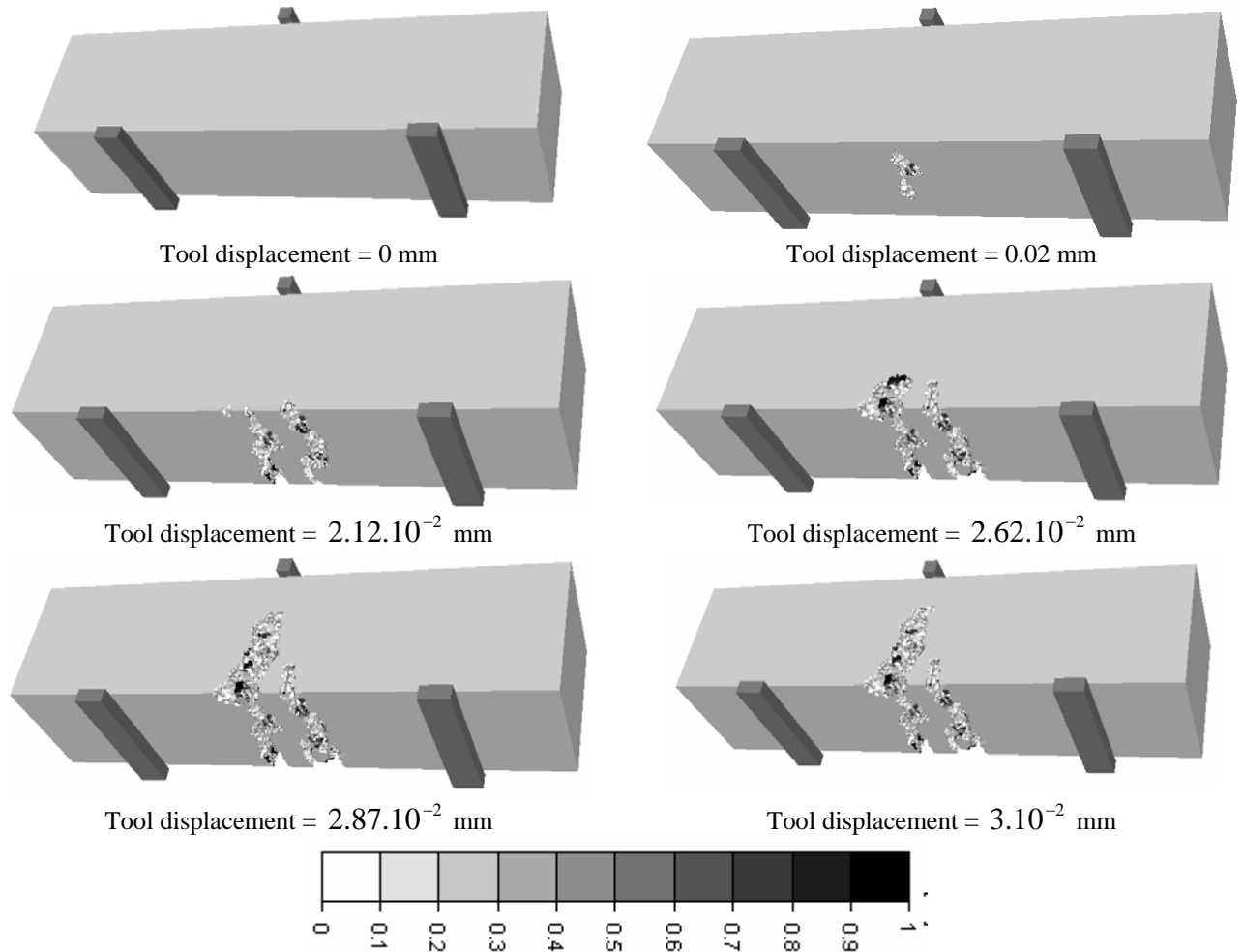


Figure 5-16. Damage evolution for a three point bending test on concrete.

The macrocrack is initiated at the location where the equivalent strain reaches the critical equivalent strain  $\tilde{\varepsilon}_T^{Crit}$ . Damage initiates on the lower part of the beam and evolves along the load axis. We notice also that the damage evolution is non symmetric on the lower part of the beam. It is due to the aggregates skeleton which imposes a specific path for the damage and the macrocracks evolution. Figure 5-17 shows a comparison between numerical and experimental results on concrete at seven days. The difference from the two numerical curves comes from the initial time step (lower for the brown curve).

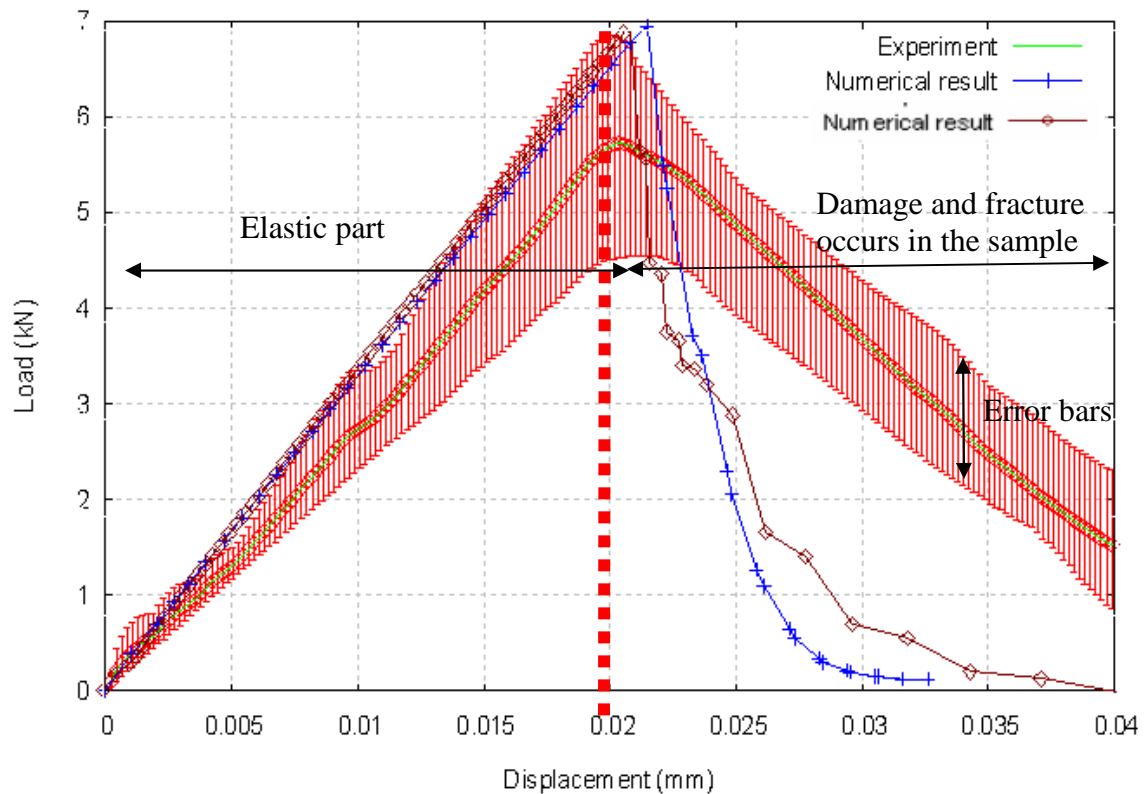


Figure 5-17. Load-displacement curve for the three point bending test on concrete

Figure 5-17 shows first a linear response up to the peak. Despite this linear aspect damage and cracks have already begun to propagate in the sample. **The numerical peak load is reached at 6.82 kN which corresponds to a principal maximal stress equal to 5.21 MPa. It is quite well correlated to the experimental one which is equal to 4.37 MPa.** After the peak, damage and cracks grow quickly in the sample. It is very difficult to obtain the same smooth part than the experimental result. However we notice that the decrease of the initial time step leads to a better description of the smooth part. Many reasons can explain this difference:

- We use the “Kill element” technique. We have shown in chapter 4 (see section 4.5.2) that this technique is mesh dependent and leads to a more abrupt post-peak part than in the experiment;
- We do not consider the frictional effects and the progressive energy dissipation due to contact between the tool and the sample;
- We do not take into account the heterogeneous aspect of the mortar paste which can also change the crack evolution;
- It is also important to notice the dispersion of the experimental results (see error bars in figure 5-17) more particularly in the smooth part. It underlines also the difficulty to obtain uniform results in the smooth part. Indeed the brittle behavior of mortar and its initial microcracks state can induce a macrocrack evolution more or less quickly. Furthermore the experimental data come from the displacement sensor under the load

axis (see chapter 4, section 4.4.3.2). As the crack starts from this location, we are not sure of the perfect measure of this system.

In this context, we have considered this model in good agreement with the experience as soon as the elastic stage has been well described and the maximum load has been reached. It underlines the great difficulty to identify material parameters in this stage.

## 5.4.4 Identification of the damage parameters of the mortar paste in compression

Now we identify material parameters in compression.

### 5.4.4.1. Model configuration

A compression test on this quasi-brittle material is performed. The dimensions of the cylinder are 160 mm diameter and 320 mm height. The contact between the tool and the sample is frictional. We use the Coulomb law with a Tresca limit with specific parameters corresponding to a low friction ( $\bar{m} = 0.4, \mu_F = 0.2$ ). Table 5-10 shows the particle size distribution.

Average diameter (mm)	22.5	18	14.25	11.25	9	7.15
Number of aggregates	40	294	502	428	604	1110

Table 5-10. Particle size distribution with 2978 aggregates.

Only aggregates with a diameter greater than 7 mm are plotted. Figure 5-18 shows the heterogeneous aspect of the concrete sample.

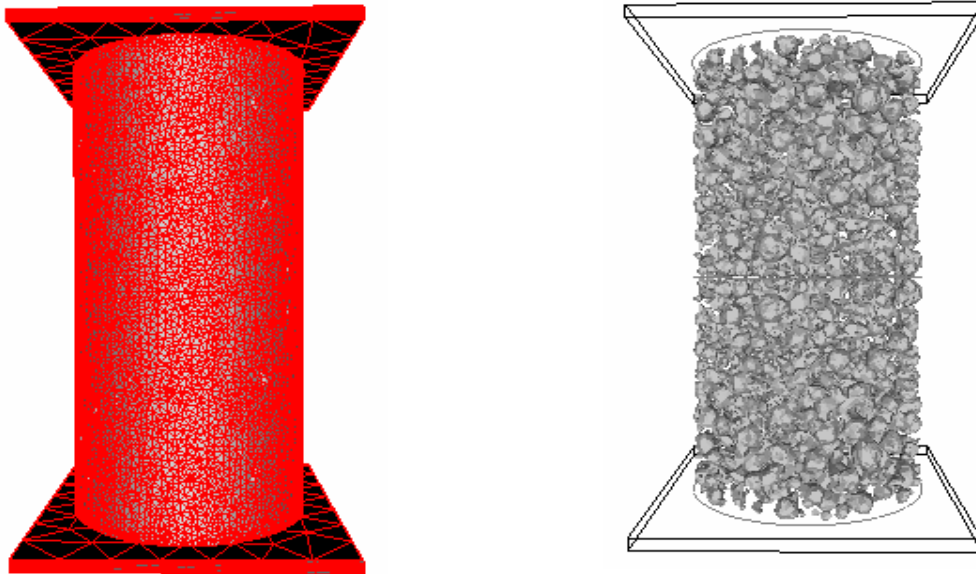


Figure 5-18. Heterogeneous aspect of the work piece; 46987 number of nodes; 250 033 number of elements.

### 5.4.4.2 Identification of parameters in compression

The identification of these parameters is made within the following range:

$$\begin{aligned} A_C &\in [0.7; 1.5] \\ B_C &\in [200; 2000] \\ \tilde{\varepsilon}_C^{Crit} &\in [5.9 \cdot 10^{-4}; 5 \cdot 10^{-3}] \end{aligned} \quad (5-7)$$

The best results obtained are the following:

$A_C$	$B_C$	$\tilde{\varepsilon}_C^{Crit}$
1.012	657.012	$8.7 \cdot 10^{-4}$

Table 5-11. Damage parameters in compression for the mortar paste.

These parameters are far from damage parameters identified on mortar. The  $B_C$  value is greater than the identified parameter on mortar. The  $\tilde{\varepsilon}_C^{Crit}$  value is lower than in mortar in order to initiate macrocracks sooner than in mortar.

### 5.4.4.3 Global response of the material

Figure 5-19 shows a comparison between numerical and experimental results on concrete at 7 days.

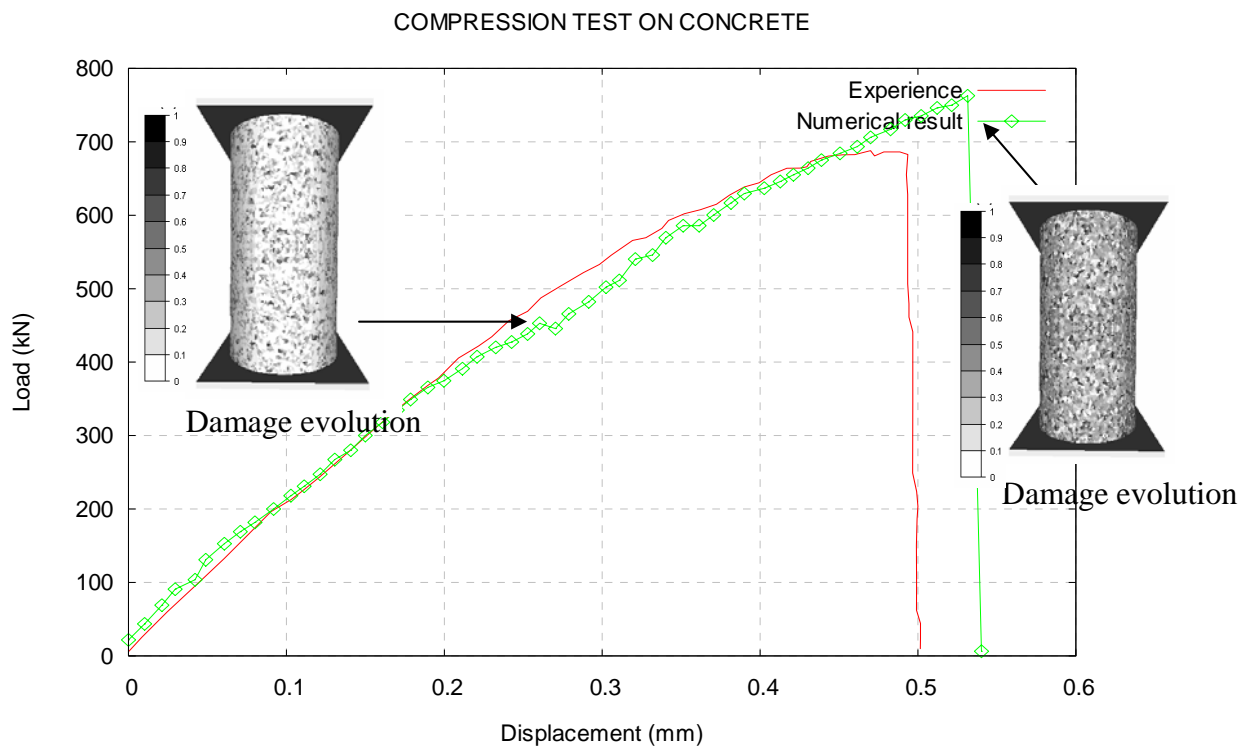


Figure 5-19. Load-displacement curve for the compression test

The CPU time for this simulation is about four hours. We first see a quasi linear response before the peak due to the fact that damage and macrocracks evolve slowly in the sample. At the end of the simulation, we observe a very fast drop of the load. It corresponds to the generation of many macrocracks in the sample. The numerical load reaches a value of 756.15 kN compared to an experimental maximum load of 686.3 kN. It corresponds to a numerical compressive strength  $\sigma_c$  equal to 37.6 MPa (34.13 MPa for the experimental one). The isovalues presented in figure 5-19 show the damage evolution (figure 5-19: white corresponds to damage equal to 0 and black corresponds to damage equal to 1). We notice that damage is homogeneous at the surface of the sample.

Figure 5-20 shows the macrocracks evolution in the sample through the Kill element technique.

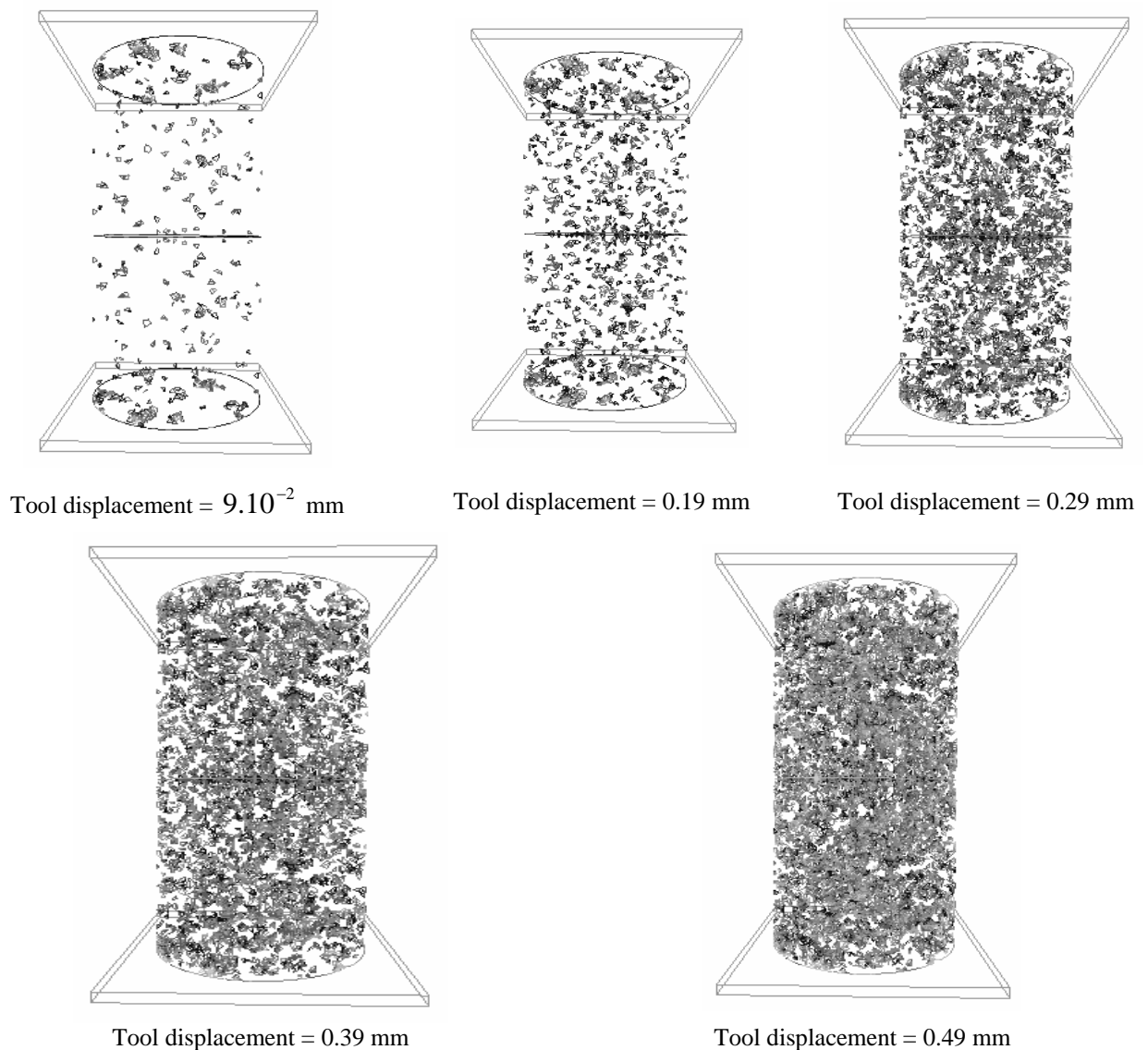


Figure 5-20. Macrocracks initiation and propagation in concrete.

We notice that the “killed” elements are initiated preferentially near to the contact with tools as the friction leads to more damage. Then they diffuse in the whole sample without a preferentially direction **due to a homogeneous repartition of the aggregates which induce local stresses**. It confirms the experiments as microcracks and voids are distributed homogeneously in the sample.

At the end of the simulation the number of “killed” elements is more important at the surface of the sample. However it is difficult to assimilate these “killed” elements with macrocracks as no privileged crack paths are identified. This homogeneous distribution is not observed in reality at the end of the simulation. We observe generally a failure surface develops at about 20 to 30° from the direction of the load (see figure 5-21).

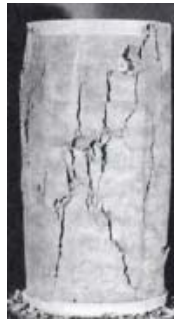


Figure 5-21. Typical failure of a concrete in compression. [Mehta et al. 1993]

In this way we consider that damage distribution is in good agreement with the experiment. Nevertheless the numerical model does not simulate correctly crack distribution. Many phenomena can explain this particular distribution:

- First the hypotheses made on concrete can explain it: we do not take into account a specific contact between aggregates and the mortar paste (it is considered as perfect). This contact needs to be modelled as it undoubtedly plays an important role on the crack pattern;
- Then we suppose the material has no damage at the beginning of the simulation which is not the case in reality. Heterogeneous materials may contain many potential fracture sites in a given volume. It should be important to consider:
  - o a statistical approach to consider aggregates with different elastic properties;
  - o a statistical and a **local approach** of the ITZ for each considered aggregate. Indeed the ITZ has a size which differs according the aggregate size and composition;
  - o a non-zero damage state at the beginning of the simulation to model initial microcracks and voids present in the sample.

#### 5.4.4.4 Local behavior of concrete

Figure 5-22 corresponds to the stress-strain relation by putting a numerical sensor at the surface of the sample. This process is discutable in the case of heterogeneous materials. It could be more appropriate to measure stress by using the load divided by the initial section in order to be independent on heterogeneities. However the goal here is to test the coherence between the local stress and the global load.

We notice that the maximal principal stress reached in compression is almost ten times higher than in tension. For the compression test, the local maximal principal stress is here evaluated to  $\sigma_1 = 37.6$  MPa compared to 32.9 MPa obtained on the global load-displacement curve (see section 5.4.4.3) and to 32.56 MPa obtained experimentally (see figure 5-19). In tension the maximal principal stress is evaluated to  $\sigma_1 = 4.86$  MPa in figure 5-17 and it corresponds also to the value of experimental peak stress established in chapter 4 where it was equal to 4.37 MPa.

Moreover the damage threshold in tension corresponds to  $\tilde{\epsilon} = 1.46 \cdot 10^{-4}$ . In compression this damage threshold corresponds to  $\tilde{\epsilon} = 1.46 \cdot 10^{-3}$  which is exactly ten times higher than the damage threshold in tension. This gap is very typical of the difference of behavior in compression and in tension.

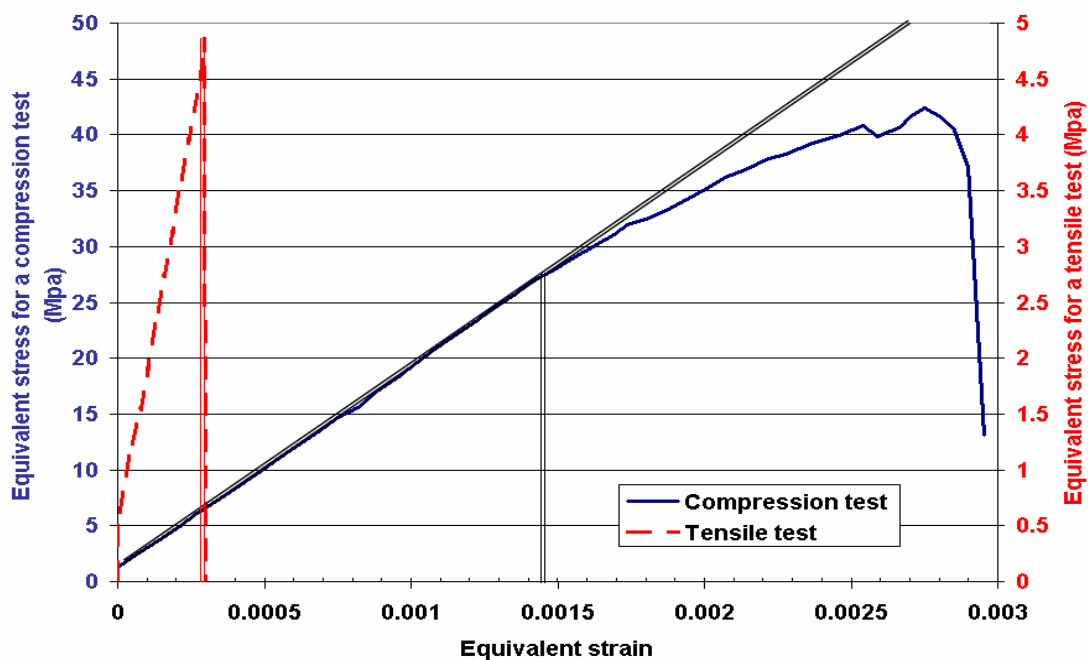


Figure 5-22. Stress-strain curves in a concrete sample under a compression test or a tensile test.

#### 5.4.4.5 Comparison between the mechanical behavior of mortar and of the mortar paste (of concrete)

We test now the material parameters we have obtained with the second approach. We use it to simulate a compression test on a homogeneous material. We compare thus these numerical results with experimental results obtained on mortar to the mechanical behavior of the mortar paste (of concrete).

Figure 5-23 shows the stress-strain curves of mortar and of the mortar paste (of concrete). The numerical stress is evaluated by computing the load divided by the initial section. It underlines that damage evolves more slowly in mortar and the reached strength is greater. Macrocracks are initiated sooner in the mortar paste as the macrocrack threshold is lower than for mortar only. It stresses hence that the numerical mechanical behavior of the mortar paste (of concrete) takes into account the cement paste, the ITZ and the contact

between the aggregates and the matrix with possible decohesions, voids, initial microcracks through its material parameters. It shows once again that mortar and the mortar paste of concrete have two distinct mechanical behaviors.

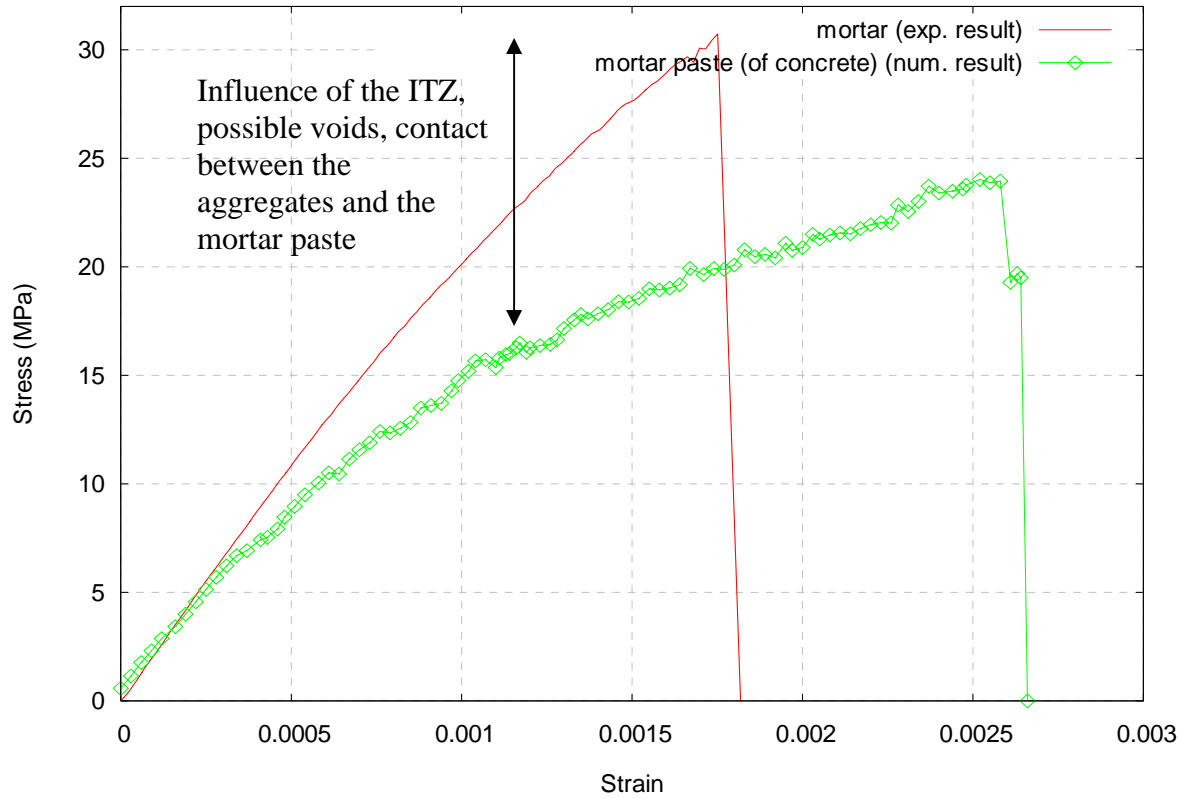


Figure 5-23. Stress-strain curves to compare the mechanical behavior of the mortar paste (of concrete) with mortar only.

The identification of concrete parameters has been directly performed on concrete. It enables to take into account the ITZ and the contact through the mechanical behavior of the mortar paste. It has led to the following parameters (see table 5-12).

Material Parameters	$E_{MP}^C$ (GPA)	$E_A^C$ (GPA)	$\nu$	$\varepsilon_{D0}$	$A_T$
	18.69	70	0.2	$9.1 \cdot 10^{-5}$	1.18
Material Parameters	$B_T$	$A_C$	$B_C$	$\tilde{\varepsilon}_T^{Crit}$	$\tilde{\varepsilon}_C^{Crit}$
	50 000	1.01	657.08	$1.63 \cdot 10^{-4}$	$8.72 \cdot 10^{-4}$

Table 5-12. Identification of damage parameters on concrete.

We have also underlined the difference of mechanical behavior between mortar and the mortar paste.

## 5.5 Application to the “Brazilian” splitting test

Now we have identified damage parameters on tension and on compression on concrete, we test the numerical model on the “Brazilian” splitting test and compare it to experimental stress-strain curves.

Due to the difficulty in applying direct tension to concrete, the split cylinder tensile test has gained with popularity. A 16×32 cm cylinder is diametrically loaded in compression between two plates. The contact is correctly taken into account with the use of two fine rods out of timber put between the plates and the cylinder. This test is very important to validate our numerical model. Indeed we use the parameters we have identified in tension and in compression (through compression and three point bending tests), and we use it to test the “Brazilian” splitting test.

For this test, the particle size distribution is the same than for the compression test as we use the same volume. Figure 5-24 shows the geometry and the mesh used for this simulation. We suppose a bilateral contact between the tool and the sample. The parallelepipedic part of the cylinder in contact with the upper and the lower tool enables a better contact. *Each of these parts of the sample is modelled with an elastic behavior whereas the rest of the sample has an elastic damage behavior.* It can be considered as the rods out of timber which are used in the experiments.

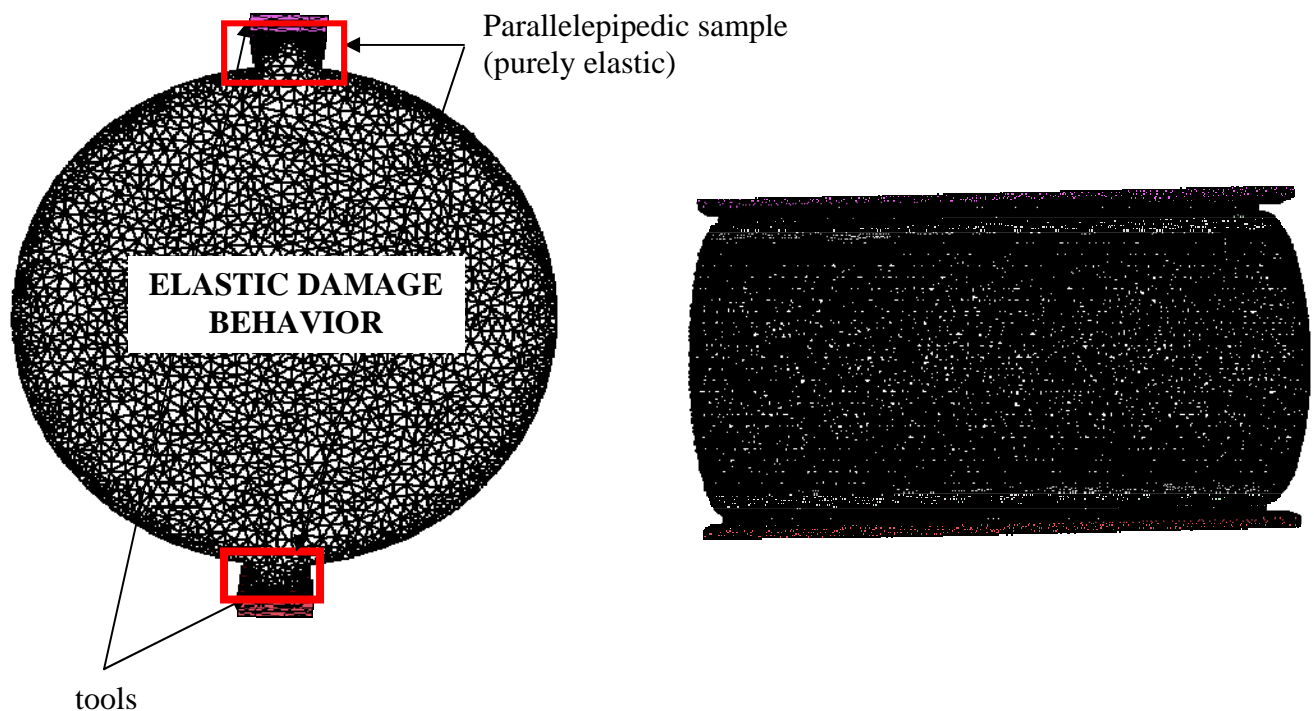


Figure 5-24. Geometry of the "Brazilian Splitting test", 139 130 nodes, 741 829 elements.

Figure 5-25 shows the granular skeleton in the cylindrical sample.

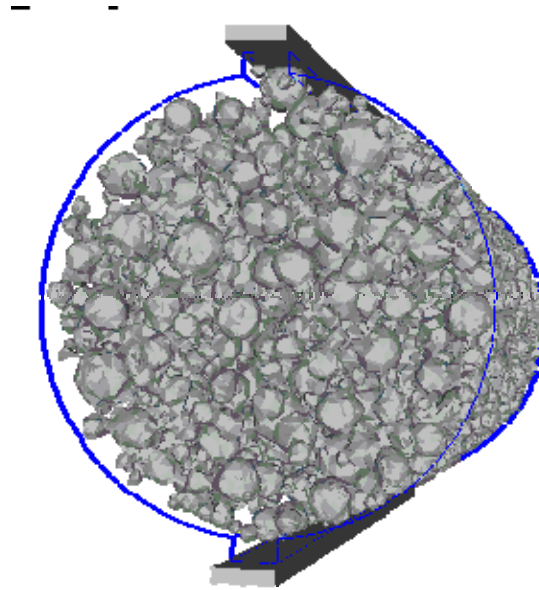


Figure 5-25. repartition of the aggregates in the sample.

According to the elasticity theory, this loading produces a nearly uniform maximum principal tensile stress along the diameter, which causes the cylinder to fail by splitting (figure 5-26). The numerical simulation confirms it as we notice stress in compression near the tools, and positive stress along the vertical axis.

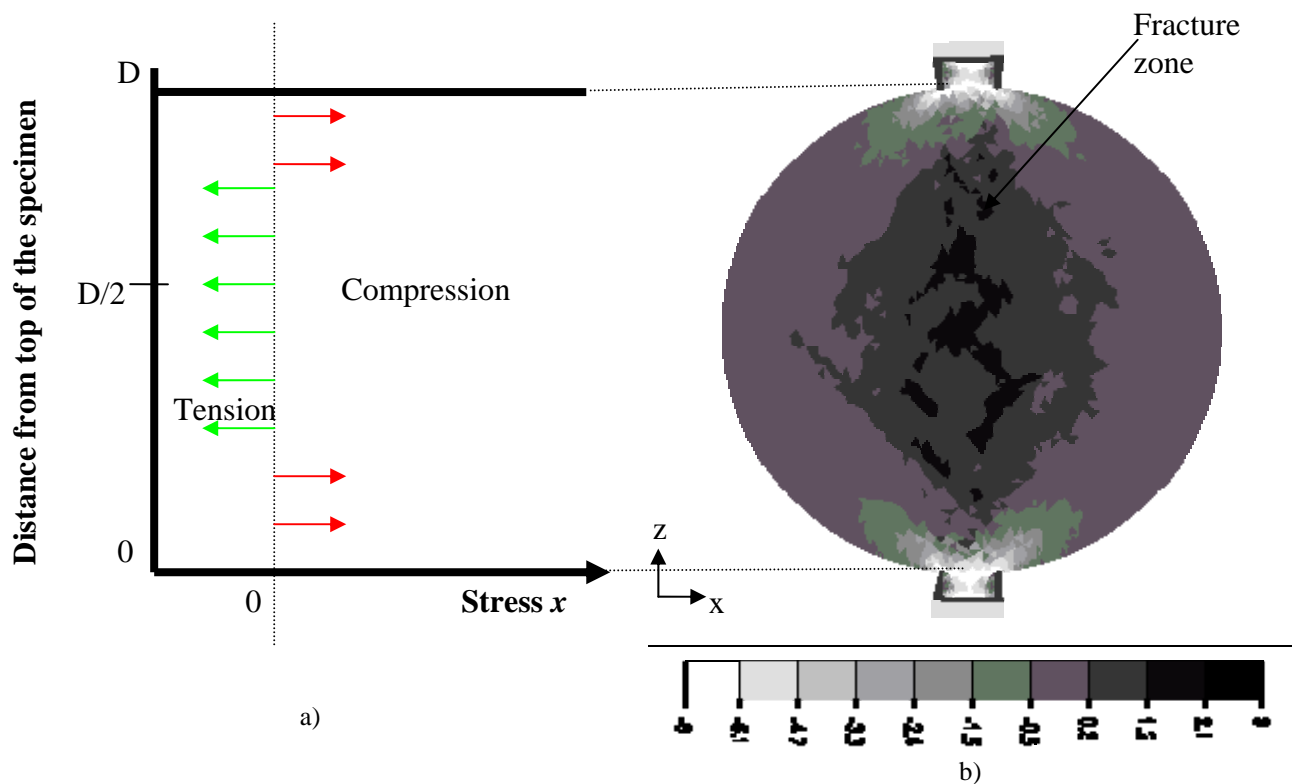


Figure 5-26. a) Determination of the tensile strenght of concrete with the "Brazilian" test; b) Distribution of the stress  $x$  on the numerical test.

For this simulation we do not use the “Kill Element” method which can lead to some numerical problems. We use the damage parameter identified in compression and in tension. Figure 5-27 shows the damage state in the volume.

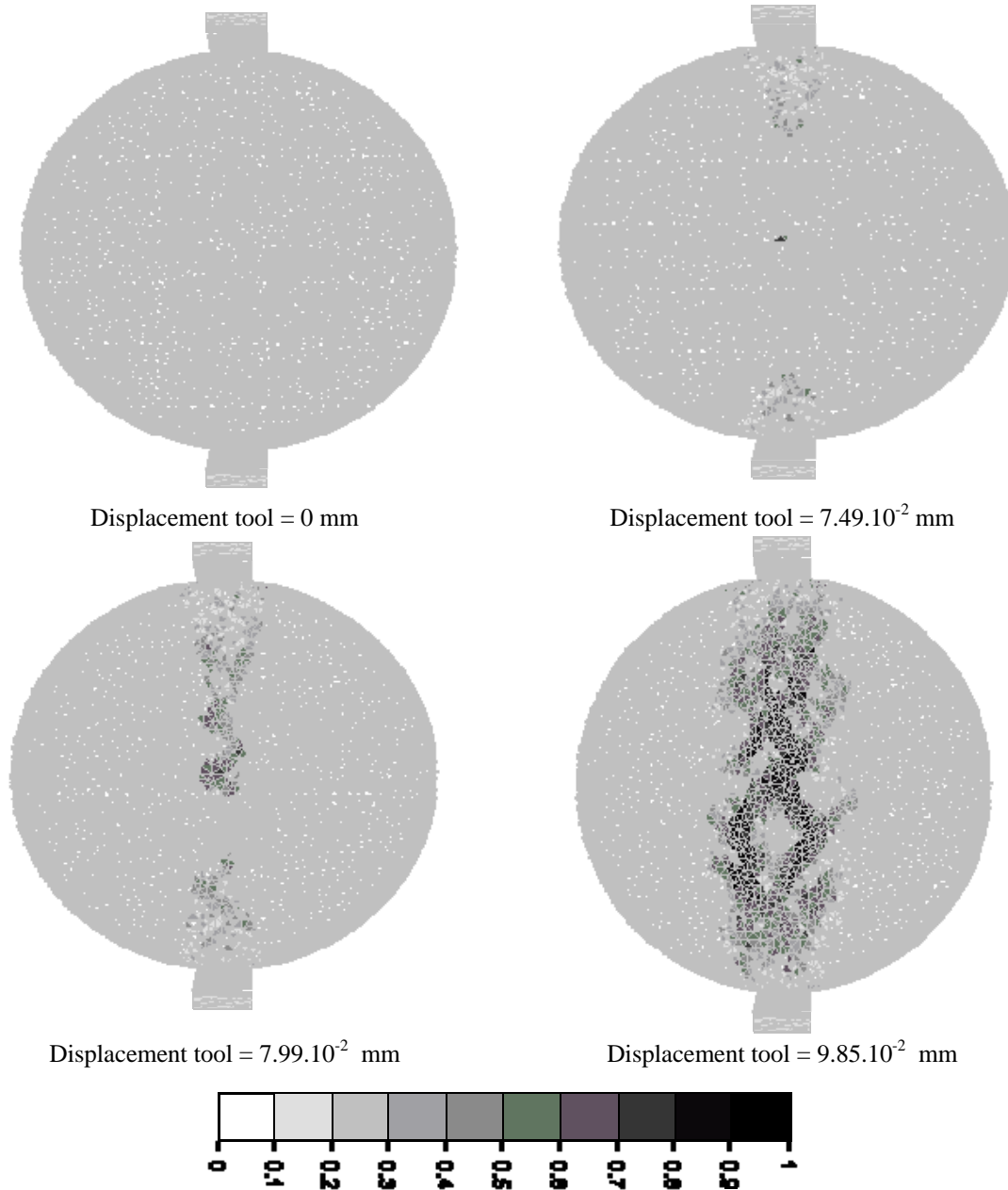


Figure 5-27. Damage evolution for the "Brazilian" Splitting test.

We notice that damage is not initiated at the centre of the cylinder but at some distance of the centre. It confirms results obtained in 2D by Saouridis [Saouridis 1988]. Then the damage reaches a critical value at the centre of the sample and generates cracks along the load axis. The evaluation of the general displacement, based on data given strain gauges, is complex as it includes the geometry of the sample, the complex boundary conditions etc. In this way, we prefer to use directly the stress-strain relation. The theoretical relationship between the load peak  $F_{\max}$  and the maximal principal stress  $\sigma_1$  is obtained as following:

$$\sigma_1 = \frac{F_{\max}}{\pi \cdot b \cdot R} \quad (5-8)$$

Where  $b$  is the depth of the sample and  $R$  is the radius of the cylinder. The experiment leads to  $\sigma_1 = 2.73$  MPa. Figure 5-28 presents the stress-strain curve based on the mean of some points placed at the centre of the sample. The maximal principal stress reached is equal to 2.33 MPa. It represents a gap of 15%. We notice a good correlation of the two curves in the post-peak part. This one was difficult to obtain with simulations on three point bending tests. It confirms that the measure system used (with a displacement sensor under the load axis of the three point bending test) is questionable.

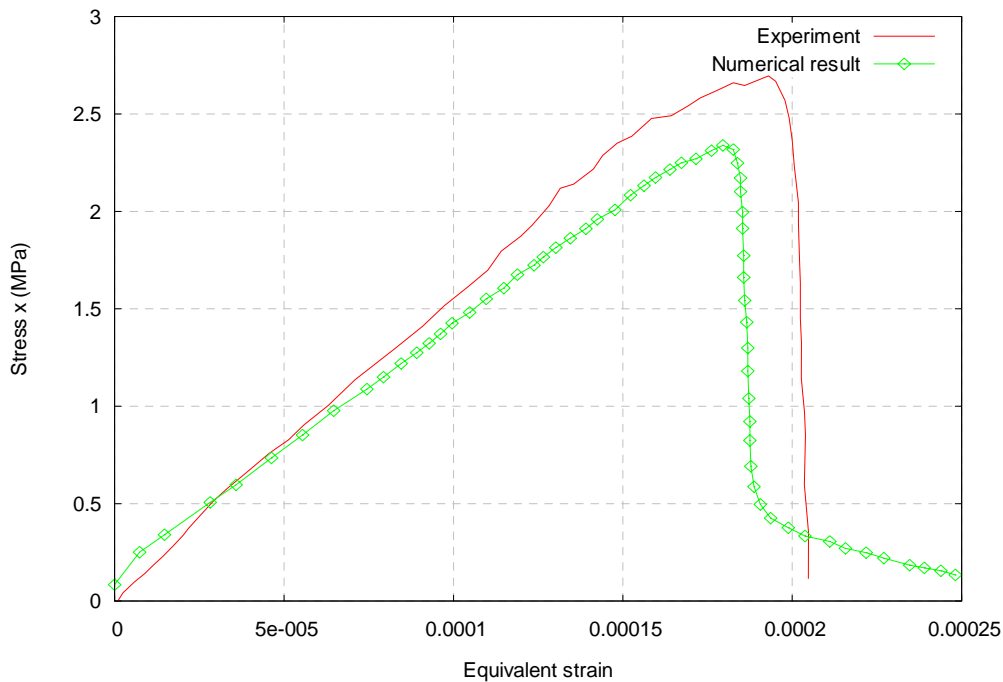


Figure 5-28. Stress-strain curve for the "Brazilian" splitting test.

The good correlation between the numerical and experimental curves permits to validate our numerical model.

## 5.6 Sensitivity analysis on aggregates parameters

Aggregates (coarse, fine grains and sand) represent 80% of the total volume of concrete. Their characteristics affect the performance of concrete. Aggregate characteristics of **shape, texture, maximum size, number, mineralogy and coating, absorption and grading** influence workability, finishability, bleeding, pumpability and segregation of concrete and affect strength, stiffness, shrinkage, creep, density, permeability, and durability of hardened concrete. An optimal mixture proportioning will produce good-quality concrete with a minimum amount of cement.

Here the main objectives of this study is to test the influence of the distribution of aggregates and the influence of the particle size distribution on the mechanical behavior for concrete when we consider concrete as a biphasic material. The numerical test is performed

with the material parameters, we have identified on concrete. We use again the non local Mazars model with an implicit gradient formulation ( $\tilde{c} = 15 \text{ mm}^2$ ).

### 5.6.1 Influence of the aggregates distribution

We test first the influence of the aggregates distribution on the global response of the material. Three concrete samples are submitted to a three point bending test. The model is configured as described in section 5.4.2.1. Figure 5-29 shows the load-displacement curves corresponding to three different randomly repartition of aggregates. We notice that aggregates distribution does not really influence load-displacement curves. It means that all results we have obtained in this work can be generalized to all concrete samples with the same formulation.

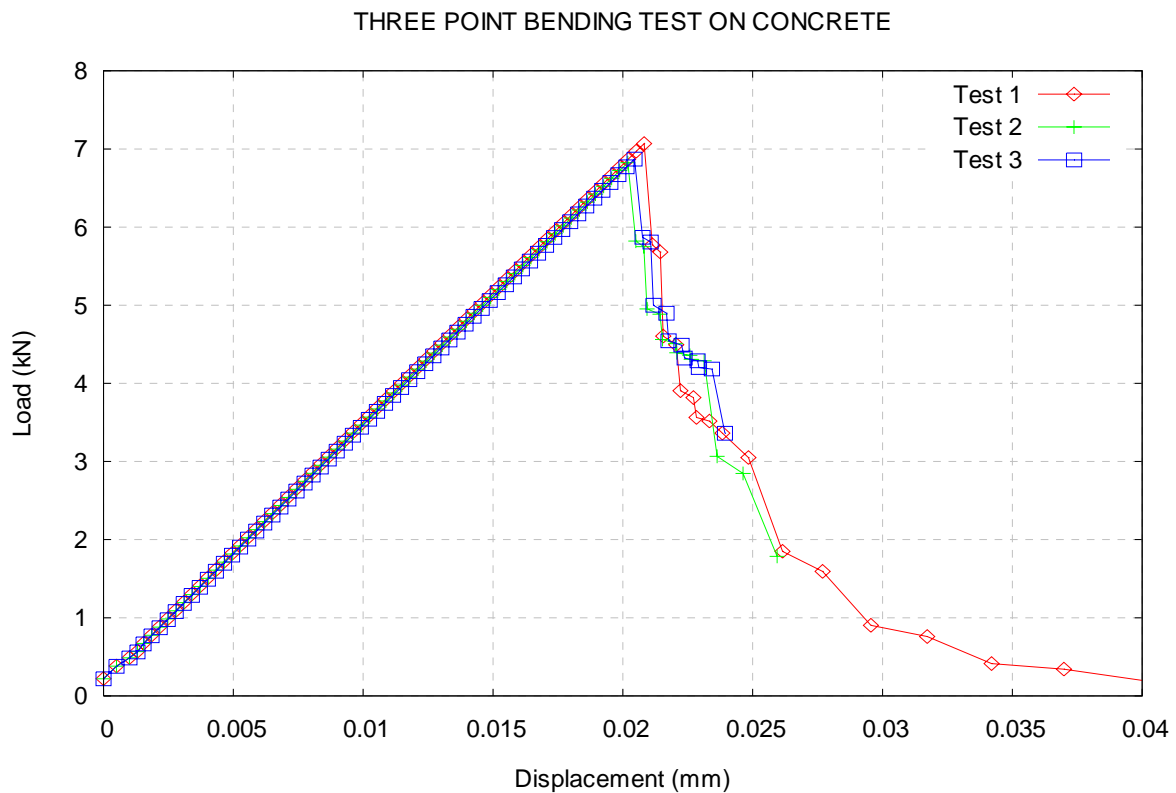


Figure 5-29. Load-displacement curves with different aggregates repartition.

## 5.6.2 Influence of the volume of aggregates

Erntroy and Shacklock [Erntroy et al. 1955] have correlated the increase of the strength to the increase of aggregates volume for standard concrete. Stock and coworkers [Stock et al. 1979] have deduced from experimental data that:

“- The addition of 20% by volume of graded aggregate to a cement paste leads to a reduced tensile strength, which remains unchanged at 40%, but increases significantly with further additions of aggregate to 60% and 80%.

-The addition of 20% by volume of graded aggregate to a cement paste also reduces the compressive strength, which remains sensibly constant up to 60% and then increases significantly.”

The reason may be found in a perturbation of the structure of the linking phase as the aggregate concentration increases (porosity increases and reduces the Young modulus). Figure 5-30 shows these relationships in compression and in tension. The free W/C ratio chosen was 0.5. The maximal aggregate diameter is of 19 mm size. The aggregates keep the same diameter for each test but their quantities increase. Compressive strengths were measured on cylindrical specimens (100 mm diameter by 300 mm long) and uniaxial tensile strength was measured by using the friction grip system on waisted specimens [Johnston 1968].

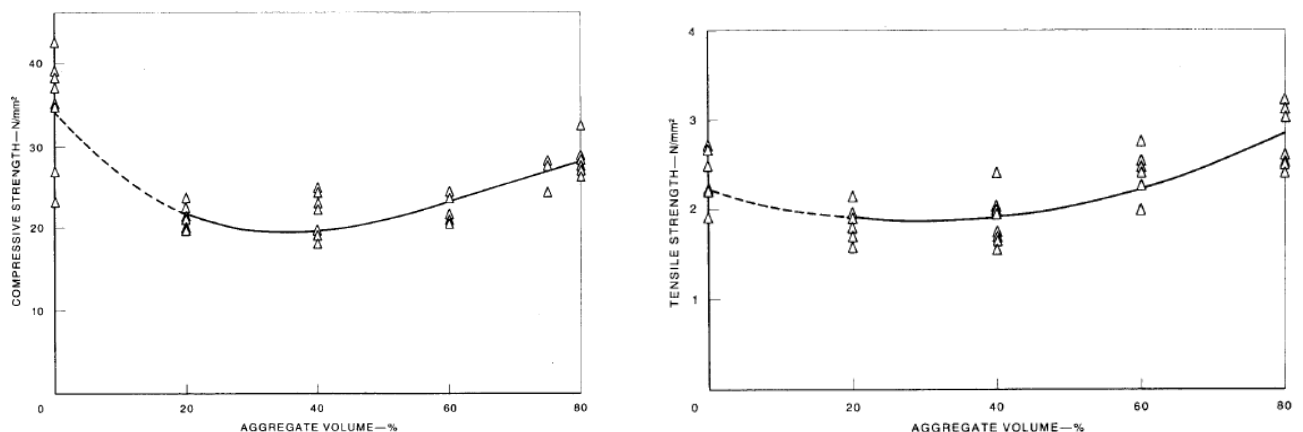


Figure 5-30. Relationship between compressive (left) / tensile (right) strength and aggregate volume from experimental test results. [Stock 1979]

Figure 5-30 shows that the relationship between the compressive and tensile strength varies no uniformly in function of the aggregate volume. The higher variability with cement paste is attributed to the difficulty of testing fine-grained material and the difficulty to control fracture in tension tests in spite of the waists formed in the specimen.

We test the influence of the volume of (coarse) aggregates generated on the compression strength. We use the same model configuration than in section 5.4.4.1. The material parameters are those we have identified (see table 5-12). Different meshes have been used to generate the granular skeleton. The more there are aggregates to generate, the finer is the mesh.

Table 5-13 shows the particle size distribution used for each distribution. At the end of the table, the volume of coarse aggregates generated in the sample is evaluated. Special

attention will be made to not confuse this last value with the aggregate volume presented in figure 5-30. To compare our numerical results with results obtained by Stock and coworkers, we have to add aggregates, with a diameter between 4 and 7.15 mm and sand.

In this way, we have already presented the concrete formulation (see chapter 4, section 4.4.2). It gives the sand content (20.8%) in a concrete sample. The volume of aggregates with a diameter between 4 and 7.15 mm corresponds to approximately 23%. So we have to add these two percents to obtain the whole aggregate volume and to compare compressive strength versus each whole aggregate skeleton.

<i>Average diameter (mm)</i>	<i>Number of aggregates</i>				
22.5	40	40	40	40	
18		294	294	294	
14.25		502	502	502	
11.25				428	428
9					604
7.15				1110	
<i>TOTAL</i>	40	836	1264	2978	
<i>Theoretical Volume <math>V_T</math> of aggregates generated (<math>cm^3</math>)</i>	238.5	1 896.9	2 215.9	2 658.9	
<i>Real Volume <math>V_R</math> of coarse aggregates generated in FEMCAM (<math>cm^3</math>)</i>	249.5	1897.2	2216.2	2659.2	
$\frac{ V_T - V_R }{V_T} (\%)$	4.6	0.018	0.013	0.011	
<i>Real coarse aggregate volume (%) in the sample</i>	3.87	29.4	34.44	41.3	
<i>Real aggregate volume (%) in the sample (coarse aggregates, fine aggregates and sand)</i>	47.8	73.46	78.4	85.3	

Table 5-13. Particle size distribution.

The (coarse) aggregate volume varies in fact from 3.5 to 40 % (corresponding to 2978 aggregates) which corresponds at the end to a standard concrete. We compare the strength evolution versus the cumulative volume aggregates. Figure 5-31 shows the linearity between the maximal load evolution and the volume of generated aggregates. It leads to the following deduction: **the strength is directly linked to the volume of aggregates in the sample for our numerical model** for an aggregate volume between 40 and 90%.

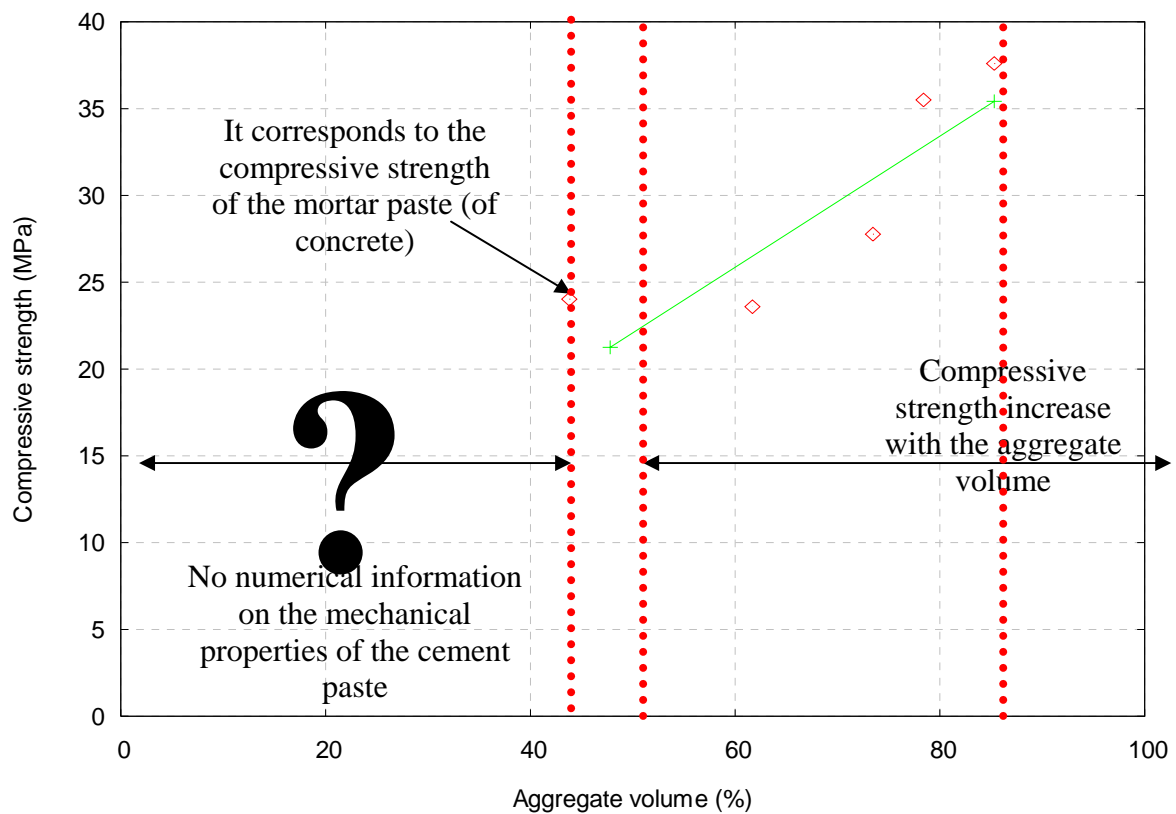


Figure 5-31. Evolution of the maximum load reached in function of the number of aggregates in the sample

For a volume of aggregates between 0 and 40%, Stock and coworkers observe a decrease of the compressive strength. It means that the more there are aggregates in the sample, the lower the mechanical properties of the mortar paste (creation of voids and microcracks in the mortar paste) [Wittmann 1993]. This is of course an indication that the volume of generated aggregates influences indirectly the maximal compressive strength. In this set of range, our numerical model is not able to give information as we consider only aggregates larger than a minimal diameter (7.5 mm here). But even if our 3D numerical model would be able to take into account fine aggregates and sand, a difference would be also observed. Indeed it comes from a major difference: by including more aggregates experimentally, the mechanical properties of the mortar paste are modified (creation of voids and microcracks, more ITZ around aggregates etc.). On the contrary the add of more aggregates in our numerical model cannot modify the initial mechanical properties of the mortar paste.

Beyond a critical aggregate concentration, properties depend on concentration. This conclusion is in good agreement with the results obtained by Stock (see figure 5-30). The rigidity given by the aggregates are more important than the mortar paste behavior and then the maximal compressive strength increases. The aggregates avoid macrocracks propagation. Hence the maximal strength and the durability of concrete are greater. **It confirms the importance to identify the mechanical properties of the mortar paste for a specific formulation of concrete in our numerical model. It underlines thus that the identification of the mortar paste depends on the aggregate size distribution.**

### 5.6.3 Influence of the maximal diameter of aggregates

Some studies have been carried out on the effect of the maximal diameter of aggregates to show the existence of an optimal maximal diameter to improve the compressive strength. The maximum size of aggregate influences workability, strength, shrinkage, and permeability. Mixtures with large maximum size of coarse aggregate tend to produce concrete with better workability, probably because of the decrease in specific surface [Washa 1998].

Cordon and coworkers [Cordon et al. 1963] have tested a change in the maximum size of a given aggregate volume. Experimentally they show that the increase of the maximal aggregate diameter has a negative impact on the compressive strength for low water to cement ratio (W/C).

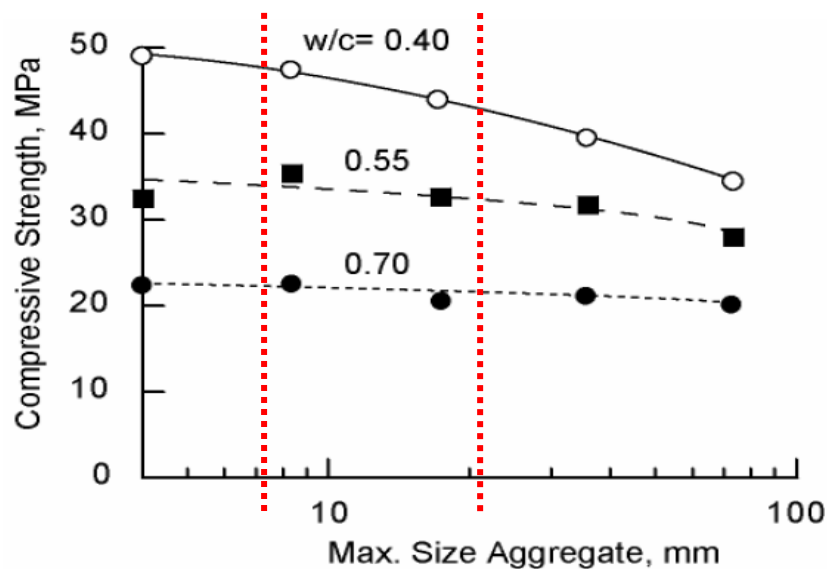


Figure 5-32. Evolution of the compressive strength in function of the maximum size of aggregate.

[Cordon et al. 1963]

We also notice in figure 5-32 that the compressive strength is linked to the W/C ratio. This relationship has been represented by the Abram rule as follows:

$$\sigma_c = \frac{k_1}{k_2^{w/c}} \quad (5-9)$$

In which  $k_1$  and  $k_2$  are empirical constants. Several reasons explain the link between the strength decrease with the maximal diameter:

- The bigger is the aggregate, the more the stress concentration is important around the considered aggregate and so, the more damage evolves quickly and reduces strength;
- The ITZ has a size which is different according to the aggregate size. The increase of the aggregates diameter engenders a greater zone of weakness which induces a lower compression strength.

Now we test the numerical influence of the dimensions of the aggregates on the load-displacement curves for a compression test. Table 5-14 shows the number of aggregates to generate for each diameter to reach the same volume in aggregates (about 381.7 cm<sup>3</sup>). If we consider the volume of generated aggregates, the maximal difference of volume is equal to 1.6%.

<i>Average diameter (mm)</i>	22.5	11.25	7.125
<i>Number of aggregates</i>	64	506	2000
<i>V<sub>R</sub> (mm<sup>3</sup>)</i>	383.8	377.57	378.7

Table 5-14. Particle size distribution for the same volume of generated aggregates.

The particle size distribution corresponds to the following repartition (figure 5-33).

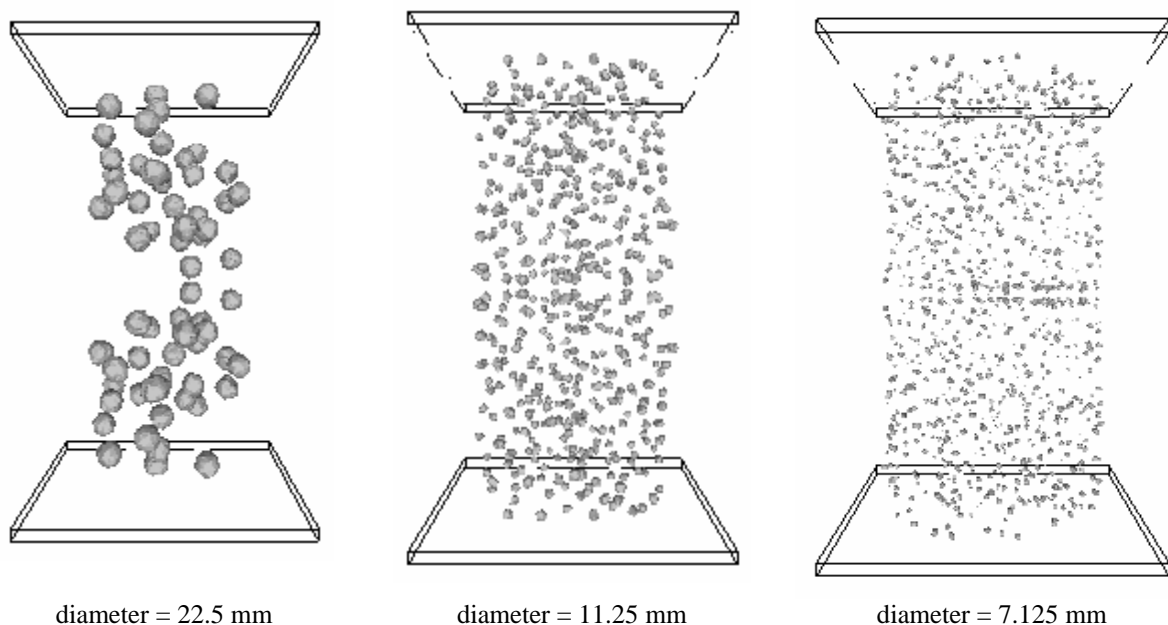


Figure 5-33. Repartition of different granular skeleton in a concrete sample.

We study the evolution of the global strength (load divided by the initial section) curve for each case.

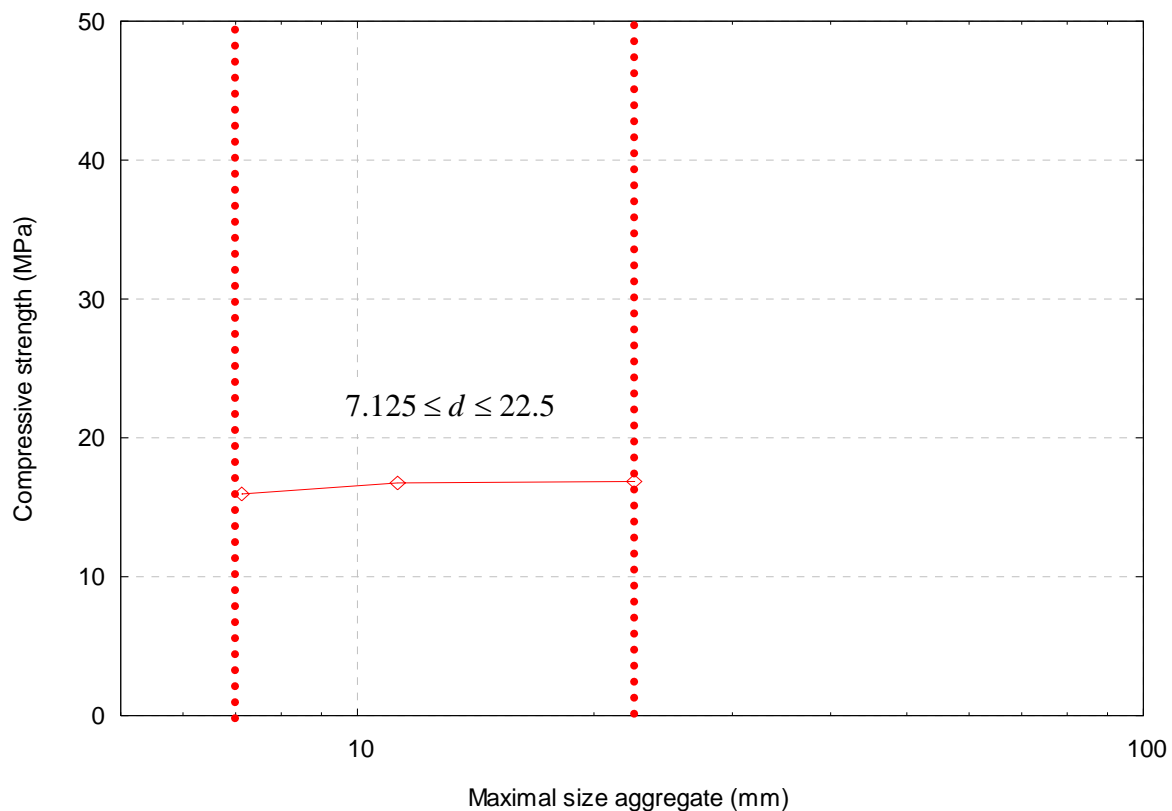


Figure 5-34. Load-displacement curves on concrete with different formulations submitted to a compression test

Figure 5-34 shows that for diameter, between 7 and 22.5 mm, the aggregate size has no effect on strength. It goes in the same way than figure 5-32 where the strength is much more influenced by the W/C ratio than by the maximal aggregate. The numerical response shows that the mechanical generated damage is equivalent for several fine aggregates and for some coarse aggregates. One hypothesis can be formulated to explain why we do not observe any change. The maximal aggregate size should influence a modification in the mechanical properties of the mortar paste. It should induce hence a modification in damage evolution. Here we have used the same material properties than identified before with a classical concrete (where the grain size comes from 7 mm to 22.5 mm). So we have not considered a modification of the material properties of the ITZ (it becomes larger with larger grains)! As these mechanical properties modifications are not taken into account in our simulations, this phenomenon does not appear in the numerical load-displacement curves.

The impossibility of our numerical model to consider a local representation of the ITZ (and so specific material parameters of the ITZ for each aggregate size) would require an identification of the material parameters for each of the three tests presented in figure 5-33).

However this deduction has to be balanced with the fact that when the diameters of the aggregates increase, less aggregates are in the sample and then the ITZ volume decreases!

The sensitivity study on the influence of aggregates has shown:

- The distribution of the aggregates has no influence on the global response of the material;
- The compressive strength increases linearly with the aggregates volume. In the numerical test, we do not detect a possible decrease of the maximal compressive strength. Our numerical model do not consider a modification of the mechanical properties of the mortar paste with the introduction of aggregates. The mechanical behavior of the mortar paste is thus dependent on the number of aggregates in the sample;
- The aggregate diameter has no influence on the global response when it is between 7.15 and 22.5 mm.

## 5.7 Conclusions

The experimental campaign, we have carried out, lead to the identification of material parameters. We have used in this study experimental mechanical properties of concrete given after seven days. The evolution algorithm has been used to identify automatically the elastic and damage parameters.

We have shown that the mortar paste of concrete cannot be identified with a study on mortar. Indeed, even if the mortar paste has the same formulation than mortar, the microcracks and voids generated by aggregates during the hardening of concrete, leads to different mechanical behaviors between the mortar paste and mortar. In a good set of range, admissible results have been found. We have also noticed the great difficulty to describe the post crack stage of load-displacement curves. Some hypotheses have been formulated to explain this difference. We have validated the model on a “Brazilian” splitting test by using the identified parameters on tension and on compression.

Moreover we have tested the effect of the grain size distribution on load-displacement curves. One conclusion emerges: the diameters and the number of grains for a constant volume of aggregates do not influence clearly the global response of the material. Hence we have noticed that for an elastic damage model at a mesoscopic scale, the volume of aggregates is the only parameter which influences the global response of the material. The model needs to be improved to take into account mechanical modifications of the ITZ in function of the grain size generated. Another interesting study would be to evaluate the effect of the aggregate grading on the concrete strength.

We can now use these material parameters in a concrete sample submitted to ASR. The aim is to check some relations between experimental results and numerical ones.

## **CHAPTER 6 : MODELLING OF THE MECHANICAL EFFECTS OF THE ASR**

6.1 INTRODUCTION .....	6-133
6.2 DESCRIPTION OF THE MODEL PROPOSED BY THE CIVIL ENGINEERING DEPARTMENT OF THE ECOLE DES MINES DE DOUAI .....	6-134
6.3 THE SELECTED MODEL IN FEMCAM .....	6-138
6.3.1 <i>The chemical-elastic problem for reactive aggregates</i> .....	6-138
6.3.2 <i>Expression of the pressure induced by the chemical reaction</i> .....	6-139
6.3.3 <i>Remark on the resolution of the whole mechanical problem</i> .....	6-140
6.4 MODELLING OF THE CONSEQUENCES OF THE ASR AFTER SEVEN DAYS .....	6-141
6.4.1 <i>Experimental data</i> .....	6-141
6.4.2 <i>Numerical data</i> .....	6-143
6.4.3 <i>Mechanical consequences of the ASR</i> .....	6-143
6.4.3.1 <i>Experiment versus numerical results</i> .....	6-144
6.4.3.2 <i>Influence of the inert aggregates</i> .....	6-151
6.4.3.3 <i>Influence of the number and the sizes of reactive aggregates</i> .....	6-153
6.5 CONCLUSIONS .....	6-155

## 6.1 Introduction

ASR is a chemical reaction between certain types of aggregates and hydroxyl ions ( $\text{OH}^-$ ) associated with alkalis in the cement. Usually, the alkalis come from the portland cement but they may also come from other ingredients in the concrete (mixing water, adjuvant etc.) or from the environment. Figure 6-1 shows an example of a thin-section cut of ASR damaged concrete.

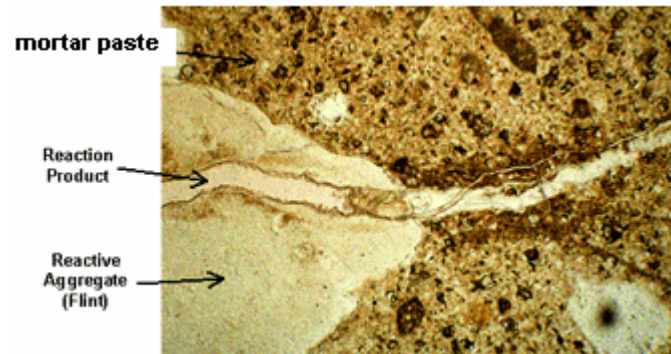


Figure 6-1. Thin-Section cut of ASR-damaged concrete showing ASR gel (through aggregate). [TFHRC 2003]

**This chapter aims at modelling the mechanical effects of the ASR in concrete.** Such a reaction is difficult to model accurately because of the complexity of the reaction: random localisation of the reactive sites, imperfect knowledge of the reaction mechanisms etc. The ASR can be described at two levels:

- *The modelling at a microscale* is interesting since the chemical reaction mechanism is local. A direct correlation can be made to study the consequences of the material swelling on the microstructures. These models are based on the description of the chemical kinetic of the reactions. They try to take into account all the chemical process of the ASR (transport mechanism of the different chemical species and kinetic). But they do not treat the mechanical consequences of the ASR. We can quote the work of **Furuzawa** [Furuzawa et al. 1994], **Xi and coworkers** [Xi et al. 1999], **Capra and Sellier** [Sellier 1995].
- *The modelling at a meso and a macro level* does not take into account chemical aspects of the reactions and model its mechanical consequences (damage, cracks) on the structure. They include parameters as temperature, ambient humidity, the reactivity potentiality of the aggregate and the imposed stress. We can quote the work of **Chatterji and Christensen** [Chatterji et al. 1990], **Capra and Sellier** [Sellier et al. 1997], **Larive and Coussy** [Larive et al. 1996] who have developed more or less complex models. The Larive model describes with a quite good accuracy the volume swelling of the aggregates. However this model depends on three new parameters to identify.

All these models suffer from the lack of a physical link between the chemical aspects of the reaction (microscale approach) and its mechanical consequences at a mesoscale. Another type of approach has hence been developed by the Ecole des Mines de Douai (GC-

Douai). This approach models the mechanical consequences of the ASR (damage, cracks) based on a chemical study. We will first present this model.

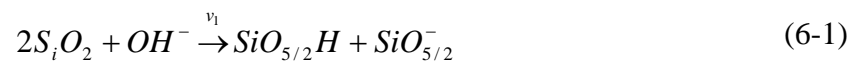
The second part is devoted to the implementation of this swelling model in FEMCAM. We detail herein the equations used to describe the ASR in the FE model.

The last part concerns a comparison between experimental results and the response of the numerical model. We use a 3D multi material modelling with material parameters identified in chapter 5. The grain size distribution used in the numerical model corresponds to the concrete formulation used by Dehaut [Dehaut 2002] already presented in chapter 4. The objective is to check the effect of the aggregates swelling on the global sample swelling. We test also the influence of the diameters and the number of reactive aggregates on the global swelling of the sample. Finally we conclude on the responses given by the model to better understand the mechanical effects of the ASR. Furthermore we underline the way to improve our model and obtain a more accurate description of this chemical reaction.

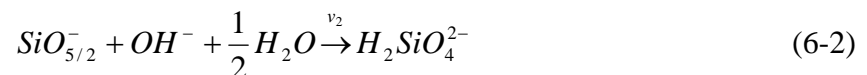
## 6.2 Description of the model proposed by the Civil Engineering Department of the Ecole des Mines de Douai

The mechanisms of the reaction have been described by various authors (Dent Glasser and Kataoka, Poole, Chatterji et al., Bulteel et al.) [Dent-Glasser et al. 1981] and an extensive literature review is given by Dehaut [Dehaut 2002]. This knowledge is essential to know the exact role of all the components of concrete in the ASR. For most authors, the ASR process is divided into two main steps:

- This first stage corresponds to the formation of  $SiO_{5/2}^-$ , with the hydrolysis of the reactive silica by  $OH^-$  to form an alkali-silica gel as indicated in Eq. ( 6-1).  $v_1$  denotes the reaction velocity.



- This second stage corresponds to the dissolution of silica by the absorption of water (see Eq. ( 6-2)).  $v_2$  denotes the reaction velocity.



Afterwards precipitation of silicate ions  $H_2SiO_4^{2-}$  (also called  $Q_0$  tetrahedrons) by the cations of the pore solution of concrete leads to the formation of C-S-H and/or C-N-S-H phases.

**Many divergences appear concerning the role of each component in the swelling mechanism.** Many approaches consider that the swelling mechanism is mainly due to the creation of C-S-H and/or C-N-S-H phases, i.e. the second stage (see Eq. ( 6-2)) of the chemical reaction is expansive. It is thus generally assumed that there exists a porous zone around the aggregates and that the expansion is initiated only when the volume of the reaction exceeds the volume of the porous zone (see figure 6-2).

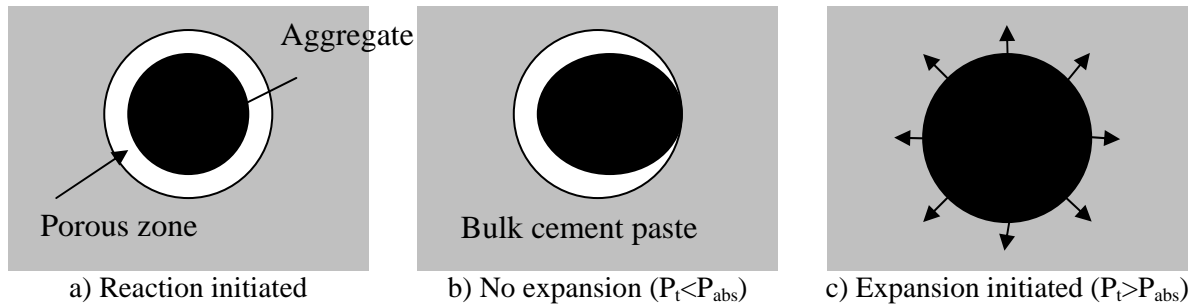


Figure 6-2. Schematic representation of an absorbing zone around the aggregate and its effect on delayed expansion initiation. [Furuzawa et al. 1994]

We know now that the two stages of the chemical reaction are at the origin of the sample swelling (see [Dehaut 2002] for more details). In this way the degradation of the aggregates submitted to the ASR has been demonstrated. However these phenomena have not been yet quantified.

For some years, the ASR belongs to the main research field of the Civil Engineering Laboratory of the Ecole des Mines de Douai (GC-Douai). Researches have been carried out with cement manufacturers in order to develop experimental methods to follow the reaction. It has led to several publications [Bulsteel et al. 2002], [Riche et al. 2002], [Garcia-Diaz et al. 2003].

The GC-Douai has developed a powerful experimental method which leads to the knowledge of the swelling of the reactive aggregate versus time. **An experimental method measures the different reaction degrees with an acid attack of the reactive sample at different ages of the chemical reaction** [Garcia-Diaz et al. 2003]. The sample is crushed to obtain a fine concrete powder which can be used to perform a chemical treatment through an acid attack [Bulsteel et al. 2002]. This model describes the chemical reaction from the microscale to a mesoscale by giving a relationship between the mortar paste swelling versus the swelling of the granular skeleton. They proposed hence a new methodology to quantify:

- the number of moles of  $SiO_{5/2}^-$  (or  $Q_3$  tetrahedrons) formed by Eq. (6-1) and consumed by Eq. (6-2);
- the number of moles of dissolved silica formed by Eq. (6-2).

This experimental methodology has been carried out to better understand the initiation and process of swelling. **This approach is the most physically realistic as it is based on experimental data.** Some major conclusions emerge from this study and leads to the proposed mechanism, illustrated in figure 6-3:

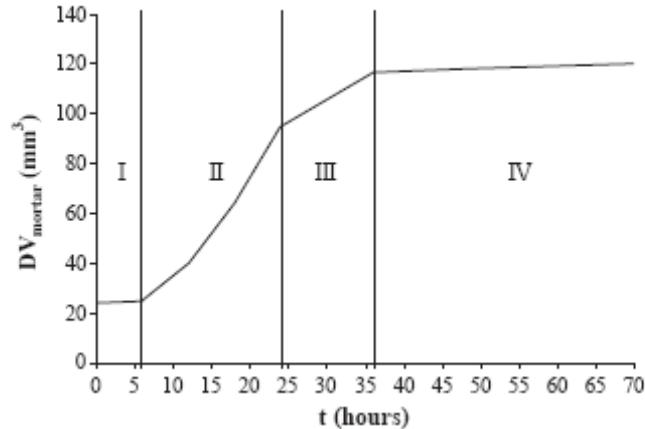


Figure 6-3. Schematic subdivision of the swelling curve – Evolution of the swelling of the mortar paste versus time. [Garcia-Diaz 2000]

- **Period I:** C-S-H/C-K-S-H phases are created. The two stages of the chemical reactions have the same velocity ( $v_1 = v_2$ ). The  $Q_3$  tetrahedrons are produced and consumed in the same time. The mortar bar does not swell during this period;

- **Period II and III:** the reaction velocity  $v_1$  of the first stage (see Eq. (( 6-1))) is faster than the reaction velocity  $v_2$  of the second step (see Eq. (6-2)): more  $Q_3$  tetrahedrons are formed than consumed by stage 2. It means that the stage 1 is expansive:  $Q_3$  tetrahedrons are at the origin of the creation of C-S-H/C-K-S-H phases which leads to a **swelling process of the reactive aggregates** (see figure 6-4).

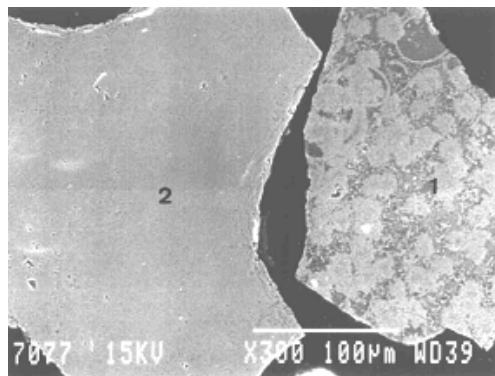


Figure 6-4. SEM. Polished section. 1) Altered flint aggregate by the creation of the chemical gel; 2) unreacted aggregate. [Bulteel 2000].

It leads then to damage and cracks in the sample. These cracks are probably at the origin of the volume amplification of the mortar bar. This is underlined in figure 6-5. It represents the volume variation of the sample  $\frac{DV}{V}$  (direct measure), measured at different time with a hydrometric weighing, versus the volume variation of the granular skeleton  $\frac{DV_g}{V_g}$  (indirect measure), given by the experimental method based on an acid attack [Bulteel et al. 2002].

Period III corresponds to a competition between the two stages. In this way the mortar paste swells but not as fast as during period II;

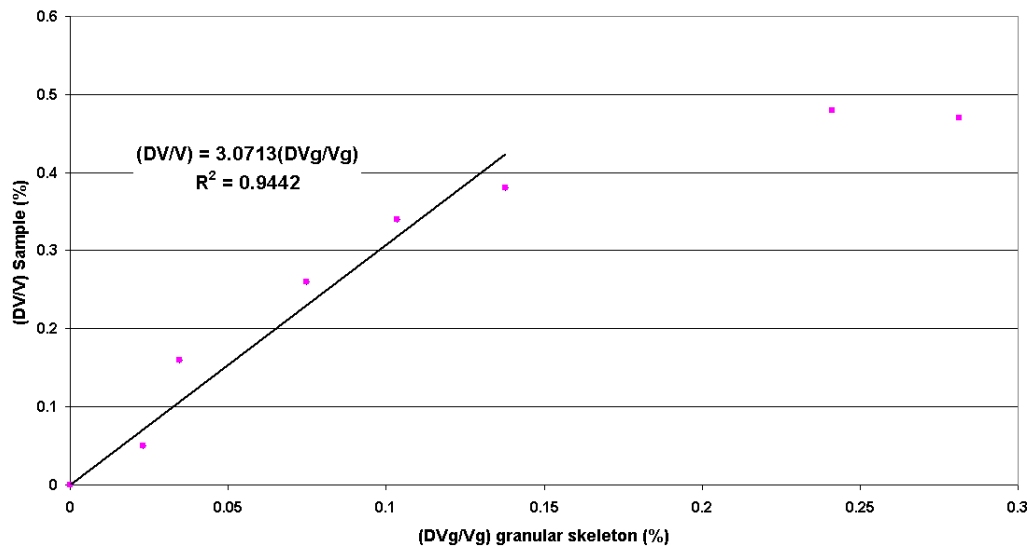


Figure 6-5. Volume variation of a sample as a function of the volume variation of the aggregates skeleton for a specific concrete formulation. [Riche 2003]

- **Period IV:** the swelling is asymptotic even though the two stages of the reactions continue. It corresponds in fact to the fill up of the reaction produces in cracks created by the ASR (cicatrisation period).

**This approach confirms that the first stage of the chemical reaction (the  $Q_4$  tetrahedrons, i.e.  $S_iO_2$  to  $Q_3$  transition) is responsible of the swelling mortar.** Furthermore recent papers have confirmed the presence of  $Q_3$  tetrahedrons in expansive gel. We can quote the work of Mitchell and coworkers [Mitchell et al. 2004]. It confirms also the initiation of the gel inside aggregates. All these experimental conclusions have led to a swelling model which establishes a link between the volume variation of the aggregates skeleton and the volume variation of the sample. Figure 6-5 plots the experimental results obtained. It leads to the following conclusion: the creation of micro and macro cracks during the expansion of the gel is possibly the reason which explains this amplification.

The GC-Douai proposed a complex model based on experimental data. It makes the link between chemical aspects and their mechanical consequences at a mesoscale. In this way the model describes the linear relation between the volume variation of the granular skeleton and the volume variation of the sample. The numerical model would enable to check it. The volume variation of the granular skeleton will be an input data of our numerical code. They are two main advantages to use it. We can directly use the experimental values of this expansion curve. Furthermore no new material parameter has to be identified and the input data correspond perfectly to the experiments. We will check the degradation and the volume variation of the reactive sample

## 6.3 The selected model in FEMCAM

We consider the aggregates as purely elastic. Consequently we do not consider any damage term in this section as we work on the aggregate, which is considered as purely elastic. The user's software introduces the experimental data: the value of the volume variation of the grain  $\left(\frac{DV}{V}\right)$  versus experimental time in FEMCAM. An interpolation is realized on these experimental values to obtain the volume variation of the granular skeleton at each time step (which can be adaptive) fixed by the user's software.

We consider herein that the experimental data gives us the exact free expansion of the aggregates. This hypothesis is not totally correct. Indeed the aggregate extraction method could induce instantaneous or differed elastic relaxation. It would mean that the measured volume variation is overestimated. However we consider that this phenomenon is very small compared to the swelling induced by the ASR.

### 6.3.1 The chemical-elastic problem for reactive aggregates

We use the same notation than in chapter 2. Our code is based on a velocity-pressure formulation. We have hence modified the constitutive equations to take into account the pressure generated by the aggregates swelling. These modifications affect only the finite elements which belong to reactive aggregate. Equilibrium equations are written in the following way:

$$\begin{cases} \text{Find } (v, p) \text{ such as :} \\ \text{div}(s) - \text{Grad}(p) = 0 \end{cases} \quad (6-3)$$

with inertia terms neglected. We add the incompressibility condition on the velocity field  $v$  :

$$\text{div}(v) = 0 \quad (6-4)$$

Using the Hooke law, we thus obtain the expression of the deviatoric part  $p$  and the spherical part  $s$  :

$$\begin{cases} s = 2\mu e \\ \dot{p} = -\chi_A^C \text{Tr}(\dot{\varepsilon}) \end{cases} \quad (6-5)$$

in which  $\chi_A^C$  is the incompressibility modulus of the reactive aggregate. In order to simplify the notations, we consider in section 6.3.1 and 6.3.2 that all parameters  $\chi_A^C, \mu_A^C, \lambda_A^C$  corresponding to elastic parameters for the reactive aggregate will be noticed  $\chi, \mu, \lambda$ . We take into account the chemical swelling by introducing now a chemical term in the total strain:

$$\dot{\varepsilon}_{ij} = \dot{\varepsilon}_{ij}^{el} + \dot{\varepsilon}_{ij}^{ASR} \quad (6-6)$$

where  $\dot{\varepsilon}_{ij}^{el}$  corresponds to elastic strain velocity and  $\dot{\varepsilon}_{ij}^{ASR}$  corresponds to the strain velocity induced by the chemical swelling in the aggregate. If the finite element belongs to a reactive aggregates,  $\dot{\varepsilon}_{ij}^{ASR} \neq 0$ . Otherwise,  $\dot{\varepsilon}_{ij}^{ASR} = 0$ . Additional terms intervene in the expression of Eq. ( 6-5). We develop now the expression of the pressure induced by the chemical reaction.

### 6.3.2 Expression of the pressure induced by the chemical reaction

We consider that the free swelling of the reactive grain is proportional to the reaction advancement  $\xi$ . If  $\xi$  is equal to zero, no gel has been created. If  $\xi$  is equal to 1, all gel has been created. In our model,  $\xi$  corresponds to the experimental data given by the volume variation of the grain  $\left(\frac{DV}{V}\right)$ . The behavior law for an **isotropic elastic-chemical behavior** is written as following:

$$\sigma_{ij} = 2\mu\varepsilon_{ij} + \lambda\varepsilon_{kk}\delta_{ij} - 3\varepsilon^\infty\chi\xi\delta_{ij} \quad (6-7)$$

where  $\chi > 0$  and  $\varepsilon^\infty$  is the asymptotic strain for a free swelling. In the case of a free expansion (i.e.  $\sigma = 0$ ), there is a linear relationship between the reaction advancement  $\xi$  and the observable strain in the material. We inverse the Eq. ( 6-7) and we obtain the following strain associated to the chemical reaction:

$$\varepsilon_{ii} = \frac{\sigma_{ii}}{2\mu + 3\lambda} + \frac{3\varepsilon^\infty\xi}{2\mu + 3\lambda} \times \frac{2\mu + 3\lambda}{3} \quad (6-8)$$

which can be rewritten:

$$\varepsilon_{ii} = \frac{\sigma_{ii}}{2\mu_A^C + 3\lambda_A^C} + \varepsilon^\infty\xi \quad (6-9)$$

If we replace the expression of  $\varepsilon_{ii}$  in the Eq. ( 6-7), we obtain:

$$\varepsilon_{ij} = \frac{\sigma_{ij}}{2\mu} - \frac{3\lambda}{2\mu} \left( \frac{1}{2\mu + 3\lambda} \sigma_{kk} \delta_{ij} + \xi \varepsilon^\infty \right) + \frac{3\chi}{2\mu} \varepsilon^\infty \xi \delta_{ij} \quad (6-10)$$

which can be rewritten as following:

$$\varepsilon_{ij} = \varepsilon_{ij}^{el} - \frac{3}{2\mu} \xi \varepsilon^\infty + \frac{3\chi}{2\mu} \xi \varepsilon^\infty \delta_{ij} \quad (6-11)$$

We denote:

$$\varepsilon_{ij}^{ASR} = -\frac{3}{2\mu} \xi \varepsilon^\infty + \frac{3\chi}{2\mu} \xi \varepsilon^\infty \delta_{ij} \quad (6-12)$$

After reducing the expression, we obtain the following relation:

$$\varepsilon_{ij}^{ASR} = \xi \varepsilon^{\infty} \delta_{ij} \quad (6-13)$$

Eventually:

$$Tr(\dot{\varepsilon}_{ij}^{ASR}) = 3\varepsilon^{\infty} \dot{\xi} \quad (6-14)$$

where  $\dot{\xi}$  is the chemical reaction kinetic. As the tensor  $\varepsilon_{ij}^{ASR}$  is purely spherical, it induces a supplementary term in the hydrostatic pressure in FEMCAM to describe the swelling of the finite elements in the reactive aggregates:

$$\begin{cases} s = 2\mu \times e^{el} \\ \dot{p} = -\chi Tr(\dot{\varepsilon}_{ij}^{el}) - \chi Tr(\dot{\varepsilon}_{ij}^{ASR}) \end{cases} \quad (6-15)$$

The weak velocity-pressure formulation associated to the chemical-elastic problem is then modified (Eq. (3-25)):

$$\begin{aligned} & \text{Find } (v, p) \in V \times P \\ & \begin{cases} \int_{\Omega} s(v) : \dot{\varepsilon}(v^*) d\Omega - \int_{\Omega} p \operatorname{div}(v^*) d\Omega - \int_{\partial\Omega} \tau_{imp} \cdot v^* dS = 0 \\ \int_{\Omega} p^* [-\operatorname{div}(v) - \frac{\dot{p}}{\chi} + 3\varepsilon^{\infty} \dot{\xi}] d\Omega = 0 \\ \forall (v^*, p^*) \in V^0 \times P \end{cases} \end{aligned} \quad (6-16)$$

The following of the resolution is the same as described in chapter 3 (see chapter 3, section 3.3.4.3).

### 6.3.3 Remark on the resolution of the whole mechanical problem

Our general 3D numerical tool models the swelling of concrete through two different behavior laws:

- an elastic damage law for finite elements belonging to the mortar paste;
- an elastic chemical law for finite elements belonging to the reactive aggregates.

Consequently the **general weak velocity-pressure formulation associated to the whole problem combines Eq. ( 6-16) and Eq. (3-25) and can be written as following:**

$$\begin{aligned}
 & \text{Find } (v, p) \in V \times P \\
 & \left\{ \begin{aligned}
 & \int_{\Omega} s(v) : \dot{\varepsilon}(v^*) d\Omega - \int_{\Omega} p \operatorname{div}(v^*) d\Omega - \int_{\partial\Omega} \tau_{imp} \cdot v^* dS = 0 \\
 & \int_{\Omega} p^* [-\operatorname{div}(v) - \frac{\dot{p}}{\chi} + \frac{\dot{\chi}}{\chi^2} p + 3\varepsilon^{\infty} \dot{\zeta}] d\Omega = 0 \\
 & \forall (v^*, p^*) \in V^0 \times P
 \end{aligned} \right. \quad (6-17)
 \end{aligned}$$

In the mechanical contribution of each finite element to the local matrices, some conditions intervene to distinguish the behavior of the finite elements of the mortar paste and the finite elements of the aggregates. In this way a finite element, belonging to the mortar paste, does not have chemical strain ( $\dot{\zeta} = 0$ ). A finite element belonging to the aggregate will have a purely elastic behavior (consequently,  $\dot{\chi}_A^C = 0$ ).

## 6.4 Modelling of the consequences of the ASR after seven days

### 6.4.1 Experimental data

We use the experimental results obtained by Dehault on a concrete with a specific formulation submitted to ASR [Dehault 2002]. The formulation of this concrete has been largely detailed in chapter 4. 50% of aggregates are flint aggregates. They are considered as reactive even if this hypothesis is strong as flint aggregates are not systematically reactive. These experiments have been carried out on  $7 \times 7 \times 28$  cm parallelepipedic samples, at  $60^\circ\text{C}$  and 100% of humidity (see figure 6-6) to accelerate ASR under controlled temperature. Concrete beams have been stored in autoclaves after seven days of hardening. *It is thus important to note that concrete has not yet reached its maximal strength.* It explains also why our identification on mechanical parameters has been carried out on concrete after seven days (see chapter 5).

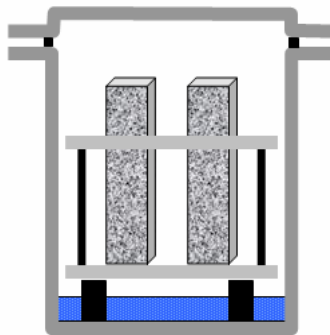


Figure 6-6. Autoclave curing of concrete samples to accelerate the ASR.

After each given time (during 26 weeks), the concrete bars length and volume have been measured. Figure 6-7 presents the evolution of the global swelling of the sample.

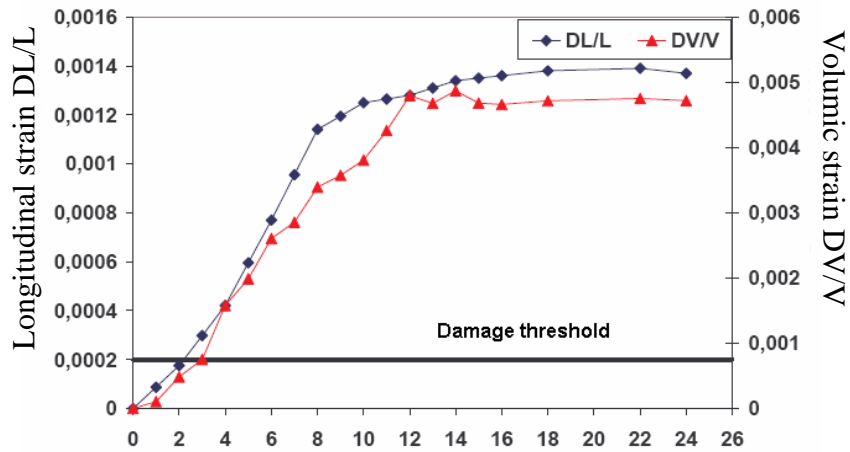


Figure 6-7. Evolution of the longitudinal strain DL/L and the volumic strain DV/V on samples submitted to ASR at 7 days. Time “0” corresponds to a concrete of seven days old [Riche 2003].

In the same time reaction degrees have been evaluated to measure the global swelling of the sample and the swelling of the aggregate skeleton (see section 6.2 for more details). Figure 6-8 presents the volume variation of the whole sample in function of the volume variation of the granular skeleton  $\left(\frac{DV_g}{V_g}\right)^*$ .

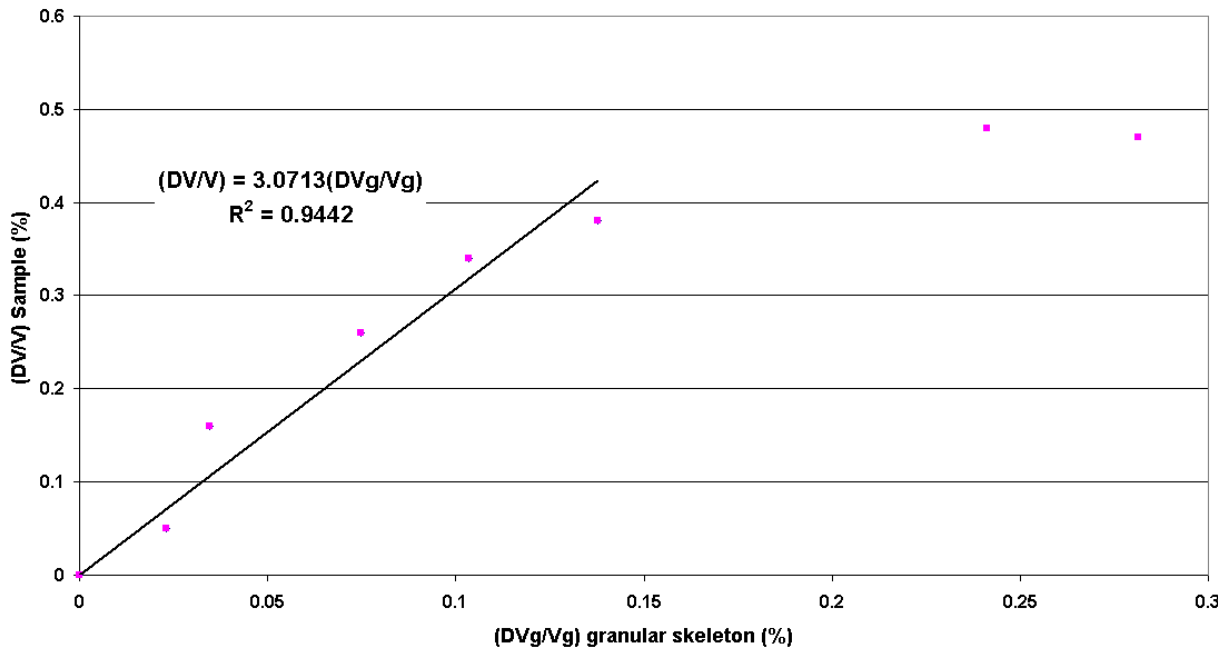


Figure 6-8. Volume variation of mortar core in function of the relative volume variation of the flint aggregates [Riche 2003].

\* The volume variation of the granular skeleton  $\left(\frac{dV_g}{V_g}\right)$  is the product of the volume variation of a grain  $\left(\frac{DV}{V}\right)_{Grain}$  by the volume percent of reactive aggregates.

We notice that the amplification coefficient is equal to 3.07. It shows that the mortar increases the effect of the expansion of the granular skeleton.

### 6.4.2 Numerical data

We consider a 3D multi-material model. The aggregates are purely elastic and the mortar paste has a damage elastic behavior. Table 6-1 summarizes material parameters obtained in chapter 5. We use them for this study.

<i>Material parameters</i>	$E_{MP}^C$ (GPa)	$E_A^C$ (GPa)	$\nu$	$\beta$	$\tilde{c}$ (mm <sup>2</sup> )	$\varepsilon_{D0}$
	18.7	70	0.2	1.05	15	$9.1.10^{-5}$
<i>Material parameters</i>	$A_T$	$B_T$	$A_C$	$B_C$	$\tilde{\varepsilon}_C^{Crit}$	$\tilde{\varepsilon}_T^{Crit}$
	1.18	50000	1.012	657.08	$8.72.10^{-4}$	$1.63.10^{-4}$

Table 6-1. Material parameter to model the mortar paste behavior.

Table 6-2 presents once again the grain size distribution used to simulate the consequences of the ASR on a concrete sample.

Average diameter (mm)	22.5	18	14.25	11.25	9	7.15
Number of aggregates	8	62	106	91	128	236

Table 6-2. Particle size distribution for ASR with 631 aggregates.

ASR induces generally macrocracks in our sample. We could model these macrocracks propagation using the “Kill element” method. However, as explained before this technique does not permit to have a volume conservation (elements are killed during the test and induce a volume lost). So this method has not been used and we consider that macrocracks are initiated when damage  $D$  reaches  $D = 0.99$ . Furthermore we consider in our study an isotropic swelling and we make the hypothesis that **aggregates have the same swelling at the same time**.

### 6.4.3 Mechanical consequences of the ASR

We present now the mechanical consequences of the ASR on the sample. Figure 6-9 presents the experimental evolution of the volume variation of a grain versus time. It constitutes the input data of the software FEMCAM. As we have already explained it, an interpolation is realized on these experimental values to obtain the volume variation of the grain at each time step (see section 6.3). And the mechanical problem is solved.

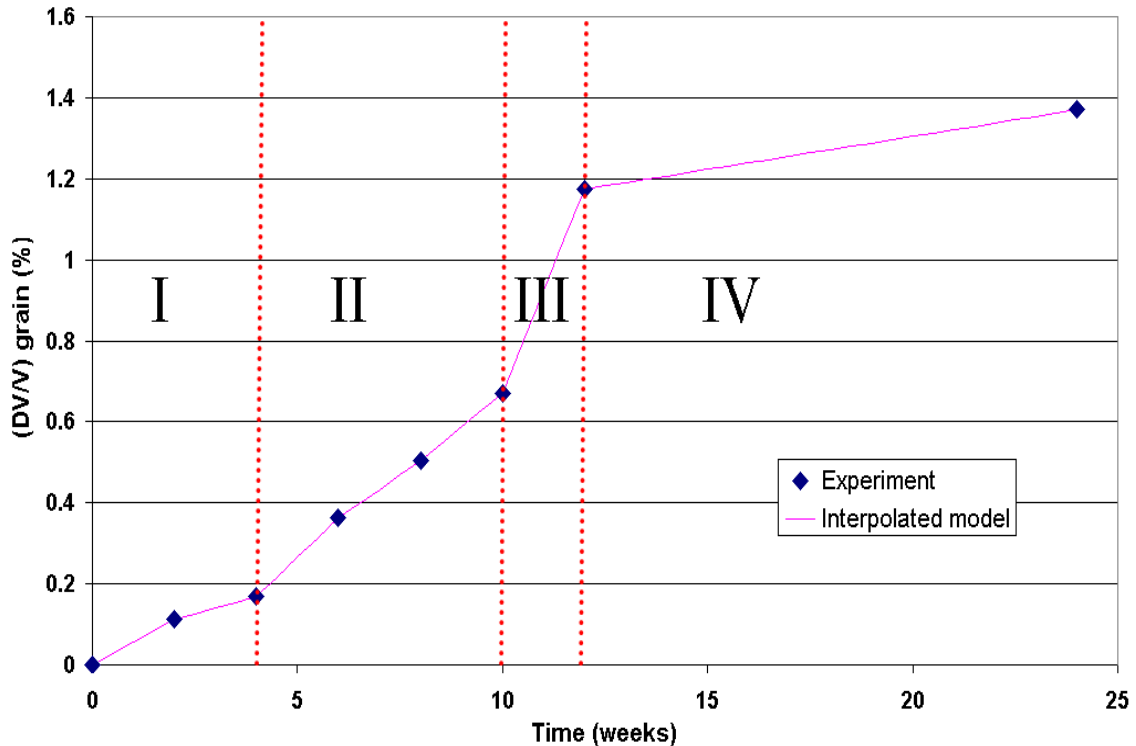


Figure 6-9. Free swelling curve of the grain versus time.

We notice thus the “S” shape of the macroscopic strain evolution. Four phases are clearly identified. This evolution first displays a fast swelling, before generally reaching a stage at the end of the reaction. The beginning of the curve corresponds to a progressive swelling period due to the creation of gel. The last phase is an asymptotic phase corresponding to a decrease of the efficiency of the products of the reactions due to an increase of the porous spaces linked to the creation of macrocracks. It corresponds exactly to the schematic model proposed by GC-Douai (as shown in figure 6-3).

#### 6.4.3.1 Experiment versus numerical results

For this simulation only one half of the aggregates are reactive (the experimental conditions imposes that one half of the aggregates are reactive flints). Figure 6-10 shows the reactive aggregates among the whole granular skeleton. **The choice of the reactive aggregates is completely random and it is uniformly present on each grain size. The nature of the swelling is isotropic.**

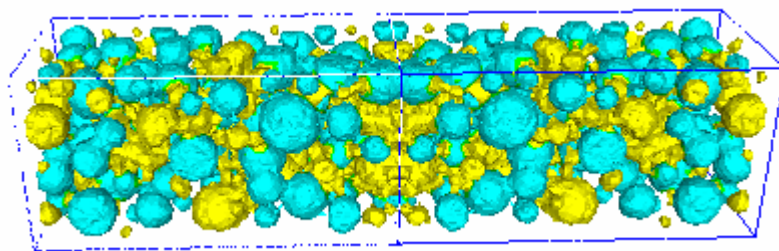


Figure 6-10. Position of the reactive aggregates (in blue) into the aggregate skeleton.

Figure 6-11 presents the volume variation of the sample submitted to ASR versus time. We distinguish clearly five different zones. To plot this figure, we have used the numerical volume variation of the sample in ordinate and the experimental volume variation of the grain in abscissa. To obtain the volume variation of the granular skeleton  $\left(\frac{DV_g}{V_g}\right)$ , we have made:

- **For the numerical curve:** the product of the experimental volume variation of the grain  $\left(\frac{DV}{V}\right)$  by the real *numerical* reactive aggregates volume (generated with our random algorithm of granular skeleton);
- **For the experimental curve:** the product of the experimental volume variation of the grain  $\left(\frac{DV}{V}\right)$  by the real *experimental* reactive aggregates volume (given by the concrete formulation).

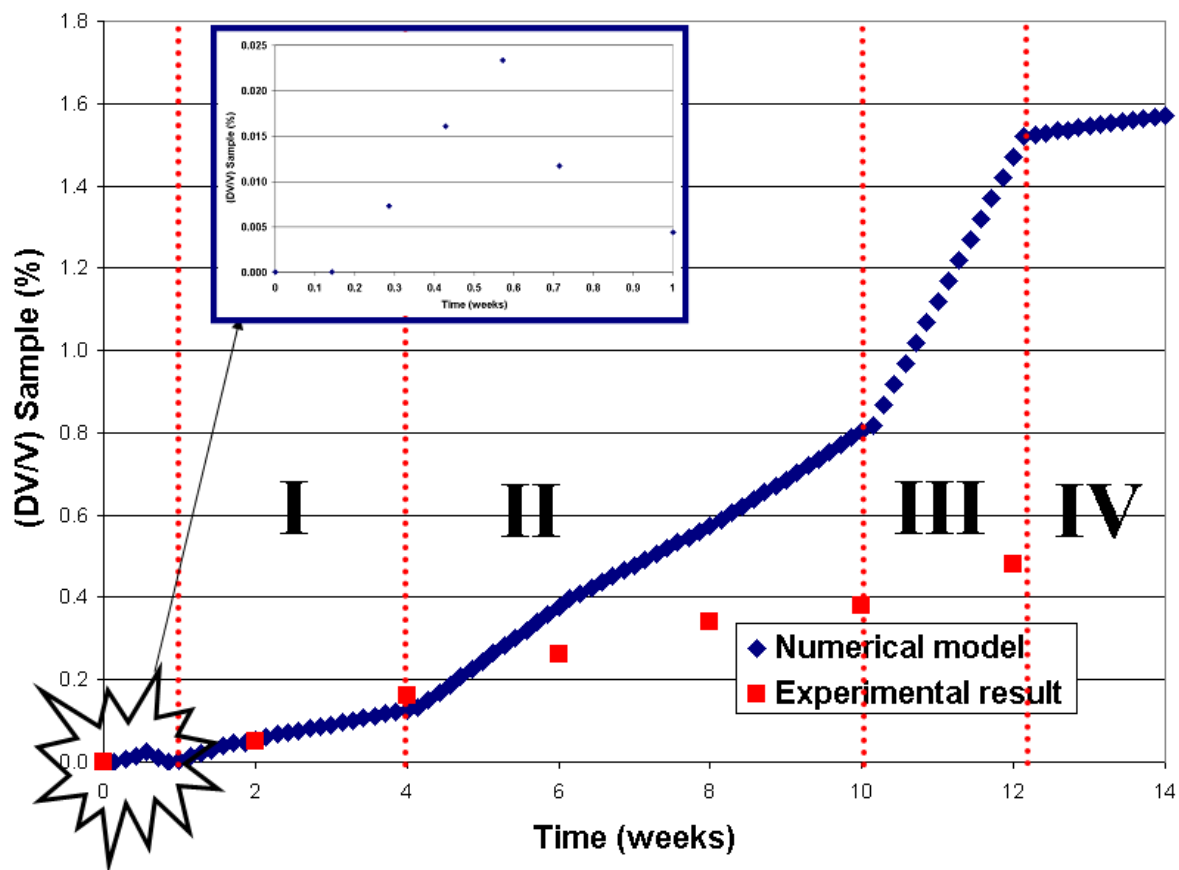


Figure 6-11. Volume variation of the sample versus time.

**The first part of the curve (from 0 to 1 week) is unstable.** We notice that the sample volume decreases whereas the ASR has already begun. One numerical reason could explain this phenomenon: damage induces a fast modification of the mechanical properties of the finite element and the mechanical problem has some difficulties to conserve the incompressibility condition. For instance we have measured the relative volume variations of some damaged finite elements in the mortar paste as shown in figure 6-12 for the first swelling steps.

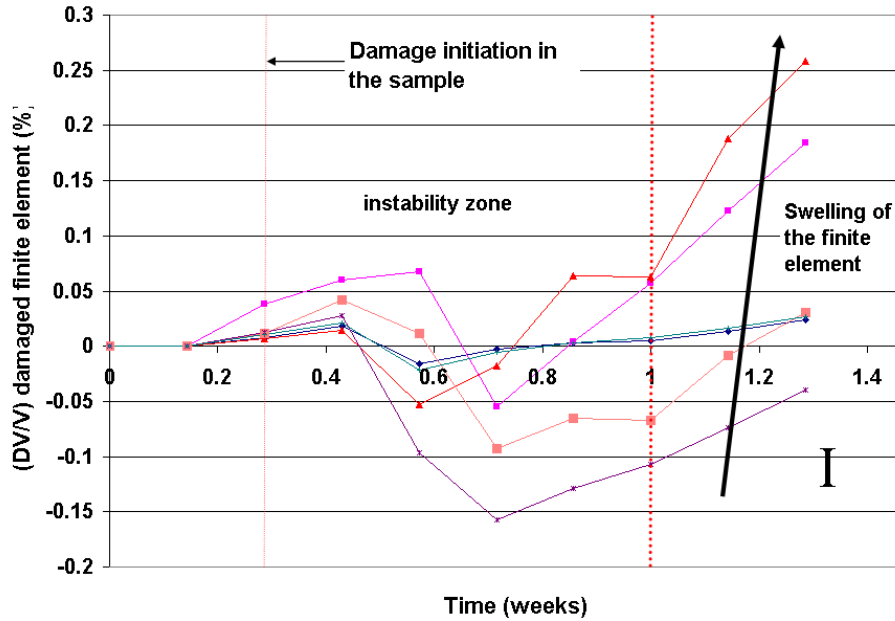


Figure 6-12. Volume variation of several damaged finite elements in the mortar paste.

Once the element is totally damaged, the sample has no other possibility than to swell. But this instability could have some physical origins. However no experimental data are available concerning the first days of the chemical reaction.

Then the following parts of the curve (*period I to IV*) show the swelling of the sample. These swellings are symmetrically and it validates the 3D numerical modelling.

We test now the volume variation of the sample versus the volume variation of the granular skeleton (figure 6-13). We compare thus this volume variation to the experimental result given in figure 6-8. We notice in figure 6-13 that points in abscissa of the numerical and experimental curves are close. It means that the random algorithm for aggregates generation gives accurate results in term of generated volume (we use the numerical method already described in this section to evaluate the volume variation of the granular skeleton  $\left(\frac{DV_g}{V_g}\right)$  in function of the volume variation of the grain and the reactive aggregates volume). We have made a correspondence between damage evolution in the sample versus time (from 0 to 4 weeks).

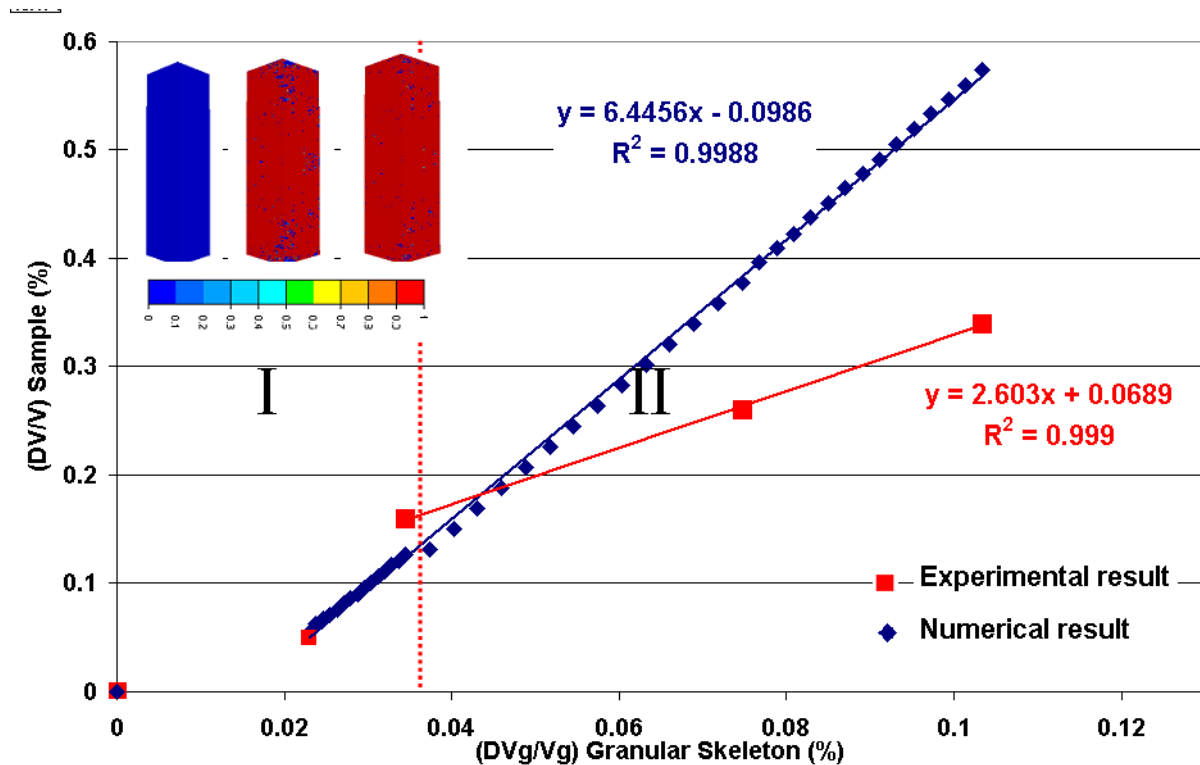


Figure 6-13. Volume variation of the sample in function of volume variation of the granular skeleton.

The experimental model shows, in a first approach, a linear relation between the volume variation of the sample and the volume variation of the granular skeleton (see figure 6-8). The numerical model distinguishes in fact two main phases:

- **The beginning of the reaction corresponds to a fast volume variation of the sample. This phase is correctly modelled by our 3D numerical model (from 0 to 4 weeks).** The instability (from 0 to 1 week) we have, observed in the previous figure is not represented. We notice that the  $\frac{A_E}{A_N}$  ratio ( $A_E$ : amplification coefficient of the experimental curve;  $A_N$ : amplification coefficient of the numerical curve) is close to 1 ( $A_N = 6.44$ ). Concerning damage, the sample is sound (damage in blue corresponds to  $D = 0$ ) at the beginning. Then it evolves in the sample due to the swelling of some aggregates and its value is nearby  $D = 0.99$  after four weeks;
- **The second part of the reaction describes a slower volume variation of the sample.** The amplification coefficient is equal to 6.44 in the first phase and then decrease to  $A_E = 2.60$  in the second phase. **This phase is not correctly described (after four weeks) by our numerical model.** The evolution of the sample volume is not representative of the experiments. Some main reasons explain this difference:
  - Aggregates are considered as purely elastic in our numerical model. Nevertheless some experimental studies [Bulteel 2002] have demonstrated aggregate degradation (under the effect of the creation of the chemical gel) which can induce the decrease of its mechanical properties (decrease of the Young modulus for example). At four weeks the grain swelling is equal to

0.2% (see figure 6-9). If we suppose that the aggregate has a damage threshold  $\varepsilon_{D0}$  about equal to 0.2% (de Larrard [de Larrard 1999] considers a Young Modulus  $E_A^C$  equal to 78 GPa and a compressive strength equal to 160 MPa for aggregates from “Savreux”), the isotropy condition leads to a volume variation threshold of 0.6% of the aggregate. This threshold is reached during period II in figure 6-9. Numerical developments will integrate an elastic damage behavior to simulate the mechanical properties of the aggregates.

- It appears that damage evolution is overestimated in the sample. The second period corresponds to macrocracks initiation in the sample. Once damage initiates and evolves in the sample, numerical macrocracks should intervene. Stress and strains would be distributed differently after the cracks initiation. Consequently damage would evolve differently.
- We have seen that we do not take into account macrocracks evolution. It is thus possible that we do not take into account possible creation of voids where the gel would go. It could have for direct consequences to slow down the whole swelling and increase the sample stiffness. In this way we notice clearly the impact of the macrocracks initiation and evolution in the sample and the role of the chemical part.
- Concrete is a “living” material. After seven days, the mortar paste continues to harden. This effect can induce a slower evolution of the sample swelling. Indeed aggregates swelling is constrained by the mortar paste hardening.

The first and the second points can be dealt with in our numerical model. In this way, the next chapter present an approach to take into account macrocracks contribution. The third and fourth points require including a chemical component in the model. More particularly the fourth point shows the interest to carry out the same swelling experiments with a concrete of 28 days old.

Figure 6-14 shows a cutting plane in the sample after 14 days of chemical reaction. We notice in blue the aggregates, which have a purely elastic behavior ( $D=0$ ) and in red the completely damaged mortar matrix ( $D=0.99$ ). We have observed on the simulations that the damage tends to be more important when it reaches the faces of the sample.

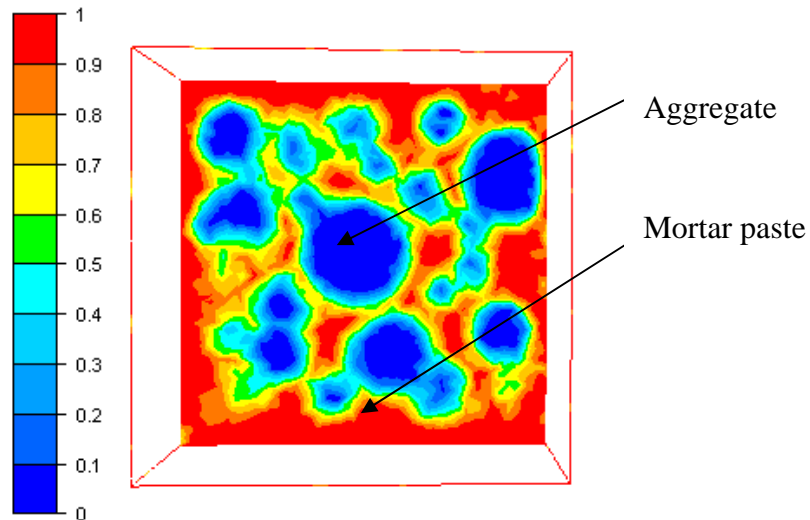
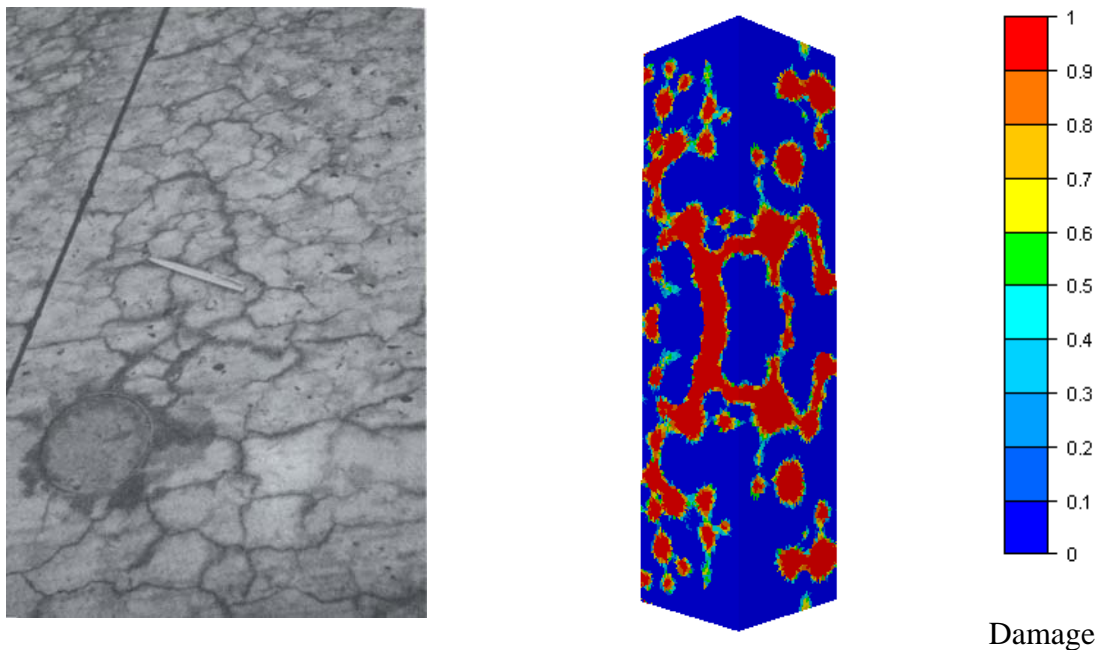


Figure 6-14. Cutting plane in the sample submitted to the ASR - Blue corresponds to the aggregates.

This result is representative of what can be observed experimentally: whereas damage evolves progressively inside, we observe a map cracking at concrete surface. Typically the crack pattern developed forms irregular polygons. An example of this map cracking is shown in figure 6-15.



a) A portion of concrete road pavement, Cape Town.  
Length of the pencil is 125 mm. [Swamy 1992]

b) Damage evolution at the surface with our 3D numerical model at the beginning of the chemical reaction.

Figure 6-15. Crack pattern developed at the surface of a concrete submitted to ASR. Comparison Experimental-Numerical results.

Swellings amplitude is characteristic of more or less anisotropy which could be explained by cracks initiation and orientation. [Clark 1991]. Indeed, on the same concrete, the amplitude of measured swellings is strongly influenced by the measurement direction. This anisotropic character was noticed on several experiments [Smaoui et al. 2003]. Regarding the

longitudinal swelling, some experimental measures have been made during the Dehaut study [Dehaut 2002] to estimate the anisotropic character of the swelling.

Figure 6-16 shows the quasi linear correlation between the transversal swelling and the longitudinal one for the experimental curves. We do not represent first numerical points which correspond to an instable zone. We notice that numerical results are in the same set of range than experimental ones. However we do not observe the same slope as in the experiment. The numerical transversal swelling is less important than the numerical longitudinal one whereas the algorithm generates randomly the granular skeleton and the swelling is isotropic. But the mechanism is complex as many phenomena intervene at the same time: the initial numerical instability (it can modify the volume of damaged finite elements and consequently modify the longitudinal and the transversal variations at the beginning), edges effect etc...

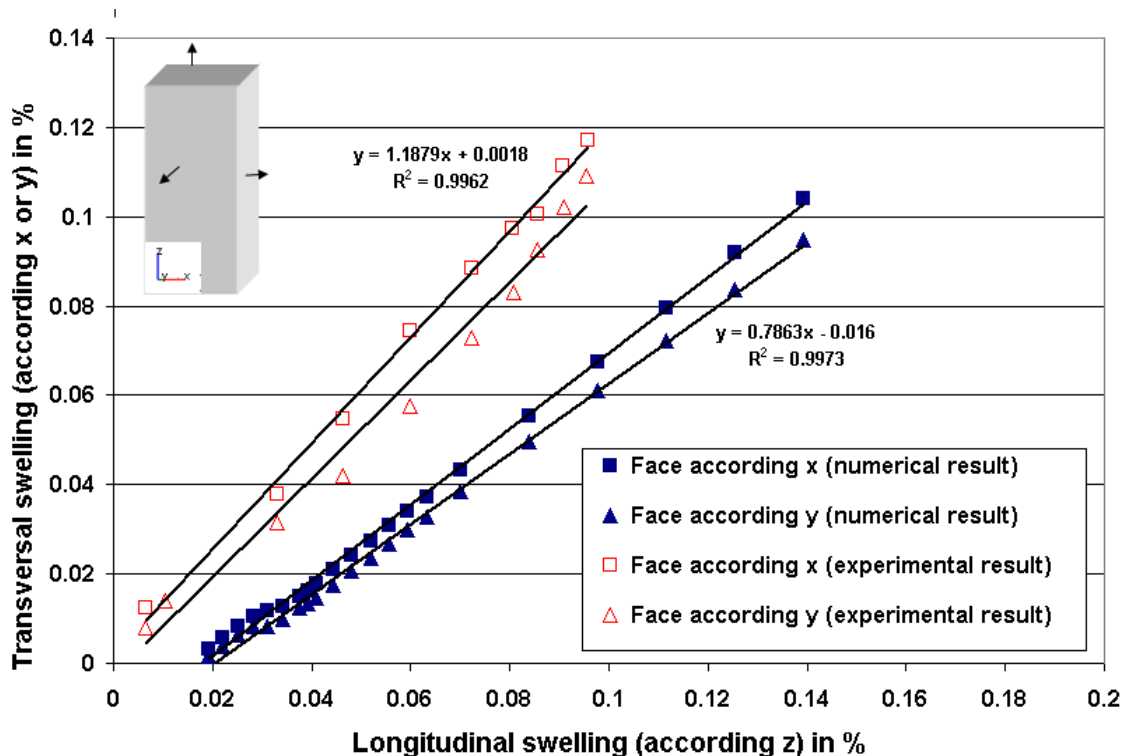


Figure 6-16. Correlation between transversal swelling and longitudinal ones.

Several studies have shown a decrease of 50% for the compressive strengths of concretes developing an ASR, compared to healthy concretes. In an experimental study, Swamy showed a 25% fall of the maximal load of beams presenting ASR compared to "pilot" beams subjected to three point bending tests [Swamy 1992]. Here we can evaluate  $\frac{E}{E_0}$  versus

time, where  $E$  is the homogenised Young modulus and  $E_0$  is the initial Young modulus. A compression test has been performed after swelling. We use the same friction conditions than already described chapter 5, section 5.4.4.1. The stiffness evolution can be divided into three parts:

- **From 0 to 2 weeks**, the chemical process is not yet active. The Young modulus increases. Concrete can get harder as we test it after 7 days. This phase can not be

described by our numerical model as it leads to the modifications of the mechanical properties of concrete;

- **From 2 to 8 weeks**, concrete is submitted to ASR. The homogenised Young modulus decreases. This phase is correctly described by our numerical model. Figure 6-17 shows that after eight weeks, we get a decrease of the homogenised Young modulus  $E$  of 31 % which is the same set of range that what we can observe during experiments;
- **After 8 weeks**, the homogenised Young modulus increases. This increase can be linked to the asymptotic phase of the swelling curve.

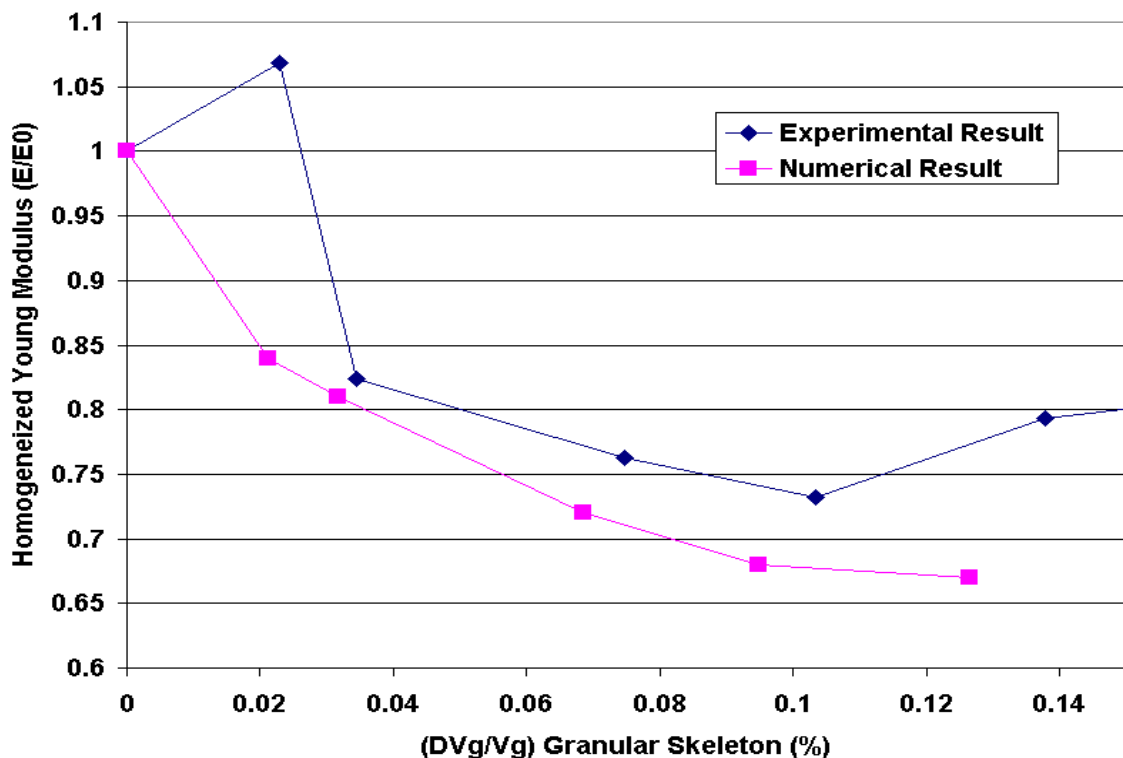


Figure 6-17. Evolution of the homogenised Young modulus versus time.

#### **The evolution of the homogenized Young modulus validates the numerical model.**

It means that the damage model describes the mechanical consequences of the ASR on the sample with accuracy. Now we test the influence of the inert aggregates, the reactive aggregates diameters and the number of reactive aggregates on the volume variation of the sample.

#### **6.4.3.2 Influence of the inert aggregates**

We test here the influence of the inert aggregates on the global response of the sample. A test has been performed in which only a half of the total granular skeleton is generated and we consider that they are all reactive. The global swelling of the sample will then be compared to the previous result. **If the inert aggregates have no role during the mechanical swelling, the curves will be completely superimposed.**

Figure 6-18 compares the volume variation of the sample containing inert aggregates with the volume variation of the sample without any inert aggregates for a period of 8 weeks (0 to 8 weeks). We observe two main phases:

- **Period I** corresponds to a great zone of instabilities (more important than for the swelling test with inert aggregates). We observe thus that the sample without inert aggregates is more submitted to contraction phenomenon induced by damage in the mortar paste. When damage occurs it leads to a contraction of each damaged finite element at the beginning of the simulation. Its volume decreases but this decrease is stopped by the presence of aggregates. These contractions are then assisted by higher mortar paste content in concrete. **The more there are aggregates in the sample, the more the amplitude of this contraction is small.** Even if some phenomena are observed in experiments (the chemical swelling is impeded by inert aggregates), it is difficult for the moment to analyse it as a physical phenomenon.
- **Period II** underlines that the two samples (with or without inert aggregates) evolve with the same velocity. It seems that the volume of the sample with inert aggregates swells a bit more than the sample without inert aggregates (the amplification coefficient is equal to 1.24). However we consider equal amplitude between the two samples. This value comes in fact from the instabilities period, which is longer for the sample without inert aggregates.

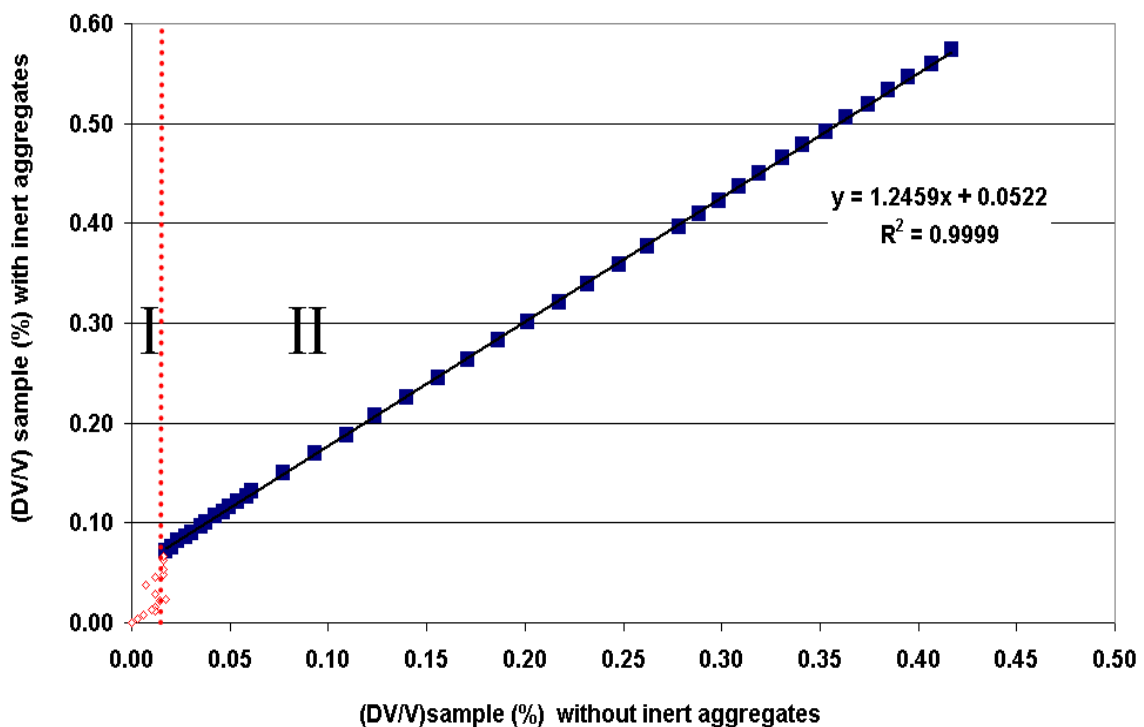


Figure 6-18. Comparison of the global swelling depending on the presence or absence of inert aggregates.

**Eventually the numerical model has underlined that inert aggregates leads to strengthen the structure.**

### 6.4.3.3 Influence of the number and the sizes of reactive aggregates

We test the number of reactive aggregates on the global response of the material in terms of volume variation of the sample. Figure 6-19 shows the volume variation of the sample in function of the volume variation of the grain. We notice that the curves have not the same evolution. **Swelling evolution of the sample depends directly on the number of reactive aggregates.** However the amplitudes, corresponding to the different curves in figure 6-19, evolve non linearly. For 10% reactive aggregates, the slope of the curve is equal to 0.3, whereas the slope is equal to 1.9 for 100% reactive aggregates. The mechanism is here very complex to analyse as the swelling of reactive aggregates induces two contrary phenomena: possible contraction of the mortar paste between two reactive aggregates or possible dilatation. These two opposite phenomena are amplified with more reactive aggregates in the sample. Furthermore when few aggregates are reactive, little damage is generated locally around the reactive aggregates. It induces less contraction of whole sample, in which less finite element are completely damaged (it is the phenomenon we have explained in section 6.4.3.1) and so a bigger measured volume of the sample. On the contrary, when 100% of the aggregates are reactive, more finite element in the mortar paste, are affected by a damage mechanism which induces a contraction phenomenon. Consequently the measured volume of the sample is lower.

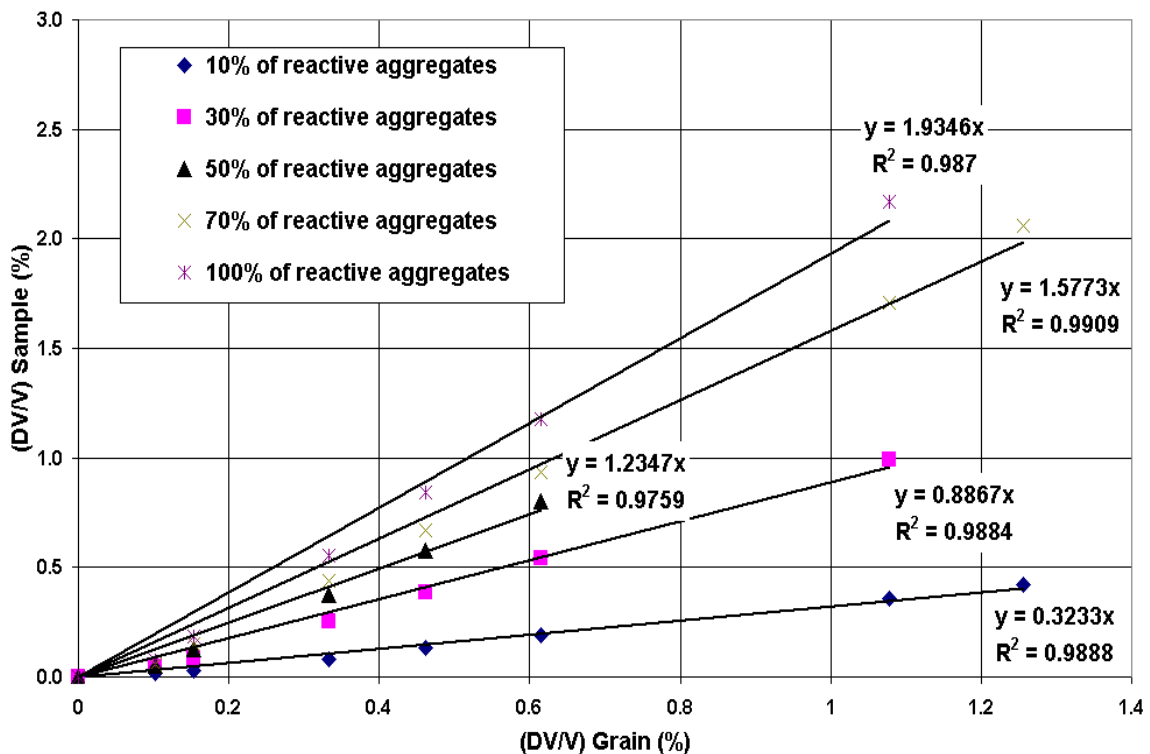


Figure 6-19. Volume variation of the sample versus volume variation of the granular skeleton according to the volume percent of reactive aggregates.

This numerical test cannot be treated easily experimentally. It could be hence very interesting to carry out an experimental campaign in which the number of reactive aggregates would be controlled. Now we want to test the effect of the diameters of reactive aggregates on the global swelling of the sample.

By using the same initial formulation, we control now which size of aggregates can be reactive. We test separately the 7.15 mm, 11.25 mm, 14.25 mm and 18 mm diameters and we compare the mechanical consequences in terms of global volume variation of the sample versus the volume variation of the granular skeleton to a classical formulation where any types of grain size can swell. In this test, in order to respect experimental conditions where 50% of the aggregates are from “Boulonnais” and non reactive, we consider than only 50% of aggregates of the same size are reactive. So we have modified the grain swelling in order to obtain the same volume variation of the granular skeleton. For example, if we consider the diameters  $d = 7.15$  mm, 118 aggregates can be reactive among the 236 aggregates of this size. It represents a reactive volume  $V_{reactive}^{7.15}$  equal to  $22.6 \text{ cm}^3$ . For a classical formulation, we know that the reactive volume  $V_{reactive}$  is approximately equal to  $279.8 \text{ cm}^3$ . In this way to obtain the same swelling of the granular skeleton we adapt the grain swelling  $\left(\frac{DV}{V}\right)_{Grain}$  based on the initial grain swelling  $\left(\frac{DV}{V}\right)_{Grain}^{Initial\_Formulation}$  as follows:

$$\left(\frac{DV}{V}\right)_{Grain} = \left(\frac{DV}{V}\right)_{Grain}^{Initial\_Formulation} \times \left(\frac{V_{reactive}}{V_{reactive}^{7.15}}\right) \quad (6-18)$$

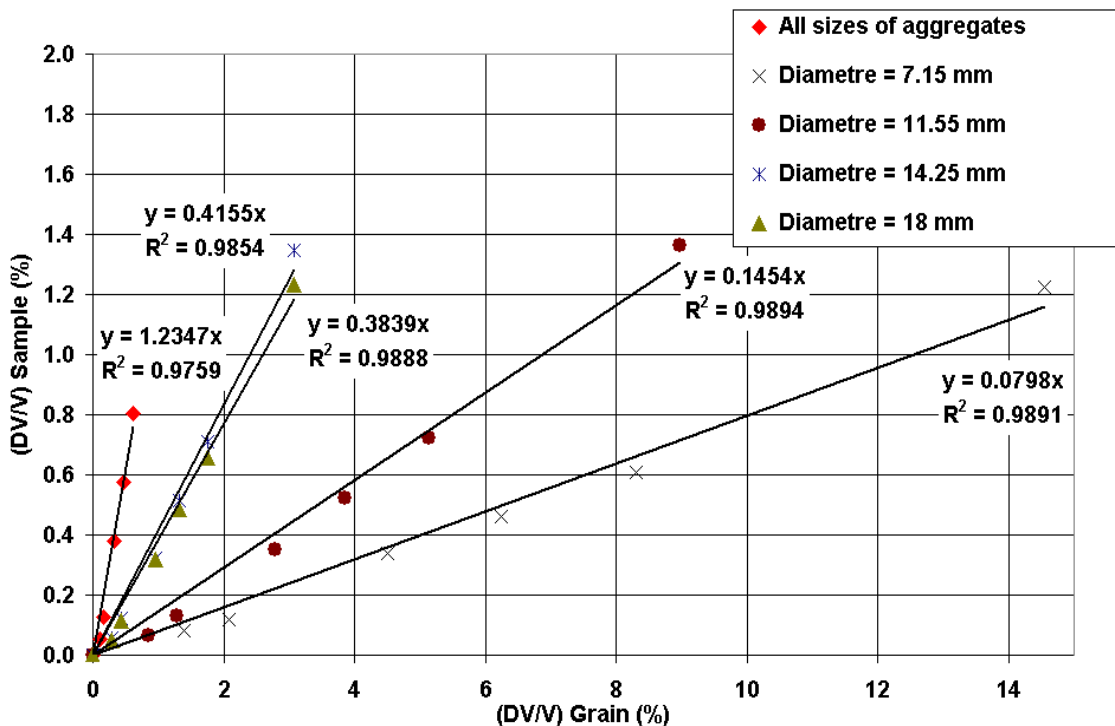


Figure 6-20. Volume variation of the sample in function of the volume variation of the granular skeleton for different sizes of reactive aggregates.

Figure 6-20 shows the volume variation of the sample versus the type of reactive aggregates. The diameter of reactive aggregates influences the global response. The greater aggregates size, the greater the volume variation of the reactive sample. Furthermore we notice an asymptotic zone which means that the global swelling do not increase beyond a

diameter (here the threshold seems to be set to 14.25 mm). Eventually we observe that the classical model, which takes into account all sizes of aggregates, leads to the greater volume variation of the sample. But this conclusion has to be balanced with the fact that the volumic fraction of reactive aggregates is modified for each test. It is thus difficult to analyse the diameters effect and the volumic fraction effect on the global response. This test could be improved by keeping the same volumic fraction of reactive aggregates in each test.

Now we use the results obtained in figures 6-19 and 6-20. We compare the evolution of the slopes of each swelling sample versus the percentage of volume of reactive aggregates in the two cases. Figure 6-21 shows that the sample swelling does not evolve linearly versus the volume percent of reactive aggregates. There are two major different evolutions for a percentage of volume of reactive aggregates inferior or superior to 20%. **The numerical model underlines that the volume of reactive aggregates controls the velocity of the sample swelling in our numerical model.** Figure 6-21 shows that the velocity of the sample swelling is more important when the percentage of volume of reactive aggregates is inferior to 20%. It is then interesting to underline that the classical test (with 20.5% of reactive aggregates) is at the border between the two evolutions.

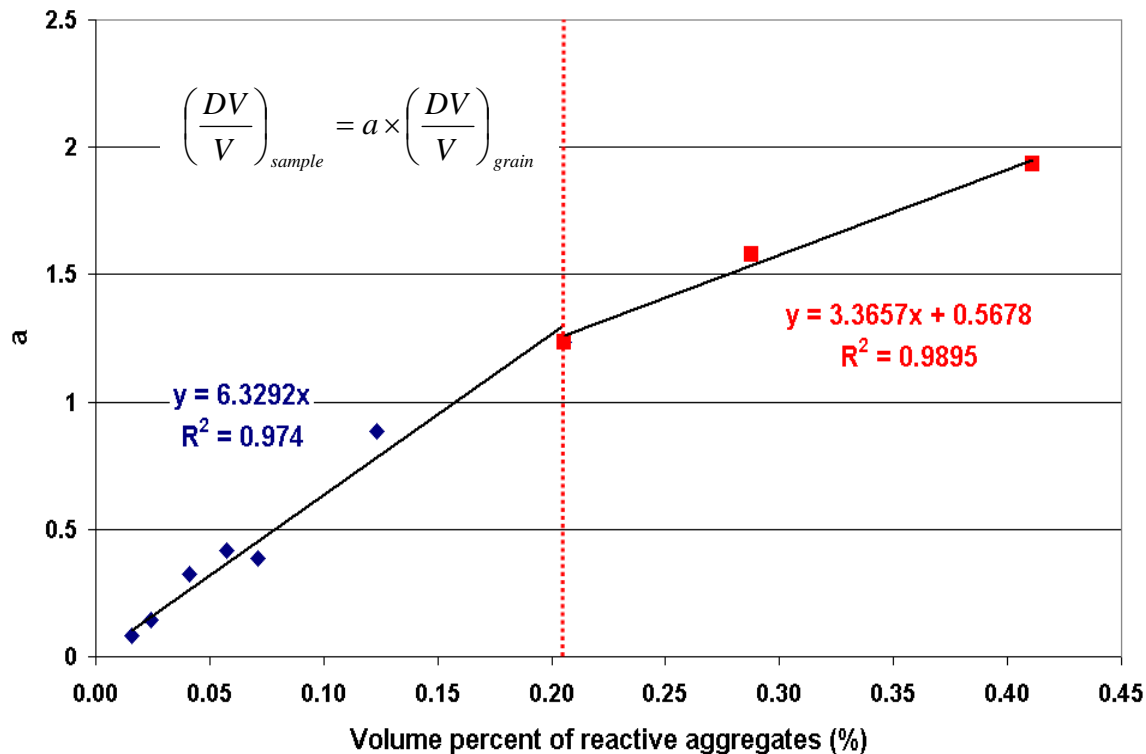


Figure 6-21. Slopes of the swelling samples versus percentage of volume of reactive aggregates.

## 6.5 Conclusions

ASR is a chemical reaction which induces mechanical consequences at a mesoscopic and macroscopic scale. The principal consequences are cracks propagation and swelling of the sample. This chapter deals with the modelling of these consequences.

In this way we have used the model developed at the Ecole des Mines de Douai (GC-Douai). This model considers ASR as an expansion of some reactive aggregates. To model it, we use the experimental data on the volume variation of the granular skeleton, which

can be used as input data in FEMCAM. And we compare the experimental and numerical volume variation of the sample.

The numerical results (volume variation of the sample) are in the same set of range than experimental results during the first phase of the chemical reaction. Furthermore the stiffness evolution of the concrete sample, submitted to ASR, gives good results. It leads to **validate the numerical model**. Moreover the 3D numerical tool contributes to improve the analysis of the mechanical consequences of the ASR. The numerical model has hence leads to describe the volume variation of the sample in two phases where the first one corresponds to a fast volume variation of the sample. However the numerical model has some limits which can lead to a bad description of the second phase of the chemical reaction. Some further numerical developments (mechanical law to describe aggregates with accuracy, macrocracks evolution in the sample) could improve the numerical tool.

We have also noticed the importance of inert aggregates which modify the global swelling of the sample. Due to these inert aggregates, the whole sample is less sensitive to contraction and thus induces an increase of the swelling phenomenon. Furthermore the effects of the number and the diameters of reactive aggregates have been studied. We have deduced that the velocity of the volume variation of the sample is function of the volume percent of reactive aggregates. The results presented here proved that numerical simulation is clearly helpful both to understand the mechanical consequences of the ASR on concrete structures and to improve concrete formulation by analysing the effect of the aggregates on the global response of the sample.

The next chapter is dedicated to the modelling of macrocracks in a sample through the Discrete Crack Approach. The aim is to be able to introduce macrocracks and observe their evolution and influence of a sample submitted to ASR.

## CHAPTER 7 : IMPROVEMENT OF THE DESCRIPTION OF THE ASR THROUGH THE DISCRETE CRACK APPROACH

7.1 INTRODUCTION.....	157
7.2 STATE OF THE ART REVIEW ON 3D NUMERICAL APPROACHES OF FRACTURE.....	158
7.2.1 <i>Smearred crack approach</i> .....	158
7.2.1.1 <i>Concept of fixed cracks</i> .....	159
7.2.1.2 <i>Concept of rotating crack models</i> .....	160
7.2.1.3 <i>Microplane models</i> .....	160
7.2.1.4 <i>The X-FEM method (eXtended Finite Element Method)</i> .....	161
7.2.2 <i>Mixed models</i> .....	163
7.2.3 <i>Discrete approaches</i> .....	167
7.2.3.1 <i>The “Kill element” method</i> .....	167
7.2.3.2 <i>The Discrete Crack Approach</i> .....	168
7.3 IMPLEMENTATION OF THE DISCRETE CRACK APPROACH IN THE FINITE ELEMENT CODE FEMCAM.....	170
7.3.1 <i>Introduction on the 3D crack modulus</i> .....	170
7.3.2 <i>“Initialization” step</i> .....	171
7.3.3 <i>“Opening” step</i> .....	172
7.3.4 <i>“Bifurcation” step</i> .....	173
7.3.1 <i>The Maximum strain energy release rate</i> .....	175
7.3.2 <i>The Circumferential Stress Criterion</i> .....	176
7.3.3 <i>Schöllmann, Richard et al. criterion [Schöllmann et al. 2002]</i> .....	178
7.3.5 <i>“Propagation” step</i> .....	180
7.4 VALIDATION OF THE 3D CRACK MODEL .....	186
7.4.1 <i>3D Crack propagation on a tensile test</i> .....	186
7.4.1.1 <i>Model configuration</i> .....	186
7.4.1.2 <i>Crack path on a uniaxial tensile test</i> .....	186
7.4.1.3 <i>Sensitivity study on the SIF</i> .....	188
7.4.2 <i>3D Crack propagation in a L-Shape structure</i> .....	191
7.4.3 <i>3D Crack propagation in a three point bending test</i> .....	192
7.4.4 <i>Influence of heterogeneities</i> .....	194
7.5 CONCLUSIONS .....	196

## 7.1 Introduction

Fracture of concrete is a very complex phenomenon that involves the initiation, growth and propagation of micro and macrocracks\*. This complexity arises principally from the heterogeneous nature of the material. Initial cracks are generally initiated at the interface between the aggregates and the mortar paste. Then they can evolve and be localized in three main zones:

- At the interface between the aggregate and the mortar paste;
- In the mortar paste;
- In the aggregate.

This evolution depends mainly on the geometry and the mechanical properties of the aggregates. If the stiffness of the aggregate is weaker than the mortar paste (case of high performance concrete) or if the inclination of the interface is close to  $90^\circ$ , the crack might propagate through the inclusion. If the aggregate is much stronger than the mortar paste or the inclination of the interface is small with respect to the crack direction, then the crack will run along the inclined interface (see figure 7-1).

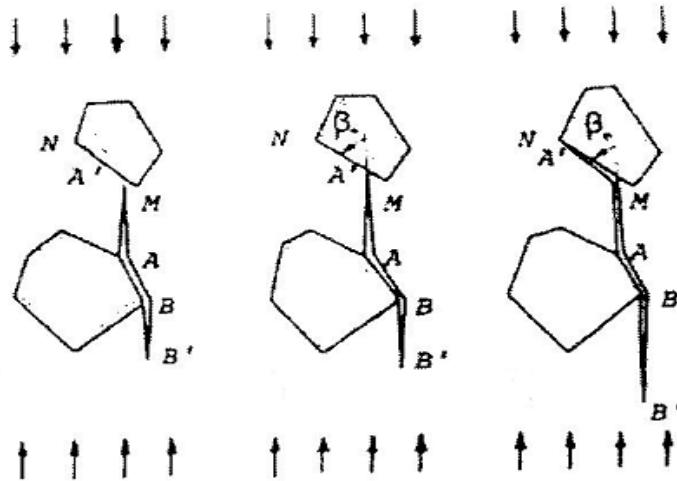


Figure 7-1. A crack path starting from an interface; a) The crack meets the second aggregate, b) and finally the crack will propagate along the interface. [Wittmann et al. 1993]

In the framework of our study the numerical modelling of macrocracks can lead to a better comprehension of the degradation of a concrete sample submitted to ASR. In this way concrete fracture has been approached from different points of view, and literature on this subject is rich of models, each claiming partial success. These models aim at describing the stages of **initiation and propagation of a crack**.

We present here a review of 3D numerical approaches of fracture. We will conclude on the choice of the “Discrete Crack Approach”, that we have chosen to implement. The second part of this chapter deals with the details of the algorithm we have implemented in FEMCAM. We will end the section by validating the algorithm and underlining the effect of the heterogeneities on the crack path.

\* A crack is an internal boundary of the material which leads to material discontinuities.

## 7.2 State of the art review on 3D numerical approaches of fracture

During these last thirty years, numerous recognized theories have been already proposed and developed to model the phenomenon of cracking in concrete [Jirasek 1999]. Among the most interesting approaches, we can quote the “Element free Galerkin Method” proposed by Belytschko [Belytschko et al. 1994], the “Arbitrary Local Mesh Replacement Method” [Rashid 1998] which consists in overlapping two meshes. More recently the Extended Finite Element Method (X-FEM) has also been presented [Sukumar 2000]. But the classical finite element method remains the most used method as we can use an extensive data base of material behaviors. However few works were completed in 3D. We classify methods for modelling discontinuities into three categories:

- continuous approaches;
- mixed approaches;
- discrete approaches.

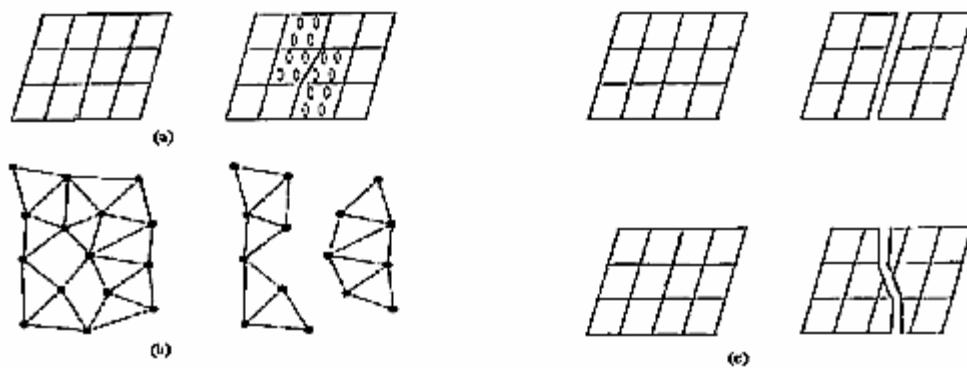


Figure 7-2. a) continuous approach, b) discrete approach, c) mixed approach. [Jirasek 1999]

After having detailed each of these approaches, we will show their advantages and their drawbacks.

### 7.2.1 Smearred crack approach

The basis of continuous models is that cracks are introduced by modifying the materials mechanical properties. A crack is therefore not represented explicitly, but modelled as a “smeared crack” by modifying the constitutive relation [De Borst et al. 2002]. Hence the remeshing process is not needed. These models allow a description of the concrete degradation due to cracking in terms of tensor relation between stress and strains. Hence, cracking laws and concrete behavior laws can be treated separately. The methodology is relatively simple to implement. Such models have been developed by Rashid (1968), Hillerborg and coworkers (1976), Gopalaratnam and Shah (1985), Bazant and Oh (1983) and Gran (1985). There are some alternatives: concepts of **fixed cracks**, **rotating crack**, multiple fixed crack, adaptative fixed crack models, statically constrained microplane model. Ohmenhäuser et al. [Ohmenhäuser et al. 1999] detail all these approaches. We present here the two main models.

### 7.2.1.1 Concept of fixed cracks

One of the earliest models for concrete has been the concept of fixed crack proposed by Rashid [Rashid 1968], who triggered fracture by the maximum tensile stress in the element: once it exceeds a critical value, the element is considered cracked. Traditionally the non cracked material is regarded as **isotropic, elastic linear**. If the crack propagates at point  $x$  of the sample, concrete becomes anisotropic and the principal axes of the material are aligned with the crack axes. The constitutive equation is then modified so that the stress normal to the discontinuity vanishes. The behavior law for the fixed cracks links the stress to the strain as following:

$$\Delta\sigma^{loc} = [D]\Delta\varepsilon^{loc} \quad (7-1)$$

Where  $\sigma^{loc}$  and  $\varepsilon^{loc}$  are respectively the local stress and strains in the crack referential (see figure 7-3).  $[D]$  is damage tensor concrete linking stress and total strains in the axis of crack and defined by nine independent modulus.

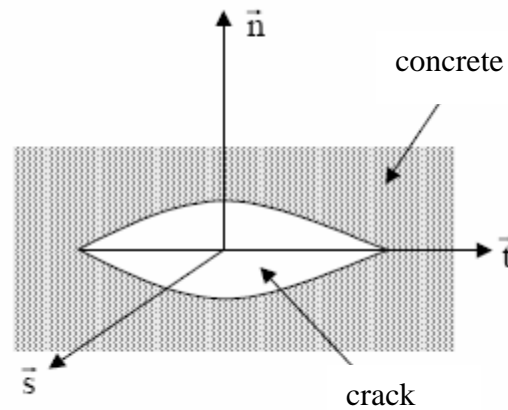


Figure 7-3. Local referential linked to the crack.

This approach is appropriated for many applications but it has some disadvantages. Initially, it is impossible to correctly combine the crack with other nonlinear phenomena (heating effects, creep etc.). A remedy for this deficiency is to cut the total strain of the cracked material into a cracking strain  $\varepsilon^{CR}$  and an elastic strain  $\varepsilon^{CO}$  [Simons et al. 1997].

$$\varepsilon^T = \varepsilon^{CO} + \varepsilon^{CR} \quad (7-2)$$

Where  $\varepsilon^T$  is the total strain. The concept of the "multiple fixed cracks" divides  $\varepsilon^{CR}$  into several parts representing each crack:

$$\varepsilon^{CR} = \varepsilon_1^{CR} + \varepsilon_2^{CR} + \varepsilon_3^{CR} + \varepsilon_4^{CR} \dots \quad (7-3)$$

The fixed crack model is well accepted for very brittle materials. However *this model can lead to a bad prediction of the crack direction*. Indeed once the crack is initiated and evolves in the sample, we suppose that the crack direction is the same during all the simulation. It is not really physical since most of the time, the direction of the maximal principal strain is different from the crack axis, especially when dealing complex loading. This involves a phenomenon of "stress locking". It produces a too stiff response compared to the experimental results because of an excessive rotation of the stress. In this way, a solution consists in introducing the possibility of several planes (normal or not to the first plane).

### 7.2.1.2 Concept of rotating crack models

This model was proposed by De Borst and Nautain 1980 and introduced by Gupta [Gupta et al. 1984]. It is based on the same approach than the fixed crack model. However the crack can reorient during crack propagation and remains normal to the major principal stress during further loading. Results are often more realistic than the first concept. The tensile strength will never be exceeded in the rotating crack model. In addition the cracks automatically reflect the anisotropy induced by cracking. One can thus interpret them like particular models of anisotropic damage. Traditional finite element modelling forces the mesh to conform to the geometry of the crack lips. In the event of propagation remeshing is necessary. These concepts thus contributed to the simplification of remeshing. But, they remain hard to implement especially in 3D [Walter 1999].

### 7.2.1.3 Microplane models

Initially applied to metallic materials, the original idea of this approach is due initially to Taylor (1938) and was generalized in 1985 by Bazant and Oh [Bazant et al. 1985] to heterogeneous materials like concrete. It consists in discretizing behavior laws following a certain number of planes (microplanes), oriented by their normal, where  $i$  represents the components of the Cartesian co-ordinates of  $(x_i)_{i=1,2,3}$ . Physically these planes can be interpreted as the weakest material planes, represented by the interface between the aggregates and the mortar paste. The material is hence characterized by a relation between the stress and the strain tensors on planes with various orientations (see figure 7-4). Those are then superimposed to obtain macroscopic stress and strains tensors.

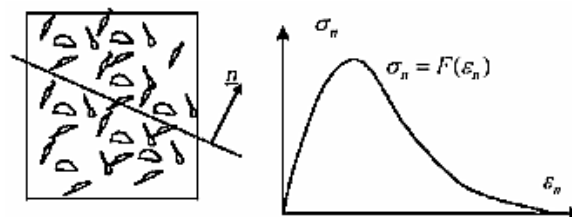


Figure 7-4. A microplane and the associated stress-strain relation [Saouridis 1988] The normal stress to a microplane is exclusively related to the normal strain to this plane.

The global stress is then obtained by integration [Jirasek 1999]:

$$\sigma = \left( \frac{3}{4\pi} \right) \int \sigma_n \bar{n} \otimes \bar{n} d\Omega_n \quad (7-4)$$

with an element of volume around the normal. This last stage is the most difficult but when several planes are activated, one must consider them simultaneously.

This model has been implemented into two and three dimensional nonlocal FE code (Castem 2000 for example [Fichant 1996]). The computation cost in the FE code [Fichant 1996] makes it almost unusable on classical computers for 3D calculations. This cost is mainly due to the calculation of the integrals. In addition, the greatest difficulty is the choice of the number of microplanes in order to find the global behavior laws. But this model has some advantages:

- It is simple, as it requires only the stress-strain relation for each of these microplanes to define the macroscopic material behavior;
- It is interesting to model anisotropic damage. Indeed one of the difficulties in the development of anisotropic damage models is the formulation of a law associated to the tensor of damage. Instead of deducing the stress-strain relationship starting from a complex damage law, this model makes it possible to deduce it from the damage tensor on each microplane starting from an equation connecting the stress to the strain;
- It gives good results with respect to experimental concrete observations.

#### 7.2.1.4 The X-FEM method (eXtended Finite Element Method)

The numerical modeling of crack propagation requires numerous expensive remeshing stages which gives raise to complex numerical difficulties in 3D. During the last ten years, many studies have been performed to dissociate the displacement discontinuity due to the crack, from the mesh topology. Meshless methods have been proposed, but they are not as robust and flexible as the FE method. The key idea of the X-FEM, suggested initially by Belytschko, is to deal with these discontinuities using **an advanced enrichment technique of the shape functions**. Conceptually this new technique to model discontinuities can be considered as a particular case of the partition-of-unity method [Melenk et al. 1996], [Babuska et al. 1997].

When a crack crosses an element, the nodes belonging to this element are located, and additional degrees of freedom are added to the element [Sukumar et al. 2000]. In this way, X-FEM extends the capabilities of the FE method without losing its advantages. The following figure shows an example of propagation without any mesh modification.

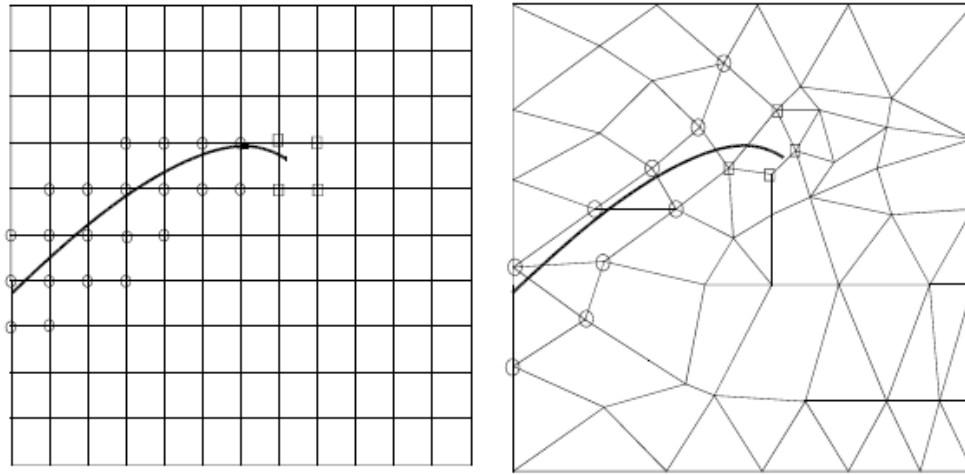


Figure 7-5. Regular and not regular meshes containing a crack and using the X-FEM. The circled nodes are enriched by the jump function  $H$  whereas the squared nodes are enriched by the branch tip function  $F$ . [Moes et al. 2002].

The square nodes correspond to the nodes of elements containing the crack tip, while circle nodes correspond to the nodes of the elements crossed by this crack. The finite element approximation is then enriched by two additional terms in order to highlight the presence of a crack:

$$u^h(x) = \sum_{i \in I} u_i N_i + \sum_{i \in L} a_i N_i H(f(x)) + \sum_{i \in K_1} N_i \left( \sum_{m=1}^4 b_{i,1}^m F_1^m(x) \right) + \sum_{i \in K_2} N_i \left( \sum_{m=1}^4 b_{i,2}^m F_2^m(x) \right) + \dots \quad (7-5)$$

Where:

- $I$  is the set of all nodes in the mesh;
- $u_i$  is the classical degree of freedom (vectorial) at node  $i$  ;
- $N_i$  is the shape function (scalar) associated with node  $i$  ;
- The  $H(.)$  function is defined as following:

$$H(x) = \begin{cases} -1 & \text{if } x > 0 \\ +1 & \text{if } x < 0 \end{cases} \quad (7-6)$$

-  $f(x)$  is the function “distance to the crack”. To evaluate  $H(f(x))$  we have to check the position of point  $x$  with respect to the crack location. To reach this goal, we use level functions ("level sets").

-  $L \subset I$  is the subset of nodes that are enriched by the crack discontinuity and the coefficient  $a_i$  are the correspondent degree of freedom (vectorial). A node belongs to  $L$  if its element is crossed by the crack but also if it does not contain any one of the tips of the crack (circled nodes in figure 7-5).

-  $K_1, K_2, \dots \subset I$  are the subset of nodes that are enriched for the first and second crack front respectively. The corresponding degree of freedom are  $b_{i,1}^m, b_{i,2}^m, m = 1..4$ . A node belongs to  $K_1, K_2, \dots$  if its element belong to the tip 1,2,... of the crack (square nodes in figure 7-5). The near-tip functions  $(F_1^m(x))_{m \in [1,4]}$  model hence the crack front :

$$\{F_1(x)\} = \left\{ \sqrt{r} \sin\left(\frac{\theta}{2}\right), \sqrt{r} \cos\left(\frac{\theta}{2}\right), \sqrt{r} \sin\left(\frac{\theta}{2}\right) \sin \theta, \sqrt{r} \cos\left(\frac{\theta}{2}\right) \sin \theta \right\} \quad (7-7)$$

Where  $(r, \theta)$  are the polar co-ordinates in the local axis at the crack front.

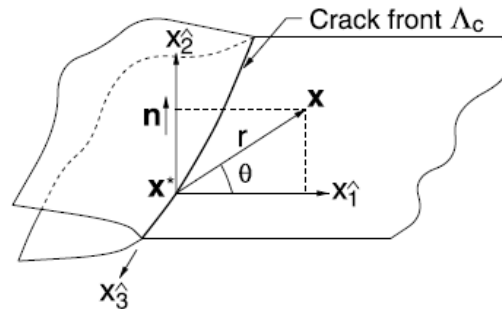


Figure 7-6. Co-ordinates configuration for crack front enrichment functions. [Sukumar et al. 2000].

The X-FEM method has three important advantages:

- It is not related to a particular behavior model (elastic, plastic etc.);
- It is no more necessary to adapt the mesh to surfaces of discontinuities;
- Enrichment is valid whatever the dimension of the problem: 1D, 2D, 3D and whatever the type of elements used.

Practically, this method presents however some difficulties: it is necessary to add degrees of freedom during simulation and to refine the diagram of integration in the zone enriched around the crack.

## 7.2.2 Mixed models

Linear Fracture Mechanics (LFM) is not sufficient for quasi-brittle materials like concrete, because of the presence of relatively large fracture process zone (FPZ) or microcrack zone, where we considered that microcracks are uniformly spread, ahead of a pre-existing macrocrack. In this zone the relation between stresses and strains is non-linear. This non-linear zone is very large in concrete compared to ductile materials. This difference comes from the heterogeneities of concrete and the large size of the aggregates. In this way, the energy dissipation is underestimated when the FPZ is neglected and consequently the material strength is overestimated. Bazant and coworkers [Bazant et al. 2002] differentiate three models depending on the structure size  $D$ , and the FPZ length  $w_f$ . It is generally assumed that  $w_f$  is proportional to the size of the aggregate:

- For  $D/wf \geq 100$ : we consider that the structures is very large (compared to the aggregate size) and the theory becomes equivalent to the LEFM;
- For  $5 \leq D/wf < 100$ : Non-linear quasi-brittle material;
- For  $D/wf < 5$ : Non local damage, discrete element methods, plasticity.



Figure 7-7. Non-linear behavior in a) brittle-ductile material, b) quasi-brittle material (concrete)

*L: linear behavior, N: non-linear behavior, f: fracture process zone [Bazant et al. 2002]*

The non-linear approach was initiated by Hillerborg et al. [Hillerborg et al. 1976] with the "fictitious model" (or "cohesive zone model") and it is widely accepted as the constitutive model to describe the mechanical behavior of quasibrittle material as concrete. Instead of considering an abrupt stress drop, this model introduces a tension - separation law which controls the progressive loss of cohesion along the line of fracture due to progressive microcracking. One then adopts a non-linear relation between the stress and the opening of the crack. Two relations are then essential to describe the behavior of concrete:

- The stress-strain relationship, which characterizes the zone away from the crack;
- The stress-displacement relationship that governs the crack opening (Crack Opening Displacement).

It is thus considered that the nonlinear behavior is located around the crack, while the material remains elastic linear elsewhere. The behavior law is no longer written in terms of stresses and strains but rather by defining a relation between the normal stress on the crack face and the normal opening of the crack. According to Hillerborg, a crack in a concrete specimen is thus characterized by two zones:

- **A real crack** ("traction free crack") where crack faces are fully separated; obviously a macro crack is formed when the energy driving the development of this crack reaches the fracture energy  $G_f$  (energy consumed in the formation and opening of all microcracks per unit area);
- **A damage zone** ("fracture process zone") in which the softening function is defined and where stresses are transferred due to frictional effects and other phenomena such as aggregate interlock.

The stress transfer normal to the crack direction can still take place. The transmitted stress (often called a "cohesive stress") is a function of the history of the opening of the crack. These cohesive traction-separation laws are based on the initial work of Dugdale [Dugdale 1960] and Barenblatt [Barenblatt 1962]. Several shapes, for the function  $f()$ , including linear,

bilinear, poly-linear and exponential, can be used to represent concrete. For a mode I crack opening, the transferred stress is normal to the face of the crack and is a function of the crack opening  $w$ :

$$\sigma = f(w) \quad (7-8)$$

This means that the cohesive forces are function of the crack width  $w$ .  $f(w)$  is considered as a material constant that can be determined by experiments. This equation is strictly valid for monotonic crack opening only.

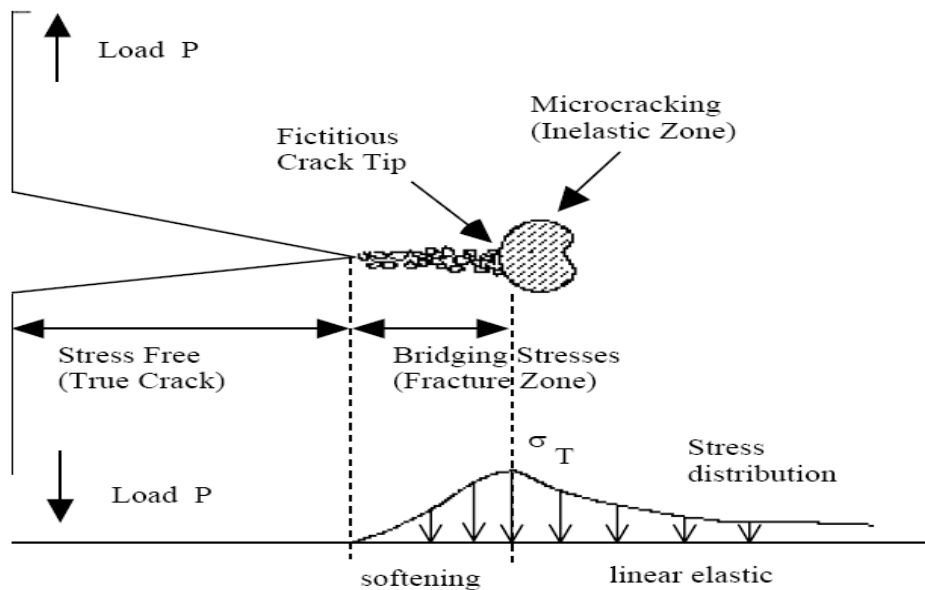


Figure 7-8. Schematic representation of the cohesive crack model and its associated shape function.

[Li et al. 2003]

For concrete and other cementitious materials a general bilinear function as a softening function, is appropriated. This function is completely characterized such by the following five parameters, known by measurements: the direct tensile strength  $\sigma_t$ , the specific fracture energy  $G_f$ ,  $\bar{w}$ ,  $w_1$  and  $w_c$  which is the critical crack opening (see figure 7-9). The identification of  $G_f$  is difficult and the RILEM (International Union of Laboratories and Experts in Construction Materials, Systems and structures) recommends to evaluate indirectly  $G_f$  by measuring the external work required to break a notched beam specimen during a stable test. One interesting result demonstrates that  $G_f$  is strongly dependent on the roughness of the inclusions [Wittmann 1993]. The determination of the softening function is the main issue for these models.

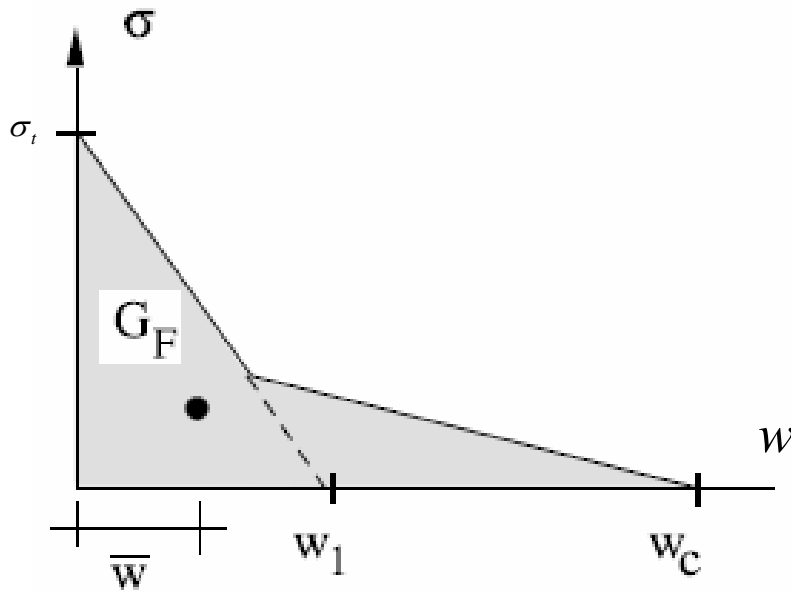


Figure 7-9. General bilinear function.[Elices et al. 2002]

The fracture energy  $G_f$  and the curve are considered as material properties and are dependent through the concept of "characteristic length"  $l_c$  (in mm):

$$l_c = \frac{EG_f}{\sigma_t^2} \quad (7-9)$$

The smaller the  $l_c$ , the more brittle the material. Early applications in the area of concrete fracture were limited to Mode I situations. This model was consequently inadapted to multiaxial stress field applications. An extension to cracks and interfaces opening under mixed-mode conditions was developed by Cervenka [Cervenka 1994], who used a loading function in the space of normal and shear tractions. These CZM models are available in FE code Cesar developed at LCPC (1998). This approach is interesting but some limits remain [Bazant et al. 2002]:

- It is convenient for the finite element analysis, especially when the fracture path is not known in advance;
- The identification of parameters of the stress-displacement curve with tensile tests are extremely difficult to obtain (multiple crack can occur in heterogeneous materials, unstable tests). We note then a great difference between the evaluated fracture energy  $G_f$  and the experimental one.

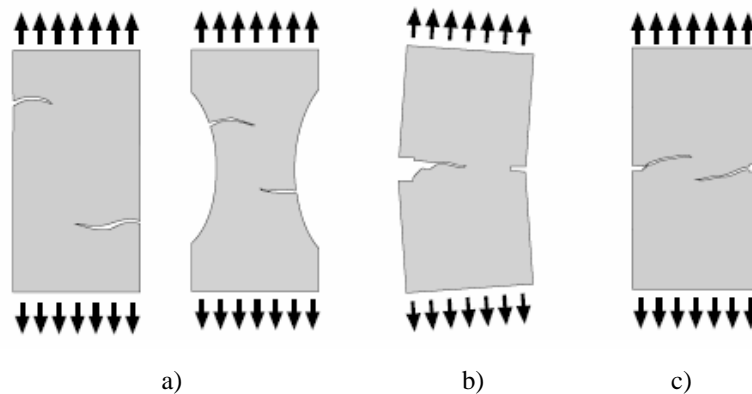


Figure 7-10. a) Multiple cracking in tensile specimens; b) Rotation of crack faces in pre-cracked specimen; c) crack overlapping. [Elices et al. 2002]

## 7.2.3 Discrete approaches

### 7.2.3.1 The “Kill element” method

This technique is largely used to model crack propagation. It is usually coupled to damage evolution. When the damage variable reaches a critical damage value within an element, the “kill element” technique is activated for 3D configurations. The element is then eliminated and its mechanical contribution is deleted. This method is rather coarse and depends on the mesh refinement. However, when the fracture process does not require the computation of accurate stress field in the fracture area, this technique is very useful to perform 3D computation up to the end of fracture. This method has been implemented in Forge3® and makes it possible to model successfully specific forming processes such as cutting, shearing etc. (see figure 7-11). The main limits of this technique are: when an element is deleted, there is a loss of volume equivalent to that of the element. Moreover, the shape of the elements deleted at a crack tip does not correspond to real crack tip shape. The stress field at the crack tip is thus depending also on the elements shape.

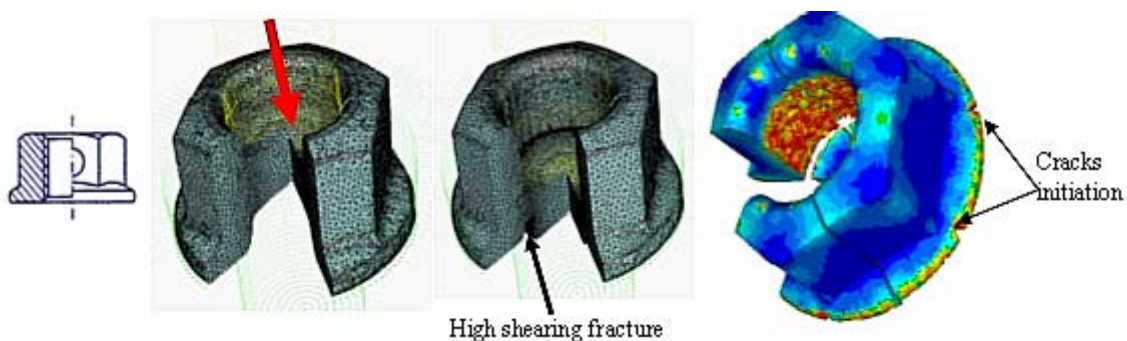


Figure 7-11. Cold forging of an hexagonal nut: the Lemaitre damage model enables to highlight the initiation of small cracks on the external part of the nut. It is also used with the “kill element” technique to model fracture during the fifth forging stage. Forging stages have been slightly modified to avoid cracks initiation in the last stage. [Bouchard 2005]

### 7.2.3.2 The Discrete Crack Approach

The first models used to model concrete fracture were discrete crack models. This approach was initially developed by Ngo and Scorledis [Ngo et al. 1967]. The cracks are modelled by a separation between the originally connected borders of elements. The FE model is then reconstructed at each step so that the element surfaces correspond to the crack. In the first approaches, crack propagation was based on a simple node splitting, meaning that crack path were dependent on the mesh topology. In order to improve the model, this approach has been modified. Automatic remesher and adaptative mesh refinement allow a better description of the crack front as well as non mesh dependent crack path.

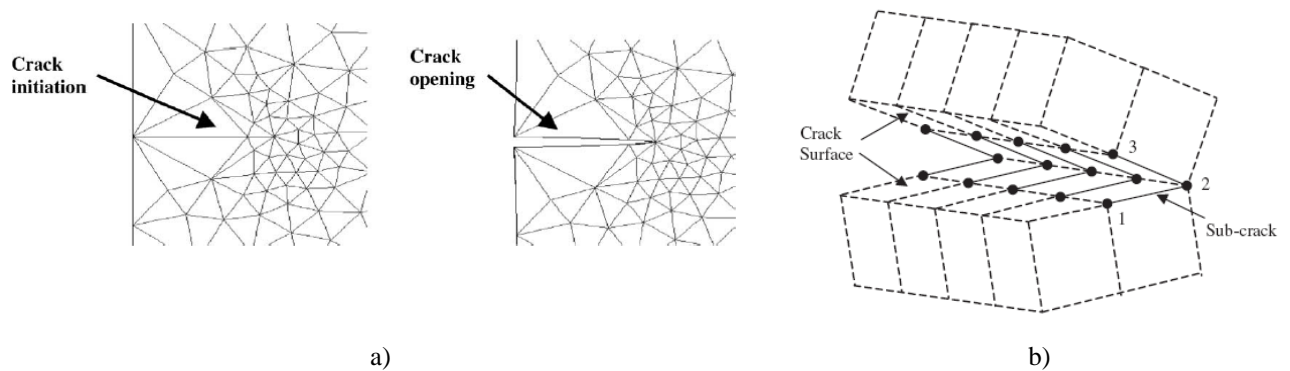


Figure 7-12. a) Crack initiation for 2D configurations [Bouchard et al. 2003], b) Decomposition of a 3D-crack tip. [Tabiei et al. 2003]

Bouchard [Bouchard et al. 2000] developed numerical tools in the code Forge2® Multimaterial making it possible to manage automatically and with accuracy the crack propagation in a 2D mesh. The following example we present cracks propagation on a pre-cracked part with two holes (see figure 7-13.a). The two cracks can be propagated with the same length since they are symmetric. Figure 7-13.b presents the Von Mises equivalent stress field in the sample and shows the influence of each crack on the other.

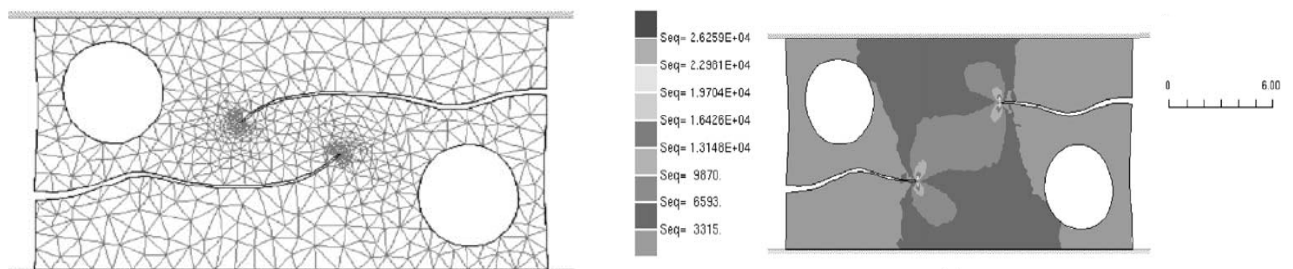


Figure 7-13. a) Crack trajectory in a pre-cracked part with two holes, b) Correspondent equivalent stress in the sample. [Bouchard et al. 2003]

Up to now, very few software tools enable discrete crack propagation in 3D. Indeed, 3D crack propagation induces numerous difficulties (two angles to estimate, generation of a 3D crack front and new free surfaces instead of a crack tip in 2D for example). The major

numerical difficulty for this 3D configuration is the continuous change of the 3D crack front which induces new free surfaces creation and modifications of surfacic and volumic mesh connectivity. Few labs are hence capable to simulate real fracture in 3D with the Discrete Crack Approach. First results obtained in 3D configurations were obtained with EPIC (Lim 1996), FRANC3D [Carter 2000] which is a three-dimensional fracture mechanics code developed by the Cornell Fracture Group for simulating arbitrary non-planar 3D crack growth, WARP3D (Koppenhoefer 1998). We can also quote the works of University of Paderborn with AdapCrack3D which uses an incremental approach with the Discrete Crack Approach [Schöllmann et al. 2003]. Figure 7-14 shows us a mode I crack propagation in a L-shape structure.

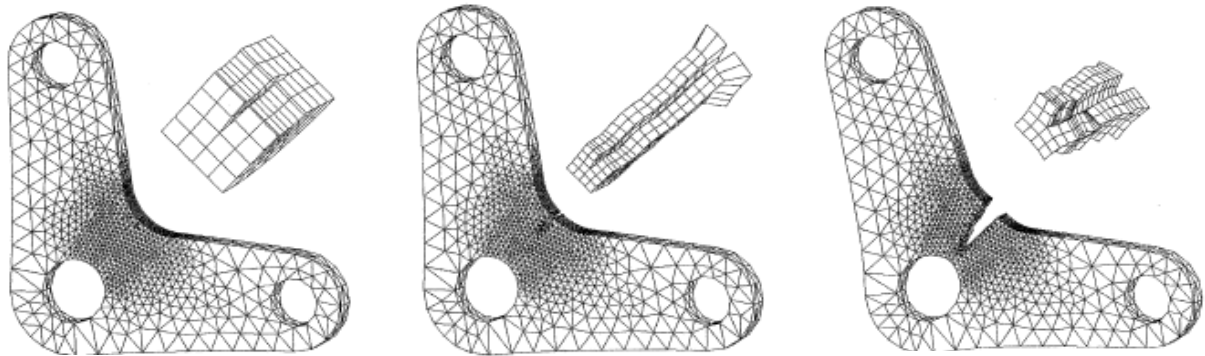


Figure 7-14. Crack growth simulation of a knee-lever with AdapCrack 3D, (a) 1st step, (b) 10th step, (c) 25th step. [Schöllmann et al. 2003]

The concept of discrete crack arises as being the approach which reflects the best the state of final damage of a concrete structure because it is based on a real geometrical description of cracks. It can also model the crack path of one or several cracks even in large strains. The automatic remesher can preserve a great accuracy of the mechanical fields around the crack front. It is also well adapted to study the influence of heterogeneities on the crack path, which is our goal in this study.

Each of these methods has substantial disadvantages. The major disadvantage of the Discrete Crack Approach method is remeshing which involves a considerable amount of engineering effort. Therefore most of the methods developed try to model crack without modification of the mesh topology. The continuous models do not make intervene the mesh topology. However these models cost a lot (in term of computation time) and are difficult to implement. Methods such as X-FEM are interesting but very recent and still require studies before being usable. The Fictitious Crack Model enables to take into account the progressive decohesion of the free surfaces of a crack. However this method is limited as it is uniaxial.

The Discrete Crack Approach thus remains the most realistic models and has reached a high state of maturity.

## 7.3 Implementation of the Discrete Crack Approach in the finite element code FEMCAM

### 7.3.1 Introduction on the 3D crack modulus

Two types of fracture mechanisms can be used to model fracture: The **Linear Fracture Mechanism (LFM)** or **The Non Linear Fracture Mechanism (NLFM)**. The LFM is used to describe the fracture of brittle and quasi-brittle material. But it can consider a plastic zone ahead of the crack front only if this zone stays confined and with constant dimensions. The NLFM integrates the possibility of plasticity around the crack front.

In our study, we will only consider LFM and model concrete using an **elastic damage behavior**. For more than two decades special purpose FE codes have been used to model crack growth. This chapter outlines the algorithm of the 3D automatic Crack Modulus in FEMCAM. Figure 7-15 describes how damage and crack propagation are used in FEMCAM and the location of the 3D crack modulus in the code. We will detail this algorithm:

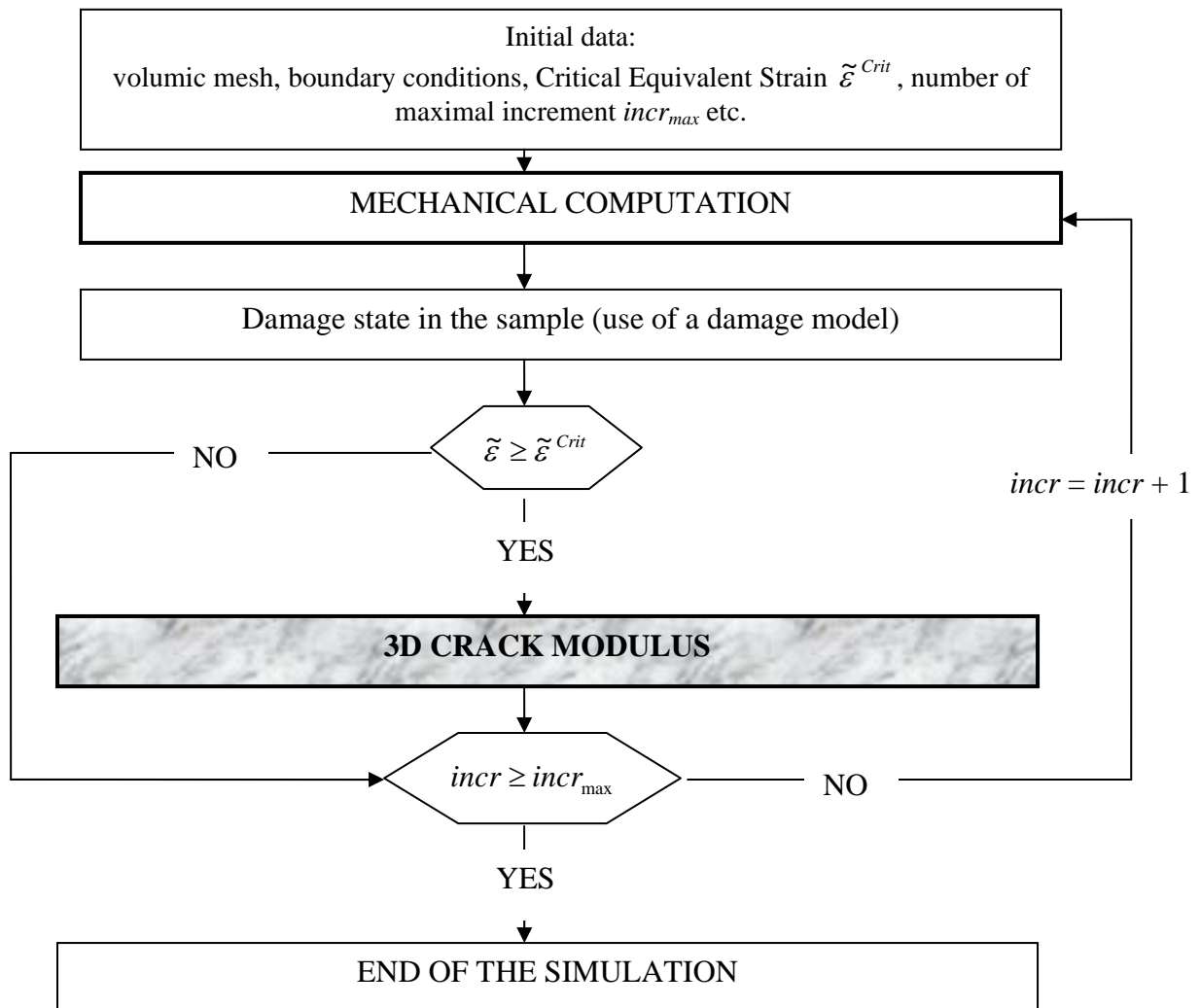


Figure 7-15. Resolution of a problem with 3D crack propagation.

At each increment, crack progress through a continuous change of the elements connectivity and the mesh topology in the crack front. It leads to the creation of new crack fronts. The generated area is thus a plane surface depicted by a number of finite element faces.

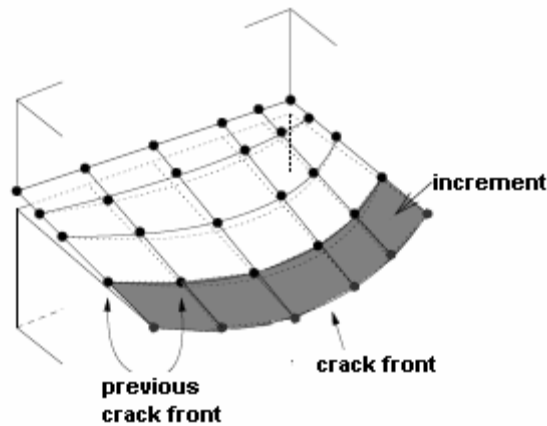


Figure 7-16. Progression of the crack front.

Four steps model the crack process to generate and propagate a crack as shown in figure 7-16:

- **The initialization** step consists in reusing the nodes of the previous crack front. If it is the first crack increment, it is then important to know where and when the crack is initiated to locate the initial nodes;
- **The opening** step which includes the evaluation of the length  $da$  and the opening  $dw$  of the crack during each crack propagation increment;
- **The bifurcation** step corresponds to the evaluation of the crack direction. We have thus to know in which direction the crack evolves;
- **The propagation** step focuses on the modification of the mesh topology in order to create a new crack front. It also integrates the **remeshing step**, which consists in a volumic remeshing of the sample for the next increment.

### 7.3.2 “Initialization” step

This step considers two cases whether the crack has already propagated in the sample or not. Many criteria can be used to predict when and where cracks initiate and propagate. We can use some critical value of the material, for example a critical stress or a critical damage  $D^{Crit}$ . Crack extensions can be provoked by these previous critical value and also through a critical stress intensity factor  $K_{IC}$ , the Crack Tip Opening Angle  $CTOA$ , or a critical energy release rate  $G_C$ . When these critical values are satisfied or are exceeded, the crack can propagate.

In chapter 2 we have presented the Mazars damage model. We have identified damage parameters and have found a critical equivalent strain  $\tilde{\varepsilon}^{Crit}$  which induces macrocracks in the sample in compression and in tension. **We use this value as a macrocrack threshold for the crack initiation and propagation.** When the threshold is exceeded in one or more elements

belonging to the crack front, they are affected by the extension (topology, nodes allocation ...) of the crack front.

Concerning the location of initiation it is more difficult to introduce a crack anywhere in the sample than to propagate it. In our 3D numerical model, we have used two possible methods:

- The first method consists in prescribing the initial nodes. The method used determines a volume  $V$  (with arbitrary lengths) in which nodes are possibly located. When crack occurs, the method searches all nodes belonging to this volume  $V$ . In the future, an initiation criterion, based on damage for example, should be added to our model to evaluate physically the location of the initial crack;
- The second method, generally proposed, consists in introducing one or several pre-cracks in the sample. Then, our method evaluates all nodes belonging to the pre-crack with the previous method.

However these methods are efficient only if they are combined to a nodes selection of the surfaces as shown in figure 7-17. We notice that the volume can contain other nodes than the nodes of the crack front. It is then useful to use the data on the finite elements in which nodes are (orientation of the faces) to obtain the good set of initial nodes.

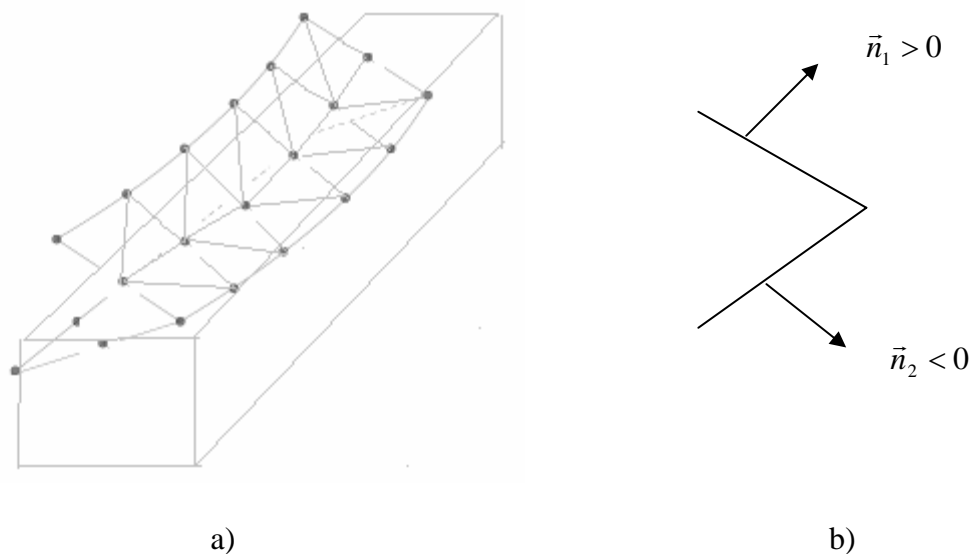


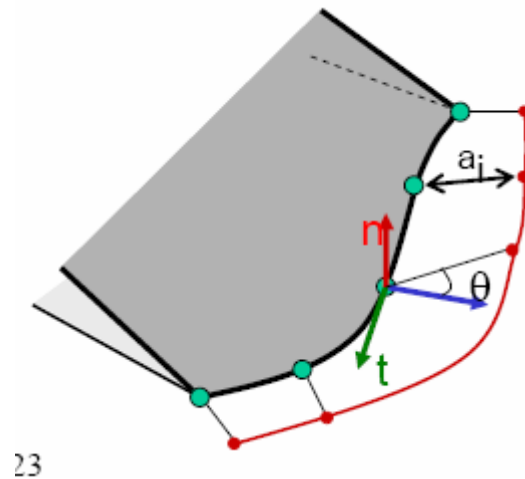
Figure 7-17. a) Volume  $V$  around the pre-crack to locate nodes of the initial crack front; b) orientation of the faces of the crack front.

### 7.3.3 “Opening” step

Fracture is characterized by two dimensions: the crack length  $da$  and the crack opening  $dw$ . Given a maximum crack increment  $a_{\max}$ , the amount of crack extension  $a_i$  at each node  $i$  of the crack front was determined based on the Paris crack growth relationship and used stress intensity factors (SIF):

$$a_i = a_{\max} \left( \frac{K_I}{K_{I,\max}} \right)^b \quad (7-10)$$

Where  $a_{\max}$  was the maximum defined crack extension along the crack front defined the software's user,  $K_{I,\max}$  is the maximum value of  $K_I$  along the crack front and  $b$  corresponds to the Paris material exponent. It underlines that the extremum nodes propagates lower than the interior nodes of the crack front (see figure 7-18).



23

Figure 7-18. Crack extension rule. [Ingraffea 2004]

However this technique requires a particular attention concerning the mesh refinement. In these conditions most studies considered these two lengths as given parameters (sometimes defined in function of the mesh size). These two dimensions are not predicted by our 3D numerical model and must be given by the user.

Then, the essential tools to predict crack propagation are a **propagation criterion** (when is the crack going to propagate?) and a **direction criterion** (in which direction is the crack going to propagate?). This part focuses on the different alternatives for these criteria.

### 7.3.4 “Bifurcation” step

Cracks do not always grow straight ahead; sometimes they reorient. Three dimensional loading conditions often occur along crack fronts of real-world structures. All loading combinations can be described by a superposition of the basic fracture modes as introduced by Irwin (see figure 7-19). It includes opening (mode I), sliding (mode II), and tiring (mode III) modes.

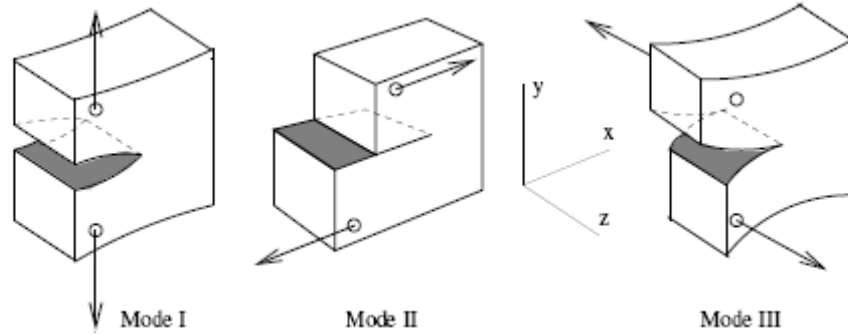


Figure 7-19. Basic fracture modes by Irwin (1957) that can be applied to a crack.

When concrete is submitted to a tensile test, the consequences are the presence of cracking in mode I. Compression test leads to cracks in mode II and mode III. However, the numerical modelling of crack propagation in concrete at a mesoscale involves a combination of the three fracture modes. Even for pure traction, the heterogeneities due to the location of aggregates lead to crack reorienting. Cracks at the interface between aggregates and mortar paste evolve. They are generally parallel to the load axis and are mainly due to the friction between the mortar paste and the aggregate [Mac Creath et al. 1696]. The stress field  $\sigma_{ij}$  for the superposition of all three fracture modes can be described by the near-field solutions:

$$\begin{aligned}
 \sigma_r &= \frac{K_I}{4\sqrt{2\pi r}} \left[ 5 \cos\left(\frac{\varphi}{2}\right) - \cos\left(\frac{3\varphi}{2}\right) \right] - \frac{K_{II}}{4\sqrt{2\pi r}} \left[ 5 \sin\left(\frac{\varphi}{2}\right) - 3 \sin\left(\frac{3\varphi}{2}\right) \right] \\
 \sigma_\varphi &= \frac{K_I}{4\sqrt{2\pi r}} \left[ 3 \cos\left(\frac{\varphi}{2}\right) + \cos\left(\frac{3\varphi}{2}\right) \right] - \frac{K_{II}}{4\sqrt{2\pi r}} \left[ 3 \sin\left(\frac{\varphi}{2}\right) + 3 \sin\left(\frac{3\varphi}{2}\right) \right] \\
 \tau_{r\varphi} &= \frac{K_I}{4\sqrt{2\pi r}} \left[ \sin\left(\frac{\varphi}{2}\right) + \sin\left(\frac{3\varphi}{2}\right) \right] - \frac{K_{II}}{4\sqrt{2\pi r}} \left[ \cos\left(\frac{\varphi}{2}\right) + 3 \cos\left(\frac{3\varphi}{2}\right) \right] \\
 \tau_{rz} &= \frac{K_{III}}{\sqrt{2\pi r}} \sin\left(\frac{\varphi}{2}\right) \\
 \tau_{\varphi z} &= \frac{K_{III}}{\sqrt{2\pi r}} \cos\left(\frac{\varphi}{2}\right) \\
 \sigma_z &= \frac{8\nu}{4\sqrt{2\pi r}} \left[ K_I \cos\left(\frac{\varphi}{2}\right) - K_{II} \sin\left(\frac{\varphi}{2}\right) \right]
 \end{aligned} \tag{7-11}$$

Where  $K_I$ ,  $K_{II}$  and  $K_{III}$  are the stress intensity factors (SIF) for the fracture in modes I, II and III,  $(r, \varphi, z)$  are the cylinder coordinates originated at the crack front and  $\nu$  is the Poisson ratio (see figure 7-20). The expression of  $\sigma_{ij}$  denotes the singularity of the stress tensor near the crack front (see figure 7-20). Stress concentration surrounding the crack front is dependant upon the direction and geometry of the crack. It can be seen that the stress decreases when getting farther from the crack. In order to capture this singularity, special elements are required [Barsoum 1976], [Bouchard et al. 2000].

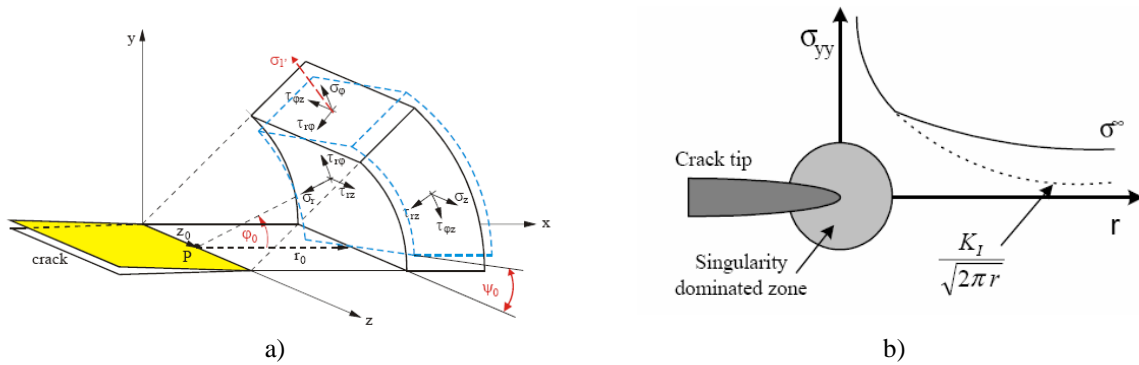


Figure 7-20. Stress components and cylinder co-ordinates near the crack front in a) 3D; b) 2D.

Two kinds of methods exist in 2D to predict the macrocracks direction: the global approaches or the local ones. The global (or energetic) approach is based on the study of the maximum strain energy release rate in a cracked sample. The local approach uses the stress and strain fields in the vicinity of the crack front.

### 7.3.1 The Maximum strain energy release rate

In their original model, Erdogan and Sih noted that “if we accept Griffith (energy) theory as the valid criteria to explain crack growth, then the crack will grow in the direction along which the elastic energy release per unit crack extension will be maximum [...]”. The angle of crack propagation  $\varphi_0$  is found by maximising  $G(\varphi)$  :

$$\frac{\partial G(\varphi)}{\partial \varphi} = 0 \quad \text{and} \quad \frac{\partial^2 G(\varphi)}{\partial \varphi^2} < 0 \quad (7-12)$$

Bouchard [Bouchard et al. 2000] has used an innovative technique, initially proposed by Destuynder: the **G $\theta$  method** [Destuynder 1983] in Forge2®. A virtual field  $\theta$  is defined on a ring surrounding the crack tip (figure 7-21) and is used to describe a virtual crack extension. An infinitesimal perturbation of the mechanical fields in a ring surrounding the crack tip enables to compute  $G$ . This method is accurate and enables a fast computation of the parameter  $G$ . It is then possible to compute  $G$  for different direction of crack extension. The good direction is the one that maximises the strain energy release rate.

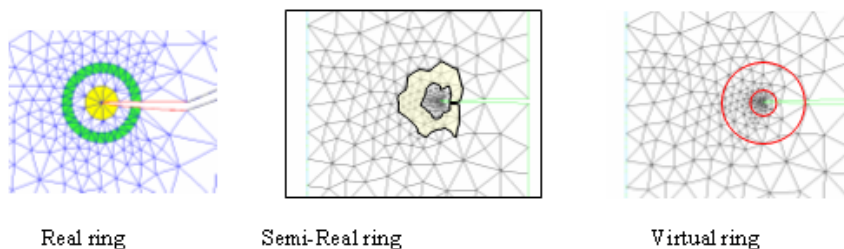


Figure 7-21. Mesh structure and ring of elements at the crack tip: special quarter-points elements have been implemented to deal with the stress singularity at the crack tip and the mesh structure is flexible enough to represent a circular ring of elements surrounding the crack tip. Different kinds of rings (real, semi-real, virtual) have been compared to check the accuracy of the strain energy release rate computation [Bouchard 2005].

The 2D automatic remeshing is then used to model the automatic crack propagation for

different configurations.

### 7.3.2 The Circumferential Stress Criterion

For Linear Elastic Fracture Mechanics, the circumferential stress criterion developed by Erdogan and Sih [Erdogan et al. 1963] enables to compute the crack propagation direction  $\varphi$ . **This criterion is based on local stress fields** and it states that crack propagates in the perpendicular direction of the maximum circumferential stress. So we have to solve a system based on SIF in order to find the angle for the crack extension:

$$K_I \sin \varphi + K_{II} (3 \cos \varphi - 1) = 0$$

with

$$\begin{cases} K_{II} \sin \varphi/2 < 0 \\ \varphi \in ]-\pi, \pi[ \\ K_I > 0 \end{cases} \quad (7-13)$$

Currently the SIF are calculated using the displacement field  $(u, v, w)$  for each node. Indeed we obtain more accurate results as the displacement field is obtained directly on each node, whereas the stress field is given, in FEMCAM within an element at an integration point. It requires then an extrapolation to obtain the field for each node. For instance, for the mode I and in 2D, we have:

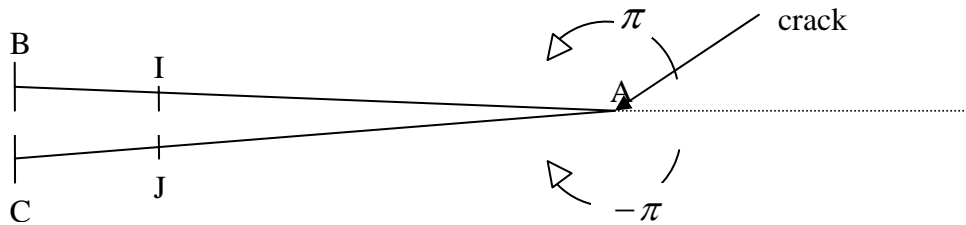


Figure 7-22. I and J are two points on each side of the crack lips for a P1+P1 finite element.

To localize the B and C nodes in the mesh, we use the following algorithm:

---

*Algorithm 7-1. Localization of nodes to evaluate displacement fields.*

---

- All triangles which contains the node A (corresponding to figure 7-22) are stored in a table;
  - A list  $\mathfrak{T}$  is created with all nodes belonging to these triangles and different from the node A;
  - We search node B such as  $d(A, B) = \min(d(A, x) | x \in \mathfrak{T} \cap \{\text{upper crack front}\})$
  - We search node C such as  $d(A, C) = \min(d(A, x) | x \in \mathfrak{T} \cap \{\text{lower crack front}\})$
-

For the mode I for example, we have:

$$K_I = \lim_{r \rightarrow 0} \frac{2\mu}{k+1} \sqrt{\frac{2\pi}{r}} v_I$$

$$K_I = -\lim_{r \rightarrow 0} \frac{2\mu}{k+1} \sqrt{\frac{2\pi}{r}} v_J$$
(7-14)

Where  $r$  is the distance to the crack front,  $\mu$  is the shear modulus and

$$k = \begin{cases} 3 - 4\nu & \text{in plane strain} \\ \frac{3 - \nu}{1 + \nu} & \text{in plane stress} \end{cases} . \text{ We obtain hence:}$$

$$K_I = \lim_{r \rightarrow 0} \frac{\mu}{k+1} \sqrt{\frac{2\pi}{r}} (v_I - v_J)$$
(7-15)

More generally the SIF implementation is given by:

$$K_I = \lim_{r \rightarrow 0} \frac{\mu}{k+1} \sqrt{\frac{2\pi}{r}} (v_I - v_J)$$

$$K_{II} = \lim_{r \rightarrow 0} \frac{\mu}{k+1} \sqrt{\frac{2\pi}{r}} (u_I - u_J)$$

$$K_{III} = \lim_{r \rightarrow 0} \frac{E}{4(1+\nu)} \sqrt{\frac{2\pi}{r}} (w_I - w_J)$$
(7-16)

Solution of the Eq. ( 7-13) gives the angle of crack extension  $\varphi_0$  :

$$\tan\left(\frac{\varphi_0}{2}\right) = \frac{1}{4} \frac{K_I}{K_{II}} \pm \sqrt{\left(\frac{K_I}{K_{II}}\right)^2 + 8}$$
(7-17)

Under pure mode I, the crack goes straight ahead. At the opposite, when  $K_I$  is null,  $\varphi$  is equal to  $-70.53^\circ$  for positive  $K_{II}$  and  $70.53^\circ$  for negative  $K_{II}$  independently of the magnitude of  $K_{II}$ . In these conditions we suppose that **the propagation is plane** so we exclude a possible propagation according to three axes. In this way we have only one angle to determinate;

This method predicts relatively well the propagation direction of a crack in a (quasi-) brittle material.

### 7.3.3 Schöllmann, Richard et al. criterion [Schöllmann et al. 2002]

This criterion is a 3D extension of the maximum circumferential stress criterion. The description of the direction of the crack propagation is provided by the definition of two deflections angles  $\varphi_0$  and  $\psi_0$  (see Eq. ( 7-21) and Eq. ( 7-22)).

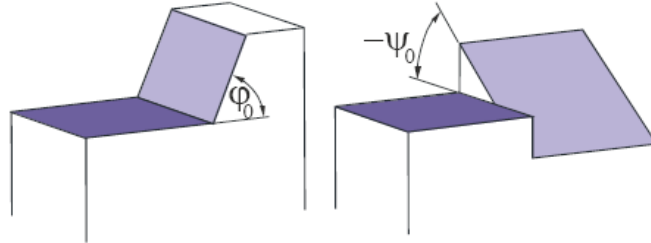


Figure 7-23. Definition of the crack deflection angles  $\varphi_0$  and  $\psi_0$ . [Fulland et al. 2003]

The angle  $\varphi_0$  describes the local crack front kinking, which is closely related to the mode II portion of each point of the crack front and it is characterized by the following relation:

$$\left. \frac{\partial \sigma'_1}{\partial \varphi_0} \right|_{\varphi=\varphi_0} = 0 \text{ and } \left. \frac{\partial^2 \sigma'_1}{\partial^2 \varphi_0} \right|_{\varphi=\varphi_0} > 0 \quad (7-18)$$

In which:

$$\sigma'_1 = \frac{\sigma_\varphi + \sigma_z}{2} + \frac{1}{2} \sqrt{(\sigma_\varphi - \sigma_z)^2 + 4\tau_{\varphi z}} \quad (7-19)$$

$\sigma_\varphi, \sigma_z, \tau_{\varphi z}$  are given in cylinder coordinates (see figure 7-20). The angle  $\psi_0$  defines the crack front twisting predominantly influenced by mode III. It is given by:

$$\psi_0 = \frac{1}{2} \arctan \left( \frac{2\tau_{\varphi z}(\varphi_0)}{\sigma_\varphi(\varphi_0) - \sigma_z(\varphi_0)} \right) \quad (7-20)$$

Eq. ( 7-18) and Eq. ( 7-20) leads to the following system. The resolution of these equations is not easy as we can see Eq. ( 7-21) and ( 7-22). Some specific tables exist to give the  $\varphi_0$  values versus  $K_I, K_{II}$  and  $K_{III}$  (see appendix A.5).

$$\begin{aligned}
 & -6K_I \tan\left(\frac{\varphi_0}{2}\right) - K_{II} \left(6 - 12 \tan^2\left(\frac{\varphi_0}{2}\right)\right) + \\
 & \left\{ \left[ 4K_I - 12K_{II} \tan\left(\frac{\varphi_0}{2}\right) \right] \times \left[ -6K_I \tan\left(\frac{\varphi_0}{2}\right) - K_{II} \left(6 - 12 \tan^2\left(\frac{\varphi_0}{2}\right)\right) \right] \times \right. \\
 & \left. \left[ -32K_{III}^2 \tan\left(\frac{\varphi_0}{2}\right) \times \left(1 + \tan^2\left(\frac{\varphi_0}{2}\right)\right) \right] \right\} \times \\
 & \left\{ \left[ 4K_I - 12K_{II} \tan\left(\frac{\varphi_0}{2}\right) \right]^2 + 64K_{III}^2 \left(1 + \tan^2\left(\frac{\varphi_0}{2}\right)\right) \right\}^{-1/2} = 0
 \end{aligned} \tag{7-21}$$

$$\psi_0 = \frac{1}{2} \arctan \left( \frac{8K_{III} \cos\left(\frac{\varphi_0}{2}\right)}{K_I \left(3 \cos\left(\frac{\varphi_0}{2}\right) + \cos\left(\frac{3\varphi_0}{2}\right)\right) - K_{II} \left(3 \sin\left(\frac{\varphi_0}{2}\right) + 3 \sin\left(\frac{3\varphi_0}{2}\right)\right)} \right) \tag{7-22}$$

The equation Eq. (( 7-21) cannot be solved in a closed form explicitly. To simplify the problem,  $\varphi_0$  and  $\psi_0$  are rewritten as follows:

$$\varphi_0 = \pm \left[ A \frac{|K_{II}|}{K_I + |K_{II}| + |K_{III}|} + B \left( \frac{|K_{II}|}{K_I + |K_{II}| + |K_{III}|} \right)^2 \right] \tag{7-23}$$

With  $\varphi_0 < 0^\circ$  with  $K_{II} > 0$  and  $\varphi_0 > 0^\circ$  with  $K_{II} < 0$  and  $K_I \geq 0$ .

$$\psi_0 = \pm \left[ C \frac{|K_{III}|}{K_I + |K_{II}| + |K_{III}|} + D \left( \frac{|K_{III}|}{K_I + |K_{II}| + |K_{III}|} \right)^2 \right] \tag{7-24}$$

With  $\psi_0 < 0^\circ$  with  $K_{III} > 0$  and  $\psi_0 > 0^\circ$  with  $K_{III} < 0$  and  $K_I \geq 0$ . When  $A=140^\circ$ ,  $B=-70^\circ$ ,  $C=78^\circ$  and  $D=33^\circ$ , angles give good approximations. So this criterion provides unique propagation directions at any point of the crack front in dependence of the local mixed mode situation [Richard et al. 2003].

This technique has been implemented in FEMCAM to predict crack direction. But today we have no possibility to have real 3D crack propagation. Indeed the geometric difficulties are numerous to do that (possible overlapping of the finite element in the case of a possible propagation of nodes at the surface into the volume sample). **Therefore we use partially this technique as we have only the Eq. ( 7-22) to solve in order to find angle  $\varphi_0$  which corresponds to a fracture in mode I+II only.** We evaluate the propagation direction for each node of the crack front with a crack growth criterion. This evaluation is based on the

stress and displacement fields evaluated during the mechanical computation. A fine mesh is recommended at the crack front since the accuracy of the computation of the crack direction depends on the accuracy of displacement or stress fields in the vicinity of the crack front.

### 7.3.5 “Propagation” step

The mesh topology is modified. This step is the most difficult in the “Discrete crack” method. It consists in modifying automatically the geometric and topologic transformations due to the crack propagation in the sample. This algorithm is based on four steps:

**Step 1** consists in extracting the surfacic mesh from a volumic mesh. This step creates new tables in which the nodes and the elements number of the initial surfacic mesh are recorded. It records also the connectivity between nodes. The number of the nodes belonging to the crack front and their coordinates are also recorded. We differentiate herein the extremum nodes and the internal nodes.

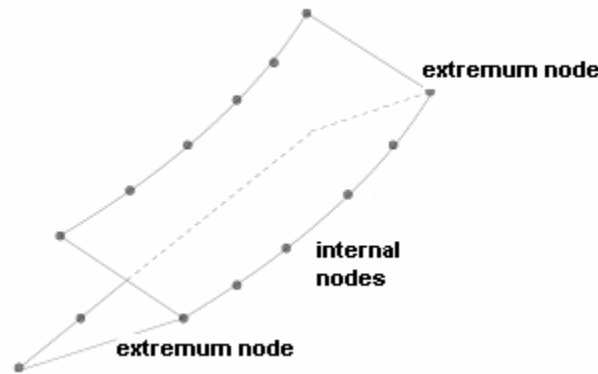


Figure 7-24. Initial nodes submitted to a future crack propagation.

**Step 2** concerns crack propagation. At each point of the crack front, a new front is computed. This step focuses on the extremum nodes:

- a) First the algorithm evaluates the position of the new extremes nodes. If the distance between the new and the old crack front is too long, in term of number of faces to cross, the problem is divided and some intermediary crack fronts are created. The aim is to obtain a new surfacic mesh with good quality elements (see figure 7-27);
- b) A new node  $n_{i+1}$  is added in the table corresponding to the new crack front. The main difficulty is to correctly identify the face which contains this new node  $n_{i+1}$ . Hence if a load is applied on the sample, the nodes can move and it is thus very difficult to identify them. It is then important to use the orientation of each face to add a supplementary mean to localize this face.
- c) The initial node  $n_i$  is splitted into two nodes,  $n_i^a$  and  $n_i^b$ , to open the crack.

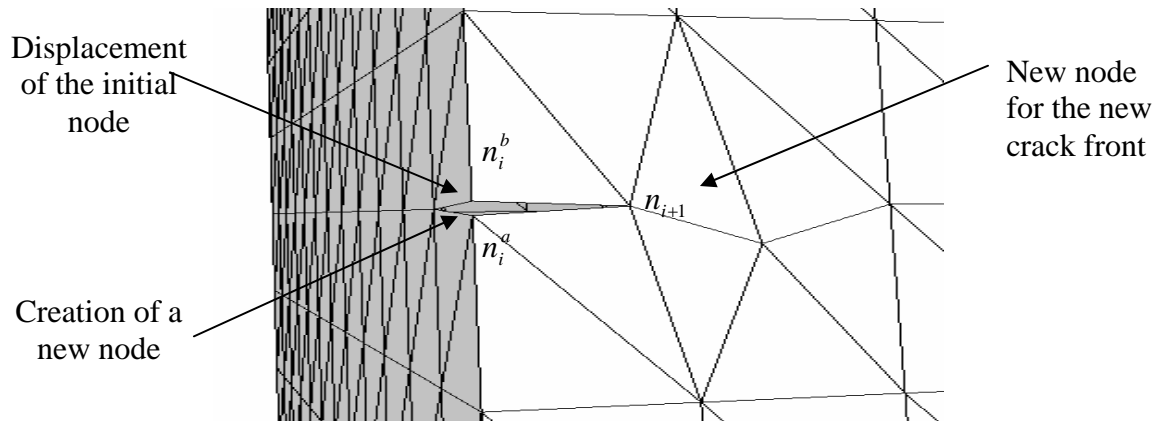


Figure 7-25. Insertion of new external nodes in the mesh for the beginning of the crack front.

The b) and c) points induce the modification of the surfacic mesh topology in order to create new surfacic elements. Once the new nodes  $n_{i+1}$  and  $n_i^b$  are created, a new topology is made. To do that:

- We evaluate the faces which are located between the old and the new front and. It consists in using the sign of the dot product (see Algorithm 7-2).

---

*Algorithm 7-2 : Algorithm of research of the location of nodes*

---

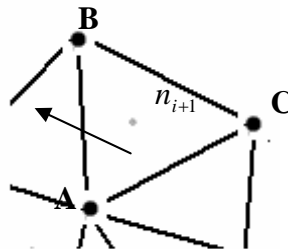


Figure 7-26. Research of the location of a node in the table of faces.

- We test all faces. Let  $(ABC)$  be a selected face;
- We test the position of  $n_{i+1}$ , by evaluates the dot product  $\alpha$  between the vector products  $\vec{AB} \wedge \vec{AC}$  and  $\vec{AB} \wedge \vec{An}_{i+1}$ ,  $\vec{BC} \wedge \vec{Bn}_{i+1}$ ,  $\vec{CA} \wedge \vec{Cn}_{i+1}$  respectively. If  $\alpha > 0$  in the three case, we consider that  $n_{i+1}$  belongs to the face  $(ABC)$ ;
- A line is plotted between the two extrema nodes  $n_i^a$  and  $n_{i+1}$  ;
- Knowing the face in which  $n_{i+1}$  is, we determine all faces crossed by the line (the technique consists in finding the intersection point between this line and the segments of the faces).

- 
- The connectivity between these faces is deleted and we only keep the nodes corresponding to these faces as shown in figure 7-27. These nodes are placed in a table and arranged in order to keep the same orientation than the other faces of the mesh.
-

- We use a technique in “star” to generate a new connectivity and create other elements.

In the schematic representation below, we present only the connectivity change induced by the creation of the node  $n_{i+1}$ .

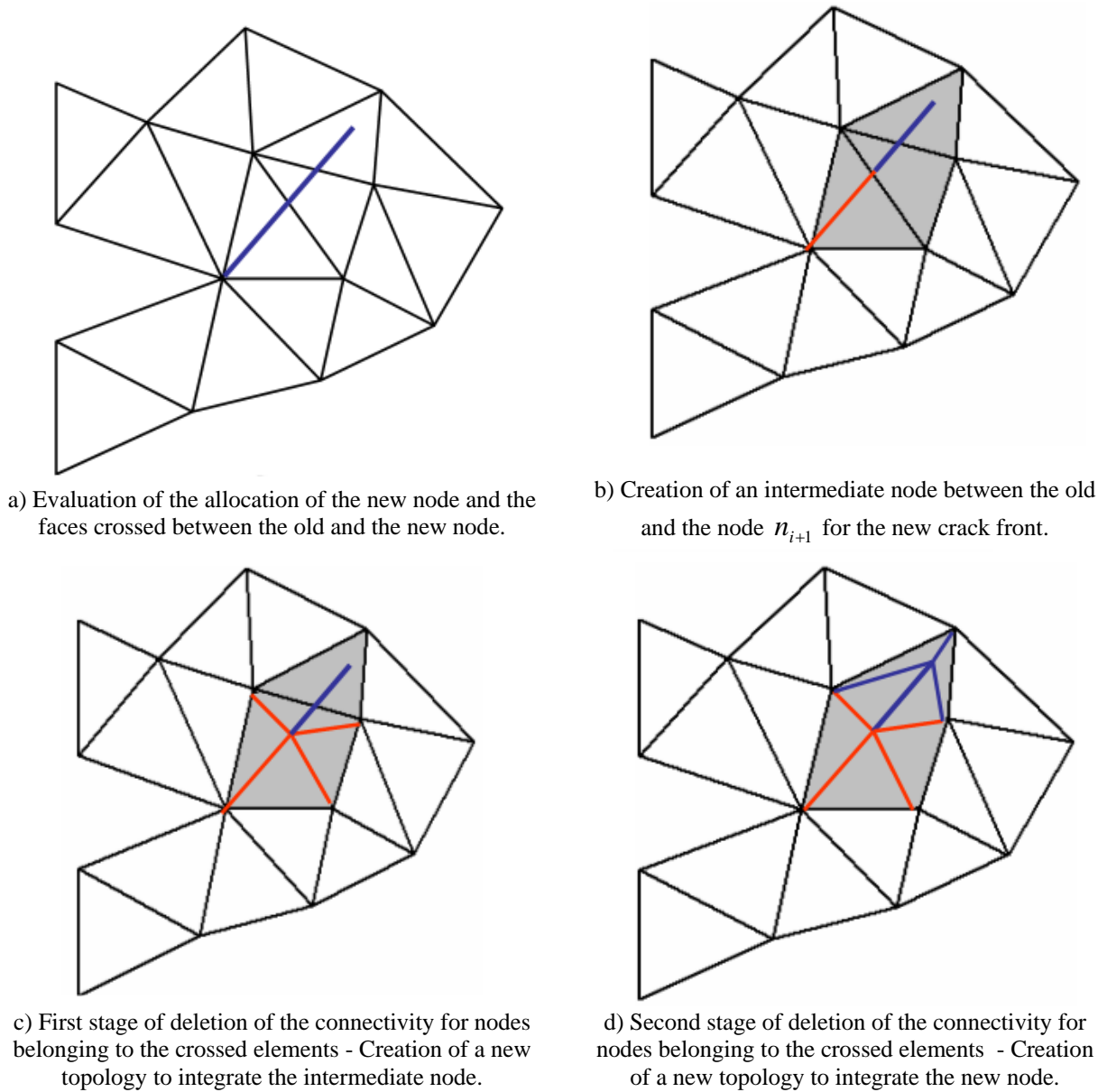


Figure 7-27. Schematic representation in 2D of the steps to create the new crack front.

**Step 3** consists in generating the crack front by adding the interior nodes. We create new nodes in the sample and connect them to the old crack front to generate new free surfaces. Figure 7-28 presents a state of crack propagation.

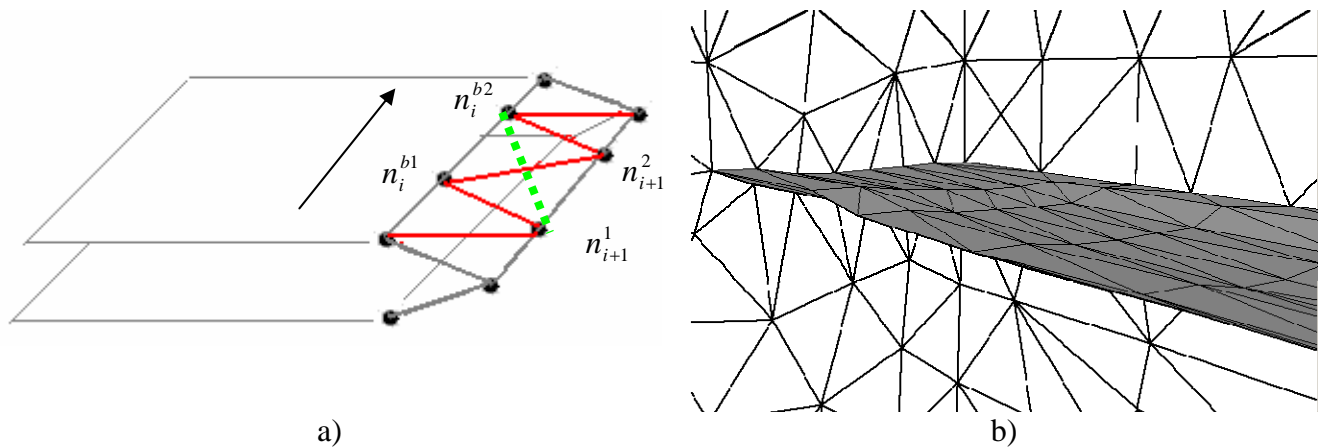


Figure 7-28. a) Schematic representation of the new faces of the crack front; b) Creation of new free surfaces to simulate the crack propagation into the volume.

The connection between the old and the new nodes can lead to geometrical problems. Sometimes the upper surface crossed the lower one. In this case, we have added a supplementary condition to change the face connectivity. Figure 7-28.a represents this problem. If we consider that the connection between  $n_i^{b1}$  and  $n_{i+1}^2$  leads to geometrical problem, we inverse the connection and connect  $n_i^{b2}$  to  $n_{i+1}^1$  (represented by the dotted line in green).

**Step 4** is necessary to use the new created mesh, containing the crack propagation, for a new mechanical computation. We use all the data we have recorded, to generate a new volumic mesh. In this way we use the powerful remesher developed at CEMEF with specific conditions as new nodes and elements have been generated. First mechanical variables are transported from the old mesh to the new one.

Furthermore the user can specify several requirements to the automatic remesher in order to improve elements quality through a data file: add or block nodes, refine the mesh in a specific area etc. We have hence transformed the “classical” remesher of FEMCAM to an adaptive remesher specific for fracture. We could obtain a better accuracy on mechanical fields closed to the crack front. Today the algorithm activates the remeshing on the whole sample. It could be optimized by reducing this remeshing to the crack zone in order to decrease the computation time.

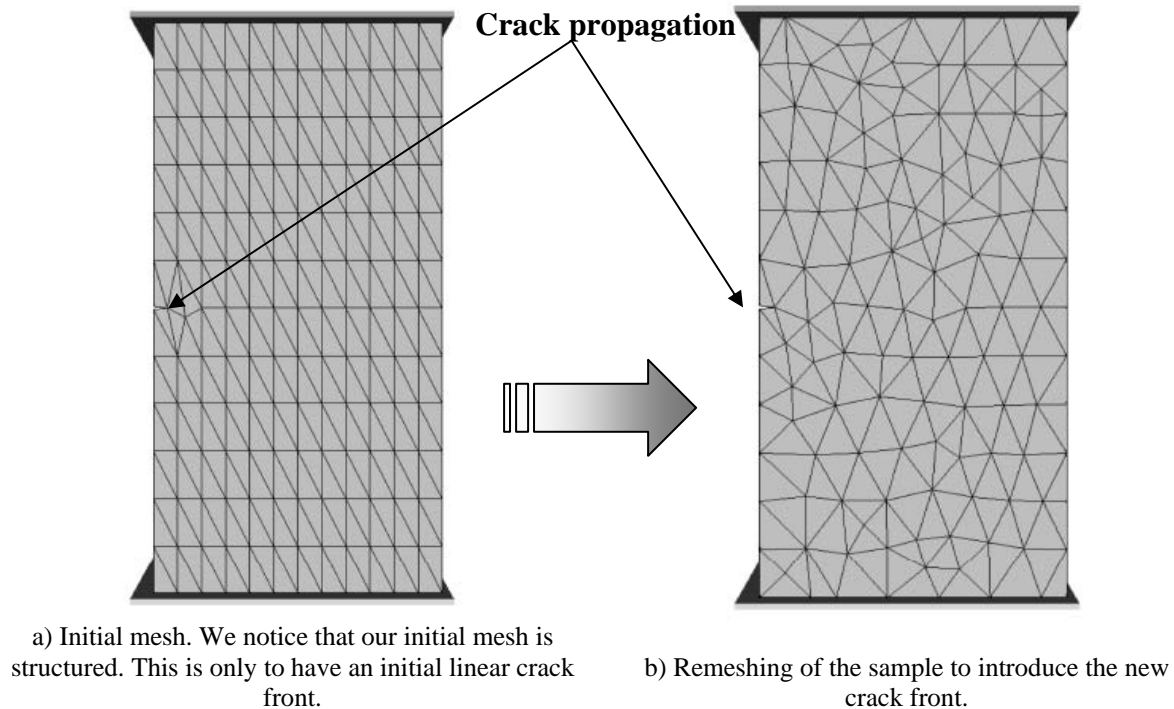


Figure 7-29. Remeshing of the sample for the next increment.

The success of this method is very dependent on two factors: the mesh we give to the remesher must be valid (connection between nodes has to be coherent). Moreover the mesh quality has to be “sufficient”. Indeed the risk is to obtain a bad quality mesh which would lead to the end of the computation.

It is thus important, before this step, to pay attention to the quality of the generated elements. This problem is mainly due to the fact that a crack insertion increases the number of nodes in the vicinity of the crack front much more than necessary for a correct geometrical description. To avoid this problem, it is useful to modify their position or erase some nodes from the mesh if necessary.

Figure 7-30 presents a mesh in which one of the faces is completely degenerated; so the algorithm moves the corresponding node to the highest angle of the degenerated element and places it at the barycentre of the considered elements.

---

*Algorithm 7-3. Barycentrage technique*

---

- List all neighbouring nodes  $n$  of  $n_{i+1}$  ;
  - **For** each node  $n$  **do**:
    - List all neighbouring nodes of the node  $n$ ;
    - Evaluate the barycentre of all these nodes
    - Displace the node  $n$  to the barycentre
- End**
-

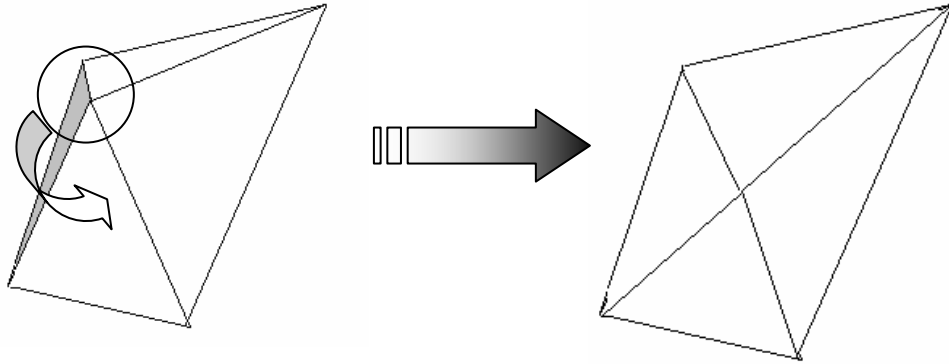


Figure 7-30. Schematic representation in 2D of a modification of the position of a node to improve the elements quality.

Another method consists in improving it by inverting the diagonals (see figure 7-28). The quality of the method depends on the measured angles  $\alpha$ . If  $\alpha > \alpha^{Crit}$ , the diagonal of the faces is inverted. This method leads to a better equilibrium in the distribution of the triangle angles.

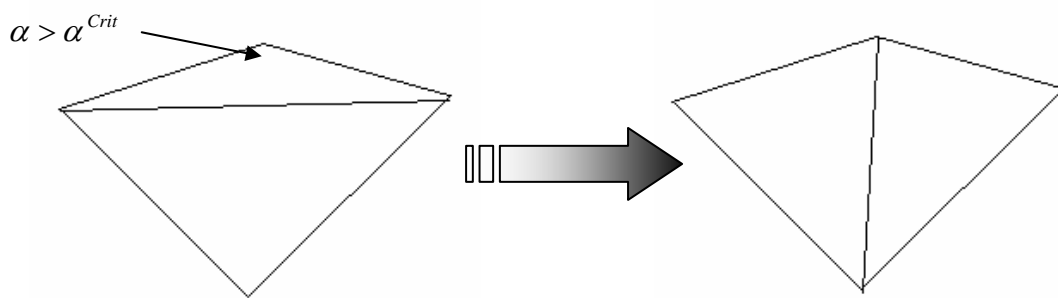


Figure 7-31. Example of a modification of the diagonal of an element in 2D to improve the elements quality.

This technique improves the elements quality but permit also to continue the crack propagation. Figure 7-32 presents the mesh problem which is solved with the inversion of diagonals.

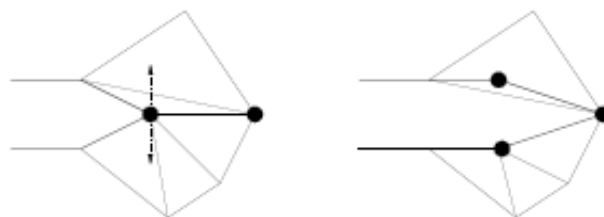


Figure 7-32. Mesh problem.

This section deals with the implementation of the algorithm used. It is based on four major points: location of initial nodes, estimation of the length, opening and direction of the crack and actually the propagation step. The last point requires specific attention as it concerns the main difficulty of the “Discrete Crack Approach”: remeshing of the volumic mesh. We have hence focused on the way to transform connectivity and the mesh topology.

## 7.4 Validation of the 3D crack model

In this part, three examples are presented to validate the algorithm: a uniaxial tension test, a L-shape submitted to a tension test and a three point bending test.

### 7.4.1 3D Crack propagation on a tensile test

#### 7.4.1.1 Model configuration

We test first this algorithm on a uniaxial tensile test. The behavior of the sample is completely elastic and we know exactly where and when fracture occurs (the mesh of the sample is initially structured). The sample is parallelepipedic (25×50×50 mm). The contact is bilateral sticking between the upper tool and the sample. Table 7-1 sums up the mechanical parameters used for this simulation.

$E$ (GPa)	$\nu$	$da$ (mm)	$dw$ (mm)
30	0.2	1.5	0.1

Table 7-1. Parameters used for the 3D crack propagation of a sample submitted to a tensile test.

#### 7.4.1.2 Crack path on a uniaxial tensile test

Figure 7-33 shows the final step of the crack propagation. We notice that the crack propagation is correct as the crack propagates in the normal direction of the load axis. Furthermore we notice the good qualities of the generated elements along the crack front.

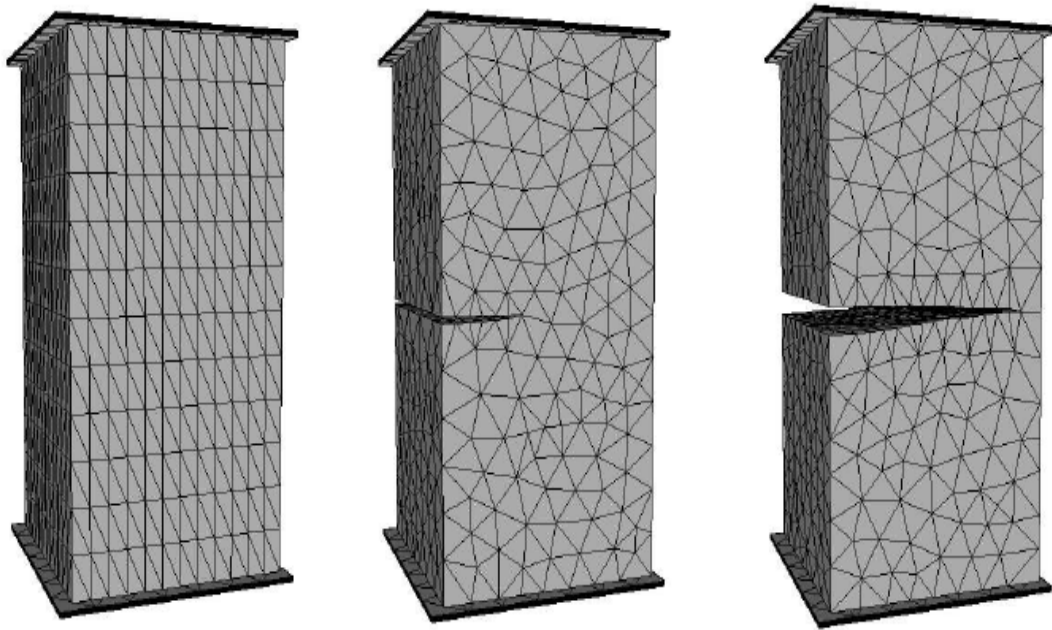


Figure 7-33. Crack path in a sample submitted to a tensile test.

We illustrate the relevance of the maximal circumferential stress criterion with the analysis of the stress field in the vicinity of the crack front. We notice that the stress field is maximal around the crack front as shown in figure 7-34.

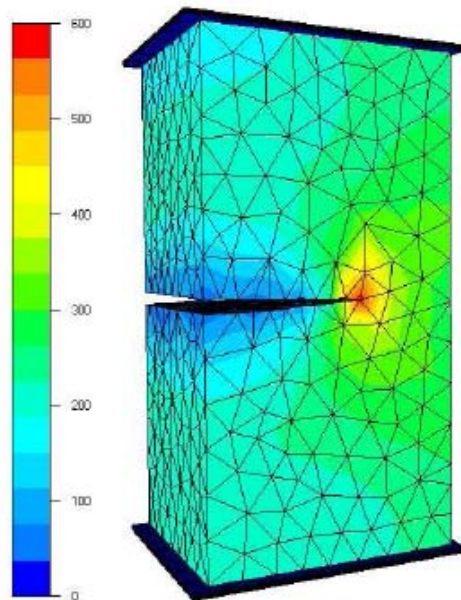
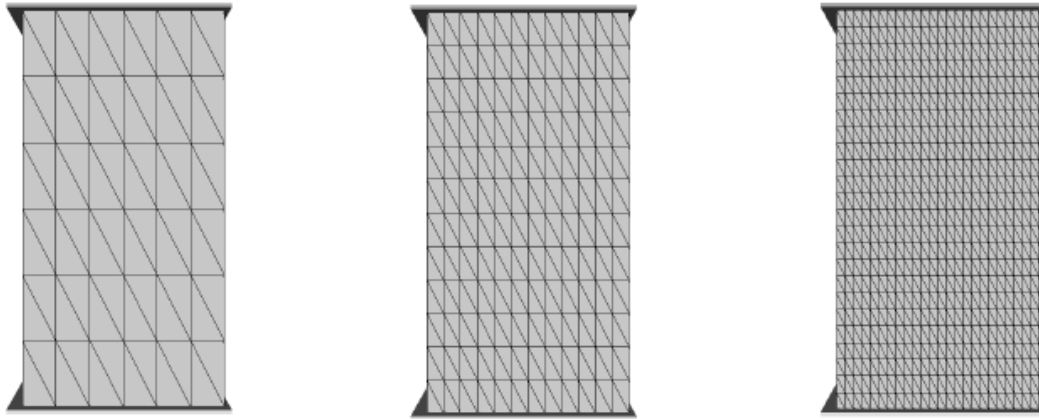


Figure 7-34. Principal maximal stress field  $\sigma_1$ .

### 7.4.1.3 Sensitivity study on the SIF

We test now the mesh refinement on the stress state near the crack front. In this way, a tensile test has been performed. Figure 7-35 presents the three types of meshes used for this simulation.



a) Coarse mesh: 343 nodes, 1296 elements, mesh size = 7.01 mm.      b) Fine mesh: 2197 nodes, 10368 elements, mesh size = 3.54 mm.      c) Very fine mesh: 15700 nodes, 83 000 elements.

Figure 7-35. Representation of the mesh used for a tensile test.

A crack propagates in this sample with the discrete crack approach. Then we constrain the crack to stop. We examine hence the SIF evolution versus time (i.e. increments). The theory gives us a simple relationship between the maximal principal stress  $\sigma_1$  in function of the distance to the crack front, where the stress is proportional to  $\frac{K_I}{\sqrt{2\pi r}}$  for pure mode I.  $r$  is the polar coordinate of the node in the local reper where  $K_I$  is evaluated. Figure 7-36 presents the numerical evaluation of the  $K_I$  values for each node of the crack front [Li Cham Yon 2005].

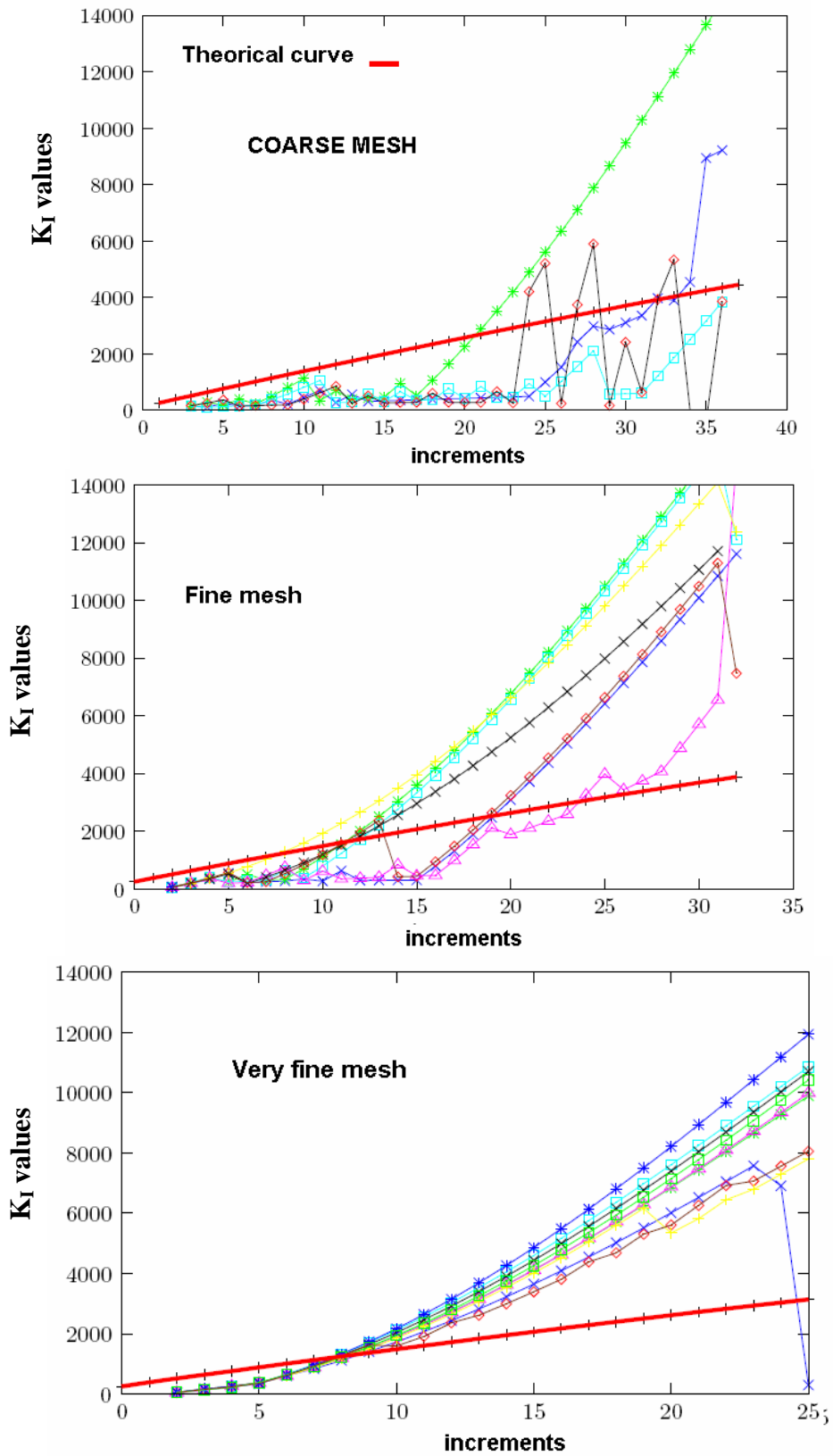


Figure 7-36. Evolution of the maximal principal stress with respect to the increments.

We notice the mesh influence in the evaluation of the SIF and so in the bifurcation angles. The finer the mesh is, the more homogeneous the behavior of the crack front is. For a very fine mesh, all nodes go in the same direction. A fine mesh improves the numerical results however it is not sufficient to capture the singularity of ahead the crack front. Indeed even if the behavior of the numerical curves are identical to the theory, linear and rising, (in the case of a very fine mesh), the slopes are different. This difference comes from the  $P_1 + / P_1$  finite element used which cannot lead to a singular stress field closed to the crack front. In order to obtain a stress field which agrees with the theoretical stress singularity of LFM at the crack front, a mid-side node at the quarter points of the side [Barsoum 1976] should be added.

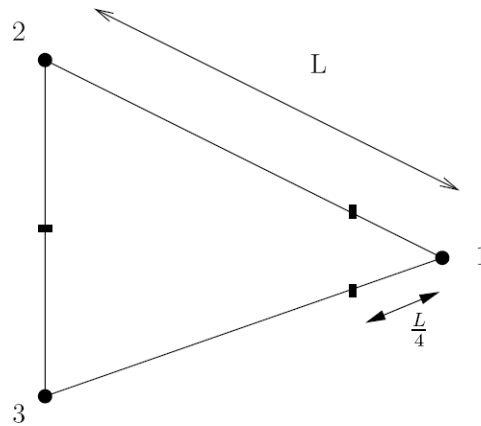


Figure 7-37. 2D triangular element with mid-sides nodes at the quarter points [Barsoum 1976].

But in the context of FEMCAM it would require the use of quadratic elements (with middle nodes) whereas we only use linear elements. It would be then interesting to develop further a numerical mesh independent method ( $G\theta$  method for instance).

### 7.4.2 3D Crack propagation in a L-Shape structure

Now we model a L-shape structure submitted to a tensile test. Displacement can be applied in different directions. Dimensions are given in centimetres and the material is elastic with the same mechanical properties as in the previous example.

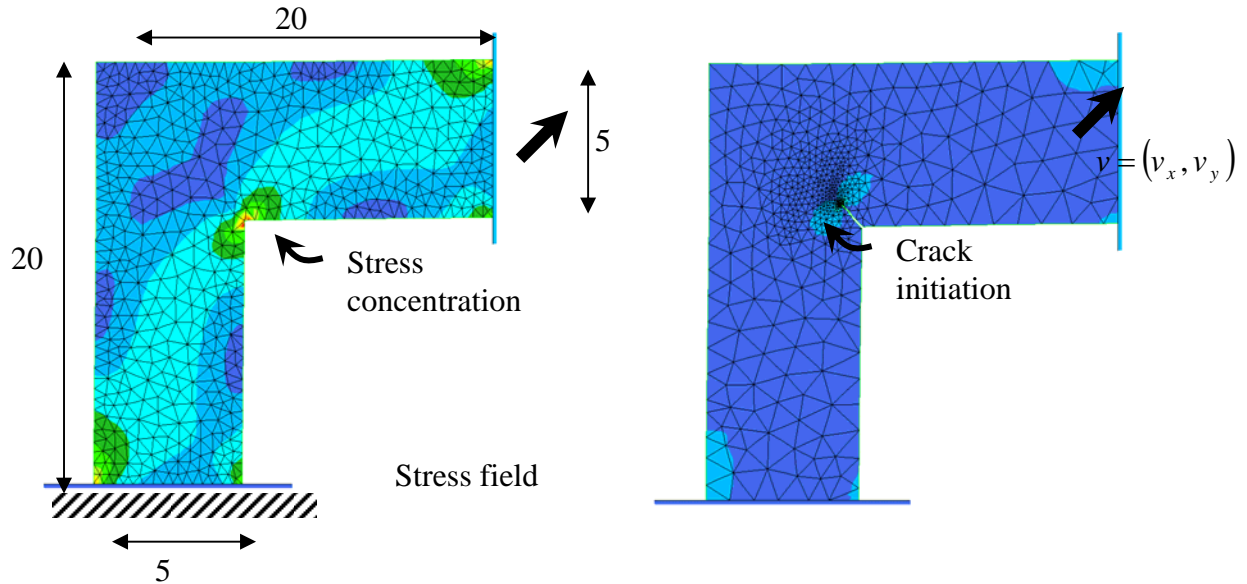


Figure 7-38. 2D representation of the crack initiation in a L-shape structure.

For the first simulation, the displacement prescribed is the same in direction  $x$  and  $z$  ( $v_x = 0.5 \text{ mm.s}^{-1}$ ;  $v_y = 0 \text{ mm.s}^{-1}$ ;  $v_z = 0.5 \text{ mm.s}^{-1}$ ). The first direction of propagation (corresponding to initiation) is given by the user since no SIF computation is possible before crack initiation. The maximal circumferential stress evaluates the direction of each node of the crack front. At each step of the crack propagation, the crack propagates with a length  $da = 0.9 \text{ mm}$  and an opening  $dw = 0.05 \text{ mm}$ . Figure 7-39 presents the cracking state at the end of the simulation. We observe that the crack propagates very uniformly during the simulation and at  $45^\circ$ . Furthermore we notice that the maximal principal stress is maximal ahead of the crack zone.

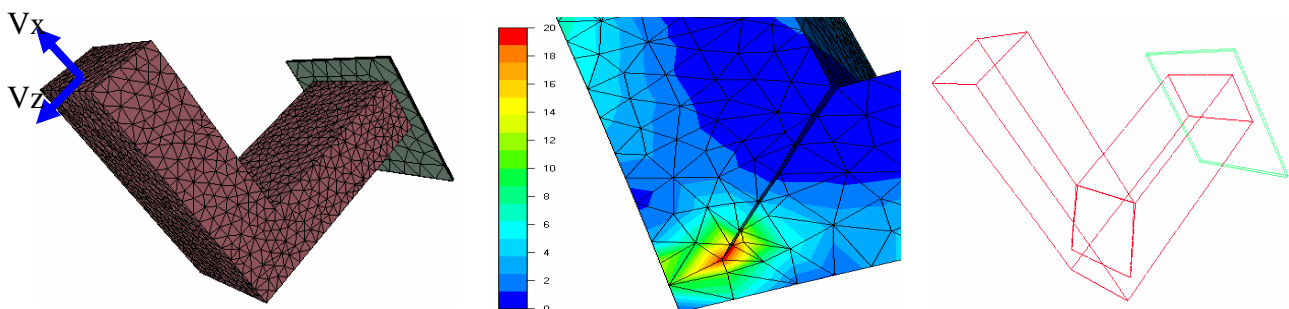


Figure 7-39. State of the maximal principal stress during the crack propagation in a L-shape structure submitted to a tension test.

Now we test the circumferential stress criterion. In this way we study the crack path according to the direction of the loads. Figure 7-40 shows the crack path for different configurations. In the first case,  $v_z$  is equal to zero, so that the crack propagates horizontally (figure 7-40.a). In the last case,  $v_x$  is equal to zero and this time the crack propagates vertically (figure 7-

40.c). When  $v_x = v_z$  (figure 7-40.b), we rekind the previous results. These directions follow the stress distribution on the sample. It underlines the ability of the bifurcation criterion to give a good prediction of the crack path.

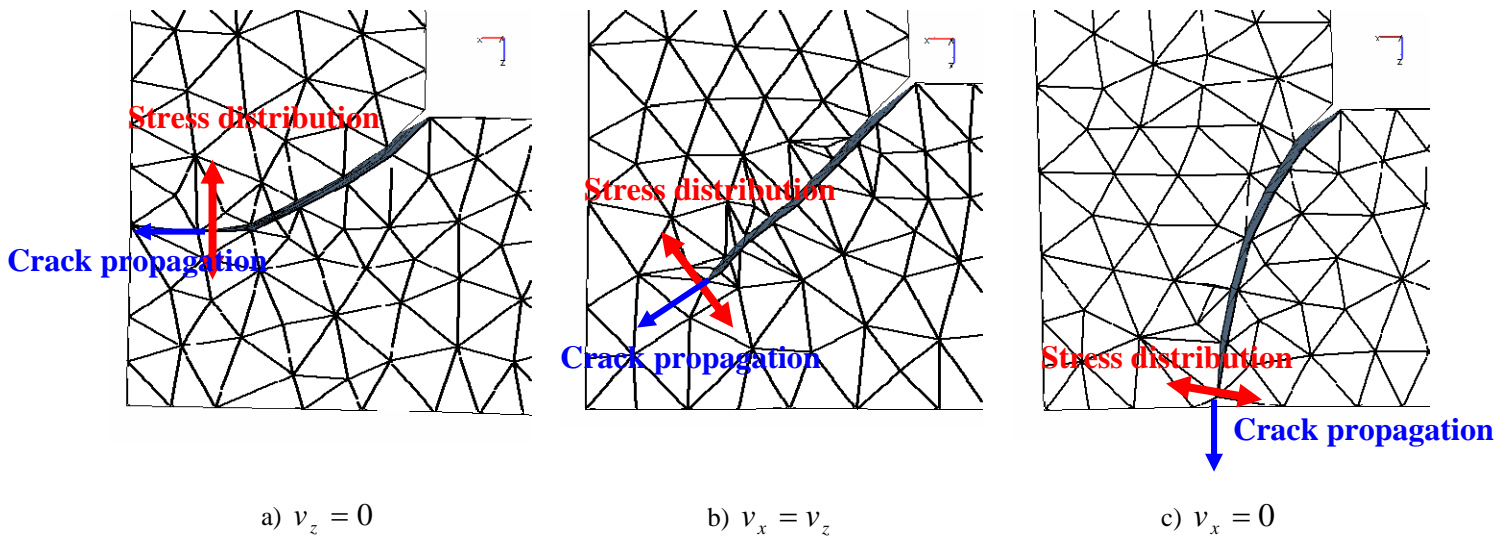


Figure 7-40. Different crack path according the load axis.

### 7.4.3 3D Crack propagation in a three point bending test

We test this algorithm on a three point bending test (40×40×160 mm, 29 000 nodes and 60 000 elements).

We test first the crack path according to the location of the crack initiation. Mechanical parameters are the same than those used in table 7-1. We test a case where the crack initiates under the load axis and another test is performed with an initial decentred crack initiation. Figure 7-41 presents the crack path in each case. Case a) shows that the crack propagates in the same direction than the load axis. Furthermore each node of the crack front evolves regularly in the same direction. It validates the implementation of the crack growth criterion for uniaxial loading. Case b) validates also the model as it shows that the crack reorients in the direction of the load axis.

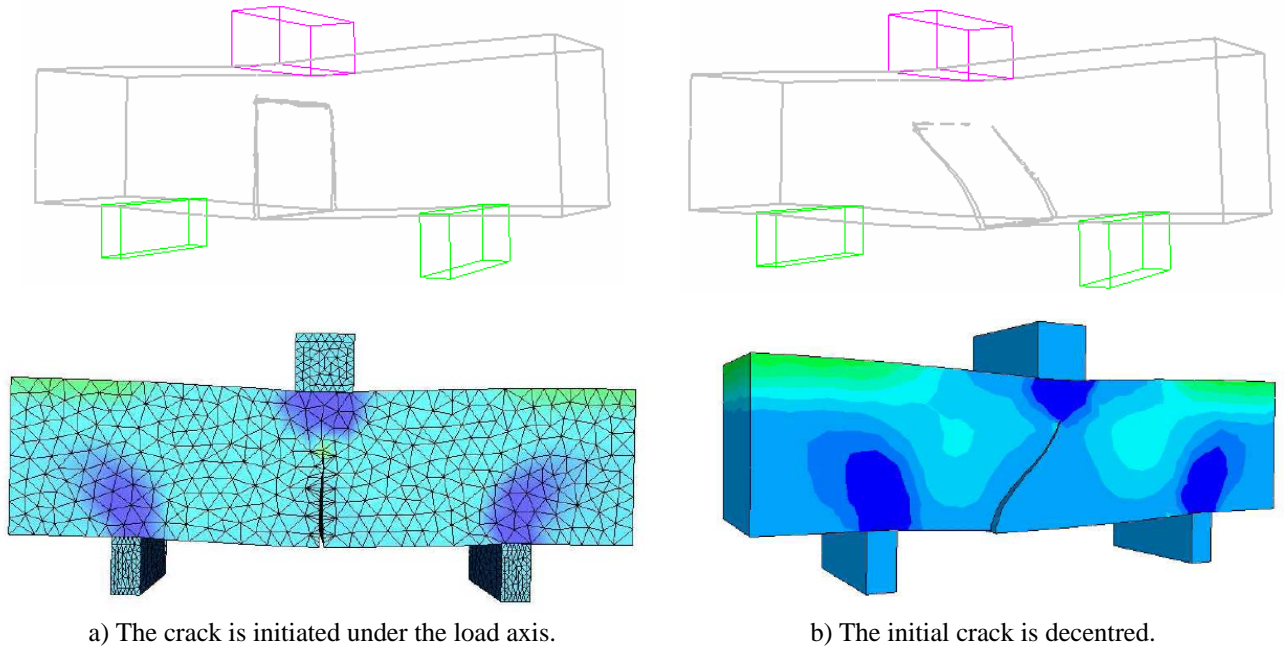


Figure 7-41. Crack path and maximal stress distribution in a three point bending test according to the location of the initial crack.

Now the beam has an elastic damage behavior. The crack is initiated under the load axis. Table 7-2 shows the material parameters used for this simulation:

$E^M$ (GPa)	$\nu^M$	$\epsilon_{d0}$	$\tilde{\epsilon}_T^{Crit}$	$\beta$	$\tilde{c}$	$A_T$	$B_T$	$A_C$	$B_C$
30	0.2	$2.25 \cdot 10^{-5}$	$3 \cdot 10^{-5}$	1.05	15	0.8	20000	1.4	1700

Table 7-2. Material parameters.

The crack initiates once damage reaches a critical value on the lower part of the beam. Afterwards the crack propagates automatically at each increment of the simulation. The crack length ( $da = 1.2$  mm) and the crack opening ( $dw = 0.3$  mm) are prescribed at each stage. These values are prescribed in function of the mesh size. Figure 7-42 shows damage evolution and crack propagation.

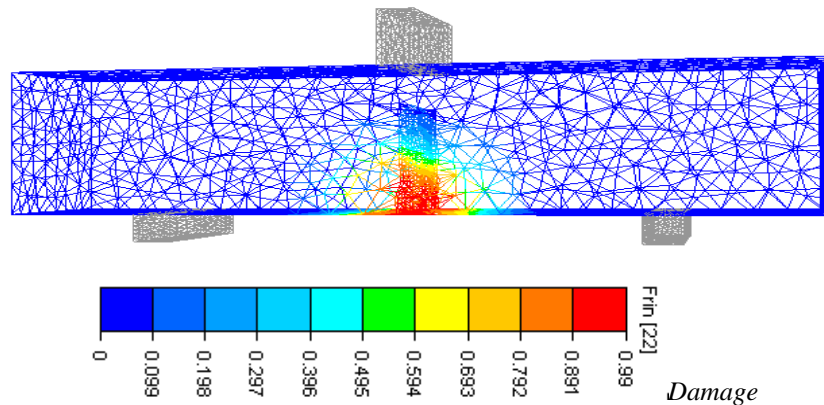


Figure 7-42. Damage evolution in a beam submitted to a three point bending test.

For the time being once the crack is initiated, the crack propagates at each increment of the simulation. This means that damage is not driven by damage evolution yet. After some loading steps damage is almost null on the crack front. Figure 7-42 shows that the crack has propagated faster than damage evolution. We are working on the coupling of damage evolution and crack propagation to improve our methodology. This improvement requires adding a loop in the finite element code corresponding to a condition on the damage state on the nodes of the crack front. And it can lead to problems as nodes would evolve with different velocity. From a geometrical view point, it is not an easy process as we are confronted to geometrical issues. For example, if the crack stops propagating, the classical remesher of FEMCAM continues to work. This could induce a modification of the shape of the crack front which is very dangerous for the crack propagation.

#### 7.4.4 Influence of heterogeneities

Concrete is a very heterogeneous material. This heterogeneity induces consequences on the crack path in the sample: arrest, branching, deviation and so on. Actually the stress distribution in the sample depends on the aggregates tensile strength, aggregate size, aggregate volume fraction and matrix fracture toughness  $K_{IC}$ . Cracks initiate preferentially in the ITZ and propagate in the mortar paste. However, when a crack propagates up to an aggregate, two solutions exist:

- If the matrix/aggregate interface is weaker than the aggregate strength, the crack reorients towards the interface. They are thus two possible paths for its further propagation. The direction of this crack has been studied by Wang [Wang 1992];
- On the contrary, the crack will propagate through the aggregate if the aggregate has lower stiffness.

With this technique, we can study the influence of inclusion/aggregates on the crack path. A first example is presented with one inclusion. We study here the influence of one heterogeneity on the crack path in a parrallelepipedic sample  $25 \times 50 \times 50$  mm submitted to a tensile test [Comby et al. 2005]. Here we consider a mortar with a purely elastic behavior (see table 7-1 for the mechanical parameters). We simulate the heterogeneity by modifying the Young modulus in a specific spherical zone in the sample. Figure 7-43 shows the crack path

that we obtain for different rigidity ratios  $R = \frac{E_{matrix}}{E_{inclusion}}$ .

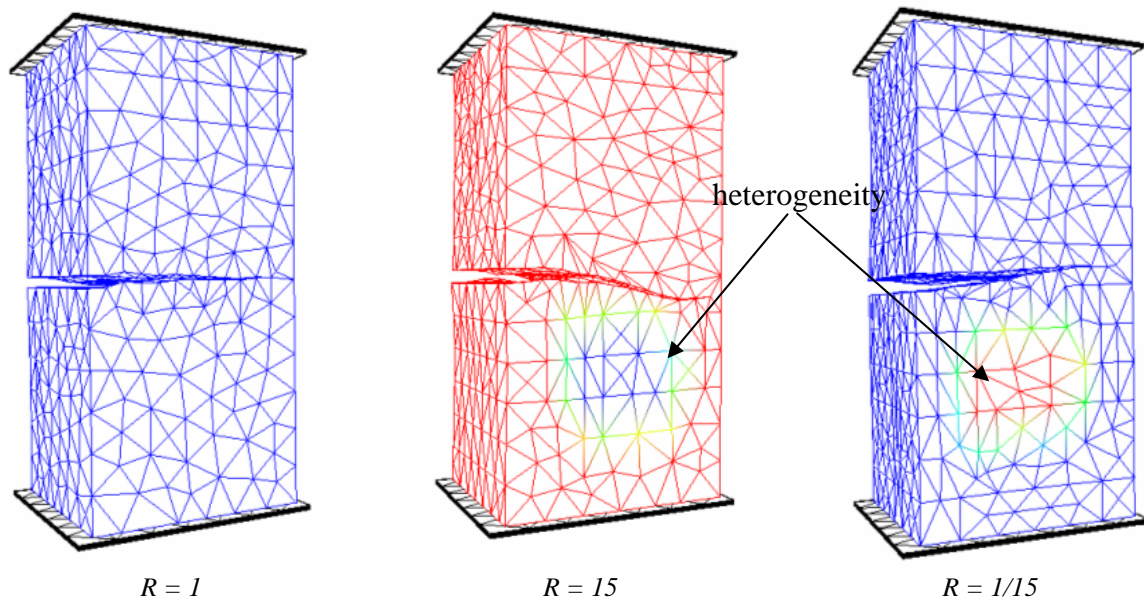


Figure 7-43. Evolution of the crack path for different mechanical property of the heterogeneity.

We observe that the crack was propagating in the direction of the inclusion when this inclusion was less rigid than matrix. Indeed the maximal principal stress is oriented at  $45^\circ$  and the crack is attracted by the inclusion. Once the inclusion has been passed, crack reorients horizontally. On the contrary the crack moves away from the inclusion if this inclusion is more rigid than the matrix. These results confirm the experiments and **underline clearly the effect of heterogeneities** in the sample on the crack path.

Concerning the CPU time, about six minutes are necessary to simulate the crack propagation on this tensile specimen. So the computation is very fast and the algorithm of the 3D Crack Modulus does not take much time. But compared to the homogeneous sample which necessities about forty seconds, it is almost ten times higher. This increase is mainly due to the remeshing modulus (*step 4* of the 3D Crack Propagation Algorithm) which is performed on the whole sample. We can improve this CPU time by remeshing only a local volume surrounding the crack front.

Now we test the crack path in a sample, submitted to a tensile test, with two inclusions in the volume.  $R$  is the ratio between the matrix rigidity and the inclusion rigidity. On the left side,  $R=1/15$ . On the right side,  $R=15$ . **We observe a real 3D shape of this numerical crack.** This is due to the fact that the direction of the crack propagation is computed at each node of the crack front. It shows us the possibility for each node to evolve independently and in function of local stresses nearby of each node. Results are quite similar to what was obtained for one inclusion.

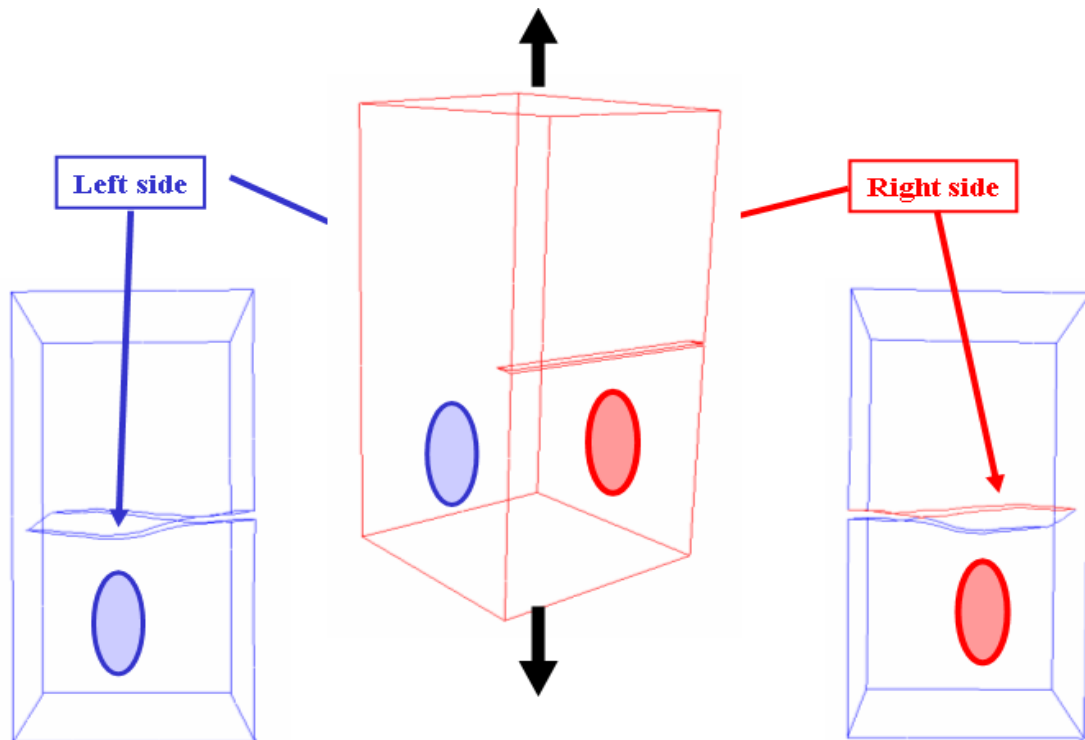


Figure 7-44. Tensile specimen – Evolution of the crack path with two spherical inclusions with different rigidities.

The numerical tests have validated the 3D crack modulus. Direct tensile test, tension on an L-shape structure, and a three point bending tests have tested the robustness of the crack propagation. The study of the SIF around the crack front has shown a mesh dependency due to the choice of the finite element in P1+/P1. Furthermore a test on a composite material underlines the great influence of the heterogeneities on the crack path.

## 7.5 Conclusions

Numerical modelling of crack propagation has given rise to a large number of methodologies such as X-FEM or Smeared Crack Approach. In order to simulate explicitly cracks we have chosen the Discrete Crack Approach, which is well suited to our concrete application at the mesoscale. This choice is completely justified. First the Discrete Crack Approach can evaluate with accuracy the crack path via the efficient mesher and remesher of FEMCAM. In the framework of this project, this accuracy is important for two reasons: cracks are often initiated at the interface (between matrix and aggregates) and the crack path depends on heterogeneities in a composite material.

The validation on tensile specimen has shown the robustness of this modulus which can predict with accuracy the crack path. We have also noticed the great influence of the heterogeneities on the crack behavior. It underlines once again the importance to take into account the heterogeneous aspect of concrete to simulate accurately crack propagation in such a heterogeneous material.

## CHAPTER 8 : GENERAL CONCLUSION AND PERSPECTIVES

### 8.1 Conclusions

**T**he Alkali Silica Reaction induces concrete degradation. This chemical reaction has been largely studied in literature. The chosen mechanism is described according to the model developed at the Ecole des Mines de Douai. The concrete expansion is the consequence of the granular skeleton swelling resulting from a gel creation in siliceous aggregates. It leads to a modification of the mechanical behavior of concrete and creation of cracks and macro cracks. If we can consider that the preventive aspect is solved, we cannot dispose of satisfactory methods in terms of diagnostic and repairing of structures submitted to ASR. **The final goal is hence to contribute to the concrete formulation and to understand the role of each component in a concrete submitted to ASR in the framework of durability issues.**

The objective of this work was to describe the mechanical consequences of the ASR on a concrete sample. It induces the description of the concrete degradation with cracks initiation. Moreover it brings us to the description of the chemical swelling process.

We have hence developed a new software, FEMCAM, based on the Forge3® finite element software package. **This new numerical model enables to describe the mechanical aspects of the swelling process and its mechanical consequences on a 3D concrete sample.**

An extensive bibliographic study has been first performed to evaluate existing data in literature on the numerical description of a 3D concrete sample. Different behavior laws can be used to describe its mechanical behavior. The Mazars model has been chosen as it is well appropriated for our study. This model has been improved to take into account strain localization. We have chosen **the non local Mazars model with an implicit formulation**. It can hence describe the mechanical behavior of the mortar paste in concrete, whereas aggregates are considered with a purely elastic mechanical behavior. The bibliographic study has also studied the ways to represent a concrete sample. Two main ways have been identified. The numerical concrete can be considered as a homogeneous material or as a heterogeneous one. Whereas most of 3D modelling considers concrete as a homogeneous material, modelling concrete as a heterogeneous material has been chosen as it enables to keep the primary role of aggregates in the chemical reaction and to describe the local aspect of the swelling process (stress concentration, crack initiation etc.). **Concrete is hence considered as a biphasic 3D material with aggregates embedded in a mortar paste.**

The third section describes the algorithm which generates aggregates in a concrete sample. This innovative description is based on a random generation of aggregates, based on a real grain size distribution given by the software's user and take into account of physical aspects in the aggregates repartition. This third section also concerned **the description of the implementation of this 3D numerical model in FEMCAM**. The specificity of this code is its velocity-pressure formulation. We have implemented the non local Mazars model. This elastic damage model can be implemented through a weak or a strong coupling. We have noticed that the weak coupling induces a faster computation only if it is associated with an

adaptive time step which can describe with a great accuracy damage initiation. This weak coupling has been hence implemented to describe the mechanical behavior of the mortar paste. Using this 3D numerical model, we have validated and justified the choice and the implementation of the model.

The fourth part focuses on the parameters identification. The “RheOConcrete” software has been used to do it. This inverse analysis modulus compares experimental and numerical global response with an evolution algorithm to adjust material parameters. Twelve parameters have been identified corresponding to parameters do describe the elastic and the elastic damage part of the load-displacement curve for the mortar paste and the aggregates of concrete. These experimental data have been obtained at the Ecole des Mines de Douai (GC-Douai). We have chosen to use a **specific formulation which is the most reactive to the ASR**. The numerical model takes into account of the grain size distribution of this specific formulation and has chosen specific material parameters to describe concrete. Actually a sensitivity study has been led to test the influence of the parameters on the global response.

In the fifth part, we have supposed unknown the mechanical behavior of the aggregates and deduced the mechanical behavior of the mortar paste of concrete in comparison with the experiments. The computation time is very long and requires a first study to reduce the set of range of each parameter to identify. Compression tests, three point bending tests and a “Brazilian” splitting test have been performed and global responses have been compared with experimental results. A sensitivity study has permit to conclude on the effect of the volume of the aggregates on the global response. We have hence noticed that the maximal strength increases linearly with the aggregates volume.

Now we have validated our 3D numerical model and identify all parameters for a specific formulation of a concrete sample particularly reactive to ASR. The next part is an application of the mechanical consequences of the ASR. In this way a bibliographic study has been carried about the swelling process induced by the ASR. We have chosen to use an isotropic dilatation phenomenon of each reactive to describe the chemical reaction. Our choice is based on the aggregate swelling experimental curve versus time, given point by point by the software’s user. The 3D numerical tool has been validated on the first phase of the chemical reaction. Furthermore it enables to describe the progressive loss of stiffness in the material with accuracy. Some supplementary numerical tests have proved the great effect of the inert aggregates which strengthen the mortar paste and decrease some contraction effect due to damage in the mortar paste. Another conclusion emerges from this numerical study: the volume percent of reactive aggregates influences the velocity of swelling of the sample. Our model has one major drawback: we cannot describe the cracks initiation and propagation in the mortar paste with the “Kill element” method, already present in FEMCAM. We have hence developed in FEMCAM a method to describe macrocrack initiation and propagation.

The last chapter describe a method to physically describe cracks initiation and evolution in a concrete sample. A bibliographic study has lead to conclude on the efficiency of the **Discrete Crack Approach**. We have hence developed an algorithm to change the mesh topology and introduce new surfaces. First validations have been realized on a mortar sample submitted to a three point bending test. We have hence underlined the necessity to take into account concrete heterogeneities to simulate crack propagation. This knowledge is all the more so important that these macrocracks are privileged paths for water and material transport which can induce an acceleration of the chemical degradation.

## 8.2 Perspectives

The knowledges obtained during this first work have shown the major interest of this 3D numerical tool. Results are promising and the perspectives are numerous to describe durability issues of concrete and more generally, of heterogeneous materials. This work has also underlined the great complexity of the material. The final goal would be to couple this numerical tool describing concrete at a micro level and another at a macro level in order to obtain a very large description of concrete.

Concerning the mechanical behavior of concrete, some previous conclusions underline a behavior law taking into account **viscosity aspect**, and a non-linear behavior by including permanent strains could improve the global response of the material. The **viscosity aspect is all the more so justified than the ASR is a very long reaction and the aspect of creep effects and strain relaxations could be modelled**. Our 3D numerical model can also be improved on one major point. It would consist in considering aggregates as an elastic damage material. Here we present briefly the effect of the mechanical behavior of the aggregates on the global response of the sample. A swelling test is performed in the same conditions than already presented in chapter 6 (section 6.4.3). The difference is in the mechanical behavior of the aggregates. To simplify the problem, we consider an elastic behavior up to four weeks of swelling, and then only *reactive* aggregates are considered with an elastic damage behavior (we have fixed arbitrary a constant damage value ( $D = 0.5$ ) in all the aggregates after four weeks). Figure 8-1 compares the swelling curve. We notice that the modification of the behavior law for aggregates has an influence on the swelling sample: the swelling slows down after four weeks. This preliminary study confirms the importance to account for a more accurate mechanical behavior (including damage) for aggregates. Nevertheless it induces more damage parameters to identify our 3D numerical model.

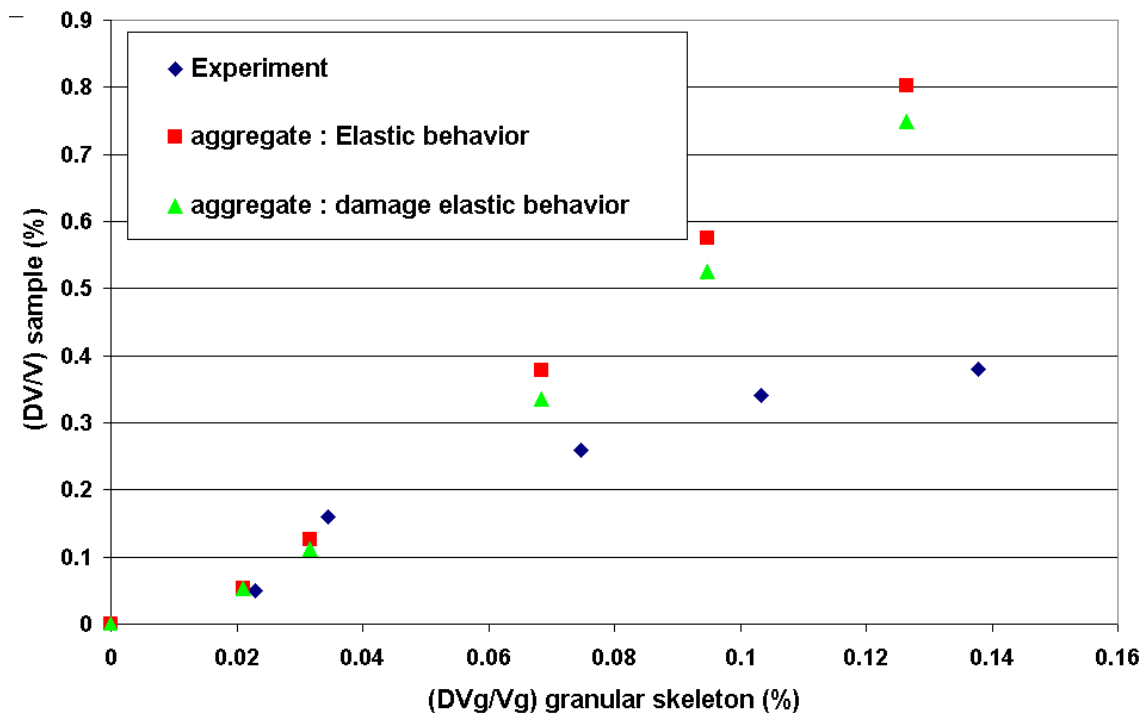


Figure 8-1. Volume variation of the sample versus volume variation of the granular skeleton according to the mechanical behavior law of the aggregates.

We have considered initial concrete without voids and possible initial cracks. An extension of this model could account for a statistic distribution of possible defaults in the initial concrete sample. Figure 8-2 compares the load-displacement curves of two 16×32 cm concrete samples submitted to a compression test. For the concrete with initial defaults, 2.5% of the mortar paste has been initially transformed into voids. The non local Mazars model with a fixed time step is used. We do not use the “Kill element” method. It underlines the important effect of the initial micro voids on the concrete behavior and the state of damage seems to be more realistic as it seems to be preferentially oriented along the z axis.

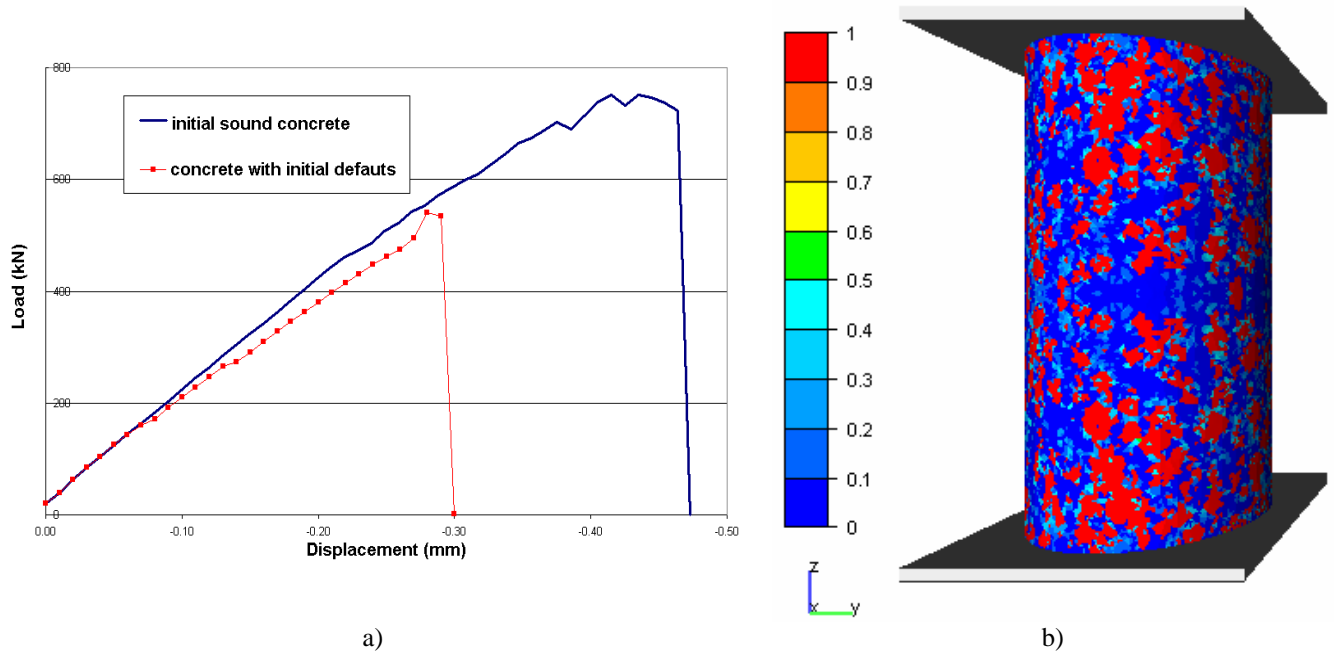


Figure 8-2. a) Comparison of load-displacement curves for a sound concrete and a concrete with initial micro voids; b) State of damage in the concrete with initial voids. The damage distribution is homogeneous and oriented to the z axis.

Our study concerning ASR has been carried out at 7 days. However concrete hardens during a minimum period of 28 days. To avoid a competition between these hardening phenomena and the swelling phenomenon a second experimental campaign could be carried out at 28 days to improve the comparison between experimental and numerical results. Furthermore some samples with specific grain size distribution or a specific distribution of aggregates in the sample could be compared with the numerical model. Other techniques could also be used as the vibration analysis. This non destructive technique follows damage of the same sample during the dilatation phenomenon induced by the ASR. On the other hand the numerical description of the ASR could be improved. **A more accurate kinetic model could be developed where the initial data could be directly linked to the products of the chemical reaction.**

This 3D numerical model has the possibility to be improved with a description still more accurate by taking into account the contact and the ITZ between the mortar paste and the aggregate. Some ways could be explored thanks to the large possibilities of FEMCAM.

The contact could be treated with the multi-domain version of this software. This multi-domain version introduces two separate bodies: a meshed cubic with a centred hole to simulate the mortar paste of concrete, and a meshed spherical body to simulate the aggregate.

Figure 8-3 shows us the comparison of load-displacement curves of a cubic concrete sample with one aggregate, submitted to a tensile test, according to the contact used.

We have first compared the two versions of FEMCAM with the same type of bilateral sticking contact: the single-domain that we have used in this work and the multi-domain version. For the single-domain version, the aggregate has been simulated with the algorithm we have developed in this work. We notice that the load-displacement curves are equivalent and the difference, that we notice, is linked to the difference of shape of the aggregate for the two versions of FEMCAM and so a minimal difference of aggregate size. The peak load, between a sliding or a friction contact and a bilateral contact, is multiplied by ten. The observed differences underline the importance of the contact used. More particularly it shows the importance of the type of contact (bilateral versus unilateral contact). However this is a critical test with a very large aggregate, which means that the differences we could observe on the real concrete sample we have already tested should be not so important.

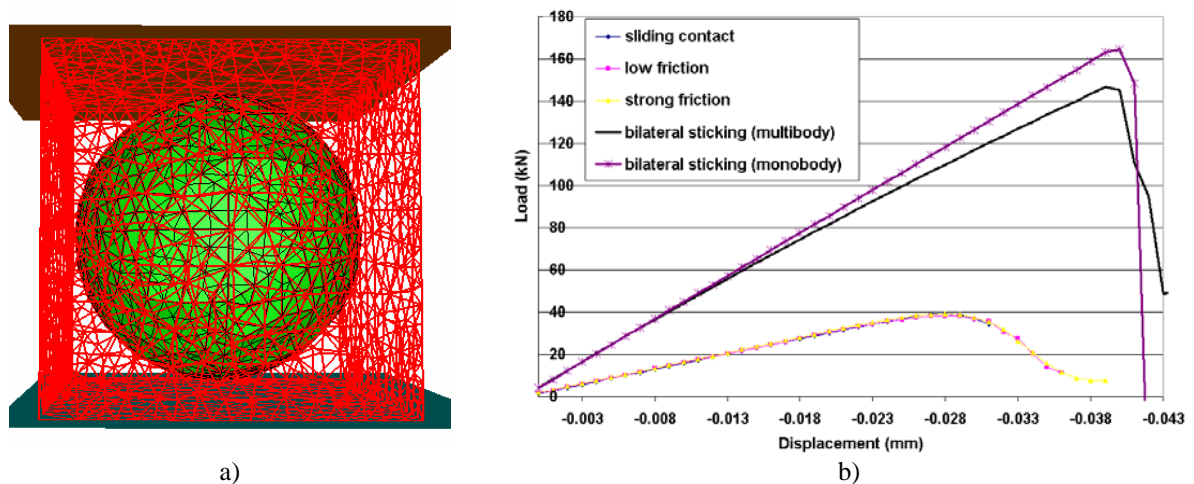


Figure 8-3. a) Geometry of the 100\*100 mm cubic sample: 4100 nodes, 17890 finite elements. We use the Non Local Mazars model with an implicit formulation

$$(A_C = 1.4, B_C = 3500, A_T = 0.8, B_T = 20000, \varepsilon_{D0} = 1.10^{-4}, \tilde{c} = 15 \text{ mm}^2).$$

b) Load-displacement curves of a cubic specimen in tension.

These observations show also the importance of the contact in the parameters identification. It may induce that the first method used to identify material parameters (identification on mortar and on concrete) should be efficient with a multi-domain version of FEMCAM by considering the contact between the aggregates and the mortar paste.

The use of this multi-domain version presents some drawbacks. We have to adapt it to not miss the random aspect of the aggregate repartitions. Furthermore the simulation of a whole concrete sample containing almost one thousand aggregates with the multi-domain version would be too much consuming in computation time. Some other ways could be envisaged. The use of zero thickness finite elements between aggregate and the ITZ could simulate the progressive decohesion at the interface.

The ITZ could be modelled by introducing initial voids at the interface between the aggregates and the mortar paste.

But as these techniques are time consuming, it would require the use of a **parallel version of the code**, already validated with Forge3®.

The knowledge of the macrocracks initiation and propagation induces some further efforts to improve the 3D crack modulus. The final goal is here to simulate multi cracks which should constitute a significative advance in the modelling of Fracture Mechanics. Concerning the possible evolutions of the 3D Crack Modulus, some aspects can be treated without difficulty. The first aspect consists in remeshing only the crack zone to improve computation time. It does not necessary mean additional computation time as this mesh refinement could be limited around the crack front and not on the whole structure. The second aspect would consist in improving the refinement in the crack zone to get a more accurate computation of the stress field near the crack front. This is of prime importance since the accuracy of the computation of the crack propagation direction depends on the accuracy of these stress and displacement fields. It would be interesting to integrate a method, which would be less mesh dependent as the  $G\theta$  method.

Other aspects as the initiation of crack inside the volume, the creation of multi cracks, the coupling of damage and crack evolution, the possible evolution of nodes in 3D (with two bifurcation angles to realize 3D crack propagation), a good representation of the ITZ and the contact at the interface of the aggregates which undoubtedly have an influence on the crack path would be interesting to improve our knowledge on concrete and the consequences of the ASR.

\*\*\*\*\*

## Appendix

### A.1 One dimensional strain-localization problem

Let us consider the one dimensional problem of the bar in figure 1. The constitutive model is an elastic model. A uniform bar, of length  $L$  and cross section  $A$ , is considered and characterized by a Young modulus  $E$ , an elastic strength  $\sigma_t$  and softening parameter  $H < 0$ .

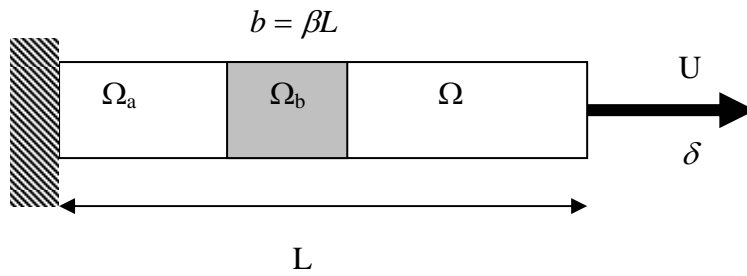


Figure 1. One dimensional bar problem

1- Elastic regime  $\left( \delta \leq \frac{\sigma_t}{E} L \right)$

$$\left. \begin{aligned} \varepsilon(x) &= \frac{\delta}{L} \quad \forall x \\ \sigma(x) &= E\varepsilon = E \frac{\delta}{L} \quad \forall x \end{aligned} \right\} \Rightarrow F = A\sigma = \frac{EA}{L} \delta \quad (1)$$

2- Elastic damage regime  $\left( \delta > \frac{\sigma_t}{E} L \right)$

At the peak stress ( $\sigma = \sigma_t$ ) let us consider that loading ( $\dot{\sigma} = E_T \dot{\varepsilon}$ ) takes place in the domain  $\Omega_b$ , of length  $b = \beta L$  ( $\beta \in [0,1]$ ), whereas unloading ( $\dot{\sigma} = E \dot{\varepsilon}$ ) occurs at the rest of the bar (domain  $\Omega_a$ ). Let  $\dot{\varepsilon}_a$  and  $\dot{\varepsilon}_b$  ( $\dot{\varepsilon}_a \neq \dot{\varepsilon}_b$ ) the rate of the strains at both domains. The equilibrium equation considers the homogeneous distribution stress in the whole bar:

$$\frac{\partial \sigma}{\partial x} = 0 \quad (2)$$

Equilibrium requires that:

$$\dot{\sigma}_a = E\dot{\epsilon}_a = \dot{\sigma}_b = E_T\dot{\epsilon}_b \Rightarrow \dot{\epsilon}_b = \frac{E}{E_T}\dot{\epsilon}_a = \frac{E+H}{H}\dot{\epsilon}_a \quad (3)$$

And compatibility requires:

$$\dot{\epsilon}_a(L-b) + \dot{\epsilon}_b L = \dot{\delta} \quad (4)$$

And substituting equations Eq. (2-32) into Eq. (4):

$$\dot{\epsilon}_a(L-b) + \dot{\epsilon}_a \frac{E+H}{H} b = \dot{\delta} \Rightarrow \dot{\epsilon}_a \left( L + \frac{E}{H} b \right) = \dot{\delta} \Rightarrow \frac{\dot{\sigma}}{E} \left( L + \frac{E}{H} \beta L \right) = \dot{\delta} \quad (5)$$

It gives the following relation:

$$\dot{\sigma} = \frac{E}{L + \frac{E}{H} \beta L} \dot{\delta} \Rightarrow F = \frac{AE}{L + \frac{E}{H} \beta L} \dot{\delta} \quad (6)$$

It results in an infinite number of solutions of the problem after bifurcation at the peak-load. The undetermination of the size of the strain localization ( $\beta$  is undetermined) is responsible for that.

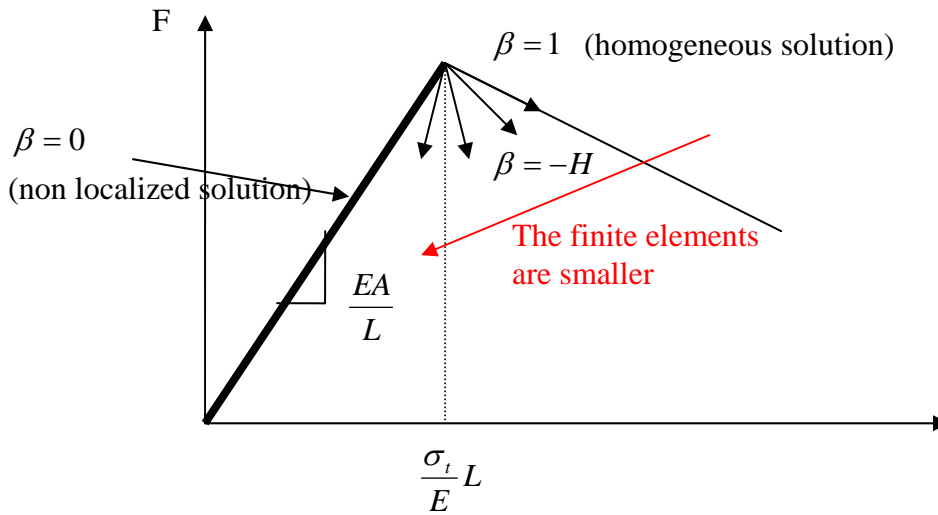


Figure 2. Solution of the 1D localization problem

## A.2 Friction laws in Forge3® code

**Tresca law (1865):** It derives from the incompressive plastic behavior law.

$$\tau = -\bar{m} \tau_{\max} \frac{\Delta v_g}{\|\Delta v_g\|} \quad (7)$$

where  $\bar{m}$  is the Tresca friction factor ( $0 < \bar{m} < 1$ ),  $\tau_{\max}$  the shear stress of the deformed material and  $v_g$  the sliding velocity.

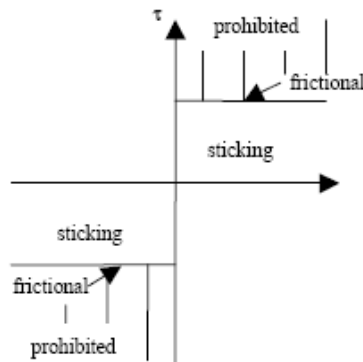


Figure 3. Representation of the Tresca's law with plastic relation  $\tau_c \leq \frac{\sigma_0}{\sqrt{3}}$

**- Coulomb law (1781):**  $\tau_c = \mu_F \sigma_n$

$$\tau = -\tau_c \frac{\Delta v_g}{\|\Delta v_g\|} : \text{slip} \quad (8)$$

where  $\tau$  is the tangential stress,  $\sigma_n$  the normal stress and  $\mu$  the Coulomb friction coefficient.

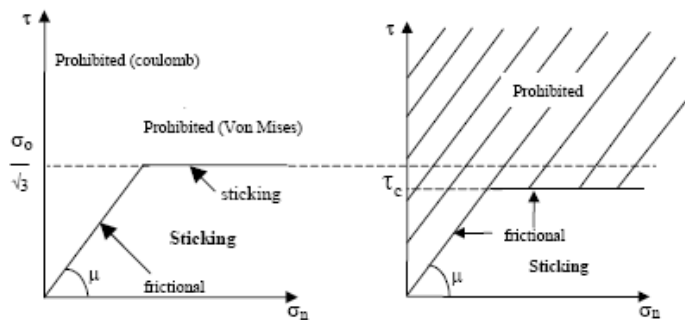


Figure 4. Representation of the Coulomb's law with von Mises plasticity limit

$$\text{left) } \tau_C = \mu_F \sigma_n \text{ and } \tau < \frac{\sigma_0}{\sqrt{3}} ; \text{ right) } \tau_C = \text{Min} \left( \mu_F \sigma_n, \tau < \frac{\sigma_0}{\sqrt{3}} \right)$$

- Coulomb law limited by the Tresca law:

$$\tau = \begin{cases} -\tau_C \frac{\Delta v_g}{\|\Delta v_g\|} & \text{if } |\tau_C| < \bar{m} \tau_{\max} \\ -\bar{m} \tau_{\max} \frac{\Delta v_g}{\|\Delta v_g\|} & \text{if } |\tau_C| \geq \bar{m} \tau_{\max} \end{cases} \quad (9)$$

### A.3 Analysis of the cement used

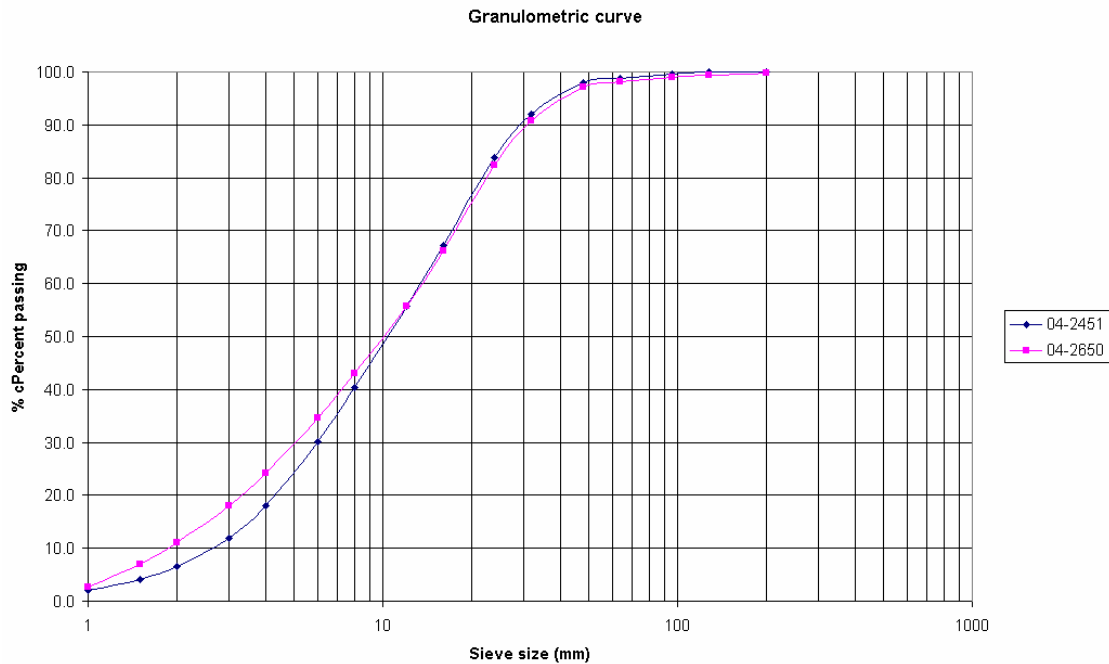
#### A.3.1 Chemical analysis

##### 1. Chemical composition

Nature	CEM I	CEM I
Producteur	Heming	Heming
Date	02/11/04	23/11/2004
Reference test	REC 136	REC 136
Sample number	04-2451	04-2650

SiO <sub>2</sub>	%	20.14	19.96
Al <sub>2</sub> O <sub>3</sub>	%	4.92	4.74
Fe <sub>2</sub> O <sub>3</sub>	%	3.06	3.32
CaO	%	59.71	60.70
Na <sub>2</sub> O <sub>fx</sub>	%	0.21	0.16
K <sub>2</sub> O <sub>fx</sub>	%	1.08	1.07
MgO	%	4.55	4.76
S SO <sub>3</sub> total	%	3.51	3.34
Mn <sub>2</sub> O <sub>3</sub>	%	0.10	0.11
TiO <sub>2</sub>	%	0.24	0.22
P <sub>2</sub> O <sub>5</sub>	%	0.31	0.32
Cl <sub>fx</sub>	%	0.030	0.010
SrO	%	0.060	0.060
Perte au Feu	%	1.41	0.61
Total	%	99.33	99.38
Na <sub>2</sub> O <sub>eq</sub>	%	1.04	0.86
NaO ICP	%	0.27	0.25
K <sub>2</sub> O ICP	%	1.16	1.13
Na <sub>2</sub> O eq ICCP	%	1.04	1.00
CL pot	%	0.04	0.01

### A.3.2 Granulometric analyse



### A.3.3 Mechanical characteristic

#### Paste and mortar characteristic

Nature	CEM I	CEM I
Producteur	Héming	Héming
Date	02/11/2004	23/11/2004
Number	042451	042650

#### 1. Paste (EN 196-3)

Consistance	%	28.2	28
DP	min	200	220
FP	min	285	310
Stabilité	mm	1	0

#### 2. Compression strength (EN196-1)

1d	N/mm <sup>2</sup>	22.2	18.6
2d	N/mm <sup>2</sup>	36.1	34.1
7d	N/mm <sup>2</sup>	54.6	52.1
28d	N/mm <sup>2</sup>	66.9	64.4

#### 3. Volumic mass and Blaine (EN 196-6)

MV	g/cm <sup>3</sup>	3.12	3.16
Blaine	cm <sup>2</sup> /g	4414	3944

## A.4 Test on mortar at 14 days

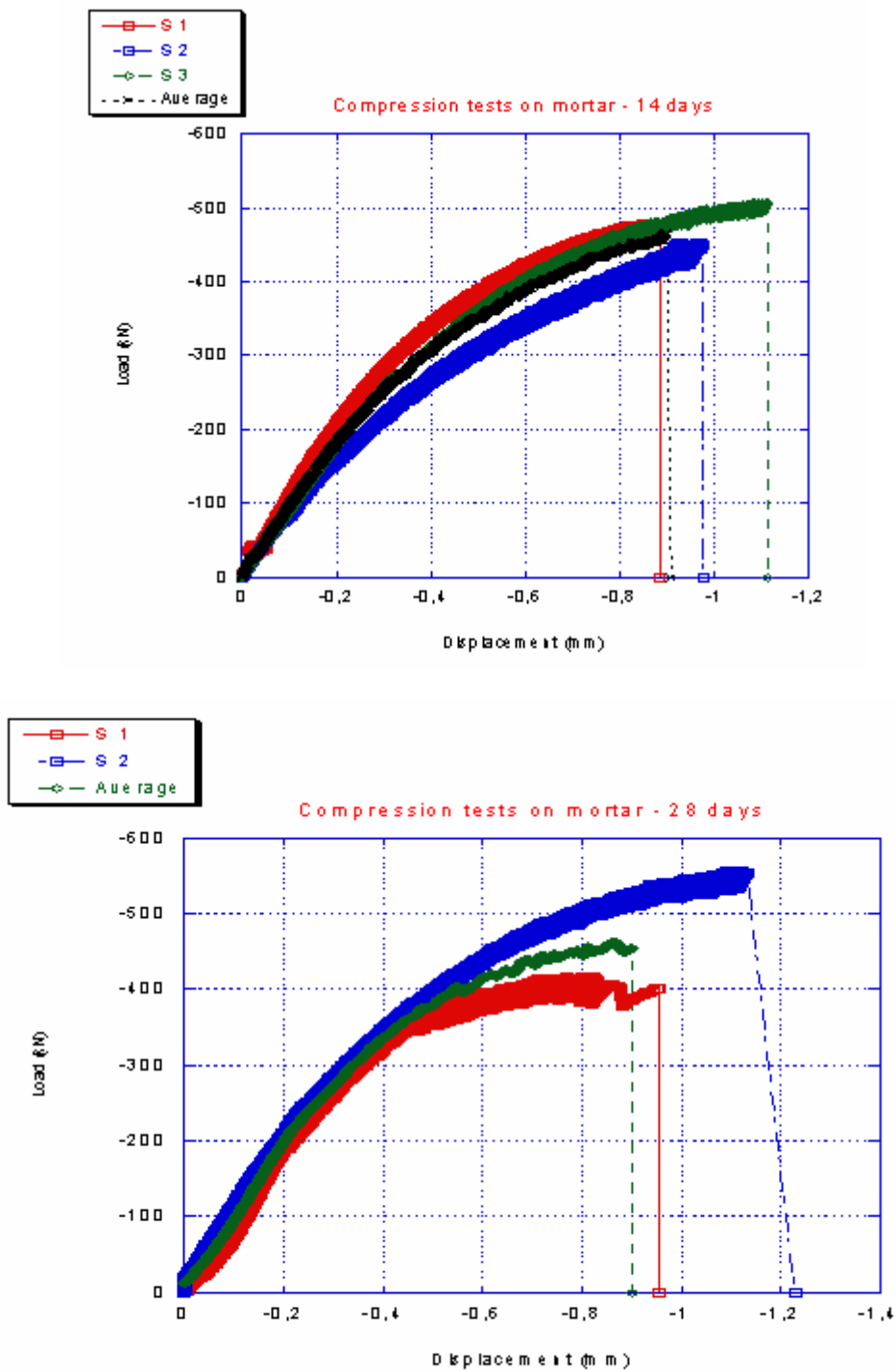
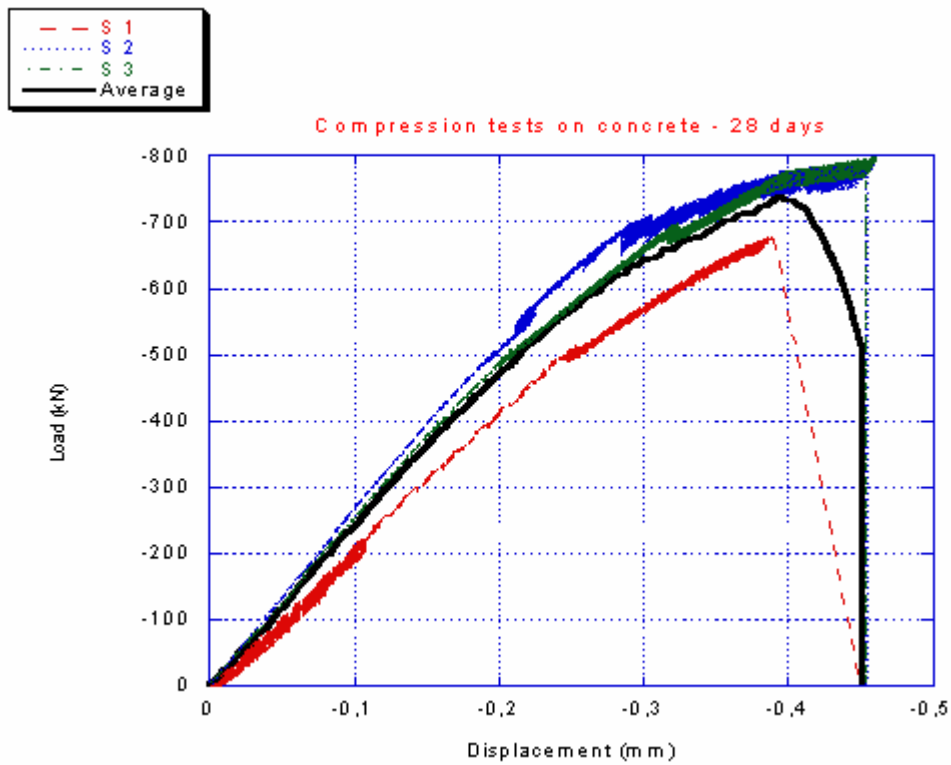
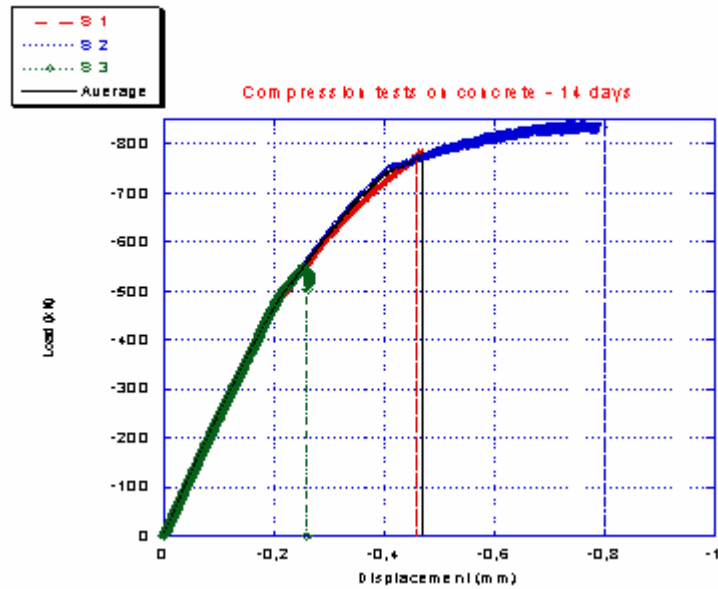


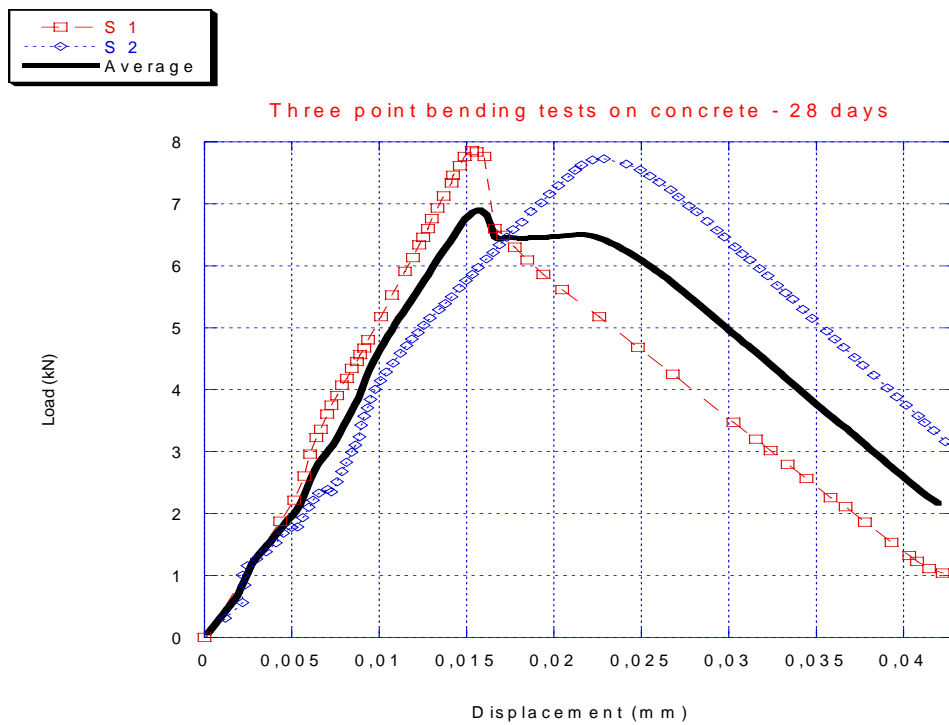
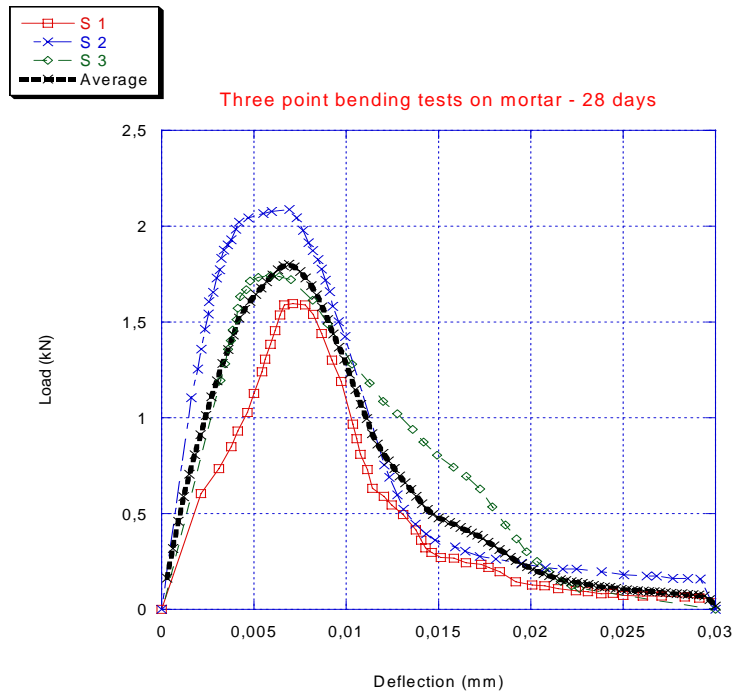
Figure 5. Compression tests at ages of 14 and 28 days.

## A.4 Test on concrete at ages of 14 and 28 days

### A.4.1 Compression tests



### A.4.2 Three point bending tests



## A.5 Table to determine crack deflection

$K_{II}^n$	$K_{III}^n$									
	0	0.1	0.2	0.3	0.4	0.5	0.6	0.8	0.9	1
0	0	0	0	0	0	0	0	0	0	0
0.05	5.99	6.63	7.25	7.79	8.21	8.5	8.7	8.82	8.89	8.92
0.1	12.38	13.71	14.97	16.04	16.84	17.39	17.73	17.92	18	18.01
0.15	18.92	20.89	22.72	24.22	25.29	25.98	26.38	26.56	26.61	
0.2	25.33	27.81	30.06	31.83	33.04	33.78	34.16	34.29	34.26	
0.25	31.37	34.2	36.68	38.58	39.84	40.56	40.88	40.94		
0.3	36.87	39.89	42.47	44.39	45.63	46.31	46.58	46.57		
0.35	41.78	44.85	47.43	49.33	50.52	51.15	51.37			
0.4	46.09	49.14	51.66	53.49	54.63	55.22	55.4			
0.45	49.85	52.82	55.25	57.01	58.1	58.66				
0.5	53.13	55.99	58.31	59.99	61.04	61.58				
0.55	55.99	58.72	60.93	62.54	63.56					
0.6	58.48	61.09	63.2	64.73	65.72					
0.65	60.67	63.15	65.16	66.63						
0.7	62.6	64.96	66.87	68.29						
0.75	64.31	66.55	68.38							
0.8	65.84	67.87	69.72							
0.85	67.2	69.23								
0.9	68.42	70.36								
1	70.53									

Table 1. Crack deflection angle (in degrees)  $\varphi_0$ .  $K_{II}^n$  and  $K_{III}^n$  depends on the SIF. [Schöllmann et al. 2002]

$K_{II}^n$	$K_{III}^n$									
	0	0.1	0.2	0.3	0.4	0.5	0.6	0.8	0.9	1
0	0	6.26	13.28	20.3	31.72	35.78	38.95	41.44	43.41	45
0.05	0	6.58	13.93	21.2	32.68	36.66	39.74	42.13	44.02	
0.1	0	6.82	14.41	21.81	33.23	37.12	40.11	42.43	41.99	
0.15	0	6.97	14.67	22.07	33.34	37.16	40.08	42.36		
0.2	0	7.02	14.70	22.02	33.09	36.84	39.73	41.99		
0.25	0	6.98	14.53	21.69	32.56	36.28	39.16			
0.3	0	6.86	14.22	21.19	31.84	35.54	38.43			
0.35	0	6.69	13.82	20.56	31.02	34.71				
0.4	0	6.49	13.36	19.87	30.13	33.81				
0.45	0	6.27	12.87	19.16	29.21					
0.5	0	6.05	12.38	18.44	28.3					
0.55	0	5.82	11.90	17.74						
0.6	0	5.6	11.43	17.06						
0.65	0	5.39	10.99	16.41						
0.7	0	5.18	10.56	15.80						
0.75	0	4.99	10.16							
0.8	0	4.81	9.78							
0.85	0	4.63								
0.9	0	4.47								
1	0									

Table 2. Crack deflection angle  $\psi_0$  (in degrees).  $K_{II}^n$  and  $K_{III}^n$  depends on the SIF. [Schöllmann et al. 2002].

---

## REFERENCES

- [Babuska 1973] Babuska, I. 1973. *The finite element method with penalty*, Math. of Comput., Vol. 27, pp. 221-228.
- [Babuska et al. 1997] Babuska, I., Melenk, J.M., 1997. *The partition of unity method*, Int. J. for Num. Meth. in Engng, Vol. 40, pp.727-758.
- [Barenblatt 1962] Barenblatt, G.I., 1962. *The mathematical theory of equilibrium of cracks in brittle fracture*, Advances in Applied Mech., Vol. 7, pp. 55-129.
- [Barsoum 1976] Barsoum, R.S. 1976, *On the use of isoparametric finite elements in linear fracture mechanics*, Int. J. for Num. Meth. in Engng, Vol. 10, pp. 25-37.
- [Bazant et al. 1979] Bazant, Z.P., Kim, S.S. 1979. *Approximate relaxation function for concrete*, J. of the Struct. Div., Vol. 105, No. 12, pp. 2695-2705.
- [Bazant et al. 1983] Bazant, Z.P., Oh, B.H. 1983. *Crack band theory for fracture of concrete*, Mat. Struct., Vol. 16, pp. 155-177.
- [Bazant et al. 1985] Bazant, Z.P., Oh, B.H. 1985. *Microplane model for progressive fracture on concrete and rock*, J. of Engng Mech., ASCE, Vol. 111, pp. 559-583.
- [Bazant 1989] Bazant, Z.P. 1989. *Identification of strain-softening constitutive relation from uniaxial tests by series coupling model for localization*, Cem. And Concr. Res., Vol. 19, pp. 973-977.
- [Bazant et al. 1990] Bazant, Z.P., Tabbara, M.R., Kazemi, M.T., Pijaudier-Cabot, G. 1990. *Random particle model for fracture of aggregate of fiber composites*, J. of Engng Mech., ASCE, Vol. 116, pp. 1686-705.
- [Bazant et al. 1998] Bazant, Z.P. Planas, J. 1998. *Fracture and size effect in concrete and other quasibrittle materials*, CRC press, Boca Raton, Florida, and London, Chap. 12.
- [Bazant et al. 2002] Bazant, Z.P. 2002. *Concrete fracture models: testing and practice*, Engng Fract Mech., Vol. 69, pp. 165-205.
- [Belytschko et al. 1994] Belytschko, T., Gu, L., Lu, Y.Y. 1994, *Fracture and Crack growth by element free Galerkin method*, Model. Simulation Mat. Sc. Engng, Vol. 2, pp. 519-534.
- [Bentz et al. 1995] Bentz, Dale P., Schlangen, E. & Garboczi, Edward J. 1995. *Computer Simulation of Interfacial Zone Microstructure and its effect on the Properties of Cement-Based Composites*, Mat. Sc. Conc. IV, <http://fire.nist.gov/bfrlpubs/build95/PDF/b95013.pdf>
- [Bentz et al. 2002] Bentz, D.P., Haecker, C.J., Feng, X.P., Stutzman, P.E. 2002. *Prediction of cement physical properties by Virtual Testing*, Fifth International VDZ Congress,

- Proceedings. Düsseldorf, Germany, Vol. 23-27, pp. 53-63, <http://ciks.cbt.nist.gov/~bentz/vdzconf/>.
- [Berro 2001] Berro, A. 2001. Optimisation multiobjectif et stratégies d'évolution en environnement dynamique, Thèse de doctorat, Université des Sciences Sociales Toulouse I, Spécialité Informatique.
- [Bouchard et al. 2000] Bouchard, P.-O., Bay, F., Chastel, Y., Tovenà, I. 2000. *Crack propagation modelling using an advanced remeshing technique*, Comp. Meth. in Applied Mech. and Engng, Vol. 189, pp. 723-742.
- [Bouchard et al. 2003] Bouchard, P.O., Bay, F., Chastel, Y. 2002. *Numerical modelling of crack propagation : automatic remeshing and comparison of different criteria*, Comput. Methods Appl. Mech. Engng., Vol. 192, pp. 3887-3908.
- [Bouchard 2005] Bouchard, P.-O. 2005. *Towards an integrated approach between forming processes and structural analysis*. [http://www-cemef.cma.fr/fr/presentation/pagesperso/pob/research\\_activities\\_POB.doc](http://www-cemef.cma.fr/fr/presentation/pagesperso/pob/research_activities_POB.doc)
- [Bournazel 1997] Bournazel, J.P., Moranville-Regourd, M. 1997. *Durability of Concrete: the crossroad between chemistry and mechanics*, Cement and Concrete Research, vol. 27, No. 10, pp. 1543-1552.
- [Bulteel et al. 2002] Bulteel, D. Garcia-Diaz, E. Siwak, Vernet, C. Zanni, 2000. *Alkali-Aggregate Reaction: A method to quantify the reaction degree*, 11<sup>th</sup> Int. Conf. on AAR in Concr., Canada, Quebec, pp. 11-20.
- [Caquot 1937] Caquot A., 1937. *Le rôle des matériaux inertes dans le béton*, Mémoires de la société des Ingénieurs civils de France, pp. 562-592.
- [Capra et al. 1998] Capra, B., Bournazel, J. P. 1998. *Modeling of induced mechanical effects of alkali-aggregate reactions*, Cement and Concr. Res., Vol. 28, No. 2, pp. 251-260.
- [Carter 2000] Carter, B.J., Wawrzynek, P.A., Ingraffea, A.R. 2000, *Automated 3D crack growth simulation*, Gallaher Special Issue of Int. J. Num. Meth. Engng, Vol. 47, pp. 229-253.
- [Chatterji et al. 1990] Chatterji, S., Christensen, P. 1990. *Studies of the Alkali-Silica Reaction: Part 7. Modeling of Expansion*, Cement and Concr. Res., Vol. 20, pp. 285-290.
- [CEB 1990] CEB-FIP Model Code 1990. *Bulletin d'information du CEB*, Vol. 21.
- [Cervenka 1994] Cervenka, J. 1994. Discrete Crack modelling in concrete structures, PhD. thesis, University of Colorado, Boulder, Colorado.
- [Clark 1991] Clark, L.A. 1991. *Modeling the Structural Effects of Alkali-aggregate Reactions on Reinforced Concrete*, ACI Mat. J., Vol. 88, No.3, pp. 271-277.
- [Cordon et al. 1963] Cordon, W.A., Gillepsie, H.A. 1963. J. ACI. Proc., Vol. 60, No. 8.

- [Coupez 1991] Coupez T., 1991. Grandes déformations incompressibles – remaillage automatique, Thèse de l'Ecole des Mines de Paris, CEMEF, Sophia-Antipolis (France).
- [De Borst et al. 2002] De Borst, R. 2002. Fracture in quasi-brittle material: A review of continuum damage-based approaches. *Engng Fracture Mech.* Vol. 69, No 2, pp. 95-112.
- [Dehaut 2002] Dehaut, S. 2002, Etude de la dégradation d'un béton soumis à la réaction alkali-granat, Ph.D thesis, Département Génie Civil de l'Ecole des Mines de Douai, Douai, France.
- [de Larrard 1999] de Larrard, F. 1999. *Concrete mixture-Proportionning – A scientific approach*, Modern Concrete Technology series, No. 9, E & FN SPON, Londres.
- [Dent-Glasser et al. 1981] Dent-Glasser, L.S., Kataoka, N. 1981. *The chemistry of alkali-aggregate reaction*, *Cement and Concr. Res.*, Vol. 11, pp. 1-9.
- [Dougill 1976] Dougill, J.W. 1976. *On stable progressively fracture solids*, *J. of Applied Math. and Physics*, Vol. 27, pp. 423-437.
- [Dugdale 1960] Dugdale, D.S., 1960. *Yielding of steel sheets containing slits*, *J. of the Mech. and Physics of Solids*, Vol. 8, pp. 100-108.
- [Elices et al. 2002] Elices, M., Guinea, G.V., Gomez, J., Planas, J. 2002. *The cohesive zone model: advantages, limitations and challenges*, *Engng Fr. Mech.*, Vol. 69, pp. 137-163.
- [Erdogan et al. 1963] Erdogan, F., Sih, G.C. 1963. *On the crack extension in plates under plane loading and transverse shear*, *J. of Basic Engng*, Vol. 85, pp. 519-527.
- [Ernstroy et al. 1955] Ernstroy, H.C. and Shacklock, B.W. 1955. *Design of high strength concrete mixes*, *Proc. of a symposium of mix design and quality Control of Concr.*, London, Cement and Concr. Ass., pp. 55-73.
- [Eshelby 1957] Eshelby, J.D., 1957. *The elastic field of an ellipsoid inclusion and related Problems*, *Proceedings of the Royal Society of London, Series A, Mathematical and Physical Sciences*, Vol. 241, No. 1226, pp. 376-396.
- [Farran 1956] Farran, J. 1956. *Contribution minéralogique à l'étude de l'adhérence entre les constituants hydrates des ciments et les matériaux enrobés*, *Revue des Matériaux de Constructions*, No. 490-91, pp. 155-172.
- [Fichant 1996] Fichant, S. 1996. Endommagement et anisotropie induite du béton de structures. Modélisations approchées, Thèse de doctorat, ENS Cachan (France).
- [Forestier 2004] Forestier, R. 2004. Développement d'une méthode d'identification de paramètres par analyse couplée inverse avec un modèle éléments finis 3D, Thèse de l'Ecole des Mines de Paris – CEMEF, Sophia-Antipolis (France).
- [Frantzeskakis 1987] Frantzeskakis, C., Contribution à la modélisation des structures en béton armé par la méthode des éléments finis, Thèse de Doctorat, ENPC (France).

- [Fulland et al. 2003] Fulland, M., Richard, H. A. 2003. *Numerical determination of crack paths in three-dimensional structures with the program system ADAPCRACK3D*, Proc. Of Int. Conference of fatigue Crack Path FCP, Parma.
- [Furusawa et al. 1994] Furusawa, Y., Ohga, H. Uomoto, T. 1994. *An analytical study concerning prediction of concrete expansion due to alkali-silica reaction*, Durability of Concrete: Third International Conference, ACI SP 145-40, pp. 757-778.
- [Garcia-Diaz et al. 2003] Garcia-Diaz E., Riche J., Bulteel D., 2003 *A new method to improve the diagnose of the alkali-silica reaction in concrete*, 1st International Conference of Concrete Repair, Proc. Of Int. Conf. of Saint Malo, Vol. 1, pp. 391-398.
- [Garcia-Diaz et al. 2004] Garcia-Diaz, E., Riche, J., Bulteel, D., Vernet, C. 2004. *Damage mechanism for a flint aggregate submitted to alkali-silica reaction*, 12th Int. Conf. on Alkali-Aggregate Reaction in Concrete, Int. Conf. of Bejin.
- [Geers et al. 1996] Geers, M.G.D, Peijs, A.A.J.M., Brekelmans, W.A.M, De Borst, R. 1996. *Experimental monitoring of strain localization and failure behaviour of composite materials*, Composite Science & Technology, Vol. 56, No. 11, pp. 1283-1290.
- [Germann et al. 1998] Germann Instruments Inc. 1998. *4C-Temperature & Stress; Temperature and Stress simulation during hardening*, User Manual, Evanston, Illinois.
- [Gupta et al. 1984] Gupta, A.K., Akbar, H. 1984. *Cracking in reinforced Concrete analysis*, Journal of Engineering Mechanics, ASCE, Vol. 110, No. 8, pp.1735-1746.
- [Häfner et al. 2006] Häfner, S., Eckardt, S., Luther, T., Könke, C. 2005. *Mesoscale modeling of concrete: Geometry and numerics*, Comp. and Struc., Vol. 84, pp. 450-461.
- [Haidar 2002] Haidar, K. 2002. *Modélisation de l'endommagement des structures en béton – Approches numériques et effet de la microstructure sur les propriétés du béton*, PhD Thesis, Ecole Centrale de Nantes (France).
- [Hill 1952] Hill, R. 1952. *The elastic behaviour of a crystalline aggregate*, Proc. Phys. And Soc., A65, Vol. 389, pp. 349-355
- [Hillerborg et al. 1976] Hillerborg, A., Modeer, M., Petersson, P.E. 1976. *Analysis of crack formation and crack growth in concrete by mean of fracture mechanics and finite elements*, Cement and Concr. Res.. Vol. 6, No. 6, pp. 773-782.
- [Jason 2004] Jason, L. 2004. *Relation Endommagement Perméabilité pour les bétons, Applications aux calculs de structures*, Thèse de Doctorat, Ecole Centrale de Nantes (France).
- [Jirasek 1999] Jirasek, M. 1999. *Numerical modeling of deformation and failure of materials*, Lecture notes.
- [Johnston 1968] Johnston, C.D., Sidwell, E.H. 1968. *Testing concrete in tension and in compression*, Mag. Of Concr. Res., Vol. 20, No. 65, pp. 223-230.

- [Kachanov 1958] Kachanov, L. M. 1958. *Time of the rupture process under creep conditions*, Izv. Akad. Nauk. S.S.R., Otd. Tekh. Nauk., No. 8, pp. 26-31.
- [Kupfer et al. 1969] Kupfer, H., Hilsdorf, H.K. and Rüschi, H. 1969. *Behavior of Concrete under Biaxial Stresses*, J. of Americal Concr. Inst., Vol. 66, No. 66-62, pp. 656-666.
- [La Borderie 2003] La Borderie, C. 2003. *Stratégie et modèle de calculs pour les structures en béton*, thèse présentée pour l'obtention à diriger les recherches, Laboratoire de Sciences Appliquées au Génie Civil Institut supérieur Aquitain du Bâtiment et des Travaux Publics Faculté des Sciences et Techniques de la Côte Basque Université de Pau et des Pays de l'Adour (France).
- [Larive et al. 1996] Larive C., Coussy, O. 1996. *Behavior of AAR-affected Concrete, Modeling, Proc.*, 10<sup>th</sup> AAR Int. Conf., Québec, Canada, pp. 662-669
- [Le Bellego 2003] Le Bellego, C., Dubé, J.F., Pijaudier-Cabot, G. Gérard, B. 2003. *Calibration of non local damage model from size effect tests*, Eur. J. of Mech. A/Solids, pp. 33-46.
- [Leite et al. 2003] Leite, J.P.B., Slowik, V., Mihashi, H. 2003. *Computer simulation of fracture processes of concrete using mesolevels models of lattices structures*, Cement and Concrete Research, Vol. 34, No. 6, pp. 1025-33.
- [Lemaître et al. 1992] Lemaître, J., Chaboche, J.L. 1992. *Mechanics of solid material*, Cambridge University Press.
- [Li et al. 2003] Li, Z.H., Chandra, N., 2003. *Analysis of crack growth and crack tip plasticity in ductile materials using cohesive zone models*, Int., J. Plast. Vol. 19, pp. 849-882.
- [Li Cham Yon 2005] Li Cham Yon, E. 2005. *Etudes de méthodes d'optimisation numérique pour la modélisation de la propagation de fissure 3D*, Rapport de stage, CEMEF.
- [Lilliu et al. 2002] Lilliu, G. Van Mier, J.G.M. 2003. *3D Lattice type fracture model for concrete*, Engng Fr. Mech., Vol. 70, pp. 927-941.
- [Lin et al. 1975] Lin, C.S., Scordelis, A. 1975. *Non Linear Analysis of RC shells of general form*, J. of Struct. Div., ASCE, Vol. 101, No. 3, pp. 523-538.
- [Lopez et al. 2001] Lopez, C.M., Murcia, J., Mestre, X., Carol, I. 2001. *Microstructural modeling of concrete using fracture and diffusion-based interface elements*, Fr. Mech. of Concr. Struct., pp 809-815.
- [Mac Creath et al. 1969] Mac Creath, D. R., Newman, J.B., Newman, K. 1969. *The influence of aggregate particles on local strain distribution and fracture mechanism of cement paste during drying shrinkage and loading to failure*, Mat. and Struct., Vol. 2, No. 7, pp. 73-84.
- [Mazars 1984] Mazars, J. 1984. *Application de la Mécanique de l'endommagement au comportement non linéaire et à la rupture du béton de structure*, Thèse de Doctorat d'état, Univ. Paris VI (France).

- [Mazars et al. 1989] Mazars, J., Berthaud, Y. 1989. *Une technique expérimentale appliquée au béton pour créer un endommagement diffus et mettre en évidence son caractère unilatéral*, C.R. Acad. Sciences. Paris, T. 308, Série II, pp. 579-584.
- [Mehta et al. 1993] Mehta, P.K., Monteiro, P.J.M. 1993. *Concrete: properties, Microstructure and Materials*, The McGraw-Hill Companies, Inc., New-York
- [Melenk et al. 1996] Melenk, J.M., Babuska, I. 1996. The partition of unity finite element method: basic theory and applications, *Comp. Methods in Applied Mech. and Engng*, Vol. 39, pp. 289-314.
- [Menou 2004] Menou, A. 2004, Etude du comportement thermomécanique des bétons à haute température : approche multi-échelles de l'endommagement thermique, PhD Thesis, CSTB-Université de Pau et des Pays de l'Adour (France).
- [Mitchell et al. 2004] Mitchell L.D., Beaudoin J.J., Grattan-Bellew P., 2004. *The effects of lithium hydroxide solution on alkali silica reaction gels created with opal*, *Cement and Concr. Res.*, Vol. 34, pp. 641-649.
- [Moës et al. 2002] Moës, N., Belytschko, T. 2002. *Extended Finite element method for cohesive crack growth*, *Engng Fr. Mech.*, Vol. 69, pp. 813-833.
- [Mounajed 2002] Mounajed, G. 2002, *Exploitation du nouveau modèle « Béton numérique dans Symphonie, Concept, homogénéisation du comportement thermomécanique des BHP et simulation de l'endommagement thermique*, Cahiers du CSTB.
- [Mülhaus et al. 1987] Mülhaus, H.B., Vardoulakis, I. 1987. *The thickness of shear bands in granular materials*, *Géotechnique*, Vol. 37, pp. 271-283.
- [Ngo et al. 1967] Ngo, D., Scordelis, A.C. 1967. *Finite element analysis of reinforced concrete beams*, *J. of the American Concr. Inst.*, Vol. 64, No. 3, pp. 152-163
- [Ohmenhäuser et al. 1999] Ohmenhäuser, F., Weihe, S., Kröplin, B. 1999. *Algorithmic implementation of a generalized cohesive crack model*, *Comp. Mat. Sc.*, Vol. 16, pp. 294-306.
- [Peerlings et al. 1996] Peerlings, R.H.J., de Borst, R., Brekelmans, W.A.M., de Vree, J.H.P., 1996. *Gradient-enhanced damage for quasi-brittle materials*. *Int. J. of Numerical Methods Engng*, Vol. 39, pp. 3391-3403.
- [Pichelin et al. 2001] Pichelin, E., Mocellin, K., Fourment, L., Chenot, J.-L., *an application of a master-slave algorithm between deformable bodies in forming processes*, *Eur. J. of Finite Elements*, Vol. 10, No. 8, pp. 857-880.
- [Pijaudier-Cabot et al. 1997] Pijaudier-Cabot, G. & Bazant, ZP. 1997. *Non local damage theory*, *ASCE, J. of Engng Mech.*, Vol. 113, pp. 1512-1533.

- [Pijaudier-Cabot et al. 1993] Pijaudier-Cabot G., Benallal A. 1993. *Strain localization and bifurcation in a nonlocal continuum*, Int. J. of Solids and Struct., Vol. 13(30), pp. 1761-1775.
- [Ramtani 1990] Ramtani, S. 1990. Contribution à la modélisation du comportement multiaxial du béton endommagé avec description du caractère unilatéral, Thèse de Génie Civil, Univ. Paris VI (France).
- [Rashid 1968] Rashid, Y.R. 1968. *Analysis of prestressed concrete pressure vessels*, Nuclear Engineering and Design, Vol. 7, pp. 334-344.
- [Rashid 1998] Rashid, M.M. 1998. *The arbitrary local mesh replacement method: an alternative to remeshing for crack propagation analysis*, Comp. Meth. in Appl. Mech. And Engng., Vol. 154, pp. 133-150.
- [Rechenberg 1973] Rechenberg, I. 1973 *Evolutionsstrategie: Optimierung technischer Systeme nach Prinzipien der biologischen Evolution*, Stuttgart.
- [Reuss 1929] Reuss, A. 1929. *Berechnung der Fließgrenz von Mischkristallen auf Grund der Plastizitätsbedingung für Einkristalle*, Math. Mech., Vol. 9, pp. 49-58.
- [Reynouard 1974] Reynouard, J.M. 1974. Structures planes en béton armé – Elaboration d’un modèle du comportement jusqu’à la ruine et résolution numérique, Thèse de Doctorat, Univ. Claude-Bernard De Lyon (France).
- [Richard et al. 2003] Richard, H.A., Fulland, M. Buchholz, F.-G., Schöllmann, M. 2003. *3D fracture criteria for structures with cracks*, Steel Research, Vol. 74, No. 8, pp. 491-497.
- [Riche et al. 2002] Riche, J. Garcia-Diaz, E. Bulteel, D., Siwak, J.M. 2002. *Mechanism of damage for the alkalisilica reaction : relationship between swelling and reaction degree*. Repair, Rejuvenation and Enhancement of Concrete, Proceedings of International Conference of Dundee, Dhir R., Roderick Jones M., Zheng Li Editors, pp. 94-102.
- [Riche et al. 2006] Riche, J., Garcia-Diaz, E., Bulteel, D., Siwak, J.-M., Vernet, C. 2006. *Mechanism of damage for the Alkali-Silica Reaction*, Cement and Concr. Res., Vol. 36, pp. 395-400.
- [Roelfstra 1989] Roelfstra, P.E. 1989. A numerical approach to investigate the properties of concrete – Numerical concrete, PhD thesis, EPFL, Lausanne (Suisse).
- [Rossi et al. 1992] Rossi, P. Wu, X. 1992. Probabilistic model for material behavior analysis and appraisalment of concrete structures, Mag. of Concr. Res., Vol. 44, No. 116, pp 271-280.
- [Rots 1988] Rots, J.G. 1988. Computational modelling of concrete fracture, PhD Thesis, Delft University of Technology, The Netherlands.
- [Sadouki et al. 1988] Sadouki, H., Wittmann, F.H. 1988. *On the analysis of the failure process in composite materials by numerical simulation*, Mat. Sc. Engng; Vol. 104, pp. 9-20.

- [Schlangen et al. 1992] Schlangen, E., Van Mier, J.G.M., 1992. *Simple lattice model for numerical simulation of fracture of concrete materials and structures*, Mater. Struct; Vol. 25, pp 534-42.
- [Schöllmann et al. 2002] Schöllmann, M. Richard, H.A., Kullmer, G., Fulland, M. 2002. *A new criterion for the prediction of crack development in multiaxially loaded structures*, Int. J. of Fr., Vol. 117, pp. 129-141.
- [Schöllmann et al. 2003] Schöllmann, M., Fulland, M., Richard, H.A., 2003. *Development of a new software for adaptive crack growth simulations in 3D structures*, Engng Fr. Mech., Vol. 70, pp. 249-268.
- [Schorn et al. 1991] Schorn, H., Rode, U. 1991. *Numerical simulation of crack propagation from microcracking to fracture*. Cem. and Concr. Composites, Vol.13, pp. 87-94.
- [Sellier 1995] Sellier, A. 1995. *Modélisations probabilistes du comportement de matériaux et structures en génie-civil*, Ph.D thesis, Ecole Normale Supérieure de Cachan, Paris (France).
- [Sellier et al. 1997] Sellier, A., Capra, B. 1997. *Modélisations physico-chimique de la réaction alcali-granat: apport au calcul des structures dégradées*, Revue fr. de génie civil, Vol. 3, pp. 445-481.
- [Simons et al. 1997] Simons, J.W., Antoun, T.H., Curran, D.R., 1997. *A finite Element Model for analysing the dynamic cracking response of concrete*, SRI International, Menlo Park, CA 94025, Presented at 8th International Symposium on Interaction of the Effects of Munitions with Structures, McClean, Virginia
- [Sluys et al. 1994] Sluys, L.J., De Borst, R. 1994. *Dispersive properties of gradient dependent and rate dependant media*, Mech. Mat., Vol. 18, pp. 131-149.
- [Smaoui et al. 2003] Smaoui, N., Bérubé, M-A., Fournier, B., Bissonnette, B. 2003. *Influence of Specimen Geometry, Orientation of casting Plane, and Mode of Concrete Consolidation on Expansion Due to ASR*, submitted to Cement, Concr. and Aggregates.
- [Stock et al. 1979] Stock, A.F., Hannan, D.J., Williams, R.I.T. 1979. *The effect of the aggregate concentration upon the strength and modulus of elasticity of concrete*, Cement and Concr. Res., pp.225-233.
- [Sukumar et al. 2000] Sukumar, N., Moës, N., Moran, B., Belytschko, T. 2000. *Extended Finite element method for three-dimensional crack modelling*, Int. J. for Num. methods in Engng, Vol. 48, pp. 1549-1570.
- [Swamy 1992] Swamy, R. N. 1992. *The Alkali-Aggregate Reaction in Concrete*, New York.
- [Tabiei et al. 2003] Tabiei, A., Wu, J. 2003. *Development of the Dyna3D simulation code with automated fracture procedure for brick elements*, Int. J. for Num. Meth in Engng, Vol.57.

- [Terrien 1980] Terrien, M. 1980. *Emission acoustique et comportement mécanique post-critique*, bulletin de liaison des laboratoires des Ponts et Chaussées, Vol. 105, pp. 65-72.
- [TFHRC 2003] *Guidelines for the use of lithium to mitigate or prevent Alkali-Silica Reaction*, FHWA-RD-03-047, US Dpt of transportation, Res., Dvpt, and Tech., <http://www.tfhrc.gov/pavement/pccp/pubs/03047/>
- [Vervuurt 1997] Vervuurt, A. 1997. *Interface Fracture in Concrete*, PhD thesis, TU Delft.
- [Voigt 1889] Voigt, W., 1889. *Über die beziehung zwischen den beiden Elastizitätskontanten isotroper Körper*, Wied. Ann. Vol. 38, pp. 573-587.
- [Walter 1999] Walter, H. 1999. *Modélisation 3D par éléments finis du contact avec frottement et de l'endommagement du béton. Application à l'étude de fixations ancrées dans une structure en béton*, PhD Thesis, Institut National des Sciences Appliquées de Lyon.
- [Wang 1994] Wang, J. 1994., *Development and application of a micromechanics-based numerical approach for the study of crack propagation in concrete*, PhD Thesis, EPFL, Lausanne (Suisse).
- [Wang et al. 1992] Wang, J., Navi, P., Huet, C. 1992. *Application of Fracture Mechanics to the study of Crack Propagation in Concrete Structures Using a granular microcracked model*, Fr. and Damage of Concr. and Rock, Ed. Rossmannith, Vienna, pp. 176-185.
- [Wang et al. 1999] Wang, Z.M., Kwan AKH, Chan AC., 1999. *Mesoscopic study of concrete I: generation of random aggregate structure and finite element mesh*, Comput. Struct; Vol. 70, No. 5, pp. 533-44.
- [Washa 1998] Washa, G.W. 1998. *Strength and Elastic Properties*, Chapter 6, Concrete Construction Handbook, ed. Dobrowolski, J. McGraw-Hill, 4th ed., New York.
- [Wittman et al. 1993] Wittmann, F.H., Sadouki, H. Steiger, T., 1993. *Experimental and numerical study of effective properties of composite materials*. In: Huet C, editor. *Micromech. of Concr. and cementitious composites*. Universitaires Romandes Lausanne; pp 59-82.
- [Xi et al. 1999] Xi, Y., Suwito, A., Meyer, C., Jin, W. 1999. *Testing and modeling of alkali-silica reaction and the associated expansion of concrete*, Mech. of Quasi-Brittle Mat. and Struct., Hermes Science Publications, pp. 217-232, Paris (France).